Solid Mechanics and Its Applications

Petia Dineva
Dietmar Gross
Ralf Müller
Tsviatko Rangelov

Dynamic Fracture of Piezoelectric Materials

Solution of Time-Harmonic Problems via BIEM

Springer

Solid Mechanics and Its Applications

Volume 212

Series editor

G. M. L. Gladwell, Elmira, Canada

For further volumes:
http://www.springer.com/series/6557

Aims and Scope

The fundamental questions arising in mechanics are: *Why?, How?,* and *Howmuch?* The aim of this series is to provide lucid accounts written by authoritative researchers giving vision and insight in answering these questions on the subject of mechanics as it relates to solids.

The scope of the series covers the entire spectrum of solid mechanics. Thus it includes the foundation of mechanics; variational formulations; computational mechanics; statics, kinematics and dynamics of rigid and elastic bodies: vibrations of solids and structures; dynamical systems and chaos; the theories of elasticity, plasticity and viscoelasticity; composite materials; rods, beams, shells and membranes; structural control and stability; soils, rocks and geomechanics; fracture; tribology; experimental mechanics; biomechanics and machine design.

The median level of presentation is the first year graduate student. Some texts are monographs defining the current state of the field; others are accessible to final year undergraduates; but essentially the emphasis is on readability and clarity.

Petia Dineva · Dietmar Gross
Ralf Müller · Tsviatko Rangelov

Dynamic Fracture of Piezoelectric Materials

Solution of Time-Harmonic Problems via BIEM

Springer

Petia Dineva
Department of Solid Mechanics
Institute of Mechanics
Bulgarian Academy of Sciences
Sofia
Bulgaria

Dietmar Gross
Division of Solid Mechanics
TU Darmstadt
Darmstadt
Germany

Ralf Müller
Department of Mechanical and Process Engineering
Institute of Applied Mechanics
TU Kaiserslautern
Kaiserslautern
Germany

Tsviatko Rangelov
Department of Differential Equations and Mathematical Physics
Institute of Mathematics and Informatics
Bulgarian Academy of Sciences
Sofia
Bulgaria

ISSN 0925-0042 ISSN 2214-7764 (electronic)
ISBN 978-3-319-03960-2 ISBN 978-3-319-03961-9 (eBook)
DOI 10.1007/978-3-319-03961-9
Springer Cham Heidelberg New York Dordrecht London

Library of Congress Control Number: 2013957124

Printed on acid-free paper

Springer is part of Springer Science+Business Media (www.springer.com)

Preface

The aim of the book is to reveal the potential of the Boundary Integral Equation Method as an efficient computational tool for treating wave propagation problems in homogeneous and smoothly inhomogeneous piezoelectric solids with defects like cracks and holes.

The interdisciplinary character of the study is based on continuum and fracture mechanics, theory of wave propagation, non-destructive evaluation, computational mechanics and mathematical physics in their pure theoretical and applied sense.

The main results and contributions are the coupled electro-mechanical models, the computational method, its validation and simulations revealing different effects useful for the engineering design and practice.

The main ideas, mechanical models, computational tools and simulation results are designed for master degree students, Ph.D. students and researches who like to specialize in the field of dynamic computational fracture mechanics and its connections with wave propagation theory and continuum mechanics.

The authors are indebted to all who have contributed to this book. Special thanks go to Tatiana Parkhomenko, MSc, who helped to prepare the final figures.

Petia Dineva
Dietmar Gross
Ralf Müller
Tsviatko Rangelov

Contents

Acronyms

AM	Average Method
BE	Boundary Element
BEM	Boundary Element Method
BIDE	Boundary Integro–Differential Equation
BIE	Boundary Integral Equation
BIEM	Boundary Integral Equation Method
BAW	Bulk Acoustic Wave
BVP	Boundary Value Problem
CPV	Cauchy Principal Value
COD	Crack Opening Displacement
DSIF	Dynamic Stress Intensity Factor
EDIF	Electrical Displacement Intensity Factor
EFCF	Electrical Field Consentration Factor
EFIF	Electrical Field Intensity Factor
FEM	Finite Element Method
FGM	Functionally Graded Material
FGPM	Functionally Graded Piezoelectric Material
GCF	Generalized Concentration Field
L	Longitudinal Wave
LQP-BE	Left Quarter Point Boundary Element
NDT	Nondestructive Testing
O-BE	Ordinary Boundary Element
ODE	Ordinary Differential Equation
PDE	Partial Differential Equation
PEM	Piezoelectric Materials
PKHS	PartonKudryavtsevHaoShen
PVDF	Polyvinylidene Fluoride
PZT	Piezoceramic Zirconate Titanate
QMCM	Quasi Monte Carlo Method
QP-BE	Quarter Point Boundary Element
RQP-BE	Right Quarter Point Boundary Element
SAW	Surface Acoustic Wave
SCF	Stress Concentration Factor
SH	Shear Horizontally Polarized Wave

SIF	Stress Intensity Factor
SPM	Shifted Point Method
SQP-BE	Singular Quarter Point Boundary Element
SV	Shear Vertically Polarized Wave

Chapter 1
Introduction

The subject of investigation is an infinite or finite piezoelectric solid with defects. Generalizing the proposed BIEM, new results for different classes of inhomogeneous piezoelectric solids are presented and discussed.

The book can be regarded as a continuation of the book by Zhang and Gross [20] which treats cracks in elastic isotropic homogeneous domains by non-hypersingular BIEM using constant boundary elements and fundamental solutions obtained by Fourier transform and expressed by Bessel functions. We extend and continue this study for cracks and holes in isotropic, anisotropic and piezoelectric domains, using non-hypersingular BIEM. The proposed numerical scheme is based on discretization by quadratic boundary elements and standard collocation method. The BIEM formulations are derived using fundamental solutions obtained by Fourier or by Radon transform. The results in the book have been obtained during the last 10 years working on different scientific projects.

Having in mind the big amount of books and papers on computational fracture mechanics and BIEM we would like to mention some of them that have strong influence on the present study: [18, 20] for the approach to solve wave propagation problems in cracked media by non-hypersingular traction BIEM; [2, 8] for asymptotic behavior of solutions of elliptic boundary value problems in domains with singularities at corners and irregular angular points; [1] with the description of quadratic boundary elements; [7, 9, 15] with the explanation of fracture parameters of piezoelectric materials and stress intensity factor; [6, 10, 16, 17] with the derivation of the fundamental solutions with Fourier and with Radon transform; [3–5, 11–14, 19] where test and benchmark examples for isotropic, anisotropic and piezoelectric domains with cracks and holes helped to test the accuracy of the presented BIEM solutions.

The present book is subdivided into three parts. In Part I the theoretical basics for the numerical studies (Chap. 4) are presented. This includes the mechanic–mathematic theoretical basis concerning the piezoelectric materials, constitutive equations and equations of motion (Chap. 2), fundamental solutions (Chap. 3) and equivalent to the formulated boundary-value problems the corresponding integro–

P. Dineva et al., *Dynamic Fracture of Piezoelectric Materials*,
Solid Mechanics and Its Applications 212, DOI: 10.1007/978-3-319-03961-9_1,

differential equations (Chap. 4). In Part II results for homogeneous cracked piezoelectric solids are presented. Several test example are solved for the uncoupled case, i.e., anisotropic materials (Chap. 5) and for piezoelectric ones in unbounded domain (Chap. 6) and in bounded domains (Chap. 7). Furthermore, different special issues are investigated with BIEM when considering curved cracks, multiple cracks and crack interaction (Chap. 8), or cracks with different electric boundary conditions (Chap. 9). For a restricted class of inhomogeneous piezoelectric materials the BIEM is applied in Part III. The in-plane case is discussed first (Chap. 10), followed by the results for the anti-plane cracked case (Chaps. 11, 12, 13), holes and hole-crack interaction (Chaps. 14, 15).

References

1. Aliabadi AM, Rooke D (1991) Numerical fracture mechanics. Computational Mechanics, Southampton
2. Balas J, Sladek J, Sladek V (1989) Stress analysis by boundary element methods. Elsevier, Amsterdam
3. Chen EP, Sih GC (1977) Scattering waves about stationary and moving cracks. In: Sih GC (ed) Mechanics of fracture: elastodynamic crack problems, Springer, Berlin, pp 119–212
4. Chirino F, Dominguez J (1989) Dynamic analysis of cracks using BEM. Engng Fract Mech 34:1051–1061
5. Dhawan GK (1982) Interaction of elastic waves by a Griffith crack in an infinite transversely-isotropic medium. Int J Fract 19:29–37
6. Gel'fand IM, Shilov GE (1964) Generalized functions, vol 1–5. New York: Academic Press
7. Gross D, Seelig T (2011) Fracture Mechanics: with an introduction to micromechanics. Springer, Berlin
8. Kondratiev V (1967) Boundary problems for elliptic equations in domain with conocal and angular points. In: Proceedings of the Moscow mathematical society, vol 16. pp 227–313
9. Müller R (2005) Configurational forces in defect mechanics and in computational methods. TU Darmstadt: Institut für Mechanik, Forschungsbericht Band 13
10. Norris AN (1994) Dynamic Greens functions in anisotropic piezoelectric, thermoelastic and poroelastic solids. Proc Royal Soc London A447:175–188
11. Ohyoshi T (1973) Effect of orthotropy on singular stresses for a finite crack. ASME J Appl Mech 40:491–497
12. Pao YH, Mow CC (1971) Diffraction of elastic waves and dynamic stress concentration. Crane Russak, New York
13. Shindo Y, Ozawa E (1990) Dynamic analysis of a cracked piezoelectric material. In: Hsieh RKT (ed) Mechanical modeling of new electromagnetic materials, Elsevier, Amsterdam, pp 297–304
14. Shindo Y, Moribayashi H, Narita F (2002) Scattering of antiplane shear waves by a circular piezoelectric inclusion embedded in a piezoelectric medium subjected to a steady-state electrical load. ZAMM-Z Angew Math Mech 82:43–49
15. Suo Z, Kuo C, Barnett D, Willis J (1992) Fracture mechanics for piezoelectric ceramics. J Mech Phys Solids 40:739–765
16. Vladimirov V (1971) Equations of mathematical physics. Marcel Dekker Inc, New York
17. Wang CY, Achenbach JD (1994) Elastodynamic fundamental solutions for anisotropic solids. Geophys Int J 118:384–392
18. Wang CY, Zhang Ch (2005) 2 D and 3 D dynamic Green's functions and time-domain BIE formulations for piezoelectric solids. Eng Anal Bound Elem 29:454–465

19. Wang XD, Meguid SA (2000a) Effect of electromechanical coupling on the dynamic interaction of cracks in piezoelectric materials. Acta Mech 143:1–15
20. Zhang C, Gross D (1998) On wave propagation in elastic solids with cracks. Computational Mechanics, Southampton

Part I
Theoretical Basics

Part I introduces 3D and 2D field equations of piezoelectric materials subjected to dynamic time-harmonic electromechanical loads, followed by formulation of boundary value problems for dynamic behavior of ant-plane and in-plane cracked unbounded and bounded piezoelectric solids in Chap. 2. Formulations of the defined anti-plane and in-plane boundary value problems by non-hypersingular traction boundary integral equations based on the frequency-dependent fundamental solutions derived in a closed form by Radon transform are presented in Chap. 3. Numerical scheme using discretization and collocation method is discussed in Chap. 4.

Chapter 2
Piezoelectric Materials

Abstract After some historical remarks the field equations for piezoelectric materials are presented for the 3D and the 2D case. Furthermore, the boundary value problems in bounded and unbounded cracked domains are formulated.

2.1 Short Historical Overview

In the middle of eighteenth century Carolus Linnaeus and Franz Aepinus first observed that certain materials, such as crystals and some ceramics, generate electric charges in case of a temperature change. Both René Just Haüy and Antoine César Becquerel subsequently attempted to investigate the phenomena further but were unsuccessful. Piezoelectricity as a research field in crystal physics was initiated by the brothers Jacques Curie (1856–1941) and Pierre Curie (1859–1906) with their studies, [4, 5]. They discovered an unusual characteristic of certain crystalline minerals as tourmaline, quartz, topaz, cane sugar and Rochelle salt. It was found that tension and compression generated voltages of opposite polarity and proportional to the applied load. This was called by Hankel [13] the piezoelectric effect. The at first discovered direct piezoelectric effect is shown schematically in Fig. 2.1a, b. The word piezoelectricity comes from Greek and means electricity resulting from pressure (Piezo means pressure in Greek). In the year following the discovery of the direct effect, Lippman [22] predicted the existence of the converse effect basing on fundamental thermodynamic principles. Before the end of 1881 the brothers Curies confirmed experimentally the existence of the converse effect. They showed that if one of the voltage-generating crystals was exposed to an electric field it lengthened or shortened according to the polarity of the field, and in proportion to its strength, see Fig. 2.2.

The study of piezoelectricity remained something of a laboratory curiosity for the years until the World War I. In this period it is worth to mention the textbook on

P. Dineva et al., *Dynamic Fracture of Piezoelectric Materials*,
Solid Mechanics and Its Applications 212, DOI: 10.1007/978-3-319-03961-9_2,

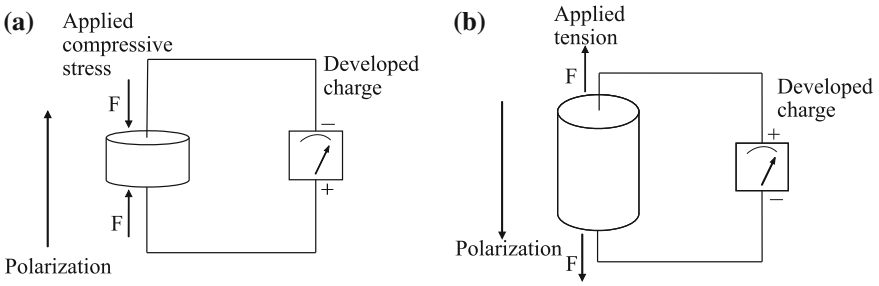

Fig. 2.1 Direct piezo-effect: **a** at applied compressive stress, **b** at applied tension

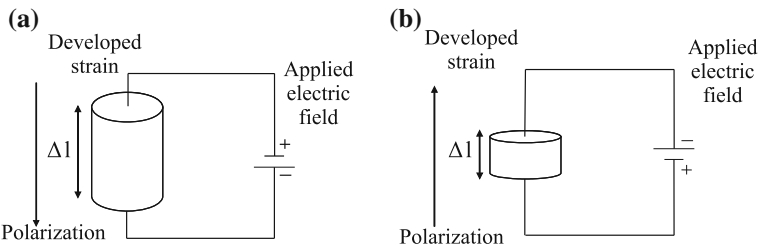

Fig. 2.2 Inverse piezo-effect at applied electric field

crystal physics of Voigt [39] where are described 20 natural crystal classes capable of piezoelectricity with their piezoelectric constants using tensor analysis.

Piezoelectric materials did not come into widespread use until the World War I, when quartz was used as resonators for ultrasound sources in SONAR to detect submarines through echolocation.

A very important stage in the research of piezoelectric materials and especially in their applications in modern engineering practice was the discovery of the phenomenon ferroelectricity by Valasek [38]. Ferroelectric materials exhibit one or more phases and have domain structure in which the individual polarization can be changed by an applied electric field. The first known ferroelectric material was Rochelle salt. Unfortunately, Rochelle salt loses its ferroelectric properties if the composition is slightly changed, which made it rather unattractive for industrial applications. Ferroelectricity was mainly regarded as an interesting physical effect.

During World War II, in the United States, Japan and the Soviet Union, isolated research groups working on improved capacitor materials discovered that certain ceramic materials (prepared by sintering metallic oxide powders) exhibited dielectric constants up to 100 times higher than common cut crystals. Furthermore, the same classes of materials (called ferroelectric) were made to exhibit similar improvements in piezoelectric properties. This led to the manufacturing of synthetic materials whose piezoelectric and dielectric properties are about 100 times higher than the ones of the natural piezoelectric. The discovery of easily manufactured piezoelectric ceramics

with astonishing performance characteristics naturally touched off a revival of intense research and development of piezoelectric devices.

In 1945, piezoelectricity started on the market when it was realized that the mixed oxide compound barium titanate $BaTiO_3$ was a ferroelectric which can easily fabricated and shaped at low price and can made piezoelectric with constants many times higher than natural materials by an electrical poling process. This material is of stable perovskite type, which is one of the fundamental crystal lattice structures. This discovery brought the perovskite type materials into the focus of investigations. Soon other perovskites with ferroelectric properties were discovered, thus opening the path to industrial application. This time could be called the beginning of the era of the piezoelectric ceramic and modern history of piezoelectricity. The following successful results were obtained in the time period 1940–1965:

- Development of the barium titanate family of piezoceramic and the lead zirconate titanate family, see Jaffe et al. [17];
- Development of an understanding of the correspondence of the perovskite crystal structure with electro-mechanical activity;
- Development of a rationale for doping both of these families with metallic impurities in order to achieve desired properties such as dielectric constants, stiffness, piezoelectric coupling coefficients, ease of poling, etc.

Piezoelectricity as one of the branches of crystal physics is now the base of the modern engineering practice in the following technologies:

- Frequency control and signal processing e.g. mechanical frequency filters, surface acoustic wave devices, bulk acoustic wave devices, etc.;
- Sound and ultrasound microphones and speakers, ultrasonic imaging, hydrophones, etc.;
- Actuators and motors based on the converse effect, i.e. when an electric field is applied to a material it will deform in a predictable way. For example, in manufacturing of piezoelectric ceramics it is possible to create rods that deform along the long axis and act like a piston. The amount of deformation can be controlled by the amount of electric field applied to the material. Since the deformations are small, usually within micrometers precision, they are excellent in application that require very small amounts of movement. They have been used as tools for micro precision placement and for micro adjustments in lens for microscopes. The converse effect is used in printers (needle drivers and ink jet), miniaturized motors, bimorph actuators (pneumatics, micropumps, Braille for the blind), multilayered actuators for fine positioning and optics, injection systems in automotive fuel valves, etc.
- Detection of pressure variations in the form of sound is the most common sensor application, e.g. piezoelectric microphones (sound waves bend the piezoelectric material, creating a changing voltage) and piezoelectric pickups for electric guitars. A piezo sensor attached to the body of an instrument or structure is known as a contact microphone giving information of deformation. This is the base of all sensors for strain, mass, flow, pressure online control. By continuously monitoring deformation, the sensors can record operational loads, compute material fatigue, and estimate remaining component life.

- Generator with application in gas and fuel ignition. Piezoelectricity can generate very high voltages but the current is very small. The amount of pressure needed to distort a piezoelectric ceramic element by 0.05 mm can generate nearly 100,000 volts. This amount of voltage is enough to create an electric spark to ignite gas in an oven, grill or pocket lighter.
- Smart structures that use discrete piezoelectric patches to control the response of a structure have been of considerable interest in recent years. The development of modern software makes it possible to fully model coupled thermo–mechanical–electrical systems and obtain reciprocal relations between piezoelectric actuator voltages and system response. By integrating such models into a closed-loop control system, very effective active control on the vibration, noise, shape, deformation, pressure, etc. can be achieved. Structural panels embedded with a series of sensors and actuators can be used in civil, industrial and aerospace structures. These panels can actively monitor the structural integrity and detect faults at early stages, thereby providing precise information on structural failure and life expectancy.
- The concept *Crowd Farm* with the basic idea that large amounts of people moving in dense areas would step on tiles embedded in the floor and these tiles would use piezoelectric materials to generate electricity that could be collected and used. A prototype of the crowd farm has already been tested in a selected number of Japanese train stations.
- Experimental science for investigation of atomistic structure of materials based on the micro-coupling of mechanical and electrical fields.

2.2 Types of Piezoelectric Materials

Piezoelectric materials can be natural or man-made. The natural PEM are crystal materials like quartz ($Si\,O_2$), Rochelle salt, Topaz, Tourmaline-group minerals and some organic substances as silk, wood, enamel, dentin, bone, hair, rubber. Figure 2.3 shows the unit cell of quartz which has specific atomic structure of the lattice which is a tetrahedron built of oxygen atoms around a silicon atom. Each oxygen atom has the same distance to the silicon atom, and the distances between the oxygen atoms are all the same. The change in the position of the atoms due to applied stress leads to the formation of net dipole moments that causes polarization and an electric field, respectively.

Man-made piezoelectric materials are crystals that are quartz analogs, ceramics, polymers and composites.

There are 32 crystal classes which are divided into the following seven groups: triclinic, monoclinic, orthorhombic, tetragonal, trigonal, hexagonal and cubic. These groups are also associated with the elastic nature of the material where triclinic represents an anisotropic material, orthorhombic represents an orthotropic material and cubic are in most cases isotropic materials. Only 20 of the 32 classes alow piezoelectric properties. Ten of these classes are polar, i.e. show a spontaneous polarization without mechanical stress due to a non-vanishing electric dipole moment associated

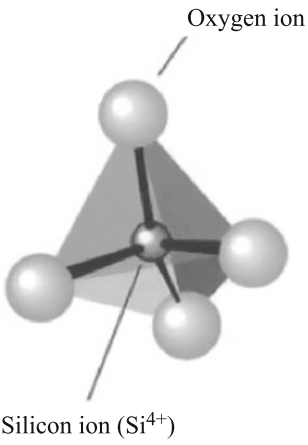

Fig. 2.3 Unit cell of quartz

with their unit cell. The remaining 10 classes are not polar, i.e. polarization appears only after applying a mechanical load.

There are the following families of man-made ceramics with crystal structure as perovskite: Barium titanate ($BaTiO_3$; Lead titanate ($PbTiO_3$); Lead zirconate titanate ($Pb[Zr_xTi_{1-x}]O_3$, $0 < x < 1$)—more commonly known as PZT; Potassium niobate ($KNbO_3$) ; Lithium niobate ($LiNbO_3$); Lithium tantalate ($LiTaO_3$), etc. and other lead-free piezoceramics. The general chemical formulae of perovskite crystal structure is ABO_3 , where A is a larger metal ions, usually lead Pb or barium Ba, B is a smaller metal ion, usually titanium Ti or zirconium Zr, see Fig. 2.4, which shows the crystal structure of a piezoelectric ceramic ($BaTiO_3$) at temperature above and below Curie point.

To prepare a piezoelectric ceramic, fine powders of the component metal oxides are mixed in specific proportions, then heated to form a uniform powder. The powder is mixed with an organic binder and formed into structural elements having the desired shape (discs, rods, plates, etc.). The elements are subsequently fired according to a specific time and temperature program, during which the powder particles sinter and the material attains a dense crystalline structure. The elements are cooled, then shaped or trimmed to specifications, and electrodes are applied to the appropriate surfaces. Above a critical temperature, the *Curie point*, each perovskite crystal in the fired ceramic element exhibits a simple cubic symmetry with no dipole moment, it is in the so-called paraelastic phase (Fig. 2.4a). At temperatures below the Curie point, however, each crystal exhibits a tetragonal or rhombohedral symmetry leading to a dipole moment; this phase of the material is called ferroelectric phase (Fig. 2.4b). When electric field of about 10^6 V/m is applied to the ferroelectric polycrystal as it passes through its Curie temperature, so that its spontaneous polarizations develop, all polarization vectors are aligned in a more or less uniform direction. This process leading to a macroscopic net polarization is called *poling*. Initially there exists a uniform distribution of all direction, i.e. no macroscopic net polarization. After poling: a distribution around the poling direction leads to a macroscopic net polarization.

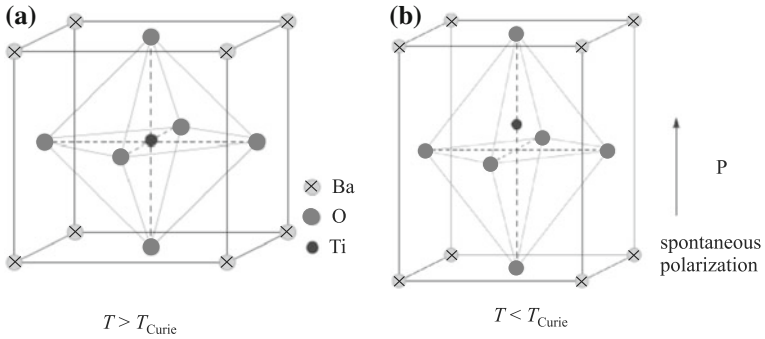

Fig. 2.4 Crystal structure of a traditional piezoelectric ceramic ($BaTiO_3$) at temperature above (**a**) and below (**b**) Curie point

Now, at this stage, when a mechanical stress is applied, the polarization will increase or decrease and the ceramic will have typical piezoelectric behavior. The mechanism of this process will be explained in Sect. 2.3.

The piezoelectricity of polyvinylidene fluoride was discovered by Kawai [18]. PVDF is a ferroelectric polymer, exhibiting piezoelectric and pyroelectric properties. These characteristics make it useful in sensor and battery applications. Thin films of PVDF are used in some newer thermal camera sensors. Piezocomposite materials are an important update of existing piezoceramic, see Newnham [26]. They can be of two types: piezo-polymer in which the piezoelectric material is immersed in an electrically passive matrix (for instance PZT in epoxy matrix) and piezo-composites that are composite materials made by two different ceramics (for example $BaTiO_3$ fibers reinforcing a PZT matrix).

2.3 Physical Peculiarities

Piezoelectric materials are anisotropic dielectrics of special type, where both fields the electrical and the elastic are coupled. Some of them (for instance ceramic) have ferroelectric properties, but the rest of them (as quartz) display no ferroelectric behaviour. In the following a brief explanation is given of the physical properties of dielectrics, ferroelectric, piezoelectric materials and the similarity and difference between them.

A dielectric material is any material that supports charge without conducting it to a significant degree. The main property is that they have no free electrical charges, but when an external electrical field is applied the electric dipoles are being created due to the interaction of the electrical field with the dielectric structure. The electric dipole, see Fig. 2.5 is an electro–neutral unit volume in which the centers of the positive $+q$ and negative $-q$ electric charges (poles) do not coincide and are at distance r, so that the dipole moment $\mu = qr$ arises. The dipole moment is a vector with direction from

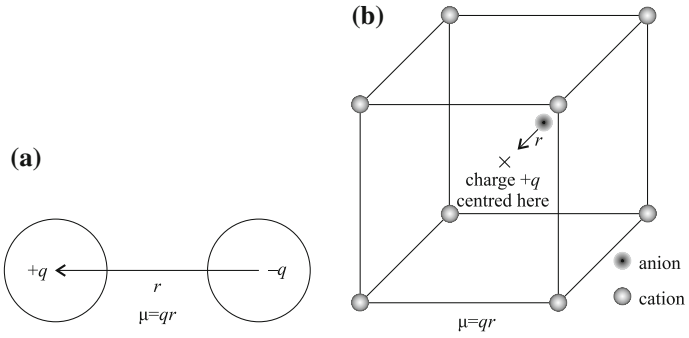

Fig. 2.5 The dipole moment

the negative to the positive pole. Because of dielectric polarization, positive charges are displaced toward the external field and negative charges shift in the opposite direction.

If the center of positive charge within a given region and the center of negative charge within the same region are not in the same position, a dipole moment μ arises. For example, in the Fig. 2.5, the center of positive charge from the eight cations shown is at X, while the center of negative charge is located some distance away on the anion. The second view of dipole moment is more useful, since it can be applied over a large area containing many charges in order to find the net dipole moment of the material.

The polarization of a material is simply the total dipole moment for a unit volume $P = \frac{1}{V}\sum_i \mu_i$, where V is the overall volume of the sample. Because $\sum_i \mu_i$ is a vector sum, a material may contain dipoles without having any net polarization, because dipole moments can cancel out. If a material contains polar molecules, they will generally be in randomly orientated when no electric field is applied, see Fig. 2.6. An applied electric field $E[N/C]$ will polarize the material by orienting the dipole moments of polar molecules in opposite direction—mainly to the applied electrical field E_a. Or, when a dielectric is placed between charged electrode plates, the polarization of the medium produces an electric field E_p opposite to the field of the charges on the plate and then the effective electrical field is: $E_e = E_a - E_p$. The dielectric constant $\varepsilon[C/NM^2]$, which is also called *permittivity*, is the main characteristic of the dielectric. It reflects the amount of reduction of effective electric field as shown in Fig. 2.6. The dielectric constant depends on the polarization properties of the dielectric material, but also on its elastic, thermal, etc. properties. The relative dielectric constant $\varepsilon_\gamma = \frac{\varepsilon}{\varepsilon_0}$ shows how many times the effective electric field decreases in a given dielectric material in comparison with the electric field between the plates when they are in vacuum with a dielectric constant $\varepsilon_0 = 8.85 \times 10^{-12}\,\mathrm{C/Nm^2}$.

Permittivity is directly related to the dimensionless characteristic *electric susceptibility* χ, which is a measure of how easily a dielectric polarizes in response

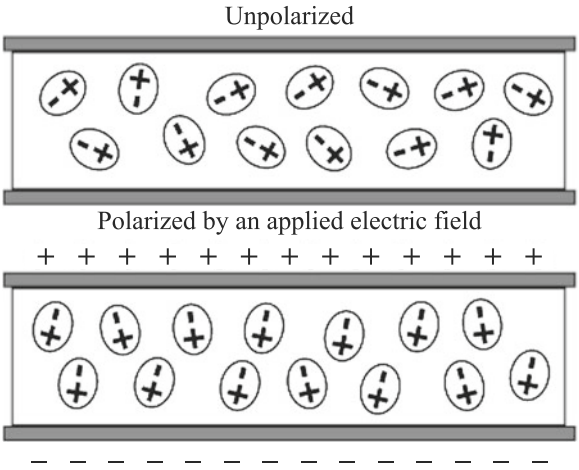

Fig. 2.6 Reduction of an effective electric field due to the polarization

to an electric field. They are related to each other through the scalar relation $\varepsilon = \varepsilon_\gamma \varepsilon_0 = (1+\chi)\varepsilon_0$ for the isotropic case and the tensor relation $\varepsilon_{ij} = (\delta_{ij}+\chi_{ij})\varepsilon_0$ for an anisotropic dielectric materials. An important property of dielectrics is that they posses naturally polarization and in the absence of applied electrical field they have no electric dipoles.

The polarization of piezoelectric material has its specific peculiarities in comparison with polarization of ordinary dielectrics. First we will consider polarization of piezoelectric materials that are not ferroelectric and will discuss the polarization process of quartz as classical representative of this class of materials.

When a piezoelectric is placed under a mechanical stress, the geometry of the atomic structure of the crystal changes, such that ions in the structure separate, and a dipole moment is formed. For a net polarization to develop, the dipole formed must not be canceled out by other dipoles in the unit cell. Therefore the piezoelectric atomic structure must be non-centrosymmetric. When a piezoelectric material is loaded electrically then the electrical dipoles appear, dipole moment is formed and this results in deformation. The polarization is linear as those shown in Fig. 2.7 and electrical dipoles nucleate only after electrical or mechanical load. The other types of piezoelectric materials are with ferroelectric properties, i.e. spontaneous polarization and electric dipoles exist in their structure even in the absence of electrical field. The piezoelectric effect in ferroelectric is strongly dependent on its atomic structure. Depending on the type of a crystal, a compressive stress can increase or decrease the polarization, or sometimes, have no effect at all. For example, let us consider again the two crystal structures of a traditional piezoelectric ceramic at temperature above and below Curie point, presented in Fig. 2.4. The ceramic phase above Curie point is cubic and has no spontaneous polarization. The ceramic phase below the Curie point is a crystal of tetragonal or rhombohedral symmetry and develops spontaneous

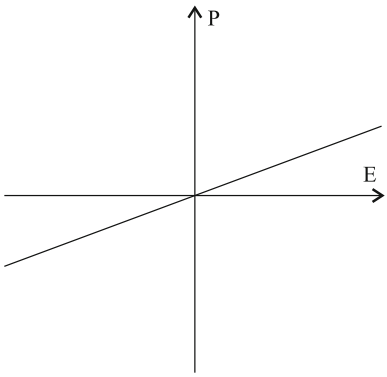

Fig. 2.7 Dielectric polarization

polarization. Piezoelectric properties can be found in the ceramic phase below the Curie point. Materials are polarized along a unique crystallographic direction, in that certain atoms are displaced along this axis, leading to a dipole moment along it. Depending on the crystal system, there may be few or many possible axes. In a crystal, it is likely that dipole moments of the unit cells in one region lie along one of the six directions. Each of these regions is called a domain. A domain is a homogenous region of a ferroelectric, in which all of the dipole moments have the same orientation. In a newly-grown single crystal, there will be many domains, with individual polarizations such that there is no overall polarization. If a mechanical stress is applied to the ferroelectric, then there are domains which will experience an increase in dipole moment and some which will experience a decrease in dipole moment. Overall, there is no net increase in polarization, see Fig. 2.8. This makes BaTiO3 useless as a piezoelectric unless it is put through some additional processing. This process is called *poling*. An electric field is applied to the ferroelectric as it passes through its Curie temperature, so that its spontaneous polarization develops and it is aligned in a single direction. All of the domains in the piezoelectric have a dipole moment pointing in that direction, so there is a net with approximately the same polarization, see Fig. 2.8. When the electric field is removed most of the dipoles are locked in a configuration of near alignment (Fig. 2.8). The full alignment is only possible in a single crystal and in a polycrystalline material there exists still a polarization distribution. The material now has a remanent polarization. The maximum possible value of the remanent polarization is called saturation polarization, i.e. this is the horizontal part of the hysteresis curve in Fig. 2.9. The distinguishing feature of PEM with ferroelectric properties is that the direction of the spontaneous polarization can be reversed by an applied electric field, yielding a hysteresis loop, see Fig. 2.9. The non- linear behavior of the polarization with respect to the applied electrical field consists of three stages which are characterized by:

- reversible domain motion;
- growth of new domains;

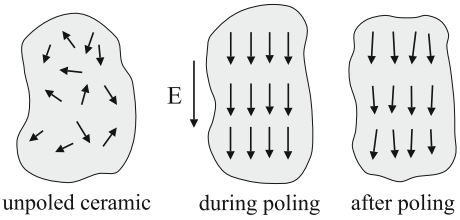

Fig. 2.8 Domain structure of ferroelectric materials and their behavior during poling process

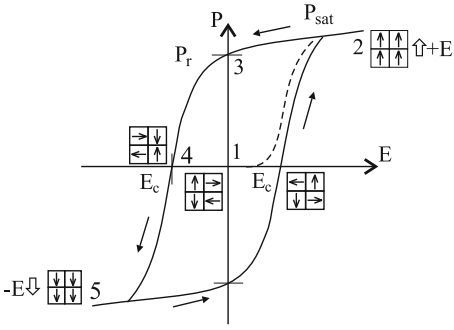

Fig. 2.9 Hysteresis *curve* for polarization of piezoelectric material

- new domains reaching the limit of their growth and reaching the saturation polarization.

Figure 2.9 shows a typical hysteresis curve created by applying an electric field to a piezoelectric ceramic element until the maximum (saturation) polarization P_{sat} is reached, reducing the field to zero determines the remanent polarization P_r reversing the field attains a negative maximum (saturation) polarization and negative remanent polarization, and re-reversing the field restores the positive remanent polarization. When the electric field is the coercive field E_c there is no net polarization due to the mutual compensation of the polarization of different domains.

Summarizing the information of the physical properties of piezoelectric materials presented above, some conclusions can be made:

- PEM is a special type of anisotropic dielectrics where electrical and mechanical fields are coupled due to both the existence of the specific asymmetric atomic structure of the lattice and the existence of spontaneous polarization at the microstructure level;
- The effective usage of both the ferroelectric properties of the piezoelectric ceramics together with the poling process during their manufacture make these materials a basic element in the modern industrial applications.

2.4 Field Equations in 3D

The macroscopic phenomenological theory of piezoelectricity, based on thermodynamic principles, can be traced back to Thompson [36]. However, significant contribution to the theory, as we know it today, was made by Voigt and Duhem. The thermodynamic approach reveals the reversibility and the equivalence of the piezoelectric constants of the direct and converse piezoelectric effects. It is noted that the full thermodynamic derivation should link mechanical, electrical and thermal effects, where the thermo-electric coupling gives rise only to the *pyroelectric* effect. However, since we will not focus on pyroelectricity and as coupling effects are assumed to be linear, the thermal influence can be safely neglected.

2.4.1 Constitutive Equations

For a general piezoelectric material, the total internal energy density U is given by the sum of the mechanical and electrical work done, i.e. in differential form it is

$$dU = \sigma_{ij} ds_{ij} + E_m dD_m. \tag{2.1}$$

Here the mechanical stress σ_{ij} and strain s_{ij} are second rank tensors, E_m is the vector of electric field, D_m is the vector of electrical displacement. All indices run from 1 to 3 and the summation convention over repeated indexes is implied. The polarization vector P_i is introduced to quantify the degree of polarization of the material and it is connected with the vectors of electric field and electrical displacement by the relation, see Parton and Kudryavtsev [29]:

$$D_i = \varepsilon_0 E_i + P_i, \quad P_i = \chi_{ij} E_j. \tag{2.2}$$

In order to derive the constitutive equations of a piezoelectric material different types of thermodynamic potentials can be used as e.g. internal energy $U = U(s_{ij}, D_i)$, the electric Gibbs energy (electric enthalpy) $G_e = G_e(s_{ij}, E_i)$, the Helmholtz free energy $F = F(\sigma_{ij}, D_i)$, the elastic Gibbs energy $G_1(\sigma_{ij}, P_i)$ and the Gibbs free energy $G = G(\sigma_{ij}, E_i)$. The different thermodynamic potentials will facilitate different sets of piezoelectric constitutive formulations, see [10, 15, 20, 29, 37]. Here the constitutive equation derived by using the Gibbs electrical function (electric enthalpy) $G_e(s_{ij}, E_i)$ is presented, assuming it is a quadratic form of s_{ij}, E_i. The Gibbs electrical function is a thermodynamic potential in which the independent variables are the strain deformation s_{ij} and the electrical field E_i, and the dependent flux variables are the stress σ_{ij} and electric displacement (electric flux density) D_i, i.e.

$$dG_e = \left(\frac{\partial G_e}{\partial s_{ij}}\right)_E ds_{ij} + \left(\frac{\partial G_e}{\partial E_m}\right)_s dE_m. \tag{2.3}$$

The differential form of $G_e = U - E_i D_i$, see Ikeda [15], is:

$$dG_e = \sigma_{ij} ds_{ij} - D_m dE_m. \tag{2.4}$$

Comparing Eqs. (2.3) and (2.4) yields

$$\sigma_{ij} = \left(\frac{\partial G_e}{\partial s_{ij}}\right)_E, \quad D_m = -\left(\frac{\partial G_e}{\partial E_m}\right)_s. \tag{2.5}$$

Having in mind that $\sigma_{ij} = \sigma_{ij}(s_{ij}, E_m)$ and $D_i = D_i(s_{ij}, E_m)$, the differentials of stress and electric displacement have the form:

$$d\sigma_{ij} = \left(\frac{\partial \sigma_{ij}}{\partial s_{kl}}\right)_E ds_{kl} + \left(\frac{\partial \sigma_{ij}}{\partial E_m}\right)_s dE_m, \tag{2.6}$$

$$dD_m = \left(\frac{\partial D_m}{\partial s_{kl}}\right)_E ds_{kl} + \left(\frac{\partial D_m}{\partial E_k}\right)_s dE_k. \tag{2.7}$$

The physical meaning of the partial derivatives is as follows:

- $\left(\frac{\partial \sigma_{ij}}{\partial s_{kl}}\right)_E = C_{ijkl}$ is the fourth rank tensor of the elastic stiffness constants at $E = \text{const}$ with $C_{ijkl} = C_{ijlk} = C_{jikl} = C_{klij}$;
- $\left(\frac{\partial \sigma_{ij}}{\partial E_m}\right)_s = -\left(\frac{\partial D_m}{\partial s_{ij}}\right)_E = -e_{ijm}$ is the third rank tensor of the piezoelectric constants at $s_{ij} = \text{const}$ with $e_{kij} = e_{kji}$;
- $\left(\frac{\partial D_m}{\partial E_k}\right)_s = \varepsilon_{mk}$ is the second rank tensor of the dielectric permittivity constants at $s_{ij} = \text{const}$ with $\varepsilon_{ik} = \varepsilon_{ki}$.

In the case of general anisotropy C_{ijkl}, e_{ijm}, ε_{mk} admit 21, 18 and 6 independent components, respectively.

After integration of Eqs. (2.6) and (2.7) at constant partial derivatives the following constitutive equations are obtained:

$$\sigma_{ij} = C_{ijkl} s_{kl} - e_{ijm} E_m, \tag{2.8}$$

$$D_m = e_{mij} s_{ij} + \varepsilon_{mk} E_k. \tag{2.9}$$

The constitutive equations for PEM show coupling between electrical and mechanical quantities. The direct piezoelectric effect or the sensorial effect is described by

Eq. (2.9). This equation shows that an electric polarization and electric field is generated by mechanical stress. The converse effect, or the actuator effect is described by Eq. (2.8) which shows that a PEM undergoes a deformation under an electric field.

The strain-displacement and the electric field-potential relations are given by

$$s_{ij} = \frac{1}{2}(u_{i,j} + u_{j,i}), \quad E_i = -\Phi_{,i}, \tag{2.10}$$

where u_i is the mechanical displacement and Φ is the electrical potential.

The symmetry of the stress tensor enables nine stress components to be reduced to six independent stress components. This also enables the tensor notation to be transformed into a pseudo-tensor form. Using this so-called contracted Voigt subscript notation: $(11) \to 1$, $(22) \to 2$, $(33) \to 3$, $(23) = (32) \to 4$, $(13) = (31) \to 5$, $(12) = (21) \to 6$, the fourth order tensor C_{ijkl} reduces to the matrix representation $C_{\alpha\beta}$ with $(ij) \to \alpha$, $(kl) \to \beta$. In the same way the third order tensor e_{kij} reduces to the matrix representation $e_{k\alpha}$ with $(ij) \to \alpha$. For the analysis of piezoelectric problems it is advantageous to use the notation introduced by Barnett and Lothe [3] and later by [6, 40]. With this notation, the elastic displacement and electric potential, the elastic strain and electric field, the stress and electric displacement, and the elastic and electric coefficients can be grouped as:

- Generalized displacements

$$u_I = \begin{cases} u_i, & I = 1, 2, 3, \\ \Phi, & I = 4 \end{cases} \tag{2.11}$$

- Generalized strain, for $j = 1, 2, 3$,

$$s_{Ij} = \begin{cases} s_{ij}, & I = 1, 2, 3, \\ -E_j, & I = 4. \end{cases} \tag{2.12}$$

- Generalized stresses, for $i = 1, 2, 3$,

$$\sigma_{iJ} = \begin{cases} \sigma_{ij}, & J = 1, 2, 3, \\ D_i, & J = 4. \end{cases} \tag{2.13}$$

- Generalized stiffness matrix for $i, j, k, l = 1, 2, 3$,

$$C_{iJKl} = \begin{cases} C_{ijkl}, & J, K = 1, 2, 3, \\ e_{lij}, & J = 1, 2, 3; , K = 4, \\ e_{ikl}, & J = 4; K = 1, 2, 3, \\ -\varepsilon_{il}, & J = K = 4. \end{cases} \tag{2.14}$$

The symmetry properties of elastic, piezoelectric and dielectric tensors $C_{ijkl}, e_{kij}, \varepsilon_{ij}$ imply the following symmetry property for the extended stiffness tensor:

$$C_{iJKl} = C_{lKJi}. \tag{2.15}$$

In this definition, the lowercase and uppercase subscripts take the values of 1, 2, 3 and 1, 2, 3, 4, respectively. In terms of this shorthand notation, the constitutive relations Eqs. (2.8), (2.9) can be unified into the one single equation

$$\sigma_{iJ} = C_{iJKl} s_{Kl}, \tag{2.16}$$

or in matrix notation

$$\begin{pmatrix} \sigma_{11} \\ \sigma_{22} \\ \sigma_{33} \\ \sigma_{23} \\ \sigma_{31} \\ \sigma_{12} \\ \sigma_{14} \\ \sigma_{24} \\ \sigma_{34} \end{pmatrix} = C \begin{pmatrix} s_{11} \\ s_{22} \\ s_{33} \\ 2s_{23} \\ 2s_{31} \\ 2s_{12} \\ -E_1 \\ -E_2 \\ -E_3 \end{pmatrix}, \tag{2.17}$$

where

$$C = \begin{pmatrix} c_{11} & c_{12} & c_{13} & c_{14} & c_{15} & c_{16} & e_{11} & e_{21} & e_{31} \\ c_{12} & c_{22} & c_{23} & c_{24} & c_{25} & c_{26} & e_{12} & e_{22} & e_{32} \\ c_{13} & c_{23} & c_{33} & c_{34} & c_{35} & c_{36} & e_{13} & e_{23} & e_{33} \\ c_{14} & c_{24} & c_{34} & c_{44} & c_{45} & c_{46} & e_{14} & e_{24} & e_{34} \\ c_{15} & c_{25} & c_{35} & c_{45} & c_{55} & c_{56} & e_{15} & e_{25} & e_{35} \\ c_{16} & c_{26} & c_{36} & c_{46} & c_{56} & c_{66} & e_{16} & e_{26} & e_{36} \\ e_{11} & e_{12} & e_{13} & e_{14} & e_{15} & e_{16} & -\varepsilon_{11} & -\varepsilon_{12} & -\varepsilon_{13} \\ e_{21} & e_{22} & e_{23} & e_{24} & e_{25} & e_{26} & -\varepsilon_{12} & -\varepsilon_{22} & -\varepsilon_{23} \\ e_{31} & e_{32} & e_{33} & e_{34} & e_{35} & e_{36} & -\varepsilon_{31} & -\varepsilon_{32} & -\varepsilon_{33} \end{pmatrix}. \tag{2.18}$$

As discussed in Sect. 2.3, piezoelectric materials show in most cases a crystal structure with a symmetry of hexagonal 6 mm class. In the case that the poling axis coincides with one of the material symmetry axes these materials become transversely isotropic. Transversely isotropic elastic materials are those with an axis of symmetry such that all directions perpendicular to this axis are equivalent. In other words, any plane perpendicular to the axis is a plane of isotropy. In the case of a transversely isotropic solid, the number of the independent elastic, piezoelectric and dielectric constants is 5, 3 and 2 respectively. In this case matrix C in Eq. (2.18) takes the form

$$C = \begin{pmatrix} c_{11} & c_{12} & c_{13} & 0 & 0 & 0 & 0 & 0 & e_{31} \\ c_{12} & c_{11} & c_{13} & 0 & 0 & 0 & 0 & 0 & e_{31} \\ c_{13} & c_{13} & c_{33} & 0 & 0 & 0 & 0 & 0 & e_{33} \\ 0 & 0 & 0 & c_{44} & 0 & 0 & 0 & e_{15} & 0 \\ 0 & 0 & 0 & 0 & c_{44} & 0 & e_{15} & 0 & 0 \\ 0 & 0 & 0 & 0 & 0 & c_{66} & 0 & 0 & 0 \\ 0 & 0 & 0 & 0 & e_{15} & 0 & -\varepsilon_{11} & 0 & 0 \\ 0 & 0 & 0 & e_{15} & 0 & 0 & 0 & -\varepsilon_{11} & 0 \\ e_{31} & e_{31} & e_{33} & 0 & 0 & 0 & 0 & 0 & -\varepsilon_{33} \end{pmatrix}, \tag{2.19}$$

where $c_{66} = \dfrac{1}{2}(c_{11} - c_{12})$

The elasticity coefficients C_{ijkl} and the dielectric constants ε_{ij} are said to be positive-definite if

$$c_{ijkl} q_{ij} q_{kl} > 0, \quad \varepsilon_{il} a_i a_l > 0 \tag{2.20}$$

for any non-zero tensor q_{ij} and any non-zero vector a_i and the following reciprocal symmetries hold due to Eq. (2.16)

$$c_{ijkl} = c_{jikl} = c_{klij}, \quad e_{ijk} = e_{ikj} \quad \varepsilon_{jk} = \varepsilon_{kj}. \tag{2.21}$$

Essentially, these constraints are thermodynamic constraints expressing that the internal energy density must remain positive since this energy must be minimal in a state of equilibrium, see Dieulesaint and Royer [7]. Specializing for the case of transversely isotropic solids, one obtains, see Alshits and Chadwick [2]:

$$c_{11} > |c_{12}|, \quad (c_{11} + c_{12}) c_{33} > 2c_{13}^2, \quad c_{44} > 0, \quad \varepsilon_{11} > 0, \quad \varepsilon_{33} > 0. \tag{2.22}$$

2.4.2 Equations of Motion

The governing equations are given by the equations of motion for the mechanical displacement and by the equations of electrostatic. The electric field that develops in piezoelectrics can assumed to be quasi-static because the velocity of the elastic waves is much smaller than the velocity of electromagnetic waves. Therefore, the magnetic field due to the elastic waves is negligible. This fact implies that the time derivative of the magnetic field B is close to zero, i.e. $\dfrac{\partial B}{\partial t} \approx 0$. Thus one of Maxwell's equations of electrodynamics becomes $\mathrm{rot} E = \dfrac{\partial B}{\partial t} \approx 0$, hence $E = -\mathrm{grad}\Phi$. Consequently, a piezoelectric continuum is based on the governing equations of elastodynamics in the case of small deformations and quasi-electrostatic fields. Restricting to the case

of time-harmonic motion with frequency ω and suppressing the common factor $e^{i\omega t}$ in all terms, the equation of motion read

$$\sigma_{ij,j} + \rho\omega^2 u_i = -b_i, \quad D_{i,i} = -q. \tag{2.23}$$

Here b_i is the body force, ρ is the mass density and q is free electric volume charge. In generalized notation Eq. (2.23) is written as

$$\sigma_{iJ,i} + \rho_{JK}\omega^2 u_K = -F_J, \tag{2.24}$$

where $F_J = (b_i, q)$ and $\rho_{JK} = \begin{cases} \rho, & J, K = 1, 2, 3 \\ 0, & J \text{ or } K = 4 \end{cases}$

The field equations are represented by Eqs. (2.10), (2.16) and (2.24). These group of equations in generalized notation lead to the following equation of motion in the absence of body forces ($b_i = 0$) and free volume charges ($q = 0$)

$$C_{iJKl}u_{K,li} + \rho_{JK}\omega^2 u_K = 0, \quad i, l = 1, 2, 3; \quad J, K = 1, \ldots, 4. \tag{2.25}$$

or in coordinate notation:

$$\begin{cases} c_{11}u_{1,11} + c_{44}u_{1,33} + (c_{13} + c_{44})u_{3,13} + c_{66}u_{1,22} + \dfrac{1}{2}(c_{11} + c_{12})u_{2,12} \\ +(e_{31} + e_{15})u_{4,13} + \rho\omega^2 u_1 = 0, \\ \dfrac{1}{2}(c_{11} + c_{12})u_{1,12} + c_{66}u_{2,11} + c_{11}u_{2,22} + c_{44}u_{2,33} + (c_{13} + c_{44})u_{3,23} \\ +(e_{31} + e_{15})u_{4,33} + \rho\omega^2 u_2 = 0, \\ (c_{13} + c_{44})u_{1,13} + c_{44}(u_{3,11} + u_{3,22}) + c_{33}u_{3,33} + (c_{13} + c_{44})u_{2,23} \\ +e_{15}(u_{4,11} + u_{4,22}) + e_{33}u_{4,33} + \rho\omega^2 u_3 = 0, \\ (e_{15} + e_{31})u_{1,13} + e_{15}(u_{3,11} + u_{3,22}) + e_{33}u_{3,33} + (e_{31} + e_{15})u_{3,23} \\ -\varepsilon_{11}u_{4,11} - \varepsilon_{11}u_{4,22} - \varepsilon_{33}u_{4,33} = 0. \end{cases} \tag{2.26}$$

Note that there is no time rate in the last equation due to the quasi-electrostatic approximation, i.e. the absence of magnetization. This means that frequency dependence is induced only by the mechanical displacement u_i.

The reason to show simultaneously the equations in generalized notation (2.25) and in coordinate notation (2.26) is that for the derivation of the fundamental solutions in Chap. 3, it is better to use a coordinate notation, while for the derivation of the integro–differential equations and for explaining the numerical solution by BIEM in Chap. 4, it is better to use the generalized notation.

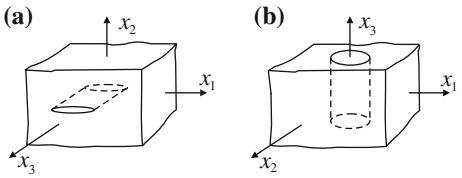

Fig. 2.10 Location of the defect in a Cartesian coordinate system $Ox_1x_2x_3$: **a** anti-plane deformation state, **b** in-plane deformation state

2.5 Field Equations in 2D

The equations of motion simplify considerably when "in-plane" or "anti-plane" problems are considered. For this purpose a Cartesian coordinate system $Ox_1x_2x_3$, see Fig. 2.10 is used. Assume that PEM shows hexagonal symmetry with respect to the Ox_3 axis and the poling axis is collinear with the Ox_3 axis. The plane Ox_1x_2 then is the isotropic plane. In what follows we will consider two coupled plane problems that are obtained from the 3D stress–strain state described in Sect. 2.4. The uncoupling of equations that would allow us to study the in-plane and anti-plane problems separately is only possible if the material is monoclinic. Fortunately the piezoelectric materials belong to this group of materials.

2.5.1 In-plane Piezoelectric Equations

Assumed is an electromechanical load as follows:

- the electric field is applied in the plane Ox_1x_3, i.e. $E_1 \neq 0$, $E_3 \neq 0$, $E_2 = 0$ and also corresponding electrical displacements are $D_1 \neq 0$, $D_3 \neq 0$, $D_2 = 0$, see Fig. 2.10a;
- the mechanical load is also in the plane Ox_1x_3 and the mechanical displacements are $u_1 \neq 0, u_3 \neq 0$, $u_2 = 0$. The nonzero stress and strain components are $\sigma_{11}, \sigma_{33}, \sigma_{13}$ and s_{11}, s_{33}, s_{13}.

2.5.1.1 Constitutive Equations

The constitutive equations are obtained from Eqs. (2.16):

$$\sigma_{iJ} = C_{iJKl}s_{Kl}, \quad i, j, l = 1, 3; J, K = 1, 3, 4. \tag{2.27}$$

or in matrix notation

$$\begin{pmatrix} \sigma_{11} \\ \sigma_{33} \\ \sigma_{31} \\ \sigma_{14} \\ \sigma_{34} \end{pmatrix} = C \begin{pmatrix} s_{11} \\ s_{33} \\ 2s_{31} \\ -E_1 \\ -E_3 \end{pmatrix}, \tag{2.28}$$

where

$$C = \begin{pmatrix} c_{11} & c_{13} & 0 & 0 & e_{31} \\ c_{13} & c_{33} & 0 & 0 & e_{33} \\ 0 & 0 & c_{44} & e_{15} & 0 \\ 0 & 0 & e_{15} & -\varepsilon_{11} & 0 \\ e_{31} & e_{33} & 0 & 0 & -\varepsilon_{33} \end{pmatrix}, \tag{2.29}$$

and in coordinate notation

$$\begin{aligned} \sigma_{11} &= c_{11}u_{1,1} + c_{13}u_{3,3} - e_{31}E_3, \\ \sigma_{33} &= c_{13}u_{1,1} + c_{33}u_{3,3} - e_{33}E_3, \\ \sigma_{13} &= c_{44}u_{1,3} + c_{44}u_{3,1} - e_{15}E_1, \\ D_1 &= e_{15}u_{1,3} + e_{15}u_{3,1} + \varepsilon_{11}E_1, \\ D_3 &= e_{31}u_{1,1} + e_{33}u_{3,3} + \varepsilon_{33}E_3. \end{aligned} \tag{2.30}$$

The strain-displacement and the electric field-potential relations are

$$s_{ij} = \frac{1}{2}(u_{i,j} + u_{j,i}), \quad E_i = -\Phi_{,i}, \quad i, j = 1, 3. \tag{2.31}$$

and the generalized displacement is $u_K = (u_1, u_3, \Phi)$.

2.5.1.2 Equation of Motion

The equations of in-plane coupled motion in the Ox_1x_3 plane is obtained from Eq. (2.25)

$$C_{iJKl}u_{K,li} + \rho_{JK}\omega^2 u_K = 0, \quad i, l = 1, 3; \quad J, K = 1, 3, 4. \tag{2.32}$$

and in coordinate notation

$$\begin{cases} c_{11}u_{1,11} + c_{44}u_{1,33} + (c_{13} + c_{44})u_{3,13} + (e_{31} + e_{15})u_{4,13} + \rho\omega^2 u_1 = 0, \\ (c_{13} + c_{44})u_{1,13} + c_{44}u_{3,11} + c_{33}u_{3,33} + e_{15}u_{4,11} + e_{33}u_{4,33} + \rho\omega^2 u_3 = 0, \\ (e_{15} + e_{31})u_{1,13} + e_{15}u_{3,11} + e_{33}u_{3,33} - \varepsilon_{11}u_{4,11} - \varepsilon_{33}u_{4,33} = 0. \end{cases} \tag{2.33}$$

Equations of motion (2.32) and (2.33) govern the solution of the 2D coupled in-plane electro-elastic problem, when the displacement and electric field are both in-plane.

2.5.2 Anti-plane Piezoelectric Equations

The electromechanical load is prescribed as follows:

- mechanical load is out of plane Ox_1x_2 and the mechanical displacements are $u_1 = 0, u_2 = 0, u_3 \neq 0$. The nonzero stress and strain components are σ_{13}, σ_{23} and s_{13}, s_{23}, see Fig. 2.10b.
- electric field is applied in plane Ox_1x_2, i.e. $E_1 \neq 0, E_2 \neq 0, E_3 = 0$ and also the corresponding electrical displacements are $D_1 \neq 0, D_2 \neq 0, D_3 = 0$.

2.5.2.1 Constitutive Equations

The constitutive equations are obtained from Eq. (2.16):

$$\sigma_{iJ} = C_{iJKl} s_{Kl}, \quad i, j, l = 1, 2; J, K = 3, 4. \tag{2.34}$$

or in coordinate notation

$$\begin{aligned} \sigma_{13} &= c_{44} u_{3,1} - e_{15} E_1 \\ \sigma_{23} &= c_{44} u_{3,2} - e_{15} E_2, \\ D_1 &= e_{15} u_{3,1} + \varepsilon_{11} E_1, \\ D_2 &= e_{15} u_{3,2} + \varepsilon_{11} E_2, \end{aligned} \tag{2.35}$$

where

$$\begin{pmatrix} \sigma_{13} \\ \sigma_{23} \\ \sigma_{14} \\ \sigma_{24} \end{pmatrix} = C \begin{pmatrix} s_{13} \\ s_{23} \\ -E_1 \\ -E_2 \end{pmatrix}, \quad C = \begin{pmatrix} c_{44} & e_{15} \\ e_{15} & -\varepsilon_{11} \end{pmatrix}. \tag{2.36}$$

2.5.2.2 Equation of Motion

The equation of anti-plane coupled motion in Ox_1x_2 plane is obtained by Eq. (2.25)

$$C_{iJKl} u_{K,li} + \rho_{JK} \omega^2 u_K = 0, \quad i, l = 1, 2; \quad J, K = 3, 4. \tag{2.37}$$

where the generalized displacement is $u_K = (u_3, \Phi)$. In coordinate notations Eq. (2.37) is

$$\begin{cases} c_{44}\triangle u_3 + e_{15}\triangle u_4 + \rho\omega^2 u_3 = 0, \\ e_{15}\triangle u_3 - \varepsilon_{11}\triangle u_4 = 0 \end{cases}. \tag{2.38}$$

where $\triangle = \partial^2_{x_1} + \partial^2_{x_2}$ is Laplace operator.

Equations of motion (2.37) and (2.38) govern the solution of the 2D coupled in-plane piezoelectric problem, when the displacement field is out of plane and the electric field is in-plane.

2.6 2D Domains with Cracks

2.6.1 Wave Propagation

Wave propagation in a media with defects, if there are no other sources of dissipation, is accompanied by wave phenomena as:

- *diffraction*, revealing the wave deviation from original wave path due to the superposition of incident and scattered wave;
- *scattering* refers to the wave radiation from defects acting as secondary sources of radiation due to the excitation of the incident wave;
- *attenuation*, i.e. the amplitude of the incident wave diminishes because during the diffraction and scattering process, a part of the incident wave energy is converted into the energy of diffracted and scattered waves;
- *dispersion*, that is energy (wave shape) distortion due to the frequency dependence of the effective wave phase velocity.

Interaction mechanism between waves and defects depend on the relation between the size c of the defect and the wavelength λ, i.e. the wave is not sensitive to the defect if $c \ll \lambda/2$. Wave scattering and diffraction is dominant at $c \approx \lambda$ and wave reflection and refraction is being realized at $c \gg \lambda$. The defects as cracks or holes are not only wave refractors and scatterers but they acts also as stress concentrators.

The evaluation of wave field distortion produced by a defect is a process studied in nondestructive testing of materials and structures, wave propagation theory with its application in seismology, modern engineering and medicine. The obstacle can be an inclusion, a hole, a crack or any existing boundary. Also, the fracture mechanics approach can be applied to the continua with existing defects like cracks and holes for assessing the initiation, growth, stability of the crack state and respectively to evaluate the resistance of the studied material or engineering structure.

In the following sections the basic 2D mechanical models describing time-harmonic wave propagation in homogeneous piezoelectric solid with cracks and holes are formulated. We are considering finite internal cracks with a straight or an

arc shape in a simply connected domain (unbounded or bounded) or in a domain with holes.

2.6.2 Fracture Mechanics Approach

Fracture mechanics provides a theoretical background for materials and structures containing cracks and faults. Stress intensity factors are key parameters in crack analysis. The classical work of Irwin [16] showed that the coefficients of the dominant singular term in the near-field solution for the stresses at the crack tip are directly related to the energy release rate (the energy released per unit of crack extension). These coefficients are referred to as the stress intensity factors. Generalized SIFs, play a dominate role because they characterize the intensity of the singular piezoelectric crack field (generalized stress and strain). The knowledge of SIFs is based on the near-field solutions and it is useful because it gives information for the strength and life time prediction of the studied solids and structures.

As can be seen from the field equations discussed in Sects. 2.4 and 2.5 we restrict our attention to the sufficiently small loading range which in a good approximation can be characterized by a linear material model with a constant polarization field. In this case we can apply the concepts of linear fracture mechanics generalized to treat the piezoelectric materials. The aim is to evaluate the influence of the electro-mechanical loads on the fracture behaviour of cracked piezoelectric solids. Following [12, 19, 27, 28, 32, 33, 35] the near-field solutions for typical crack opening mode, (see Fig. 2.11) can be expressed in polar coordinates with the origin at the crack-tip (see Fig. 2.12), as

$$\begin{aligned} \sigma_{iJ}(r,\theta,\omega) &= \frac{1}{\sqrt{r}} K_H(\omega) f_{iJ}^H(\theta), \\ u_J(r,\theta,\omega) &= \sqrt{r} K_H(\omega) g_{iJ}^H(\theta), \end{aligned} \tag{2.39}$$

where $H = I, \ldots, IV$, and the generalized stresses behave singular as $O(1/\sqrt{r})$, whereas the generalized displacements behaves as $O(\sqrt{r})$ for $r \to 0$. The angular functions $f_{iJ}^H(\theta)$, $g_{iJ}^H(\theta)$ depend only on the material constants. The coefficients K_I, K_{II} and K_{III} are the mechanical stress intensity factors, which are complemented by the new forth "electric" intensity factor K_{IV}, that characterizes the electric field singularity. In the general case the stresses and displacements are the sum of the four terms and they can only be separated in specific loading cases. Note that the behaviour of the stresses and displacements near the crack-tip is fully prescribed by the theoretical study of the asymptotic behaviour of solutions of elliptic boundary value problems in the domain with singularities, like angular points, see Kondratiev [19]. Correspondingly the K-factors K_H are coefficients of the representation of the solution near the crack-tip. From Eq. (2.39) the following conclusions can be drawn:

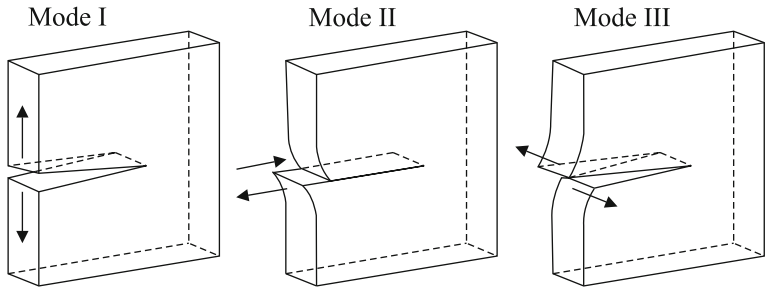

Fig. 2.11 Crack opening modes

Fig. 2.12 Stress components and reference system in the neighborhood of the crack

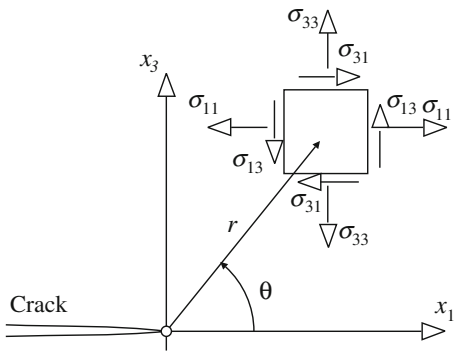

- The mutual interdependence between mechanical and electrical crack tip parameters;
- Angular functions f_{iJ}^H, g_J^H do not depend on the applied load and the domain geometry;
- The generalized SIFs K_H depend strongly on the applied load.

The numerical calculation of the SIFs is based on then well-known displacement or traction formulae, see [1, 12, 35, 43]. The traction formulae will be explained and used here.

Consider an in-plane crack along the segment AB with local coordinate of points $A(-c, 0)$, $B(c, 0)$ in the plane Ox_1x_3 and subjected to an electro-mechanical load in the crack plane. The following expressions for the generalized K-factors are obtained in this case, see [1, 41]:

$$\begin{aligned} K_I &= \lim_{x_1 \to \pm c} t_3 \sqrt{2\pi (x_1 \mp c)}, \\ K_{II} &= \lim_{x_1 \to \pm c} t_1 \sqrt{2\pi (x_1 \mp c)}, \\ K_{IV} &= \lim_{x_1 \to \pm c} t_4 \sqrt{2\pi (x_1 \mp c)}, \end{aligned} \tag{2.40}$$

where t_J is the traction at a point close to the crack-tips.

For an anti-plane crack subjected to mechanical load out of plane $x_3 = 0$ and electrical load in the plane $x_3 = 0$ the corresponding formulae are:

$$\begin{aligned} K_{III} &= \lim_{x_1 \to \pm c} t_3 \sqrt{2\pi (x_1 \mp c)}, \\ K_{IV} &= \lim_{x_1 \to \pm c} t_4 \sqrt{2\pi (x_1 \mp c)}. \end{aligned} \tag{2.41}$$

2.6.3 Boundary Value Problems

Selection of the adequate boundary condition on the crack faces in piezoelectric fracture mechanics has been discussed over the past 2 decades. It is a well-known fact that there are discrepancies between the experimental measurements and the theoretical predictions based on linear piezoelectric crack models. The character of the electrical boundary conditions is discussed in a number of papers, see [8, 9, 11, 14, 21, 23–25, 30, 32, 34, 42], etc.

Different types of crack surface boundary conditions belonging to the linear models are addressed:

- impermeable crack with mechanical traction-free surface;
- permeable crack with mechanical traction-free surface;
- limited permeable crack or deformation dependent electrical PKHS (PartonKudryavtsevHaoShen) boundary condition with mechanical traction-free surface;
- energetically consistent cracks with mechanical non-traction-free surface.

The BIEM that we apply for the numerical study of crack problems in 2D piezoelectric domains is a linear method—i.e. it presumes a linear boundary value problem. Therefore, we will deal in most cases with impermeable or permeable electrical boundary conditions along the crack line. Under some additional restrictions, the limited permeable cracks can also be considered. The detailed description of the electric boundary conditions together with comparative numerical studies is provided in Chap. 9. In the following we formulate the basic boundary-value problems for the in-plane and anti-plane problems of Sect. 2.5 that will be solved numerically with BIEM.

With respect to the domain we consider two types of BVP for cracks—(i) in bounded domains, and (ii) in infinite domains. The problem (i) aims to estimate the global behaviour of the solution in the presence of cracks in the domain and to evaluate the dependance of the SIFs on the geometry parameters of the external boundary. Such a problem is related to the eigenvalue problem and correspondingly to inverse problems. The solution of the problem (ii) gives an information about the local behaviour of the wave field near the cracks and the evaluation of the SIFs.

Denote by G a bounded domain with smooth boundary $S = \partial G$ in the plane $R^2 = Ox_1x_3$ for the in-plane case and $R^2 = Ox_1x_2$ for the anti-plane case and by $S_{cr} = S_{cr}^+ \cup S_{cr}^-$ an internal crack—an open arc. Suppose that $S = S_u \cup S_t$, $S_u \cap S_t = \emptyset$ and that there are prescribed displacements, $\bar{u}_J$ on S_u and prescribed tractions $\bar{t}_J$ on S_t.

The BVP in G with impermeable boundary conditions on S_{cr} is defined as

$$\begin{vmatrix} \sigma_{iJ,i} + \rho_{JK}\omega^2 u_K = 0 \quad \text{in } G\backslash S_{cr}, \\ u_J|_{S_u} = \bar{u}_J, \quad t_J|_{S_t} = \bar{t}_J, \\ t_J|_{S_{cr}} = 0. \end{vmatrix} \tag{2.42}$$

Solution of Eq. (2.42) is a vector-valued function with components $u_J \in C^2(G\backslash S_{cr})$ that satisfies the equation and boundary conditions. We will transform the problem (2.42) in Chap. 4 into an integro–differential equation on $S \cup S_{cr}$ with the unknowns u_J on S_t; t_J on S_u and the jump of displacement across the crack line, i.e. the crack opening displacement $\Delta u_J = u_J|_{S_{cr}^+} - u_J|_{S_{cr}^-}$.

The BVP in G with permeable boundary conditions on S_{cr} is defined as

$$\begin{vmatrix} \sigma_{iJ,i} + \rho_{JK}\omega^2 u_K = 0 \quad \text{in } G\backslash S_{cr}, \\ u_J|_{S_u} = \bar{u}_J, \quad t_J|_{S_t} = \bar{t}_J, \\ t_i|_{S_{cr}} = 0, \quad u_4|_{S_{cr}^+} = u_4|_{S_{cr}^-}. \end{vmatrix} \tag{2.43}$$

Solution of Eq. (2.43) is a vector-valued function with components $u_J \in C^2(G\backslash S_{cr})$ that satisfies the equation and boundary conditions. In Chap. 4 after the transformation of the problem (2.43) into an integro–differential equation on $S \cup S_{cr}$, the unknowns are: u_J on S_t; t_J on S_u, the crack opening displacement Δu_i and t_4 on S_{cr}.

The BVP in the plane $R^2 = Ox_1x_3$ for the in-plane case and $R^2 = Ox_1x_2$ for the anti-plane case with impermeable boundary conditions on S_{cr} is defined as

$$\begin{vmatrix} \sigma_{iJ,i} + \rho_{JK}\omega^2 u_K = 0 \quad \text{in } R^2\backslash S_{cr}, \\ t_J|_{S_{cr}} = 0. \end{vmatrix} \tag{2.44}$$

In addition the unknown u_J must satisfies the Sommerfeld's type condition at infinity, see Sommerfeld [31]. Solution of Eq. (2.44) is a vector-valued function with components $u_J \in C^2(R^2\backslash S_{cr})$ that satisfies the equation and boundary condition. In Chap. 4 after the transformation of the problem (2.44) into an integro–differential equation on S_{cr}, the unknown is the crack opening displacement $\Delta u_J = u_J|_{S_{cr}^+} - u_J|_{S_{cr}^-}$.

The BVP in the plane $R^2 = Ox_1x_3$ for the in-plane case and $R^2 = Ox_1x_2$ for the anti-plane case with permeable boundary conditions on S_{cr} is defined as

$$\begin{vmatrix} \sigma_{iJ,i} + \rho_{JK}\omega^2 u_K = 0 \quad \text{in } R^2\backslash S_{cr}, \\ t_i|_{S_{cr}} = 0, \quad u_4|_{S_{cr}^+} = u_4|_{S_{cr}^-} \end{vmatrix} \tag{2.45}$$

In addition the unknown u_J must satisfies the Somerfield type condition at infinity. Solution of Eq. (2.45) is a vector-valued function with components $u_J \in C^2(R^2\backslash S_{cr})$ that satisfies the equation and boundary condition. In Chap. 4 after the transformation of the problem (2.45) into an integro–differential equation on S_{cr}, the unknown is the crack opening displacement Δu_i and t_4.

Note that the field equations for the in-plane case, are prescribed in Sect. 2.5.1 for $i = 1, 3$, $J, K = 1, 3, 4$, while field equations for the anti-plane case are in Sect. 2.5.2 for $i = 1, 2$, $J, K = 3, 4$.

The non-hypersingular traction BIEM and its numerical solution are discussed in Chap. 4. Different illustrative numerical examples are presented in Chaps. 5–15, where we consider uncoupled problems, multiple cracks and dynamic crack interaction phenomena, unbounded and bounded domains, inhomogeneous domains, domains with hole or crack and hole. For every particular case the BVP will be stated together with the corresponding boundary integral equation formulation.

References

1. Aliabadi AM, Rooke D (1991) Numerical fracture mechanics. Computational Mechanics, Southampton
2. Alshits VIA, Chadwick P (1997) Concavities on the zonal slowness section of a transversely isotropic elastic material. Wave Motion 25:347–359
3. Barnett DM, Lothe J (1975) Dislocations and line charges in anisotropic piezoelectric insulators. Physica Status Solidi B76:105–111
4. Curie J, Curie P (1880a) Développement, par pression, de l'électricité polaire dans les cristaux hémièdres faces ' inclinées. C R Acad Sci Gen 91:294–295
5. Curie J, Curie P (1880b) Sur l'électricité polaire dans les cristaux hémièdres ' faces inclinées. C R Acad Sci Gen 91:383–386
6. Davi G, Milazzo A (2001) Multidomain boundary integral formulation for piezoelectric materials fracture mechanics. Int J Solids Struct 38:7065–7078
7. Dieulesaint E, Royer D (1974) Elastic wave in solids. Wiley, New York
8. Dunn ML (1994) Electroelastic Green's functions for transversely isotropic piezoelectric media and their application to the solution of inclusion and ingomogeneity problems. Int J Eng Sci 32(1):119–131
9. Enderlein M, Ricoeur A, Kuna M (2005) Finite element technique for dynamic crack analysis in piezoelectrics. Int J Fract 134:191–208
10. Eringen AC, Maugin GA (1990) Electrodynamics of continua I: foundations and solid media. Springer, Berlin
11. Gao C, Fan W (1999) A general solution for the plane problem in piezoelectric media with collinear cracks. Int J Eng Sci 37:347–363
12. Gross D, Seelig T (2011) Fracture mechanics: with an introduction to micromechanics. Springer, Berlin
13. Hankel WG (1881) Uber die aktinound piezoelektrischen eigen schaften des bergkrystalles und ihre beziehung zi den thermoelektrischen. Abh Sachs 12:457
14. Hao TH, Shen ZY (1994) A new electric boundary condition of electric fracture mechanics and its applications. Eng Fract Mech 47:793–802
15. Ikeda T (1990) Fundamentals of piezoelectricity. Oxford University Press, Oxford
16. Irwin GR (1957) Analysis of stresses and strains near the end of a crack traversing a plate. J Appl Mech 24:361–364
17. Jaffe B, Roth RS, Marzullo S (1954) Piezoelectric properties of lead zirconate-lead titanate solid-solution ceramic ware. J Appl Phys 25:809–810
18. Kawai H (1969) Japanese. J Appl Phys 8:975
19. Kondratiev V (1967) Boundary problems for elliptic equations in domain with conocal and angular points. In: Proceedins of the Moscow mathematical society, vol 16. pp 227–313
20. Landau DL, Lifshitz EM (1960) Electrodynamics of continuous media. Pergamon Press, Oxford

21. Landis CM (2004) Energetically consistent boundary conditions for electromechanical fracture. Int J Solids Struct 41:6241–6315
22. Lippman G (1881) Principe de la conservation de l'électricité. Ann Chimie Phys 24:145
23. McMeeking RM (1989) Electrostrictive stresses near crack-like flaws. J Appl Math Phys 40:615–627
24. McMeeking RM (1999) Crack tip energy relase rate for a piezoelectric compact tension specimen. Eng Fract Mech 64:217–244
25. McMeeking RM (2004) The energy release rate for a Griffith crack in a piezoelectric material. Eng Fract Mech 71:1149–1163
26. Newnham RE (1980) Composite piezoelectric transducers. Mater Eng 2:93–106
27. Pak YE (1992b) Linear electro-elastic fracture mechanics of piezoelectric materials. Int J Fract 54:79–100
28. Park SB, Sun CT (1995) Effect of electric field on fracture of piezoelectric ceramics. Int J Fract 70(3):203–216
29. Parton VZ, Kudryavtsev BA (1988) Electromagnetoelasticity. Gordon and Breach Science, New York
30. Shindo Y, Murakami H, Horiguchi K, Narita F (2002) Evaluation of electric fracture properties of piezoelectric ceramics using the finite element and single-edge precracked beam methods. J Am Ceramic Soc 85:1243–1248
31. Sommerfeld A (1949) Partial differential equations in physics. Academic Press, New York
32. Sosa H (1991) Plane problems in piezoelectric media with defects. Int J Solids Struct 28:491–505
33. Sosa H (1992) On the fracture mechanics of piezoelectric solids. Int J Solids Struct 29:2613–2622
34. Sosa H, Khutoryansky N (1996) New developments concerning piezoelectric materials with defects. Int J Solids Struct 33:3399–3414
35. Suo Z, Kuo C, Barnett D, Willis J (1992) Fracture mechanics for piezoelectric ceramics. J Mech Phys Solids 40:739–765
36. Thompson W (1878) On the thermoelastic, thermomagnetic and puro-electric properties of matter. Phil Mag 5:4–27
37. Tiersten HF (1969) Linear piezoelectric plate vibrations. Plenum Press, New York
38. Valasek J (1920) Piezoelectric and allied phenomena in Rochelle salt. Phys Rev 15:537
39. Voigt W (1910) Lehrbuch der Kristallphysik. Teubner, Leipzig
40. Wang CY, Zhang Ch (2005) 2 D and 3 D dynamic Green's functions and time-domain BIE formulations for piezoelectric solids. Eng Anal Bound Elem 29:454–465
41. Wang X, Yu S (2001) Transient response of a crack in a piezoelectric strip subjected to the mechanical and electrical impacts: mode- I problem. Mech Mater 33:11–20
42. Xu LY, Rajapakse RKND (2001) On a plane crack in piezoelectric solids. Int J Solids Struct 38:7643–7658
43. Zhang C, Gross D (1998) On wave propagation in elastic solids with cracks. Computational Mechanics, Southampton

Chapter 3
Fundamental Solutions

Abstract Fundamental solutions for time-harmonic 2D dynamic problems of piezoelectric materials are derived in a closed form by Radon transform. In addition the state of the art in the field is discussed.

3.1 State of the Art

The formulation of a boundary-value problem in terms of BIE requires two basic ingredients: a reciprocal relation and a fundamental solution or Green's function. The reciprocal relation for elastodynamics, as established by Graffi [22] and extended by Wheeler and Sternberg [50], is independent on the fact that the body is isotropic, anisotropic or piezoelectric, see Khutoryansky and Sosa [29, 30] and Pan and Amadei [35]. The main difficulty is, therefore, to obtain a fundamental solution which can be efficiently evaluated and implemented easily in a corresponding numerical scheme. Fundamental solutions for piezoelectricity are studied mainly in order to use them in BIEM. Since the system of partial differential equations describing PEM has constant coefficients, the fundamental solution exists according to the theorem of Ehrenprise–Malgrange, see Iosida [27]. There are also many works in which the fundamental solution is derived in order to find out an analytical solution for specific initial and boundary conditions.

In the mathematical literature the term "fundamental solution" is used only for the solution of a differential equation with Dirac—function on the right-hand side and the term "Green's function" means the fundamental solution which additionally satisfies the corresponding boundary conditions. The Green's function, if it exists, is unique. The fundamental solution which is usually very complicated, is not unique and it is determined up to a function which solve the correspondingly homogeneous system. The aim of this chapter is to derive a fundamental solution suitable for numerical usage in dynamic 2D BIEM. With regard to the state of the art we will keep the original terms (Green's function or fundamental solution) used by the authors in the mechanical literature.

P. Dineva et al., *Dynamic Fracture of Piezoelectric Materials*,
Solid Mechanics and Its Applications 212, DOI: 10.1007/978-3-319-03961-9_3,

3.1.1 Static Fundamental Solutions

The amount of papers on static fundamental solutions for piezoelectric materials is big and we will pay more attention to some of the recent works. As a rule the static fundamental solutions are obtained in a closed form. The most common techniques used for derivation of fundamental solutions are based on Stroh's complex variable formalism, extended Lekhnitski's formalism and integral transforms methods applying mostly Fourier or Radon transform.

One of the first results was that of Deeg [10], where the transformation technique was used to obtain a fundamental solution in a non-closed form due to the general anisotropy consideration. Chen [4] and Chen and Lin [5] expressed the piezoelectric fundamental solution and its derivatives in terms of a contour integral over a unit circle using Fourier transform.

Dunn [16] obtained a fundamental solution for PEM of general anisotropy by using Radon transform with Fourier transformation and residual calculation. In the case of transversely isotropic PEM Dunn [16] presented an explicit fundamental solution. A 2D fundamental solution in a closed form was obtained in Lee and Jiang [32] by using integral transform method. Ding et al. [13] obtained a general 3D PEM fundamental solution in closed form via the theory of volume potential function. A 2D fundamental solution was derived in Lee [31] by Fourier transforms for transversely isotropic PEM. The boundary element formulation was then numerically implemented by spline interpolations. As a numerical example, stress analysis was performed for an infinite piezoceramic medium (PZT-4) containing a cylindrical defect under several mechanical and electrical boundary conditions. A general solution in terms of harmonic functions and fundamental solutions were obtained in Ding et al. [14] for plane PEM problems. Numerical calculations by BIEM were performed for the stress concentration coefficient of an infinite piezoelectric plane with a circular hole as well as for the stress and electric intensity factors of a central crack located in an infinite plate.

Dunn and Wienecke [17] derived explicit expressions for a fundamental solution by developing a general solution procedure in terms of piezoelectric potentials. It was shown that when the piezoelectric system is decoupled the corresponding fundamental solutions reduce to the ones for the elastic transversely isotropic and electrostatic cases obtained by Pan and Chou [36].

The fundamental solutions for the point force/charge and the displacement/electric potential discontinuity was derived in closed form in Denda and Lua [11] using Stroh's complex variable formalism for piezoelectricity. By them the integral representation of Somigliana's identity was developed as the foundation of the direct BEM formulation for piezoelectricity.

The fundamental solution and Green's function for piezoelectric 2D solids in an infinite plane, a half plane and two joined dissimilar half-planes were derived using the complex variable function method in Pan and Amadei [35].

Piezoelectric fundamental solutions based on the extended Lekhnitski's formalism and distributed dislocation modeling were presented in Rajapakse and Xu [37].

Special solutions were obtained for a conducting or impermeable crack in an infinite medium. The BIEM was applied for studying branched cracks, forked cracks and microcrack clusters.

3.1.2 Dynamic Fundamental Solutions

There is a very limited number of papers which consider for PEM the dynamic fundamental solutions suitable for BIEM implementation. The basic work of Norris [34] described a procedure for the derivation of fundamental solutions for different time-harmonic 3D problems with extra field variables. The method has been applied for the piezoelectricity, thermoelectricity and poroelasticity. The time-harmonic anisotropic and elliptic coupled system for the additional variable (electric potential or temperature) was transformed with a plane wave representation and the fundamental solution was expressed as an integral over the unit sphere in 3D. The space dimension three is essential for the simple plane wave representation of the Dirac delta function. Once the time-harmonic fundamental solution was found, the transient time dependent fundamental solution could be obtained by applying inverse Fourier transform. The work of Norris [34] is purely theoretical and it is not suitable for the direct BIEM implementation.

Other interesting papers on this topic are the works of Khutoryansky and Sosa [29, 30] and later Sosa and Khutoryansky [41, 42]. These works concern the derivation of the 3D time-domain fundamental solution for PEM and its numerical implementation in a BIEM. The transient fundamental solutions in Khutoryansky and Sosa [29, 30] were obtained through the plane wave transform method, see Gel'fand and Shilov [18]. The method generalized the Burridge [3] results and the obtained fundamental solution was presented as an integral over the unit sphere in 3D. The representation formulas of the governing transient PEM equations were obtained and their numerical BIEM implementations were discussed. In the sequel works of Sosa and Khutoryansky [41] three alternatives for 3D fundamental solutions were presented. They discussed in detail a representation of the fundamental solution via slowness surfaces. Numerical examples were provided for a class of piezoceramics in order to illustrate this representation. The work of Sosa and Khutoryansky [42] was build upon the results discussed above. Essentially they reformulated the representations of the fundamental solution and its derivatives in a more convenient mathematical form.

A dynamic fundamental solution for 3-D transversely isotropic PEM was derived by Daros and Antes [8]. In this work the potentialities of the Hergloz-Petrowski formulas for the case of transversely isotropic materials were studied in detail. These formulas presented the integral formulation of the fundamental solution over the slowness surface. The idea of this representation was given in the books of John [28], Gel'fand and Shilov [18] and a possible simplification leading to line integral representations was discussed in Duff [15]. In the paper of Daros and Antes [9] numerical results were presented concerning both convex and non-convex slowness

surfaces and interesting physical phenomena as cusps and conical points on the wave surface resulting in different types of wave front singularities. In the paper of Daros [6] the dynamic fundamental solution for the displacement fields along the symmetry axis of the piezoelectric crystal of classes 6 mm and 622 were obtained applying an integration technique of Burridge [2]. Also the Herglotz-Petrowsky formulae were given and numerical results were shown for some PEMs. One of the important results in this work is that only when specific conditions regarding the piezoelectric constants are satisfied, the differential operator after reducing the electric potential is hyperbolic, which guarantees the well-posedness and solvability of the Cauchy problem. In Daros [7] a fundamental solution for transient 2D and 3D piezoelectric solids of crystal class 6 mm was derived. The hyperbolicity of the equations was recovered assuming an average dielectric tensor and making use of the Lorentz gauge condition. The derived solution is unique as a consequence of the hyperbolicity of the differential equations.

In Wang and Meguid [49] a fundamental solution was derived for the 2D anti-plane PEM problem. It was used to study the dynamic PEM behavior, without harking back to the BIEM. They also studied the interaction between two arbitrary located and oriented cracks. The fundamental solution was derived using Fourier transform and the appropriate singular integral equations. Numerical examples were presented to show the significant effect of electromechanical coupling upon the stress intensity factors.

The fundamental solutions for both the transversely isotropic piezoelectric solid and the transversely isotropic elastic solid have similarities and common parts. Therefore, it is worth to describe shortly the recent works on the fundamental solutions for transversely isotropic elastic solids and their BIEM implementation.

Wang and Achenbach [44, 45] and Wang et al. [47] derived in the series of works fundamental solutions for general anisotropic materials and illustrated them by examples of transversely isotropic solids. In Wang and Achenbach [44, 45] 2D and 3D time-domain and time-harmonic elastodynamic solutions for linearly elastic anisotropic materials were obtained. The main tool in this work is the Radon transformation, see Ludwig [33], Gel'fand et al. [20] and Helgason [26]. The solutions are represented in the form of a surface integral over a unit sphere in the 3D case and a contour integral over a unite circle in the 2D case. The solutions are separated into the singular part that corresponds to the elastostatic fundamental solution and the regular part. A novel BIEM approach using this integral expression of the fundamental solution was presented in Wang et al. [47]. Furthermore, the numerical BIEM solution was compared with the analytical solutions for isotropic solids. Saez and Dominguez [39] developed a BIE approach for wave propagation problems in 3D transversely isotropic solids. They transformed the fundamental solution obtained by Wang and Achenbach [45] in order to obtain expressions which are simpler with respect to numerical computations. Applying this method solutions of different wave scattering problems in the frequency domain were discussed. A general 3D BIE analysis of dynamic fracture mechanics problems for transversely isotropic media was presented in Saez and Dominguez [40] where the authors used the frequency dependent formulation. An original way for computation of the fundamental solutions and their

derivatives was proposed in Saez and Dominguez [39] . The numerical technique was based on a simplified way of the fundamental solution calculation, the multidomain approach and the usage of special crack-tip elements.

Applying Radon transformation, see Ludwig [33], and using the theory of generalized functions, see Gel'fand and Shilov [18, 19], transient and time-harmonic fundamental solutions for 2D piezoelectric solids were presented in Gross et al. [23–25]. Dynamic fundamental solutions in the time and frequency domain were also derived by Wang et al. [48] and Wang and Zhang [46] by using Radon transforms technique. Denda et al. [12] applied the obtained fundamental solutions to study 2D eigenvalue problems.

Fundamental solutions for homogeneous isotropic/anisotropic elastic solids were obtained in Rangelov et al. [38] and for piezoelectric solids in Gross et al. [23–25] and in the next sections we will follow these works.

3.2 Preliminaries

Fundamental solutions are generalized functions and the method to derive them is based on integral transformation technique. Following Vladimirov [43], Gel'fand et al. [20], Gel'fand and Shilov [18], Ludwig [33] and Gel'fand et al. [26] let us recall some definitions and properties of Fourier and Radon transforms in R^2. Some fundamental solutions of second order ordinary differential equations with constant coefficients will be considered too.

Denote by $\Im(R^2)$ the set of all $C^\infty(R^2)$ functions φ that decreases together with all their derivatives faster than any power of $|x|^{-1}$ for $|x| \to \infty$. By $\Im'(R^2)$ the set of generalized functions ψ of slow growth is denoted, i.e. the set of linear functionals on $\Im$ and

$$(\varphi, \psi) = \int_{R^2} \varphi(x)\psi(x)dx, \quad \text{for every } \varphi \in \Im, \psi \in \Im'. \tag{3.1}$$

For example the Dirac's function δ is a generalized function $\delta \in \Im'$ with compact support, defined as

$$(\delta, \varphi) = \int \delta(x)\varphi(x)dx = \varphi(0), \quad \text{for every } \varphi \in \Im. \tag{3.2}$$

3.2.1 Fourier Transform in R^2

Functions $g \in \Im(R^2)$ are integrable and the Fourier transform is defined as

$$F(g)(\eta) = \frac{1}{2\pi} \int_{R^2} g(x)e^{-i\langle x,\eta\rangle}dx \tag{3.3}$$

where $\langle ., . \rangle$ is a scalar product in R^2. The Fourier transform for generalized functions $f \in \Im'$ is defined as

$$(F(f), g) = (f, F(g)), \quad \text{for every } g \in \Im \tag{3.4}$$

We usually use the short notation $F(f)$ also for $f \in \Im'$ having in mind the definition (3.4).

Denote by $D^\alpha = \partial_{x_1}^{\alpha_1} \partial_{x_2}^{\alpha_2}$, $(ix)^\alpha = (ix_1)^{\alpha_1}(ix_2)^{\alpha_2}$, $\bar{\alpha} = \alpha_1 + \alpha_2$ with α_1, α_2 positive integers. The Fourier transform has the following properties for generalized functions $f, g \in \Im'$

- $F(af + bg) = aF(f) + bF(g)$, with a, b complex numbers;
- $D^\alpha F(f) = F((ix)^\alpha f)$;
- $F(D^\alpha f) = (-i\eta)^\alpha F(f)$;
- $F(f(x - x_0)) = e^{-i\langle x_0, \eta \rangle} F(f)$;
- $F(f)(\eta + \eta_0) = F(e^{-i\langle x_0, \eta \rangle} f)(\xi)$.

Applying F to the δ-function and using the properties of the Fourier transform we get the formulas

$$\begin{aligned} F(\delta(x)) &= \frac{1}{2\pi}, \delta(x) = F^{-1}\left(\frac{1}{2\pi}\right) = \frac{1}{2\pi} F(1), \\ F(D^\alpha \delta) &= (-i\eta)^\alpha F(\delta) = (-i\eta)^\alpha \frac{1}{2\pi}, \\ F(x^\alpha) &= (-1)^{\bar{\alpha}} D^\alpha F(1) = 2\pi(-1)^{|\alpha|} D^\alpha \delta(\eta). \end{aligned} \tag{3.5}$$

For $g \in \Im'$ with compact support and $f \in \Im'$, a convolution is defined as $f \star g = \int_{R^2} f(x - s) g(s) ds$ with the Fourier transform of convolution and of product being

$$F(f \star g) = 2\pi F(f) F(g), \quad F(f)F(g) = 2\pi F(f) \star F(g). \tag{3.6}$$

The inverse Fourier transform F^{-1} is defined as

$$F^{-1}(f) = F(f(-x)), \quad f \in \Im', \tag{3.7}$$

then F and F^{-1} are one-to-one on $\Im'$ i.e.

$$F^{-1}(F(f)) = f, \quad F(F^{-1}(f)) = f, \quad f \in \Im'. \tag{3.8}$$

Using the properties of Fourier transform and calculus with generalized functions, see Gel'fand and Shilov [18], Vladimirov [43] the following formulas are obtained that we need to use in the next sections

$$F^{-1}\left(\frac{1}{|\eta|^2-k^2}\right)=-\frac{1}{2\pi}K_0(ik|x|),$$
$$F^{-1}\left(\frac{1}{|\eta|^2}\right)=-\ln|x|, \tag{3.9}$$
$$F^{-1}\left(\frac{1}{|\eta|^2+k^2}\right)=-\frac{1}{2\pi}K_0(k|x|),$$

where $k>0$ and $K_\nu(z)$ is the Kelvin function of order ν, see [1, 21].

3.2.2 Radon Transform in R^2

The Radon transform is defined on $f\in\Im$ as

$$R(f)(s,m)=\int_{\langle x,m\rangle=s} f(x)dS=\int f(x)\delta(s-\langle x,m\rangle)dx,\quad s\in R^1,\quad m\in S^1. \tag{3.10}$$

where $S^1=\{m=(m_1,m_2)\in R^2,|m|=1\}$ is the unit circle in R^2.

There is a relation between Fourier and Radon transforms. From Eq. (3.10) with $\eta=rm, r\in R^1, m\in S^1$ we obtain for the Fourier transform of f at point rm

$$F(f)(rm)=\frac{1}{2\pi}\int_{R^2} e^{-i\langle x,m\rangle r}f(x)dx. \tag{3.11}$$

So, for x in the plane $\langle x,m\rangle=s$ the equality (3.11) becomes

$$F(f)(rm)=\frac{1}{2\pi}\int_{R^1} e^{-isr}R(f)(s,m)ds. \tag{3.12}$$

Hence, $R(f)$ can be obtained applying the inverse Fourier transform to Eq. (3.12) from which we get a relation between Radon and Fourier transform in the form

$$R(f)(s,m)=\int_{R^1} e^{ism}F(f)(rm)dr. \tag{3.13}$$

By this relation, Radon transform can be defined on the set of generalized functions $\Im'$.

Radon transforms have the following properties

- $R(af+bg)=aR(f)+bR(g)$, with a,b complex numbers;
- $R(D^\alpha f(x))=m^\alpha\partial_s^{\tilde{\alpha}}R(f)(s,m)$;
- $R(f)(\gamma s,\gamma m)=|\gamma|^{-1}R(f)(s,m)$, with γ non zero number;
- $R(\delta(x,\xi))=\delta(s-\langle m,\xi\rangle)$.

The inverse Radon transform in 2D is defined as

$$R^{-1}(g(s,m)) = f(x), \quad R^{-1} = R^* K, \tag{3.14}$$

where

$$\begin{aligned} h(s,m) = K(g)(s,m) &= \int_{R^1} \frac{\partial_\sigma g(\sigma,m)}{s-\sigma} d\sigma, \\ f(x) = R^*(h)(x) &= \frac{1}{4\pi^2} \int_{|m|=1} K(g)(s,m)|_{s=<x,m>} dm. \end{aligned} \tag{3.15}$$

The transformation K is the Hilbert transform in R^2.

We will use the Radon transform for deriving fundamental solutions of a system of partial differential equations with constant coefficients. The direct Radon transform R is done by using properties listed above and leads to an ODE with coefficients, dependent on parameters on the unit circle. After deriving a fundamental solution of this ODE, which is shown on the model example in the next subsection, we have to apply the Hilbert transform K as a first step of the inverse Radon transform. In the cases that are considered later, we need to find K of three types of functions:

$$e^{ik|s-\tau|}, \quad |s-\tau|, \quad e^{k|s-\tau|} \tag{3.16}$$

where $k > 0, \tau = \langle \xi, m \rangle, x_0 \in R^2, m \in S^1, s \in R^1$. Using the calculus with generalized functions, see Gel'fand and Shilov [18] we obtain

$$\begin{aligned} K(e^{ik|s-\tau|}) &= -ik\{i\pi e^{ik\beta} - 2[\mathrm{ci}(k\beta)\cos(k\beta) + \mathrm{si}(k\beta)\sin(k\beta)]\}|_{\beta=|s-\tau|}, \\ K(|s-\tau|) &= 2\ln|s-\tau|. \\ K(e^{k|s-\tau|}) &= k\{\cosh k\beta + 2[\mathrm{chi}(k\beta)\cosh(k\beta) - \mathrm{shi}(k\beta)\sinh(k\beta)]\}|_{\beta=|s-\tau|} \end{aligned} \tag{3.17}$$

where

$$\mathrm{ci}(p) = -\int_p^\infty \frac{\cos t}{t} dt, \quad \mathrm{si}(p) = -\int_p^\infty \frac{\sin t}{t} dt,$$

are the cosine integral and sine integral functions and

$$\mathrm{chi}(p) = -\int_0^p \frac{\cosh t - 1}{t} dt + \ln p + C, \quad \mathrm{shi}(p) = -\int_0^p \frac{\sinh t}{t} dt,$$

are the hyperbolic cosine and sine integral functions with Euler's constant C, see Bateman and Erdelyi [1].

3.2.3 Fundamental Solution of ODE

We consider second order ODEs with constant coefficients of the form

$$\partial_s^2 Z(s,\tau) + \alpha Z(s,\tau) = \gamma\delta(s-\tau) \tag{3.18}$$

where α, γ, τ are constants. Following Vladimirov [43] the solution of Eq. (3.18) is a generalized function $Z(s,\tau) = \theta(s-\tau)Y(s,\tau)$, where θ is the Heaviside function or unit step function and $Y(s,\tau)$ is the solution of the initial-value problem

$$\begin{cases} \partial_s^2 Y(s,\tau) + \alpha Y(s,\tau) = 0, \\ Y(0,\tau) = 0, \quad Y'(0,\tau) = \gamma. \end{cases} \tag{3.19}$$

With respect to α there are three cases for the solutions of Eq. (3.19):

- If $\alpha > 0$, then $Y(s,\tau) = \dfrac{\gamma}{\sqrt{\alpha}} \sin\sqrt{\alpha}(s-\tau)$;
- If $\alpha = 0$, then $Y(s,\tau) = (s-\tau)$;
- If $\alpha < 0$, then $Y(s,\tau) = \dfrac{\gamma}{\sqrt{|\alpha|}} \sinh\sqrt{|\alpha|}(s-\tau)$.

Multiplying $Y(s,\tau)$ by $\theta(s-\tau)$ we obtain in a more compact form solutions of Eq. (3.19)

$$\begin{aligned} Z(s,\tau) &= -\frac{i\gamma}{2k} e^{ik|s-\tau|} \quad \text{for } \alpha > 0 \quad \text{and } \sqrt{\alpha} = k, \\ Z(s,\tau) &= \frac{\gamma}{2}|s-\tau| \quad \text{for } \alpha = 0, \\ Z(s,\tau) &= \frac{\gamma}{2k} e^{k|s-\tau|} \quad \text{for } \alpha < 0 \quad \text{and } \sqrt{-\alpha} = k. \end{aligned} \tag{3.20}$$

Here we use the fact that solutions of Eq. (3.19) are invariant with respect to replacing s with $-s$.

3.3 Anti-plane Piezoelectric Case

We first show the derivation of the fundamental solution for the simple case when the Eq. (2.38) is decoupled to elastic isotropic anti-plane case. Subsequently, the fundamental solution for the coupled system is derived, and finally fundamental solutions for some restricted classes of inhomogeneous piezoelectric materials are presented in Part III. In the piezoelectric anti-plane case fundamental solutions can be obtained in a closed form by Fourier or Radon transforms. For the numerical realization of the traction BIEM we prefer to work with the Radon form. Reason is it's better suitability for numerical calculations as the singular part of the fundamental solution's derivatives coincide with the static one. This advantage of the fundamental solution obtained by Radon transform will be commented in details at the end of the section.

3.3.1 Uncoupled Anti-plane Case

In the uncoupled case $e_{15} = 0$ and Eq. (2.38) takes the form

$$\begin{cases} c_{44}\triangle u_3 + \rho\omega^2 u_3 = 0, \\ -\varepsilon_{11}\triangle u_4 = 0. \end{cases} \tag{3.21}$$

Fundamental solution is a matrix valued generalized function

$$u^* = \begin{pmatrix} u^*_{33} & u^*_{34} \\ u^*_{43} & u^*_{44} \end{pmatrix},$$

which is the solution of the system of equations

$$\begin{cases} c_{44}\triangle u^*_{3J} + \rho\omega^2 u^*_{3J} = -\delta(x-\xi)\delta_{3J}, \\ -\varepsilon_{11}\triangle u^*_{4J} = -\delta(x-\xi)\delta_{4J}, \quad J = 3, 4. \end{cases} \tag{3.22}$$

where δ_{KJ} is Kroneker symbol. Since the fundamental solution is not unique and is defined with respect to the solution of Eq. (3.21) we can assume that $u^*_{34} = u^*_{43} = 0$. From Eq. (3.22) we then have the equations for u^*_{33}, u^*_{44}

$$\begin{cases} c_{44}\triangle u^*_{33} + \rho\omega^2 u^*_{33} = -\delta(x-\xi), \\ \varepsilon_{11}\triangle u^*_{44} = \delta(x-\xi). \end{cases} \tag{3.23}$$

The solutions of Eq. (3.23) are well known, see Vladimirov [43]—the first is the fundamental solution of Helmholtz' equation, the second is fundamental solution of the Laplace equation. Nevertheless, let us show the derivation of the fundamental solutions using both Fourier and Radon transforms, because we have to use similar methods later for the derivation of fundamental solutions for more complicated equations.

3.3.1.1 Fourier Transform for Fundamental Solution Derivation

Applying Fourier transform to both sides of Eq. (3.23) and considering for simplicity $\xi = 0$, we obtain

$$\begin{aligned} (-|\eta|^2 + k^2)F(u^*_{33}) &= -\frac{1}{c_{44}}, \\ |\eta|^2 F(u^*_{44}) &= \frac{1}{\varepsilon_{11}}, \end{aligned} \tag{3.24}$$

where $k = \omega\sqrt{\dfrac{\rho}{c_{44}}}$ and

$$F(u_{33}^*) = -\frac{1}{c_{44}}\frac{1}{k^2 - |\eta|^2},$$
$$F(u_{44}^*) = \frac{1}{\varepsilon_{11}}\frac{1}{|\eta|^2}. \tag{3.25}$$

Replacing x by $x - \xi$, so that $r = |x - \xi| = \sqrt{(x_1 - \xi_1)^2 + (x_2 - \xi_2)^2}$ and using Eq. (3.9) we get the solutions

$$u_{33}^* = \frac{1}{2\pi c_{44}} K_0(-ikr),$$
$$u_{44}^* = \frac{1}{2\pi \varepsilon_{11}} \ln r, \tag{3.26}$$

The derivatives of the fundamental solution are

$$u_{33,j}^* = -\frac{ik}{2\pi c_{44}} K_1(-ikr) r_{,j}$$
$$u_{44,j}^* = \frac{1}{2\pi \varepsilon_{11}} \frac{1}{r} r_{,j}\,. \tag{3.27}$$

The asymptotic behaviour of u_{33}^*, u_{44}^* for small arguments does not depend on k, i. e. on the frequency ω and for $r \to 0$ it is as follows

$$u_{33}^* \approx -\frac{1}{2\pi c_{44}} \ln r, \quad u_{33,j}^* \approx -\frac{1}{2\pi c_{44}} \frac{1}{r} r_{,j},$$
$$u_{44}^* \approx \frac{1}{2\pi \varepsilon_{11}} \ln r, \quad u_{44,j}^* \approx \frac{1}{2\pi \varepsilon_{11}} \frac{1}{r} r_{,j}. \tag{3.28}$$

3.3.1.2 Radon Transform for Fundamental Solution Derivation

Applying the Radon transform to both sides of Eq. (3.23) and having in mind $m = (m_1, m_2)$, $|m| = 1$ and $\tau = \langle \xi, m \rangle$, we obtain

$$\begin{cases} (\partial_s^2 + k^2) R(u_{33}^*) = -\dfrac{1}{c_{44}} \delta(s - \tau), \\ \partial_s^2 R(u_{44}^*) = \dfrac{1}{\varepsilon_{11}} \delta(s - \tau). \end{cases} \tag{3.29}$$

where $k = \omega \sqrt{\dfrac{\rho}{c_{44}}}$. Solutions of Eq. (3.29) are obtained using expressions (3.20)

$$
\begin{aligned}
R(u_{33}^*)(s,m) &= \frac{i}{2kc_{44}} e^{ik|s-\tau|}, \\
R(u_{44}^*)(s,m) &= \frac{1}{\varepsilon_{11}} |s-\tau|.
\end{aligned}
\tag{3.30}
$$

Now, we apply the inverse Radon transform to Eq. (3.30) and in a first step from Eq. (3.17) we get

$$
\begin{aligned}
K(R(u_{33}^*))(s,m) &= \frac{1}{2c_{44}} \{ i\pi e^{ik\beta} - 2[\mathrm{ci}(k\beta)\cos(k\beta) + \mathrm{si}(k\beta)\sin(k\beta)]\}|_{\beta=|s-\tau|}, \\
K(R(u_{44}^*))(s,m) &= \frac{1}{\varepsilon_{11}} \ln|s-\tau|.
\end{aligned}
\tag{3.31}
$$

The second step in the inverse Radon transform consists in the representation as an integral over the unit circle

$$
u_{JJ}^*(x,\xi) = \frac{1}{4\pi^2} \int_{|m|=1} K(R(u_{JJ}^*))(s,m) dm. \tag{3.32}
$$

From Eqs. (3.31) and (3.32) the fundamental solutions yield as

$$
\begin{aligned}
u_{33}^*(x,\xi) &= \frac{1}{8\pi^2 c_{44}} \int_{|m|=1} \{ i\pi e^{ik\beta} - 2[\mathrm{ci}(k\beta)\cos(k\beta) \\
&\quad + \mathrm{si}(k\beta)\sin(k\beta)]\}|_{\beta=|\langle x-\xi,m\rangle|} dm. \\
u_{44}^*(x,\xi) &= \frac{1}{4\pi^2 \varepsilon_{11}} \int_{|m|=1} \ln|<x-\xi,m>|dm.
\end{aligned}
\tag{3.33}
$$

The derivatives of the fundamental solution are

$$
u_{JJ,k}^*(x,\xi) = \frac{1}{4\pi^2} \int_{|m|=1} \partial_s K(R(u_{JJ}^*))(s,m) m_k dm, \tag{3.34}
$$

where

$$
\begin{aligned}
\partial_s K(R(u_{33}^*))(s,m) &= \frac{1}{2c_{44}} \{ -k\pi e^{ik\beta} - \frac{2}{\beta} + 2k[\mathrm{ci}(k\beta)\sin(k\beta) \\
&\quad - \mathrm{si}(k\beta)\cos(k\beta)]\}|_{\beta=|s-\tau|} \mathrm{sgn}(s-\tau).
\end{aligned}
\tag{3.35}
$$

The asymptotic behaviour of u_{33}^* and u_{44}^* for small arguments is again given by the expressions (3.28) due to the behaviour of $\mathrm{ci}(z) = O(\ln z)$, $\mathrm{si}(z) = O(z)$ for $z \to 0$, see Bateman and Erdelyi [1], the form of u_{33}^* in Eq. (3.33) and of $u_{33,k}^*$ in Eq. (3.34).

3.3.1.3 Comparison of Both Solutions

In order to compare the fundamental solutions obtained with the Fourier transform (3.26), (3.27) and with the Radon transform (3.33), (3.34) we denote the solution (3.26) with u^F_{JJ} and the solution (3.33) with u^R_{JJ}.

First we note that $u^{*F}_{44} \equiv u^{*R}_{44} = u^*_{44}$ what follows from the following representations given in John [28]

$$\begin{aligned} &\int_{|m|=1} \ln|\langle x-\xi, m\rangle| dm = 2\pi \ln r, \\ &\int_{|m|=1} \frac{m_k}{\langle x-\xi, m\rangle} dm = 2\pi \frac{1}{r} r_{,k}. \end{aligned} \tag{3.36}$$

Let us denote by $g(r) = u^{*F}_{33}(r) - u^{*R}_{33}(r)$, then $g(r)$ is a smooth function satisfying the first equation in (3.21). This means that the singular parts of u^{*F}_{33}, u^{*R}_{33} like $O(\ln r)$ and $u^{*F}_{33,k}$, $u^{*R}_{33,k}$ like $O(1/r)$ coincide. These singular parts do not depend on k, i.e. on ω and with respect to the multiplicity by constants they are the same as for the static case, i.e. like u^*_{44} and $u^*_{44,k}$. Moreover the singular part of $u^{*R}_{33,k}(r)$ is equal to its asymptotic $-\dfrac{1}{2\pi c_{44}} \dfrac{1}{r} r_{,j}$ what follows by Eqs. (3.34) and (3.35) and formulas (3.36), but for $u^{*F}_{33,k}(r)$ this is not the case.

From the above we can conclude that if we deal with displacement BIE it is better to use u^{*F}, but if we deal with integro-differential equations as in traction BIEM, then it is better to use u^{*R}, because its singular part for any arguments is as in the static case. For u^{*F} the singular part has a simple form only for small arguments. This is one of the reasons to use u^{*R}, instead u^{*F} in traction BIEM even for anti-plane problems.

3.3.2 Coupled Anti-plane Case

In the coupled case $e_{15} \neq 0$ and we have to find a fundamental solution of Eq. (2.38). It is a matrix valued function

$$u^* = \begin{pmatrix} u^*_{33} & u^*_{34} \\ u^*_{43} & u^*_{44} \end{pmatrix},$$

which is the solution of the systems of equations

$$\begin{cases} c_{44}\triangle u^*_{3J} + e_{15}\triangle u^*_{4J} + \rho\omega^2 u^*_{3J} = -\delta(x-\xi)\delta_{3J}, \\ e_{15}\triangle u^*_{3J} - \varepsilon_{11}\triangle u^*_{4J} = -\delta(x-\xi)\delta_{4J}, \quad J = 3, 4. \end{cases} \tag{3.37}$$

Applying Radon transform to Eq. (3.37) we obtain the differential equation in matrix form

$$(M\partial_s^2 + \rho\omega^2 J_2)\hat{u}^* = -\delta(s-\tau)I_2, \tag{3.38}$$

where $R(u^*) = \hat{u}^*$, $\tau = \langle \xi, m\rangle$, $m = (m_1, m_2)$, $|m| = 1$ and

$$M = \begin{pmatrix} c_{44} & e_{15} \\ e_{15} & -\varepsilon_{11} \end{pmatrix}; \quad J_2 = \begin{pmatrix} 1 & 0 \\ 0 & 0 \end{pmatrix}; \quad I_2 = \begin{pmatrix} 1 & 0 \\ 0 & 1 \end{pmatrix}.$$

Multiplying the second row of Eq. (3.38) by $\dfrac{e_{15}}{\varepsilon_{11}}$ and after adding it to the first row, the system decouples for the unknowns $\hat{u}^*_{3K}$, $K = 3, 4$ to the equations

$$\begin{cases} \partial_s^2 \hat{u}^*_{33} + k^2 \hat{u}^*_{33} = -\dfrac{1}{a_0}\delta(s-\tau), \\ \partial_s^2 \hat{u}^*_{34} + k^2 \hat{u}^*_{34} = -\dfrac{e_{15}}{\varepsilon_{11} a_0}\delta(s-\tau), \end{cases} \tag{3.39}$$

where $a_0 = c_{44} + \dfrac{e_{15}^2}{\varepsilon_{11}}$, $k = \omega\sqrt{\dfrac{\rho}{a_0}}$. From Eq. (3.20) we obtain the solutions

$$\begin{aligned} \hat{u}^*_{33} &= \frac{i}{2a_0 k} e^{ik|s-\tau|}, \\ \hat{u}^*_{34} &= \frac{i e_{15}}{2\varepsilon_{11} a_0 k} e^{ik|s-\tau|} = \frac{e_{15}}{\varepsilon_{11}} \hat{u}^*_{33}. \end{aligned} \tag{3.40}$$

From the second row in Eq. (3.38) and from Eq. (3.40) it is obvious that $\hat{u}^*_{43} = \hat{u}^*_{34}$. It remains to solve the equation for $\hat{u}^*_{44}$. From Eq. (3.38) we have

$$e_{15}\partial_s^2 \hat{u}^*_{34} - \varepsilon_{11}\partial_s^2 \hat{u}^*_{44} = -\delta(s-\tau),$$

and using Eq. (3.40) we get the equation

$$\partial_s^2 \hat{u}^*_{44} = -\frac{i e_{15}^2 k}{2\varepsilon_{11}^2 a_0} e^{ik|s-\tau|} + \left(\frac{1}{\varepsilon_{11}} - \frac{e_{15}^2}{\varepsilon_{11}^2 a_0}\right)\delta(s-\tau). \tag{3.41}$$

Solving Eq. (3.41) by applying the formulas in (3.40), we finally obtain

$$\hat{u}^*_{44} = \frac{e_{15}^2}{\varepsilon_{11}^2}\hat{u}^*_{33} + \frac{1}{2\varepsilon_{11}}|s-\tau|. \tag{3.42}$$

Applying the inverse Radon transform to $\hat{u}^*_{JK}$, using the formulas (3.17) we get

$$
\begin{aligned}
u^*_{33}(x,\xi) &= \frac{1}{8\pi^2 a_0}\int_{|m|=1}\{i\pi e^{ik\beta} - 2[\mathrm{ci}(k\beta)\cos(k\beta) \\
&\qquad + \mathrm{si}(k\beta)\sin(k\beta)]\}|_{\beta=|\langle x-\xi,m\rangle|}dm, \\
u^*_{34}(x,\xi) &= u^*_{43}(x,\xi) = \frac{e_{15}^2}{\varepsilon_{11}}u^*_{33}(x,\xi), \\
u^*_{44}(x,\xi) &= \frac{e_{15}^2}{\varepsilon_{11}^2}u^*_{33}(x,\xi) + \frac{1}{2\pi\varepsilon_{11}}\ln|x-\xi|.
\end{aligned}
\tag{3.43}
$$

The derivatives $\hat{u}^*_{JK,p}$ are

$$
\begin{aligned}
u^*_{33,p}(x,\xi) &= \frac{1}{8\pi^2 a_0}\int_{|m|=1}\{-k\pi e^{ik\beta} - \frac{2}{\beta} + 2k[\mathrm{ci}(k\beta)\sin(k\beta) \\
&\qquad - \mathrm{si}(k\beta)\cos(k\beta)]\}|_{\beta=|\langle x-\xi,m\rangle|}\,\mathrm{sgn}\langle x-\xi,m\rangle m_p dm, \\
u^*_{34,p}(x,\xi) &= u^*_{43,p}(x,\xi) = \frac{e_{15}^2}{\varepsilon_{11}}u^*_{33,p}(x,\xi), \\
u^*_{44,p}(x,\xi) &= \frac{e_{15}^2}{\varepsilon_{11}^2}u^*_{33,p}(x,\xi) + \frac{1}{2\pi\varepsilon_{11}|x-\xi|}\frac{x_p-\xi_p}{|x-\xi|}.
\end{aligned}
\tag{3.44}
$$

The asymptotic behaviour of u^*_{JK} for small arguments $r \to 0$, is obtained as in the uncoupled case

$$
\begin{aligned}
&u^*_{33} \approx -\frac{1}{2\pi a_0}\ln r, \quad u^*_{33,p} \approx -\frac{1}{2\pi a_0}\frac{1}{r}r_{,p}, \\
&u^*_{34} = u^*_{43} \approx -\frac{e_{15}}{\varepsilon_{11}}\frac{1}{2\pi a_0}\ln r, \quad u^*_{34,p} = u^*_{43,p} \approx -\frac{e_{15}}{\varepsilon_{11}}\frac{1}{2\pi a_0}\frac{1}{r}r_{,p}, \\
&u^*_{44} \approx \frac{1}{2\pi\varepsilon_{11}}\left(-\frac{e_{15}^2}{\varepsilon_{11}}+1\right)\ln r, \quad u^*_{44,p} \approx \frac{1}{2\pi\varepsilon_{11}}\left(-\frac{e_{15}^2}{\varepsilon_{11}}+1\right)\frac{1}{r}r_{,p}.
\end{aligned}
\tag{3.45}
$$

3.4 In-plane Piezoelectric Case

As in the previous section we start with the simple case of a decoupled in-plane system that corresponds to the elastic anisotropic/isotropic case.

3.4.1 Uncoupled In-plane Case

In this case $e_{15} = e_{31} = e_{33} = 0$ and Eq. (2.33) reduces to

$$\begin{cases} c_{11}u_{1,11} + c_{44}u_{1,33} + (c_{13} + c_{44})u_{3,13} + \rho\omega^2 u_1 = 0, \\ (c_{13} + c_{44})u_{1,13} + c_{44}u_{3,11} + c_{33}u_{3,33} + \rho\omega^2 u_3 = 0, \\ -\varepsilon_{11}u_{4,11} - \varepsilon_{33}u_{4,33} = 0. \end{cases} \tag{3.46}$$

The fundamental solution is a matrix valued generalized function

$$u^* = \begin{pmatrix} u^*_{11} & u^*_{13} & u^*_{14} \\ u^*_{31} & u^*_{33} & u^*_{34} \\ u^*_{41} & u^*_{43} & u^*_{44} \end{pmatrix},$$

which solves the following system of equations

$$\begin{cases} c_{11}u^*_{1J,11} + c_{44}u^*_{1J,33} + (c_{13} + c_{44})u^*_{3J,13} + \rho\omega^2 u^*_{1J} = -\delta(x - \xi)\delta_{1J}, \\ (c_{13} + c_{44})u^*_{1J,13} + c_{44}u^*_{3J,11} + c_{33}u^*_{3J,33} + \rho\omega^2 u^*_{3J} = -\delta(x - \xi)\delta_{3J}, \\ -\varepsilon_{11}u^*_{4J,11} - \varepsilon_{33}u^*_{4J,33} = -\delta(x - \xi)\delta_{4J},\ J = 1, 3, 4. \end{cases} \tag{3.47}$$

Since the fundamental solution is defined with respect to solution of Eq. (3.46) we can set $u^*_{14} = u^*_{34} = u^*_{41} = u^*_{43} = 0$. The unknowns in Eq. (3.47) are $u^*_{11}, u^*_{13} = u^*_{31}, u^*_{33}$, which are solutions of the first two systems of anisotropic equations and u^*_{44} which is a solution of the last electrostatic equation. For the solution of Eq. (3.47) we will use the Radon transform. Applying it to (3.47) we obtain

$$\begin{cases} [C(m)\partial_s^2 + \rho\omega^2]\hat{U}^* = -\delta(s - \tau)I_2, \\ -(\varepsilon_{11}m_1^2 + \varepsilon_{33}m_3^2)\partial_s^2\hat{U}^*_{44} = -\delta(s - \tau), \end{cases} \tag{3.48}$$

where $m = (m_1, m_3)$, $|m| = 1$, $\tau = \langle x - \xi, mrangle$, $x = (x_1, x_3)$, $\xi = (\xi_1, \xi_3)$ and

$$\hat{U}^* = \begin{pmatrix} R(u^*_{11}) & R(u^*_{13}) \\ R(u^*_{31}) & R(u^*_{33}) \end{pmatrix},$$

$$C(m) = \begin{pmatrix} c_{11}m_1^2 + c_{44}m_3^2 & (c_{13} + c_{44})m_1m_3 \\ (c_{13} + c_{44})m_1m_3 & c_{44}m_1^2 + c_{33}m_3^2 \end{pmatrix}. \tag{3.49}$$

Due to conditions (2.20) and since $|m| = 1$, the matrix $C(m) = \{C_{ij}(m)\}$ is symmetric and positive definite, i.e. $C(m) > 0$, and has two different positive eigenvalues

$$a_j(m) = \frac{1}{2}\left(\mathrm{Tr}C + (-1)^{j+1}\sqrt{(\mathrm{Tr}C)^2 - 4\det C}\right), \tag{3.50}$$

where $\mathrm{Tr}C = C_{11} + C_{22}$ is the trace of the matrix C. The unit eigenvectors $g_j(m)$ corresponding to the eigenvalues $a_j(m)$ are orthogonal and can be chosen as

$$g_1 = \frac{1}{\sqrt{(C_{11}-a_1)^2+C_{12}^2}}(-C_{12}, C_{11}-a_1),$$
$$g_2 = \frac{1}{\sqrt{(C_{22}-a_2)^2+C_{12}^2}}(-C_{22}+a_2, C_{12}), \tag{3.51}$$

where at the points m at which the denominators vanish, the components are defined by their limit values. Denoting by

$$T = \begin{pmatrix} g_1^1 & g_2^1 \\ g_1^2 & g_2^2 \end{pmatrix},$$

the orthogonal matrix and with the replacement $\hat{U}^*(s,m) = T\hat{V}(s,m)$, Eq. (3.48) becomes:

$$[CT\partial_s^2 + \rho\omega^2 T]\hat{V} = -\delta(s-\tau)I_2. \tag{3.52}$$

$$[CT\partial_s^2 + \rho\omega^2 T]\hat{V} = -\delta(s-\tau)I_2. \tag{3.53}$$

Multiplying Eq. (3.53) from the left with T^{-1} and since

$$T^{-1}CT = A = \begin{pmatrix} a_1 & 0 \\ 0 & a_2 \end{pmatrix},$$

the following equation is obtained

$$[A\partial_s^2 + \rho\omega^2]\hat{V} = -\delta(s-\tau)T^{-1}. \tag{3.54}$$

Equation (3.54) consists of four ordinary differential equations of the type

$$[a\partial_s^2 + \rho\omega^2]\hat{v} = -\delta(s-\tau)\gamma. \tag{3.55}$$

Using Eq. (3.20), the solution of Eq. (3.55) is $\hat{v} = \alpha\gamma e^{ik|s-\tau|}$, $k = \omega\sqrt{\frac{\rho}{a}}$, $\alpha = \frac{i}{2ak}$.

Then

$$\hat{U}^* = T\hat{V} = \begin{pmatrix} g_1^1 & g_2^1 \\ g_1^2 & g_2^2 \end{pmatrix}\begin{pmatrix} \hat{V}_{11} & \hat{V}_{12} \\ \hat{V}_{21} & \hat{V}_{22} \end{pmatrix} \tag{3.56}$$

where $\hat{V}_{jl} = \alpha_j g_l^j e^{ik_j|s-\tau|}$ with $k_j = \sqrt{\frac{\rho}{a_j}}\omega$ and $\alpha_j = \frac{i}{2a_j k_j}$. Using Eq. (3.17) it holds

$$\tilde{V}_{jl}(s,m) = K(\hat{V}_{jl}) = -ik_j\alpha_j g_l^j\{i\pi e^{ik_j\beta} - 2[\mathrm{ci}(k_j\beta)\cos(k_j\beta) + \mathrm{si}(k_j\beta)\sin(k_j\beta)]\}|_{\beta=|s-\tau|}. \tag{3.57}$$

After applying inverse Radon transform to $\hat{U}^* = T\tilde{V}$, the fundamental solution and its derivatives are

$$u^*(x,\xi) = \frac{1}{4\pi^2}\int_{|m|=1}\begin{pmatrix} g_1^1 & g_2^1 \\ g_1^2 & g_2^2 \end{pmatrix}\begin{pmatrix} g_1^1\tilde{u}_1 & g_1^2\tilde{u}_1 \\ g_2^1\tilde{u}_2 & g_2^2\tilde{u}_2 \end{pmatrix}|_{s=|\langle x-\xi,m\rangle|}dm \tag{3.58}$$

$$u^*_{,p}(x,\xi) = \frac{1}{4\pi^2}\int_{|m|=1}\begin{pmatrix} g_1^1 & g_2^1 \\ g_1^2 & g_2^2 \end{pmatrix} \times \begin{pmatrix} g_1^1\partial_s\tilde{u}_1 & g_1^2\partial_s\tilde{u}_1 \\ g_2^1\partial_s\tilde{u}_2 & g_2^2\partial_s\tilde{u}_2 \end{pmatrix}|_{s=|\langle x-\xi,m\rangle|}m_p\,\mathrm{sign}\langle m, x-\xi\rangle dm. \tag{3.59}$$

where from Eq. (3.17)

$$\tilde{u}_j(s,m) = \frac{1}{2a_j}\{i\pi e^{ik_j s} - 2[\mathrm{ci}(k_j s)\cos(k_j s) + \mathrm{si}(k_j s)\sin(k_j s)]\}, \tag{3.60}$$

and

$$\partial_s\tilde{u}_j(s,m) = \frac{1}{2a_j}\{-\pi k_j e^{ik_j s} - \frac{2}{s} + 2k_j[\mathrm{ci}(k_j s)\sin(k_j s) - \mathrm{si}(k_j s)\cos(k_j s)]\}. \tag{3.61}$$

The near field asymptotics of u^*_{il} and $u^*_{il,p}$ are

$$u^*_{il} \approx b_{il}\ln r \quad \text{and} \quad u^*_{il,p} \approx d_{ilp}\frac{1}{r}r_{,p} \quad \text{as} \quad r \to 0, \tag{3.62}$$

where due to the orthogonality of matrix T, the coefficients b_{il} and d_{ilp} depend only on the elastic constants and on the density, but not on the frequency.

The asymptotic behaviour of the fundamental solution u^*_{il} as $r \to 0$ is represented by integrals of linear combinations of $\tilde{u}_j(s,m)$ over the unit circle and its leading term is evaluated from $\mathrm{ci}(k_j s) \to O(\ln r)$. The asymptotic behaviour of the derivatives $u^*_{il,p}$ as $r \to 0$ is represented by integrals of linear combinations of $\partial_s\tilde{u}_p(s,m)$ over the unit circle and their leading term is $O(1/r)$.

We obtain the solution u^*_{44} of the last equation in (3.46) by proceeding as in Sect. 3.3. The direct Radon transform gives for $\hat{U}_{44} = R(u^*_{44})$ with $C_{44}(m) = \varepsilon_{11}m_1^2 + \varepsilon_{33}m_3^2$

$$\partial_s^2\hat{U}_{44} = \frac{1}{C_{44}(m)}\delta(s-\tau) \tag{3.63}$$

This equation is as Eq. (3.18) with $\alpha = 0, \gamma = \dfrac{1}{C_{44}(m)}$. Its solution is as in Eq. (3.20)

$$\hat{U}_{44} = \frac{1}{2C_{44}(m)}|s - \tau|. \tag{3.64}$$

Applying the inverse Radon transform to Eq. (3.64) we obtain

$$u^*_{44} = \frac{1}{4\pi^2}\int_{|m|=1} \frac{\ln|\langle x-\xi, m\rangle|}{C_{44}(m)} dm. \tag{3.65}$$

Note that only if $\varepsilon_{11} = \varepsilon_{33}$, then $C_{44}(m) = \varepsilon_{11}$ and the solution of Eq. (3.65) is the same as the solution of Eq. (3.33).

As an example we will write down the fundamental solution and its derivatives for the time-harmonic elastic-isotropic plane derived by the Radon transform. The independent material constants are: $c_{11} = c_{33} = \lambda + 2\mu$ and $c_{13} = c_{44} = \mu$, where λ, μ are the Lamé constants with $\lambda + \mu > 0$.

The matrix $C(m)$ in Eq. 3.49 has the form

$$C(m) = \begin{pmatrix} (\lambda+2\mu)m_1^2 + \mu m_2^2 & (\lambda+\mu)m_1 m_2 \\ (\lambda+\mu)m_1 m_2 & \mu m_1^2 + (\lambda+2\mu)m_2^2 \end{pmatrix}. \tag{3.66}$$

In this case the eigenvalues a_i of matrix $C(m)$ defined in Eq. (3.50) do not depend on m, $a_1 = \lambda + 2\mu, a_2 = \mu$, the eigenvectors are $g_1 = (m_1, -m_2)$, $g_2 = (m_2, m_1)$ and $k_1 = \omega\sqrt{\dfrac{\rho}{\lambda+2\mu}}$, $k_2 = \omega\sqrt{\dfrac{\rho}{\mu}}$. The matrices T, A are

$$T = \begin{pmatrix} m_1 & m_2 \\ -m_2 & m_1 \end{pmatrix}, \quad A = \begin{pmatrix} \lambda+2\mu & 0 \\ 0 & \mu \end{pmatrix}, \tag{3.67}$$

and for the fundamental solution and its derivatives we obtain

$$\begin{aligned} u^*(x,\xi) = \frac{1}{4\pi^2}\int_{|m|=1} &\begin{pmatrix} m_1 & m_2 \\ -m_2 & m_1 \end{pmatrix} \\ &\times \begin{pmatrix} m_1\tilde{u}_1 & -m_2\tilde{u}_1 \\ m_2\tilde{u}_2 & m_1\tilde{u}_2 \end{pmatrix}\Big|_{s=|\langle x-\xi,m\rangle|} dm, \end{aligned} \tag{3.68}$$

$$\begin{aligned} u^*_{,p}(x,\xi) = \frac{1}{4\pi^2}\int_{|m|=1} &\begin{pmatrix} m_1 & m_2 \\ -m_2 & m_1 \end{pmatrix} \\ &\times \begin{pmatrix} m_1\partial_s\tilde{u}_1 & -m_2\partial_s\tilde{u}_1 \\ m_2\partial_s\tilde{u}_2 & m_1\partial_s\tilde{u}_2 \end{pmatrix}\Big|_{s=|\langle x-\xi,m\rangle|} m_p \operatorname{sign}\langle x-\xi, m\rangle dm. \end{aligned} \tag{3.69}$$

Correspondingly, the asymptotics is given by

$$u^*_{il} \approx b_{il}\ln r \quad \text{and} \quad u^*_{il,p} \approx d_{ilp}\frac{1}{r}r_{,p} \quad \text{as} \quad r \to 0. \tag{3.70}$$

3.4.2 Coupled In-plane Case

In the coupled case at least one of the piezoelectric constants e_{15}, e_{31}, e_{33} is not zero and the fundamental solution is a matrix valued generalized function

$$u^* = \begin{pmatrix} u^*_{11} & u^*_{13} & u^*_{14} \\ u^*_{31} & u^*_{33} & u^*_{34} \\ u^*_{41} & u^*_{43} & u^*_{44} \end{pmatrix},$$

which is the solution of the system of equations

$$\begin{cases} c_{11}u^*_{1J,11} + c_{44}u^*_{1J,33} + (c_{13}+c_{44})u^*_{3J,13} + (e_{31}+e_{15})u^*_{4J,13} \\ +\rho\omega^2 u^*_{1J} = -\delta(x-\xi)\delta_{1J}, \\ (c_{13}+c_{44})u^*_{1J,13} + c_{44}u^*_{3J,11} + c_{33}u^*_{3J,33} + e_{15}u^*_{4J,11} + e_{33}u^*_{4J,33} \\ +\rho\omega^2 u^*_{3J} = -\delta(x-\xi)\delta_{3J}, \\ (e_{15}+e_{31})u^*_{1J,13} + e_{15}u^*_{3J,11} + e_{33}u^*_{3J,33} \\ -\varepsilon_{11}u^*_{4J,11} - \varepsilon_{33}u^*_{4J,33} = -\delta(x-\xi)\delta_{4J}, \quad J = 1,3,4. \end{cases} \tag{3.71}$$

Applying the Radon transform to the system (3.71), and using its properties, we obtain the following matrix equation

$$[C(m)\partial_s^2 + \rho\omega^2 J_3]\hat{U}^*(s,m) = -\delta(s-\tau)I_3, \tag{3.72}$$

where $\hat{U}^* = R(u^*)$, $\tau = \langle \xi, m \rangle$,

$$I_3 = \begin{pmatrix} 1 & 0 & 0 \\ 0 & 1 & 0 \\ 0 & 0 & 1 \end{pmatrix}, \quad J_3 = \begin{pmatrix} 1 & 0 & 0 \\ 0 & 1 & 0 \\ 0 & 0 & 0 \end{pmatrix},$$

and the matrix $C(m) = \{C_{JK}(m)\}$ is given by

$$C(m) = \begin{pmatrix} c_{11}m_1^2 + c_{44}m_3^2 & (c_{13}+c_{44})m_1m_3 & (e_{31}+e_{15})m_1m_3 \\ (c_{13}+c_{44})m_1m_3 & c_{44}m_1^2 + c_{33}m_3^2 & e_{15}m_1^2 + e_{33}m_3^2 \\ e_{15}m_1^2 + e_{33}m_3^2 & (e_{31}+e_{15})m_1m_3 & -\varepsilon_{11}m_1^2 - \varepsilon_{33}m_3^2 \end{pmatrix}. \tag{3.73}$$

The matrix Eq. (3.72) consists of three systems with three linear ODEs. After expressing the functions $\partial_s^2 \hat{U}^*_{4J}$ by

$$\partial_s^2 \hat{U}^*_{4J} = C_{44}^{-1}(C_{k4}\partial_s^2 \hat{U}^*_{kJ} + \delta_{4J}\delta(s-\tau)), \tag{3.74}$$

the Eq. (3.72) is reduced to the matrix equation

$$[D(m)\partial_s^2 + \rho\omega^2 I_2]\hat{V}^*(s,m) = -F(m)\delta(s-\tau), \tag{3.75}$$

consisting of three systems with two ODEs where $\hat{V}^*$ is a 2×3 matrix (the first two rows of $\hat{U}^*$). The so-called 'stiffened matrix' $D(m)$, see Daros [6], is a 2×2 matrix with components

$$d_{ij}(m) = C_{ij}(m) - C_{44}^{-1}(m) C_{i4} C_{j4}(m),$$

and $F(m)$ is a 2×3 matrix with components

$$f_{jK}(m) = \delta_{jK} - C_{44}^{-1}(m) \delta_{4J}(\delta_{j1} + \delta_{j3}).$$

The matrix Eq. (3.75) In order to solve the matrix Eq. (3.75), we transform it into canonical form. On account of the properties of the material constants C_{iJKl}, see Eq. (2.20), the matrix $D(m)$ is symmetric and positive definite. So, as in the uncoupled case in Sect. 3.4.1, the matrix $D(m)$ for $m = (m_1, m_3)$, $|m| = 1$ has two different positive eigenvalues $a_1(m) > a_2(m) > 0$ defined as

$$a_j(m) = \frac{1}{2} \left(\mathrm{Tr} D + (-1)^{j+1} \sqrt{(\mathrm{Tr} D)^2 - 4 \det D} \right). \tag{3.76}$$

The unit eigenvectors $g_j(m)$ corresponding to $a_j(m)$ are orthogonal and can be defined as

$$\begin{aligned} g_1 &= \frac{1}{\sqrt{(d_{11} - a_1)^2 + d_{12}^2}} (-d_{12}, d_{11} - a_1), \\ g_2 &= \frac{1}{\sqrt{(d_{22} - a_2)^2 + d_{12}^2}} (-d_{22} + a_2, d_{12}), \end{aligned} \tag{3.77}$$

where at the points m at which the denominators vanish the components are defined by their limit values.

The orthogonal matrix

$$T(m) = \begin{pmatrix} g_1^1 & g_2^1 \\ g_1^2 & g_2^2 \end{pmatrix},$$

changes the basis to the basis of the eigenvectors. With the substitution

$$\hat{V}^*(s, m) = T(m) V(s, m), \quad H(m) = T(m) F(m), \tag{3.78}$$

into Eq. (3.75), multiplying from the left side with $T^{-1}(m)$ and having in mind that

$$T^{-1}(m) D(m) T(m) = A(m) = \begin{pmatrix} a_1(m) & 0 \\ 0 & a_2(m) \end{pmatrix},$$

the system of Eq. (3.75) decouples:

$$[A(m) \partial_s^2 + \rho \omega^2 I_2] V(s, m) = -H(m) \delta(s - \tau). \tag{3.79}$$

Equations in (3.79) form six ODEs of the type

$$[b(m)\partial_s^2 + \rho\omega^2]v(s,m) = -h(m)\delta(s-\tau), \tag{3.80}$$

with the solutions, see Eq. (3.20),

$$v(s,m) = \alpha h e^{ik|s-\tau|}, \quad k = \omega\sqrt{\rho/a(m)}, \quad \alpha = i(2a(m)k(m))^{-1}. \tag{3.81}$$

Therefore we have

$$\begin{array}{l} \hat{V}^* = T(m)V(s,m), \quad V_{pq}(s,m) = \alpha_p g_q^p e^{ik_p|s-\tau|}, \\ k_p = \omega\sqrt{\rho/a_p(m)}, \quad \alpha_p = i(2a_p(m)k_p(m))^{-1}. \end{array} \tag{3.82}$$

The components $\hat{U}^*_{kj}$ of $\hat{U}^*_{KJ}$ are determined by $\hat{U}^*_{kj} = \hat{V}^*_{kj}$, while $\hat{U}^*_{4J}$ is obtained by Eq. (3.74). From the 2×2 matrix $\hat{U}^*$ the fundamental solution u^* is constructed through inverse Radon transform.

Applying the above described procedure, the functions $u^*_{ij}, i, j = 1, 3$ can be written as

$$u^*_{ij}(x,\xi) = \frac{1}{4\pi^2}\int_{|m|=1} \begin{pmatrix} g_1^1 & g_2^1 \\ g_1^2 & g_2^2 \end{pmatrix} \begin{pmatrix} g_1^1 W_1 & g_1^2 W_1 \\ g_2^1 W_2 & g_2^2 W_2 \end{pmatrix} |_{s=|\langle x-\xi,m\rangle|} dm \tag{3.83}$$

where, from Eq. (3.17) can be seen that

$$\begin{array}{ll} W_j(s) & = A_j[\pi e^{ik_j s} - 2(\mathrm{ci}(k_j s)\cos(k_j s) + \mathrm{si}(k_j s)\sin(k_j s))], \\ A_j & = (8\pi^2 a_j)^{-1}. \end{array} \tag{3.84}$$

The functions u^*_{i4} for $i = 1, 3$ take the form

$$u^*_{i4}(x,\xi) = \frac{1}{4\pi^2}\int_{|m|=1} \begin{pmatrix} g_1^1 & g_2^1 \\ g_1^2 & g_2^2 \end{pmatrix} \begin{pmatrix} g_4^1 W_1 \\ g_4^2 W_2 \end{pmatrix} |_{s=|<x-\xi,m>|} dm, \tag{3.85}$$

where $g_4^k = -d_{44}^{-1}(d_{14}g_k^1 + d_{34}g_k^2)$, $k = 1, 2$ and finally

$$u^*_{44}(x,\xi) = h_1(x,\xi) + h_2(x,\xi), \tag{3.86}$$

where

$$\begin{array}{l} h_1(x,\xi) = \left\langle \displaystyle\int_{|m|=1} \begin{pmatrix} g_1^1 & g_2^1 \\ g_1^2 & g_2^2 \end{pmatrix} (-d_{44}^{-1}) \begin{pmatrix} d_{14}g_4^1 W_1 \\ d_{34}g_4^2 W_2 \end{pmatrix} |_{s=|\langle x-\xi,m\rangle|} dm, (1,1) \right\rangle, \\ h_2(x,\xi) = \dfrac{1}{4\pi^2}\displaystyle\int_{|m|=1} d_{44}^{-1} \ln|s||_{s=|\langle x-\xi,m\rangle|} dm. \end{array} \tag{3.87}$$

The derivatives of the fundamental solution u^* and its corresponding stress σ^* can be found using the function

$$\partial_s W_j(s) = A_j[-\pi k_j e^{ik_j s} - \frac{2}{s} + 2k_j(\mathrm{ci}(k_j s)\sin(k_j s) - \mathrm{si}(k_j s)\cos(k_j s))]. \quad (3.88)$$

Furthermore, the near-field asymptotic expressions are

$$u^*_{IJ} \approx b_{IJ} \ln|x - x_0|, \quad u^*_{kI,J} \approx d_{kIJ} \frac{1}{|x - x_0|}, \text{ for } x \to x_0, \quad (3.89)$$

where b_{IJ} and d_{kIJ} depend on the elastic, dielectric and piezoelectric constants and the density, but not on the frequency ω. This can be shown as it was done in the uncoupled case, see Sect. 3.4.1.

References

1. Bateman H, Erdelyi A (1953) Higher transcendental functions. McGraw-Hill, New York
2. Burridge R (1966) Lacunas in two-dimensional wave propagation. Proc Camb Phil Soc 63:819–825
3. Burridge R (1967) The singularity on the plane lids of the wave surface of elastic media with cubic symmetry. Quart J Mech Appl Math 20:41–56
4. Chen T (1993) Green's function and the non-uniform transformation problem in a piezoelectric medium. Mech Res Commun 20(3):271–281
5. Chen ZT, Lin FZ (1993) Numerical evaluation of derivatives of the anisotropic piezoelectric Green's functions. Mech Res Commun 20(6):501–517
6. Daros CH (1999) Wave propagation in unbounded piezoelectric media of transversely isotropic symmetry. Ph.D. thesis, Series on Mechanics, No. 39, Technical University of Braunschweig, Braunschweig
7. Daros CH (2002) A fundamental solutions for transversely isotropic, piezoelectric solids under electrically irrotational approximation. Mech Res Commun 29:61–71
8. Daros CH, Antes H (2000a) Dynamic fundamental solutions for transversely isotropic piezoelectric materials of crystal class 6mm. Int J Solids Struct 37:1639–1658
9. Daros CH, Antes H (2000b) On strong ellipticity conditions for PEM of the crystal classes 6mm and 622. Wave Motion 31:237–253
10. Deeg WF (1980) The analysis of dislocation, cracks and inclusion problems in piezoelectric solids. Ph.D. thesis, Stanford University, Stanford, California
11. Denda M, Lua J (1999) Development of the boundary element method for 2D piezoelectricity. Compos Part B 30:699–707
12. Denda M, Araki Y, Yong YK (2004) Time-harmonic BEM for 2-D piezoelectricity applied to eigenvalue problems. Int J Solids Struct 41:7241–7265
13. Ding SH, Liang J, Chen B (1996) Fundamental solutions for transversely isotropic piezoelectric media. Sci China Ser A 39(7):766–775
14. Ding SH, Wang G, Chen W (1998) A boundary integral formulation and 2D fundamental solutions for piezoelectric media. Comput Meth Appl Mech Eng 158:65–80
15. Duff GFD (1977) Hyperbolic differential equations and waves. In: Garnir HG (ed) Boundary value problems for linear evaluation of partial differential equations. pp 27–155
16. Dunn ML (1994) Electroelastic Green's functions for transversely isotropic piezoelectric media and their application to the solution of inclusion and ingomogeneity problems. Int J Eng Sci 32(1):119–131

17. Dunn ML, Wienecke HA (1996) Green's functions for transversely isotropic piezoelectric solids. Int J Solids Struct 33:4571–4581
18. Gel'fand IM, Shilov GE (1964a) Generalized functions, properties and operations, vol 1. Academic Press, New York
19. Gel'fand IM, Shilov GE (1964b) Generalized functions, spaces of fundamental and generalized functions, vol 2. Academic Press, New York
20. Gel'fand IM, Graev MI, Vilenkin NY (1966) Generalized functions, integral geometry and representation theory, vol 5. Academic Press, New York
21. Gradshteyn IS, Ryzhik IM (1965) Tables of integrals, series, and products. Academic Press, New York
22. Graffi D (1946) Sul teorema di reciprocita nella dinamica dei corpi elastici. Mem Accad Sci Bologna Ser 104:103–111
23. Gross D, Dineva P, Rangelov T (2002) Dynamic fracture behaviour of a multilayered piezoelectric solid, Part 1. Technical report. DFG grant 436 BUL 113/118-1, TU Darmstadt
24. Gross D, Dineva P, Rangelov T (2004) Dynamic fracture behaviour of a multilayered piezoelectric solid, Part 2. Technical report. DFG grant 436 BUL 113/118-1, TU Darmstadt
25. Gross D, Rangelov T, Dineva P (2005) 2D Wave scattering by a crack in a piezoelectric plane using traction BIEM. Struct Integr Dur 1(1):35–47
26. Helgason S (1980) Radon transform. Birkäuser, Boston
27. Iosida K (1965) Functional analysis. Springer, Berlin
28. John F (1955) Plane waves and spherical means applied to partial differential equations. Wiley International Science, New York
29. Khutoryansky NM, Sosa H (1995a) Dynamic representation formulas and fundamental solutions for piezoelectricity. Int J Solids Struct 32:3307–3325
30. Khutoryansky NM, Sosa H (1995b) Construction of dynamic fundamental solutions for piezoelectric solids. Appl Mech Rev 48(11):222–229
31. Lee JS (1995) Boundary element method for electroelastic interaction in piezoceramics. Eng Anal Bound Elem 15:321–328
32. Lee JS, Jiang L (1994) A boundary integral formulation and 2D fundamental solution for piezoelectric media. Mech Res Commun 21(1):47–54
33. Ludwig D (1966) The radon transform on euclidean space. Comm Pure Appl Math 29:49–81
34. Norris AN (1994) Dynamic Greens functions in anisotropic piezoelectric, thermoelastic and poroelastic solids. Proc Royal Soc Lond A447:175–188
35. Pan E, Amadei B (1999) Boundary element analysis of fracture mechanics in anisotropic bimaterials. Eng Anal Bound Elem 23:683–691
36. Pan YC, Chou TW (1976) Point force solution for an infinite transversely isotropic solid. ASME J Appl Mech 43:608–612
37. Rajapakse RKND, Xu XL (2001) Boundary element modelling of cracks in piezoelectric solids. Eng Anal Bound Elem 25:771–782
38. Rangelov T, Manolis G, Dineva P (2005) Elastodynamic fundamental solutions for 2D inhomogeneous anisotropic domains: basic derivations. Eur J Mech A Solids 24:820–836
39. Saez A, Dominguez J (1999) BEM analysis of wave scattering in transversely isotropic solids. Int J Numer Meth Eng 44(9):1283–1300
40. Saez A, Dominguez J (2001) Dynamic crack problems in three-dimensional transversely isotropic solids. Eng Anal Bound Elem 25:203–210
41. Sosa H, Khutoryansky N (1999) Transient dynamic response of piezoelectric bodies subjected to internal electric impulses. Int J Solids Struct 36:5467–5484
42. Sosa H, Khutoryansky N (2001) Further analysis of the transient dynamic response of piezoelectric bodies subjected to electric impulses. Int J Solids Struct 38:2101–2114
43. Vladimirov V (1971) Equations of mathematical physics. Marcel Dekker Inc, New York
44. Wang CY, Achenbach JD (1994) Elastodynamic fundamental solutions for anisotropic solids. Geophys Int J 118:384–392
45. Wang CY, Achenbach JD (1995) Three-dimensional time-harmonic elastodynamic Green's functions for anisotropic solids. Proc R Soc Lond A 449:441–458

46. Wang CY, Zhang Ch (2005) 2D and 3D dynamic Green's functions and time-domain BIE formulations for piezoelectric solids. Eng Anal Bound Elem 29:454–465
47. Wang CY, Achenbach JD, Hirose S (1996) Two-dimensional time domain BEM for scattering of elastic waves in solids of general anisotropy. Int J Solids Struct 33:3843–3864
48. Wang CY, Zhang C, Hirose S (2003) Dynamic fundamental solutions and time domain BIE formulations for piezoelectric solids. In: Gallego R, Aliabadi MH (eds) Advances in boundary element techniques IV. pp 215–225
49. Wang XD, Meguid SA (2000b) Modelling and analysis of the dynamic behaviour of piezoelectric materials containing interfacing cracks. Mech Mater 32:723–737
50. Wheeler LT, Sternberg E (1968) Some theorems in classical elastodynamics. Arch Rat Mech Appl 31:51–90

Chapter 4
Numerical Realization by BIEM

Abstract Non-hypersingular traction integro-differential equations are derived for the solution of the BVPs formulated in Chap. 2 for bounded and unbounded solids. The numerical realization by the BIEM is presented and a description of the programm codes is given.

4.1 Introduction Remarks

The BIEM is an attractive candidate for modelling wave propagation in media with coupled properties because of certain advantages, namely:

(a) the integral equation formulation used is equivalent to the original governing equations and boundary conditions. This fact, coupled with the use of fundamental solutions for these governing equations, guarantees a high level of accuracy;
(b) the fundamental solutions obey the Sommerfeld's radiation condition and thus infinitely extended boundaries are automatically accounted for without resorting to special types of viscous boundaries;
(c) since only surfaces need to modelled, there is reduction of the problem dimensionality, with a corresponding reduction in the size of the system matrices as compared with domain-type numerical methods;
(d) selective solution at internal points in the domain of interest is possible once the BVP has been solved, which obviates the large scale volume discretization;
(e) flexibility in modelling arbitrary geometry;
(f) concurrent recovery of both displacements and tractions at a comparable accuracy level;
(g) high computational accuracy at solution of problems with stress gradient as are problems in fracture mechanics.

However, it is well known that the conventional displacement BIE formulation degenerates for crack problems and it cannot be directly applied to them, see Cruse [9] and Sladek and Sladek [23]. Generally there are five methods to overcome this difficulty:

P. Dineva et al., *Dynamic Fracture of Piezoelectric Materials*,
Solid Mechanics and Its Applications 212, DOI: 10.1007/978-3-319-03961-9_4,

- The multi-domain technique with fictitious boundaries was used in Sladek and Sladek [24] and Chirino et al. [6]. In this case the usual displacement BIEM can be applied, but it requires more processor time.
- The usage of the Green's function for crack problems. In case that Green's function is available, the usual displacement BIEM can be applied without crack discretization, but usually these functions are not available for the elasto-dynamic crack problems, see Snyder and Cruse [25].
- The traction BIE, which can be obtained by differentiating the displacement representation formula, then substituting it into the Hooke's law and applying an usual limiting process. This conventional derivation of the traction BIE is based on the Betti-Rayleigh elasto-dynamic reciprocal theorem. The traction BIEs are hypersingular and do not converge even in the sense of Cauchy principal values due to the additional differentiation of the stress Green's function, see Balas et al. [1]. There are two methods for the solution of these hypersingular equations:
  - The hypersingular integrals are regarded as Hadamard finite-part integrals and will be directly integrated analytically [3, 14].
  - By applications of a regularization procedure, the hypersingular integrals are regularized to CPV integrals and after that the modified BIEs are solved numerically. Most regularization techniques use partial integration to shift the derivative of the stress Green's function to the unknown crack opening displacements, see [11, 24].
- Non-hypersingular traction BIE is derived by using a two-state conservation integral of elasto-dynamic, see [28, 30].
- A combination of displacement and hyper-singular traction BIE, see Chen and Hong [5], mixed BIEM proposed by Chirino and Abascal [7], dual BIEM discussed by Fidelinski et al. [12], displacement and traction BIDE by Sladek and Sladek [24]. The cited authors use quadratic and semi-continuous BEs to satisfy the smoothness requirements in the hypersingular traction BIE.

It is obvious that the use of the displacement BIE analysis technology is limited. The complex dynamic non-symmetric crack problems for finite bodies demands the usage of the traction BIE. In the past this method was restricted to static problems, see Portela and Aliabadi [20] or dynamic problems for crack embedded in an infinite space, see Zhang [29].

Together with the description of the numerical realization in terms of the non-hypersingular traction BIEM, this chapter deals with the investigation of the accuracy and the convergence of the non-hypersingular traction BIEM solution for time-harmonic SIFs computation of cracks in finite and infinite domains.

In contrast to the above mentioned methods we use continuous parabolic approximation. Here some new numerical methods are proposed, as a.g. the average method and the shifted point method, to approximate the tangential derivatives of displacements that appear in the traction BIDE. This is done in order to satisfy the smoothness requirements of the BIEM solution.

4.2 Traction BIEM

The non-hypersingular traction based BIE is derived following the procedure given in Zhang and Achenbach [28], Zhang [29] and Zhang and Gross [30] for the homogeneous elastic isotropic case and in Gross et al. [13] and Wang and Zhang [27] for the piezoelectric one.

Let us assume that G is a 2D piezoelectric domain. There are several cases, defined in Sect. 2.6, for which we can derive an integro-differential equation equivalent to the corresponding boundary-value problems:

(a) With respect to the domain: if $G = R^2$; if $G = R^2 \backslash K$, where K is bounded domain (open arc—crack, or convex domain—hole); if $G \subset R^2$ we consider the case of bounded domain with internal cracks or holes.
(b) With respect to the type of deformation state and wave polarization: in-plane or anti-plane strain state.
(c) With respect to the number of cracks: single or multiple.
(d) With respect to the material: homogeneous or graded one belonging to restricted classes of inhomogeneous materials.
(e) With respect to the electrical boundary condition along the crack: impermeable, permeable, limited permeable crack models.

The idea is in all cases listed above, to transform the corresponding BVP to IDE along the exterior and interior boundary (if any) and along the crack line such that the singularities in the kernels of the IDE are only of CPV type.

Here we will show shortly the transformation of the BVP to the equivalent IDE, following Wang and Zhang [27]. We will use the formulation by IDE for the solution of different BVPs in Parts II and III. For any of such problems (inhomogeneous, multiple cracks, holes, crack-hole interaction etc.) the IDE is obtained by the method described below.

The derivation is done here for the in-plane case (small indexes for the x-coordinates $i, j, \ldots = 1, 3$; capital indexes $J, K, \ldots = 1, 3, 4$, see Sect. 2.5.1), and as to the anti-plane case (small indexes for the x-coordinates $i, j, \ldots = 1, 2$; capital indexes $J, K, \ldots = 3, 4$, see Sect. 2.5.2) the derivation follows the same scheme.

4.2.1 Bounded Domain

Let $G \subset R^2$ be a bounded domain with a smooth boundary $S = \partial G$ and an internal crack $S_{cr} = S_{cr}^+ \cup S_{cr}^-$, see Fig. 4.1. Denote by G^ε a domain with smooth boundary $S^\varepsilon = \partial G^\varepsilon$, such that $S_{cr} \subset G^\varepsilon$, $S^\varepsilon \cap S_{cr} = \emptyset$ and $S^\varepsilon \to S_{cr}$ for $\varepsilon \to 0$. Consider the BVP (2.42) with $S_u = \emptyset$ and $S_t = S$ in $\Omega \backslash S_{cr}$

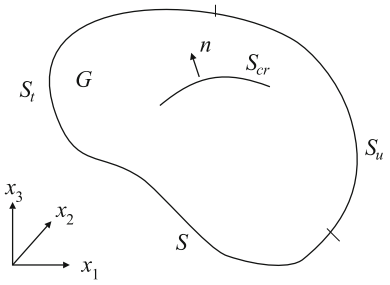

Fig. 4.1 Finite cracked piezoelectric solid

$$\begin{cases} \sigma_{iJ,i} + \rho_{JK}\omega^2 u_K = 0 \quad \text{in } G\backslash S_{cr}, \\ u_J|_{S_u} = \bar{u}_J, \quad t_J|_{S_t} = \bar{t}_J, \\ t_J|_{S_{cr}} = 0. \end{cases} \tag{4.1}$$

Note that the domain G can be simple connected or multiply connected if it contains holes.

The first step in deriving the IDE is the use of the conservation integral of linear dynamic piezoelectricity, see Wang and Zhang [27] in the domain $H^\varepsilon = G\backslash G^\varepsilon$ with boundary $\partial H^\varepsilon = S \cup S^\varepsilon$ for the equation

$$\sigma_{iJ,i} + \rho_{JK}\omega^2 u_K = -F_J \quad \text{in } G\backslash G^\varepsilon, \tag{4.2}$$

where F_J is the generalized force vector. The conservation integral of Eq. (4.2) is

$$\begin{aligned} J_p(u) = \int_{\partial H^\varepsilon} \Big[\frac{1}{2}(\sigma_{iJ} u_{J,i} - \rho_{JK}\omega^2 u_J u_K)\delta_{qp} \\ - \sigma_{qJ} u_{J,p} \Big] n_q d\Gamma - \int_{H^\varepsilon} F_J u_{J,p} dH = 0, \end{aligned} \tag{4.3}$$

where $n = (n_1, n_3)$ is the unit outward normal vector on ∂G^ε. Equation (4.3) is obtained as in the isotropic case, see Zhang and Gross [30] using the divergence form of equation of motion (4.2) and the Gauss-Ostrogradsky theorem for smooth functions in regular domains.

The second step is to obtain for two independent states

$$\{u_J^k(x), \sigma_{iJ}^k(x), F_J^k(x)\}, \quad k = 1, 2$$

the following formula:

$$\int_{\partial G^\varepsilon}\Big[\frac{1}{2}(\sigma^1_{iJ}u^2_{J,i}+\sigma^2_{iJ}u^1_{J,i}-\rho_{JK}\omega^2(u^1_Ju^2_K+u^2_Ju^1_K)\delta_{qp} - (\sigma^1_{qJ}u^2_{J,p}+\sigma^2_{qJ}u^1_{J,p})\Big]n_q d\Gamma-\int_{G^\varepsilon}(F^2_Ju^1_{J,p}+F^1_Ju^2_{J,p})dG=0. \tag{4.4}$$

The third step is to consider two special states:

$$\{u^*_{JM}(x,\xi),\sigma^*_{iJM}(x,\xi),\delta(x-\xi)\},$$

one is for the fundamental solution, see Sect. 3.4.2 and the other is the solution of the BVP (4.1). We fix $x\in H^\varepsilon$ and get a circle $B_\eta(x)$ with small radius η and center x, so that both states are smooth in $H^\varepsilon\backslash B_\eta(x)$. Letting $\eta\to 0$ and using the properties of δ-function from Eq. (4.4) we obtain

$$\alpha(x)u_{M,p}(x)=\int_{\partial H^\varepsilon}\Big[(\sigma^*_{iJM}(x,\xi)u_{J,i}(\xi)-\rho_{JK}\omega^2u_J(\xi)u^*_{KM}(x,\xi))\delta_{qp} - (\sigma_{qJ}(\xi)u^*_{JM,p}(x,\xi)+\sigma^*_{qJM}(x,\xi)u_{J,p}(\xi))\Big]n_q(\xi)d\Gamma, \tag{4.5}$$

where

$$\alpha(x)=\begin{cases}1, & x_0\in H^\varepsilon\\ 1/2, & x_0\in\partial H^\varepsilon\end{cases}.$$

Since $t_J=C_{iJMp}u_{M,p}n_i$ we get

$$\alpha(x)t_J(x)=C_{iJMp}n_i(x)\int_{\partial H^\varepsilon}\Big[(\sigma^*_{iJM}(x,\xi)u_{J,i}(\xi)-\rho_{JK}\omega^2u_J(\xi)u^*_{KM}(x,\xi))\delta_{qp} - (\sigma_{qJ}(\xi)u^*_{JM,p}(x,\xi)+\sigma^*_{qJM}(x,\xi)u_{J,p}(\xi))\Big]n_q(\xi)d\Gamma. \tag{4.6}$$

Now with the limit $\varepsilon\to 0$, i.e. $S^\varepsilon\to S_{cr}$ we obtain

$$\begin{aligned}\beta(x)t_J(x)=C_{iJMp}n_i(x)&\int_S\Big[(\sigma^*_{iJM}(x,\xi)u_{J,i}(\xi)\\ &-\rho_{JK}\omega^2u_J(\xi)u^*_{KM}(x,\xi))\delta_{qp}-\sigma^*_{qJM}(x,x_0)u_{J,p}(x))\Big]n_q(x)\\ &-\bar{t}_J(\xi)u^*_{JM,p}(x,\xi)dS\\ &+C_{iJMp}n_i(x)\int_{S_{cr}}\Big[(\sigma^*_{iJM}(x,\xi)\Delta u_{J,i}(\xi)-\rho_{JK}\omega^2\Delta u_J(\xi)u^*_{KM}(x,\xi))\delta_{qp}\\ &-\sigma^*_{qJM}(x,\xi)\Delta u_{J,p}(\xi)\Big]n_q(\xi)dS_{cr},\end{aligned} \tag{4.7}$$

where

$$\beta(x)=\begin{cases}1, x\in S_{cr},\\ 1/2, x\in S.\end{cases}.$$

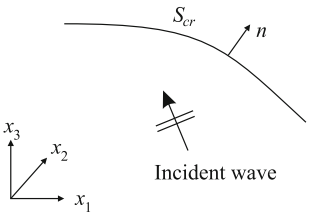

Fig. 4.2 Infinite cracked piezoelectric solid

Equation (4.7) is IDE with respect to the unknowns $\Delta u_J \in C^{1+\gamma}(S_{cr})$, $u_J \in C^{1+\gamma}(S)$, $\gamma \in (0,1)$. Having the solution of Eq. (4.7) we can find the solution $u_J(x)$ of the BVP (4.1) and the stress $\sigma_{iJ}(x)$ in any point $x \in G \backslash S_{cr}$:

$$\begin{aligned} u_J(x) = &- \int_S \sigma^*_{iJM}(x,\xi) u_{J,i}(\xi) n_i(\xi) + u^*_{KM}(x,\xi) t_J(\xi) dS \\ &- \int_{S_{cr}} \sigma^*_{iJM}(x,\xi) \Delta u_J(\xi) n_i(\xi) dS_{cr}, \end{aligned} \tag{4.8}$$

$$\begin{aligned} \sigma_{iJ}(x) = &\int_S \Big[(\sigma^*_{iJM}(x,\xi) u_{J,i}(\xi) - \rho_{JK}\omega^2 u_J(\xi) u^*_{KM}(x,\xi)) \delta_{qp} \\ &- \sigma^*_{qJM}(x,\xi) u_{J,p}(\xi)) \Big] n_q(\xi) - \bar{t}_J(\xi) u^*_{JM,p}(x,\xi) dS \\ &+ \int_{S_{cr}} \Big[(\sigma^*_{iJM}(x,\xi) \Delta u_{J,i}(\xi) - \rho_{JK}\omega^2 \Delta u_J(\xi) u^*_{KM}(x,\xi)) \delta_{qp} \\ &- + \sigma^*_{qJM}(x,\xi) \Delta u_{J,p}(\xi) \Big] n_q(\xi) dS_{cr}. \end{aligned} \tag{4.9}$$

Note that the same procedure is applied for obtaining the IDE for the BVP in the case of anti-plane strain, considered in Sect. 2.6.3. Here we restrict us to the model example but in the next chapters for every particular case the IDE will be derived separately.

4.2.2 Unbounded Domain

Let us consider an infinite domain $G = R^2$, where S_{cr} is a finite arc crack in this domain and let us focus on Eq. (2.4.4), governing the time-harmonic wave propagation in piezoelectric material, see Fig. 4.2. We are studying the wave scattering induced by the interaction of an incident plane wave with the crack. The total wave field is the sum of the incident and the scattered wave field

$$u_J(x) = u^{in}_J(x) + u^{sc}_J(x), \quad \sigma_{iJ}(x) = \sigma^{in}_{iJ}(x) + \sigma^{sc}_{iJ}(x) \tag{4.10}$$

where $x = (x_1, x_3)$, $u_J^{in}(x)$, $\sigma_{iJ}^{in}(x)$ are the generalized displacement and generalized stress components of the incident wave, while $u_J^{sc}(x)$, $\sigma_{iJ}^{sc}(x)$ are the components of the scattering wave. Recalling that all functions depend on the frequency, we can omit the respective term for simplicity. The scattered wave should satisfy the BVP (2.44) and Sommerfeld's radiation condition at infinity, see Sommerfeld [26]. From the traction free boundary condition in Eq. (2.44) it follows that

$$t_J^{sc}(x) = -t_J^{in}(x) \quad \text{on } S_{cr}. \tag{4.11}$$

Thus, to solve the BVP (2.44) we must know the incident wave field for any direction of propagation in R^2 and then use Eq. (4.11) to transform the BVP to the equivalent IDE on S_{cr}.

4.2.2.1 Plane Wave Solution

The incident wave displacement u_J^{in} is obtained as solution of Eq. (2.32) using the plane wave decomposition method, see Courant and Hilbert [8]. At a fixed frequency ω we seek a solution in form of a plane wave

$$\bar{U}(x, \eta) = p \exp\{-i\bar{k}\langle x, \eta\rangle\} \tag{4.12}$$

where $\eta = (\eta_1, \eta_3)$, $\eta_1 = \cos\theta$, $\eta_3 = \sin\theta$, with θ being the direction of wave propagation with respect to Ox_1 axis. Vector $p = (p_1, p_3, p_4)$ is the polarization vector and $\bar{k}$ is the real wave number which has to be determined from the condition that the vector function $\bar{U}$ satisfies Eq. (2.32)

$$(C(\partial) + \rho\omega^2 J_3)\bar{U}(x, \eta) = 0. \tag{4.13}$$

Here $C(\partial)$ and J_3 are matrices defined in Sect. 3.4, in Eq. (3.73) (we formally replace $m = (m_1, m_3)$ by $\partial = (\partial_1, \partial_3)$) i.e. matrix $C(\partial)$ has elements $C_{JK}(\partial) = C_{iJKl}\partial_i\partial_l$. From Eq. (4.13), simplifying the common factor $\exp\{-i\bar{k}\langle x, \eta\rangle\}$, we obtain a homogeneous system of 3 linear equation for $\bar{k}$ and p

$$(-\bar{k}^2 C(\eta) + \rho\omega^2 J_3)p = 0. \tag{4.14}$$

Reducing the last equation by replacing $p_4 = -C_{44}^{-1}(\eta)C_{i4}p_i$, we obtain a homogeneous system of 2 linear equations for $\bar{k}$ and $\bar{p} = (p_1, p_3)$:

$$(-\bar{k}^2 D(\eta) + \rho\omega^2 I_2)\bar{p} = 0. \tag{4.15}$$

The matrix of the system $D(\eta) = \{d_{ij}(\eta)\}$, $i, j = 1, 2$, $|\eta| = 1$ is the stiffness matrix, defined in Sect. 3.4.2. It is positively definite since and has two different positive eigenvalues

$$a_j(\eta) = \frac{1}{2}\left(\mathrm{Tr}D + (-1)^{j+1}\sqrt{(\mathrm{Tr}D)^2 - 4\det D}\right),\ j = 1, 2. \tag{4.16}$$

and two unit orthogonal eigenvectors $\bar{p^l}$, $l = 1, 2$, for example

$$\begin{aligned} p^2 &= \frac{1}{\sqrt{(d_{11} - a_1)^2 + d_{12}^2}}(d_{12}, -d_{11} + a_1), \\ p^2 &= \frac{1}{\sqrt{(d_{22} - a_2)^2 + d_{12}^2}}(d_{22} - a_2, -d_{12}), \end{aligned} \tag{4.17}$$

where at the points η, where the denominators are zero, the components are defined by their limit values.

With the wave numbers $\bar{k}_j = \omega\sqrt{\rho/a_j(\eta)}$, $j = 1, 2$ and using the expression for p_4^j, the generalized plane wave solution is found as a superposition of the two types of incident plane waves

$$\bar{U}^j(x, \eta) = p^j \exp\{-i\bar{k}_j < x, \eta >\}, \quad j = 1, 2. \tag{4.18}$$

The linear combination $\bar{U} = \alpha_1\bar{U}^1 + \alpha_2\bar{U}^2$ represents the set of all plane wave solutions of Eq. (2.32) where $\alpha_1 = 1, \alpha_2 = 0$ corresponds to L-waves, while $\alpha_1 = 0, \alpha_2 = 1$ corresponds to SV-waves. Note, that in contrast to isotropic elasticity, in anisotropic and piezoelectric cases the eigenvalues a_1, a_2 depend on the wave propagation direction η. Using the constitutive Eq. (2.27), the generalized incident stress tensor and corresponding traction vector on the crack S_{cr}^+ that appears on the left hand side of Eq. (4.11), can be determined.

4.2.2.2 BIDE Along the Crack

Denote by $G_R \supset S_{cr}$ a disk with a sufficiently large radius R where S_R is the circle $S_R = \partial G_R$. Applying the BIDE (4.7) to the domain G_R, we obtain the following BIDE for $x \in S_{cr}$

$$\begin{aligned} t_J(x) = C_{iJMp}n_i(x) \int_{S_R} \Big[&(\sigma^*_{iJM}(x, \xi)u_{J,i}(\xi) - \rho_{JK}\omega^2 u_J(\xi)u^*_{KM}(x, \xi))\delta_{qp} \\ &- \sigma^*_{qJM}(x, \xi)u_{J,p}(\xi))\Big]n_q(\xi) - \bar{t}_J(\xi)u^*_{JM,p}(x, \xi)dS \\ &+ C_{iJMp}n_i(x) \int_{S_{cr}} \Big[(\sigma^*_{iJM}(x, \xi)\Delta u_{J,i}(\xi) - \rho_{JK}\omega^2 \Delta u_J(\xi)u^*_{KM}(x, \xi))\delta_{qp} \\ &- \sigma^*_{qJM}(x, \xi)\Delta u_{J,p}(\xi)\Big]n_q(\xi)dS_{cr}. \end{aligned} \tag{4.19}$$

Letting $R \to \infty$ and using Sommerfeld's condition, the integrals over S_R tend to 0 and only the integral over S_{cr} remains in Eq. (4.19), i.e.

$$t_J(x) = C_{iJMp} n_i(x) \int_{S_{cr}} \Big[(\sigma^*_{iJM}(x,\xi) \Delta u_{J,i}(\xi) - \rho_{JK}\omega^2 \Delta u_J(\xi) u^*_{KM}(x,\xi)) \delta_{qp} - \sigma^*_{qJM}(x,\xi) \Delta u_{J,p}(\xi) \Big] n_q(\xi) dS_{cr}. \tag{4.20}$$

Having obtained Δu_J we can find the scattered displacement $u^{sc}_J(x)$ and stress $\sigma^{sc}_{iJ}(x)$ in any point $x \in R^2 \backslash S_{cr}$ by the integral representations

$$u^{sc}_J(x) = -\int_{S_{cr}} \sigma^*_{iJM}(x,\xi) \Delta u_J(\xi) n_i(\xi) dS_{cr}, \tag{4.21}$$

$$\sigma^{sc}_{iJ}(x) = \int_{S_{cr}} \Big[(\sigma^*_{iJM}(x,\xi) \Delta u_{J,i}(\xi) - \rho_{JK}\omega^2 \Delta u_J(\xi) u^*_{KM}(x,\xi)) \delta_{qp} - \sigma^*_{qJM}(x,\xi) \Delta u_{J,p}(\xi) \Big] n_q(\xi) dS_{cr}, \tag{4.22}$$

and thus the total wave field is given by

$$u_J(x) = u^{in}_J(x) + u^{sc}_J(x), \quad \sigma_{iJ}(x) = \sigma^{in}_{iJ}(x) + \sigma^{sc}_{iJ}(x).$$

4.3 Numerical Realization

The numerical solution of the problem follows the usual procedures of the BIEM based on discretization and collocation technique. The boundary is discretized into elements using parabolic approximations. Quadratic boundary elements are used for both the displacement and the traction quantities.

4.3.1 Discretization

Let us denote the boundary for the discretization by $S_w = S \cup S_{cr}$, where $S = \partial G$ is the exterior boundary of the domain G and $S = \emptyset$ for the problems in the whole plane; S_{cr} is the crack line and $S_{cr} = \emptyset$ for the problems in the domain without cracks. A discretization of the boundary $S_w = \cup_1^M \Gamma_s$ is used and u^s_i, t^s_i denote the components of displacement and traction along the s-th boundary element (BE), then: $u^s_i = u_i \chi_s$, $t^s_i = t_i \chi_s$ where χ_s is the characteristic function on Γ_s, i.e.

$$\chi_s = \begin{cases} 1, & x \in \Gamma_s, \\ 0, & x \bar{\in} \Gamma_s. \end{cases}$$

The following principles are used to approximate the displacements u_i, derivatives $u_{i,j}$ and tractions t_i:

(Hö) Hölder continuity
Functions $u_i \in C^{1+\gamma}(S)$, $\Delta u_i \in C^{1+\gamma}(S_{cr})$, $t_i \in C^{\gamma}(S)$, $0 < \gamma < 1$. These conditions have to be satisfied at least in the collocation points.

(Cr) Behavior at the crack-tips
The asymptotic expressions for the displacement and traction near the crack-tip in the two-dimensional case are well known [15, 22]. The asymptotic behavior of the displacements is $u_i \sim O(\sqrt{r})$ and of the tractions is $t_i \sim O(1/\sqrt{r})$, $r \to 0$.

(Irr) Irregular points
An irregular point is a point at which the boundary is not smooth, i. e. the normal vector does not exist (can not be uniquely defined) or the (Hö) conditions fails. The crack-tip and corners of a domain are particular examples of irregular points. Since the traction BIE exists only at points where the interpolation functions are Hölder continuously differentiable, the boundary must be smooth and the irregular points (tips and corners) should not be used as collocation points.

4.3.1.1 Quadratic Boundary Elements

In the following the necessary transformations are describe for passing from the global coordinate system to intrinsic coordinates.

Let us denote the coordinates of the nodes of the q-th boundary element with a length l by: (x_1^{jq}, x_3^{jq}), $j = 1, 2, 3$ and the coordinates of the field point by (x_1^p, x_3^p). Then the distances between the field point and the odd boundary nodes are given by

$$r_{x_k^1} = x_k^{1q} - x_k^p, \quad r_{x_k^3} = x_k^{3q} - x_k^p,$$

$k = 1, 3$. The transformation to the intrinsic coordinates ξ, and the expressions for the Jacobian and the normal vectors are as follows:

- For ordinary (O) BE:

$$r_{x_k} = r_{x_k^1} + \frac{1+\xi}{2}(r_{x_k^3} - r_{x_k^1}); \quad r_{x_k^m} = x_k^{mq} - x_k^p; \quad n_{x_k} = \frac{2}{l}\frac{d}{d\xi} r_{x_k}$$

$$\frac{d}{d\xi} r_{x_k} = \frac{1}{2}(r_{x_k^3} - r_{x_k^1}); \quad J = \left[\left(\frac{d}{d\xi} r_{x_1}\right)^2 + \left(\frac{d}{d\xi} r_{x_3}\right)^2\right]^{1/2} = \frac{l}{2};$$

.

- For left quarter-point (LQP) BE:

$$r_{x_k} = r_{x_k^1} + \left(\frac{1+\xi}{2}\right)^2 (r_{x_k^3} - r_{x_k^1}); \quad r_{x_k^m} = x_k^{mq} - x_k^p; \quad n_{x_k} = \frac{2}{l(1+\xi)} \frac{d}{d\xi} r_{x_k};$$

$$\frac{d}{d\xi} r_{x_k} = \frac{1+\xi}{2} (r_{x_k^3} - r_{x_k^1}); \quad J = \left[\left(\frac{d}{d\xi} r_{x_1}\right)^2 + \left(\frac{d}{d\xi} r_{x_3}\right)^2 \right]^{1/2} = (1+\xi)\frac{l}{2};$$

.

- For right quarter-point (RQP) BE:

$$r_{x_k} = r_{x_k^1} + \left(\frac{1-\xi}{2}\right)^2 (r_{x_k^3} - r_{x_k^1}); \quad r_{x_k^m} = x_k^{mq} - x_k^p; \quad n_{x_k} = \frac{2}{l(1-\xi)} \frac{d}{d\xi} r_{x_k};$$

$$\frac{d}{d\xi} r_{x_k} = \frac{\xi-1}{2} (r_{x_k^3} - r_{x_k^1}); \quad J = \left[\left(\frac{d}{d\xi} r_{x_1}\right)^2 + \left(\frac{d}{d\xi} r_{x_3}\right)^2 \right]^{1/2} = (1-\xi)\frac{l}{2};$$

.

The quadratic shape functions and their derivatives are:

$$N_1 = \frac{\xi(\xi-1)}{2}; \quad N_2 = 1 - \xi^2; \quad N_3 = \frac{\xi(\xi+1)}{2};$$

$$N_1' = \xi - \frac{1}{2}; \quad N_2' = -2\xi; \quad N_3' = \xi + \frac{1}{2}.$$

The special singular quarter point (SQP) shape functions are:

- Right SQP-BE defined on $[-1, 1)$ and

$$N_i^{*r} = \frac{2}{N_2 + 2N_1} N_i, \quad N_3^{*r} \approx O(1/(1-\xi)) \text{ for } \xi \to 1;$$

- Left SQP-BE defined on $(-1, 1]$ and

$$N_i^{*l} = \frac{2}{N_2 + 2N_3} N_i, \quad N_1^{*l} \approx O(1/(1+\xi)) \text{ for } \xi \to -1.$$

To form a linear algebraic system of equations from the integro-differential Eq. (4.7) or (4.10) we use the shifted point method, see Rangelov et al. [21], described in details in Sect. 4.3.2.2. The essence is that after discretization of the boundary S with continuous quadratic BEs and having in mind the parabolic approximation of the unknowns, we form for any BE and for any component of the unknowns two linear equations: (a) one using as a field point the second nodal point along the BE $(x_1^{2q} x_3^{2q})$; (b) the second using a point close to the odd nodal point along the BE—

named shifted point. In this way all integrals with such a field point are at least CPV integrals and the smoothness requirements of the approximation hold. Remind that the unknowns are the values of displacement, traction or COD at the nodal points, and the quadratic BEs are continuous.

4.3.1.2 Quadratic Approximation

If Γ_s is an ordinary BE the approximation of u_J^s, t_J^s is:

$$u_J^s(\xi) = \sum_1^3 u_J^{sk} N_k(\xi), \quad t_J^s(\xi) = \sum_1^3 t_J^{sk} N_k(\xi). \tag{4.23}$$

Here u_J^{sk} denotes the J-th displacement component in the k-th local node of the s-th boundary element.

Let us now verify how the standard quadratic approximation satisfies the principles (Cr), (Hö) and (Irr).

In order to satisfy the principle (Cr), following Blandford et al. [2] two special crack-tip boundary elements are used: (a) quarter-point boundary elements (QP-BE) LQP and RQP, for modeling the asymptotic behavior of displacement; (b) traction singular QP-BE (SQP-BE) for modeling the asymptotic behavior of traction. The special shape functions N_k^* for the traction SQP-BE are used for the case of a crack along the external boundary. The approximation for u_J^s, t_J^s in the case of traction SQP-BE is

$$u_J^s(\xi) = \sum_1^3 u_J^{sk} N_k(\xi), \quad t_J^s(\xi) = \sum_1^3 t_J^{sk} N_k^*(\xi). \tag{4.24}$$

The approximations (4.23) and (4.24) are continuous at the collocation points. The tangential derivatives of the displacements at the nodal points are expressed as derivatives of the approximated displacements

$$\frac{\partial}{\partial r_{x_i}}(u_J^s) = \frac{\partial u_J^s}{\partial \xi}\frac{\partial \xi}{\partial r_{x_i}} = \sum_1^3 u_J^{sk}\frac{\partial N_k(\xi)}{\partial \xi}\frac{\partial \xi}{\partial r_{x_i}} = \sum_1^3 u_J^{sk} N_k'(\xi)\xi_{,i}, \tag{4.25}$$

where $k = 1, 2, 3$.

When the collocation point does not coincide with the initial or the final point of the boundary element, then the principle (Hö) is satisfied. In what follows we will call the initial or the final node of the BE also as odd node or odd point, since when numbering all nodes in a subsequent order, the initial or the final node appear with an odd number.

It is evident from Eq. (4.25) that the approximation of the tangential derivatives of the displacement does not satisfy (Hö) condition at the odd points of the BE,

since $N_3'(1) \neq N_1'(-1)$. However, it is common practice to have the collocation points on the nodes of the element, where the solution is continuous, but does not satisfy the smoothness requirement. To circumvent this problem, one could choose nonconforming elements, where the collocation points are away from the nodes. If the collocation points are located at the nodes of the element, spurious results would be obtained, see Krishnasamy et al. [16]. Respective results seem to change dramatically with changes in the discretization mesh.

At the corners the boundary is not smooth and the normal vector does not exist. At the crack-tips the (Hö) condition fails. Therefore, irregular points should not be used as collocation points Balas et al. [1].

At the end of this section we would like to summarize that the standard continuous quadratic approximation can be used only after overcoming the following disadvantage. The irregular points of a finite cracked body such as crack-tips, corners and the odd discretization nodes should not be used as collocation points in the traction BIEM. The traction BIDE is not well defined in these points and this will lead to computational errors. In order to use the standard parabolic approximation avoiding the above-mentioned obstacles, we need to apply the parabolic approximation for $u_J, t_J, \Delta u_J$ near the irregular point and near the odd collocation points such that the principle (Hö) is fulfilled. We propose below two different ways for this purpose.

4.3.2 Numerical Schemes

4.3.2.1 Numerical Scheme AM

This approximation method helps in overcoming the disadvantage of the parabolic approximation at the odd discretization nodes.

The following approximation is proposed for the derivatives of the displacement on the BE Γ_s with three local nodes z_k^s, $k = 1, 2, 3$

$$u_{J,i}^s(\xi) = \sum_1^3 v_J^{s,k} N_k \xi_{,i}, \tag{4.26}$$

where $v_J^{s,k}$ is the average value of the tangential derivatives of u_J^s over elements Γ^{s-1}, Γ^s, Γ^{s+1} at z_k^s, $k = 1$ or 3. Note that in this case the equality $v_J^{s-1,3} = v_J^{s,1}$ holds and the condition (Hö) is fulfilled. This scheme gives a global approximation of tangential derivative of the displacement. Thus, along any odd collocation point we get the average value of displacement's derivative over the elements Γ^{s-1}, Γ^s, Γ^{s+1} at z_k^s.

Consider the matrix

$$L' = \begin{pmatrix} \frac{1}{2l'_{s-1}} & -\frac{2}{l'_{s-1}} & \left(\frac{3}{2l'_{s-1}} - \frac{3}{2l'_s}\right) & \frac{2}{l'_s} & -\frac{2}{l'_s} & 0 & 0 \\ 0 & 0 & -\frac{1}{l'_s} & 0 & \frac{1}{l'_s} & 0 & 0 \\ 0 & 0 & \frac{1}{2l'_s} & -\frac{2}{l'_s} & \left(\frac{3}{2l'_s} - \frac{3}{2l'_{s+1}}\right) & \frac{2}{l'_{s+1}} & -\frac{1}{2l'_{s+1}} \end{pmatrix}.$$

where the l', depending on the BEs, are defined as follows. If Γ^{s-1}, Γ^s, Γ^{s+1} are ordinary BE, then $l'_m = l_m$ which is the length of the BE Γ^m. If Γ^s is RQP-BE just before the crack-tip, Γ^{s+1} is a left SQP-BE and Γ^{s-1} is not a crack-tip BE, then $l'_s = 2l_s$. If Γ^s is a left SQP-BE next to the crack-tip, Γ^{s-1} is a RQP-BE and Γ^{s+1} is not a crack-tip BE, then $l'_s = 2l_s$. In all other cases $l'_s = l_s$. Note that the principle (Hö) is satisfied for the odd collocation points, i.e. $u_J^{s-1,3} = u_J^{s,1}, u_J^{s,3} = u_J^{s+1,1}$. The value of $v_J^{s,k}$ is defined by

$$\begin{pmatrix} v_J^{s,1} \\ v_J^{s,2} \\ v_J^{s,3} \end{pmatrix} = L' \begin{pmatrix} u_J^{s-1,1} \\ u_J^{s-1,2} \\ u_J^{s,1} \\ u_J^{s,2} \\ u_J^{s+1,1} \\ u_J^{s+1,2} \\ u_J^{s+1,3} \end{pmatrix}. \tag{4.27}$$

As can be seen from the traction BIDE, in general the unknowns are traction, displacements and their tangential derivatives, i.e., the values $v_J^{s,k}$ become unknowns too. However, adding the relation (4.26), the traction and the displacements become the only unknowns in the traction BIDE.

4.3.2.2 Numerical Scheme SPM

This approximation method is used to overcome the disadvantage of the parabolic approximation at the odd discretization nodes, corners and crack-tips.

A further possibility to use the standard global parabolic approximation for $u_J^s, t_J^s, u_{J,i}^s$ is to use all even nodal points as collocation points, but instead of the odd nodal points to use points close to them - called shifted points. We use this possibility to express the unknowns u_J^s, t_J^s at the collocation points (they are now internal points of the BE) by the unknowns at the nodes of the boundary element using their parabolic approximation over the element. This allows to form a global algebraic system for the unknowns at the boundary nodal points.

For example, let us denote the s-th BE as Γ^s, the $s+1$-th BE as Γ^{s+1} and their nodal points as z_1^s, z_2^s, z_3^s and $z_1^{s+1}, z_2^{s+1}, z_3^{s+1}$ correspondingly, where $z_3^s = z_1^{s+1}$. Instead of the point z_1^{s+1}, we use as a collocation point , the point which is close to

it i.e. $z_{11}^{s+1} \in (z_1^{s+1}, z_2^{s+1})$. Suppose for example that the unknown on the BE Γ^s and Γ^{s+1} is p_J. Applying Eq. (4.24) it can be represented on Γ^{s+1} as

$$p_J(z) = \sum_1^3 p_J^{s+1,k} N_k(\xi), \quad \xi = 2\frac{|z - z_1^{s+1}|}{|z_3^{s+1} - z_1^{s+1}|} - 1, \tag{4.28}$$

where $z = (x_1, x_3)$, $|z| = \sqrt{x_1^2 + x_3^2}$.

For the unknown $p_J^{s,3} = p_J^{s+1,1}$ at the node $z_3^s = z_1^{s+1}$ we have to form one linear equation following the standard procedure of BIEM. Using the traction BIEs we form an equation with a field point z_{11}^{s+1} and obtain an expression for $p_J(z_{11}^{s+1})$ through all unknowns at the nodal points, which is written in the form

$$p_J(z_{11}^{s+1}) = A^s p_J^{s,3} + A^{s+1} p_J^{s+1,1} + \Sigma, \tag{4.29}$$

where Σ contains all the other unknowns. Coefficient A^s is calculated solving a regular integral over Γ^s, while A^{s+1} is calculated solving a CPV integral over Γ^{s+1}.

On the other hand, over the BE Γ^{s+1} due to the parabolic approximation (4.27) $p_J(z_{11}^{s+1})$ is represented as

$$p_J(z_{11}^{s+1}) = \sum_1^3 p_J^{s+1,k} N_k(\xi_{11}^{s+1}), \quad \xi_{11}^{s+1} = 2\frac{|z_{11}^{s+1} - z_1^{s+1}|}{|z_3^{s+1} - z_1^{s+1}|} - 1. \tag{4.30}$$

Replacing $p_j(z_{11}^{s+1})$ from Eq. (4.30) into Eq. (4.29) we obtain the equation

$$[N_1(\xi_{11}^{s+1}) - A^s - A^{s+1}] p_J^{s+1,1} = \Sigma, \tag{4.31}$$

Note that for almost every z_{11}^{s+1} the coefficient of $p_j^{s+1,1}$ is not equal to zero because $N_1(\xi_{11}^{s+1})$ is real and $\mathrm{Im}(A^s + A^{s+1}) \neq 0$ due to the form of the time-harmonic fundamental solution and its traction.

For the unknowns at any odd nodal point, at any corner nodal point and at the crack-tip, in the case that the crack-tip is a part of the boundary, we form equations using the shifted points as collocation points by repeating the above described procedure. In such a way at all collocations points the principles (Hö), (Cr) and (Irr) are fulfilled.

It is a well known truth that the satisfaction of smoothness requirements for the field variables' approximations prescribed by the theory of elliptic partial differential equations and satisfaction of asymptotic behaviour near the crack-tip leads to a stable and accurate numerical solution. The advantages of the proposed AM and SPM schemes are that they help to solve the traction BIE in the case, when the continuous quadratic BEs are used, i.e. the approximation of the functions u_J and t_J is continuous. This is contrary to the application of the nonconforming BE where in order to solve properly the singular integral, the approximation of u_J and t_J is

discontinuous. So, the preferences should be given to these numerical schemes where the traction BIE is solved and a-priori conditions (Hö), (Cr) are satisfied.

4.3.3 Solution of the Integrals

To form a linear algebraic system of equations from the integro-differential Eqs. (4.7) or (4.20), we use the SPM, described above. The essence is that after discretization of the boundary S and of the crack lines S_{cr} with continuous quadratic BEs, all integrals are at least CPV integrals and the smoothness requirements of the approximation hold. Recall that the unknowns are the values of displacement, traction or COD at the nodal points and that the quadratic BEs are continuous.

The following types of double integrals with respect to the intrinsic variable $z \in [-1, 1]$ and $\varphi \in [0, 2\pi]$, where $m_1 = \cos\varphi$, $m_2 = \sin\varphi$ appears after discretization of Eqs. (4.7) or (4.20):

(U) Integrals with a kernel u^*_{JK};
(Σ) Integrals with a kernel $u^*_{JK,l}$.

4.3.3.1 Solution of the Integrals of Type (U)

If the field point and the running point do not belong to the same BE, the double integral is solved using the Quasi Monte Carlo Method. If the field point and the running point belong to the same BE then the integral is divided into a sum of two integrals - a regular one $(U)^{reg}$ and a singular one $(U)^{sing}$. The integrals $(U)^{reg}$ are solved numerically using the QMCM. The integrals $(U)^{sing}$ have a weak singularity of logarithmic type due to the asymptotic behavior in the fundamental solution of the cosine integral function for small arguments. Using the asymptotic representation, for example Eq. (3.89) for a small neighborhood of the field point the integral $(U)^{sing}$ is solved as a CPV integral, while on the rest of the interval it is solved numerically using the QMCM.

4.3.3.2 Solution of the Integrals of Type (Σ)

Let us divide those integrals into the sum of two integrals - the singular $(\Sigma)^{sing}$ with a kernel coming from $\dfrac{1}{s}$ in Eq. (3.88) and the regular $(\Sigma)^{reg}$. The integrals $(\Sigma)^{reg}$ are solved numerically by the QMCM. The singular integrals $(\Sigma)^{sing}$ are solved using Fubini's theorem analytically with respect to the intrinsic variable $z \in [0, 1]$ and then numerically on $\varphi \in [0, 2\pi]$ with Gauss's integration scheme. The corresponding formulae are as follows.

- Integrals over O-BE.
  Let's denote $\gamma = m_k r_{x_k} = A + Bz$. Over the boundary S and over the crack S_{cr} the integrals contain the shape functions N_k, which we denote by

$$\int_0^{2\pi}\int_{-1}^{1} f_{lJK} N_j \frac{1}{\gamma}\frac{L}{2} dz d\varphi = \int_0^{2\pi} f_{lJK} W_j^{ord} d\varphi.$$

  Additionally over S there exist integrals with N_k', which are denoted as

$$\int_0^{2\pi}\int_{-1}^{1} g^1_{lJK} N_j' \frac{1}{\gamma} dz d\varphi = \int_0^{2\pi} g^1_{lJK} V_j^{ord} d\varphi,$$

  where

$$\begin{aligned}
W_1^{ord} &= \frac{1}{B}\left[-2\left(\frac{A}{B}+1\right) + \left(\frac{A^2}{B^2}+\frac{A}{B}\right)\ln\left|\frac{A+B}{A-B}\right|\right] L,\\
W_2^{ord} &= \frac{1}{B}\left[4\frac{A}{B} - 2\left(\frac{A^2}{B^2}-1\right)\ln\left|\frac{A+B}{A-B}\right|\right] L,\\
W_3^{ord} &= \frac{1}{B}\left[-2\left(\frac{A}{B}-1\right) + \left(\frac{A^2}{B^2}-\frac{A}{B}\right)\ln\left|\frac{A+B}{A-B}\right|\right] L,
\end{aligned} \tag{4.32}$$

$$\begin{aligned}
V_1^{ord} &= \frac{1}{B}\left[2 - \frac{2A+B}{2B}\ln\left|\frac{A+B}{A-B}\right|\right],\\
V_2^{ord} &= \frac{1}{B}\left[-4 + 2\frac{A}{B}\ln\left|\frac{A+B}{A-B}\right|\right],\\
V_3^{ord} &= \frac{1}{B}\left[2 - \frac{2A-B}{2B}\ln\left|\frac{A+B}{A-B}\right|\right].
\end{aligned} \tag{4.33}$$

- Integrals over LQP-BE.
  Let's denote

$$\gamma = m_k r_{x_k} = C + D(\frac{z+1}{2})^2.$$

  Over the crack S_{cr} integrals with shape functions N_k', occur, denoted by

$$\int_0^{2\pi}\int_{-1}^{1} g^2_{lJK} N_j' \frac{1}{\gamma} dz d\varphi = \int_0^{2\pi} g^2_{lJK} V_j^{lqp} d\varphi,$$

where

$$V_1^{lqp} = \frac{2}{D}\ln\left|\frac{D+C}{C}\right| - \frac{3}{\sqrt{CD}}\arctan\sqrt{\frac{D}{C}},$$

$$V_2^{lqp} = -\frac{4}{D}\ln\left|\frac{D+C}{C}\right| + \frac{4}{\sqrt{CD}}\arctan\sqrt{\frac{D}{C}}, \tag{4.34}$$

$$V_3^{lqp} = \frac{2}{D}\ln\left|\frac{D+C}{C}\right| - \frac{1}{\sqrt{CD}}\arctan\sqrt{\frac{D}{C}}.$$

- Integrals over RQP-BE.
  Let's denote

$$\gamma = m_k r_{x_k} = F + H(\frac{z-1}{2})^2.$$

Over the crack S_{cr} integrals with shape functions N_k' occur, denoted by

$$\int_0^{2\pi}\int_{-1}^{1} g_{lJK}^3 N_j' \frac{1}{\gamma} dz d\varphi = \int_0^{2\pi} g_{lJK}^3 V_j^{rqp} d\varphi,$$

where

$$V_1^{rqp} = -\frac{2}{H}\ln\left|\frac{F+H}{F}\right| + \frac{1}{\sqrt{FH}}\arctan\sqrt{\frac{H}{F}},$$

$$V_2^{rqp} = \frac{2}{H}\ln\left|\frac{F+H}{F}\right| - \frac{4}{\sqrt{FH}}\arctan\sqrt{\frac{H}{F}}, \tag{4.35}$$

$$V_3^{rqp} = -\frac{2}{H}\ln\left|\frac{F+H}{F}\right| + \frac{3}{\sqrt{FH}}\arctan\sqrt{\frac{H}{F}}.$$

4.4 Programme Code, Material Constants

4.4.1 Programme Code

For the numerical solution by the BIEM, programme codes with both FORTRAN, see [19] and Mathematica, see [18] have been created. The programme scheme consists of the following parts:

(1) Definition of the material parameters, the domain and the crack geometry;
(2) Creating of the BIEM mesh, i.e., boundary elements and quadratic approximation;
(3) Definition of the fundamental solution, its derivatives and the asymptotic behaviour for small arguments;

Table 4.1 Material constants

Material	Elastic stiffness (10^{10}N/m^2)				Piezoelectric coefficient (C/m^2)			Dielectric constants (10^{-10}C/Vm)		Density (10^3kg/m^3)
	c_{11}	c_{13}	c_{33}	c_{44}	e_{31}	e_{33}	e_{15}	ε_{11}	ε_{33}	ρ
PZT-4	13.9	7.43	11.3	2.56	−6.98	13.84	13.44	60	54.7	7.5
PZT-5H	12.6	8.41	11.7	2.30	−6.50	23.30	17.44	150.3	130	7.6
PZT-6B	16.8	6.0	16.3	2.71	−0.9	7.1	4.6	36	34	7.55
PZT-7A	14.8	7.42	13.1	2.54	−2.1	9.5	9.7	81.1	73.5	7.5
$BaTiO_3$	16.6	7.75	16.2	4.29	−4.40	18.60	11.60	14.34	16.823	5.8
GaN	39.0	10.6	39.8	10.6	−0.3	0.65	−0.3	0.8407	0.9204	6.5

(4) Definition of the functions under the integrals of the integro-differential equations and definition of the type and characteristics of the applied load;
(5) Solution of the integrals and forming the system of linear equations for the unknowns;
(6) Solution of the linear system;
(7) Formulae for the solution at any point of the domain following the integral representative expressions;
(8) Computation of the stress intensity factors—the leading coefficients in the asymptotic of the solution near the crack edges.
(9) Computation of the stress concentration factor in the case of holes.

The most important points in the solution procedure are (4) and (5). In (4) the integrals over the BEs are two-dimensional (in the intrinsic coordinates in the domain $(z, \varphi) \in [-1, 1] \times [0, 2\pi]$) with regular and singular kernels: with weak singularity as $O(\ln r)$ and with strong singularity as $O(1/r)$. The regular integrals are solved using the QMCM with an appropriate number of points. The singular integrals are solved analytically with respect to r and numerically with respect to φ, as it is shown in Sect. 4.3. The difficulties in (6) are due to the fact that the material constants vary in the range of 10^{10} for elastic stiffness, in the range of 10 for the piezoelectric coefficients and in the range of 10^{-10} for the dielectric constants.

4.4.2 Material Constants

In the numerical calculations we will use data for different piezoelectric materials as shown in Table 4.1. The first five data sets are taken from Dieulesaint and Royer [10] and the GaN constants are taken from Bykhovski et al. [4] and Levinshtein et al. [17].

References

1. Balas J, Sladek J, Sladek V (1989) Stress analysis by boundary element methods. Elsevier, Amsterdam
2. Blandford GE, Ingrafea AR, Ligget JA (1981) Two-dimensional stress intensity factor computations using the boundary element method. Int J Numer Meth Eng 17:387–404
3. Budreck DE, Achenbach JD (1988) Scattering from three-dimensional planar cracks by the BIEM. ASME J Appl Mech 55:405–412
4. Bykhovski AD, Gelmond BL, Shur MS (1997) Elastic strain relaxation and piezoeffect in Ga N- AIN, Ga N- Al Ga N and Ga N- In Ga N superlattices. Appl Phys 81(9):6332–6338
5. Chen J, Hong HK (1999) Review of dual boundary element methods with emphasis on hypersingular integrals and divergent series. Appl Mech Rev 52:17–33
6. Chirino F, Gallego R, Dominguez J (1994) A comparative study of three boundary element approaches to transient dynamic crack problems. Eng Anal Bound Elem 13:11–19
7. Chirino F, Abascal R (1998) A comparative study of three boundary element approaches to transient dynamic crack problems. Int J Numer Meth Eng 43:365–388
8. Courant R, Hilbert D (1962) Methods of mathematical physics, vol II. Willey, New York
9. Cruse TA (1978) Two-dimensional BIE fracture mechanics analysis. Appl Math Model 2:287–293
10. Dieulesaint E, Royer D (1974) Elastic wave in solids. Wiley, New York
11. Dineva P, Gross D, Rangelov T (1999a) Ultrasonic wave scattering by a line crack in a solder joint. Res Nondestr Eval 11:117–135
12. Fidelinski P, Aliabadi M, Rooke D (1993) The dual boundary element method in dynamic fracture mechanics. Eng Anal Bound Elem 12:203–210
13. Gross D, Rangelov T, Dineva P (2005) 2D Wave scattering by a crack in a piezoelectric plane using traction BIEM. Struct Integr Dur 1(1):35–47
14. Hirose S, Achenbach JD (1988) Application of BEM to transient analysis of a 3-D crack. In: Tanaka M, Cruse TA (eds) BEM in applied mechanics. Pergamon Press, Oxford, pp 255–264
15. Kondratiev V (1967) Boundary problems for elliptic equations in domain with conocal and angular points. In: Proceedins of the Moscow mathematical society, v. 16, pp 227–313
16. Krishnasamy G, Schmerr LW, Rudolphi TJ, Rizzo FJ (1990) Hypersingular boundary integral equations: some applications in acoustic and elastic wave scattering. Trans ASME 57:404–414
17. Levinshtein ME, Rumyantsev SL, Shur MS (2001) Properties of advanced semiconductor materials GaN, AIN, InN, BN and SiGe. Wiley, London
18. Mathematica 6.0 for MS Windows (2007) Wolfram Research, Champaign, Illinois
19. MS visual studio (2005) professional edition. Redmond, Washington
20. Portela A, Aliabadi MN (1992) The dual boundary BEM: effictive implementation for cracked problems. Int J Numer Meth Eng 33:1269–1287
21. Rangelov T, Dineva P, Gross D (2003) A hyper-singular traction BIEM for stress intensity factor computation in a finite cracked body. Eng Anal Bound Elem 27:9–21
22. Sih GC, Loeber JE (1969) Wave propagation in an elastic solid with a line of discontinuity or finite crack. Quart J Appl Math 27:193–213
23. Sladek J, Sladek V (1984) Transient elastodynamic three-dimensional problems in cracked bodies. Appl Math Model 8:2–10
24. Sladek J, Sladek V (1987) A BIEM for dynamic crack problems. Eng Fract Mech 27:269–277
25. Snyder MD, Cruse TA (1975) BIE analysis of cracked anisotropy plates. Int J Fract 11:315–328
26. Sommerfeld A (1949) Partial differential equations in physics. Academic Press, New York
27. Wang CY, Zhang Ch (2005) 2D and 3D dynamic Green's functions and time-domain BIE formulations for piezoelectric solids. Eng Anal Bound Elem 29:454–465
28. Zhang C, Achenbach JD (1989) A new boundary integral equation formulation for elastodynamic and elastostatic crack analysis. ASME J Appl Mech 56:284–290
29. Zhang C (1991) A novel derivation of non-hypersingular time-domain BIEs for transient elastodynamic crack analysis. Int J Solids Struct 28:267–281
30. Zhang C, Gross D (1998) On wave propagation in elastic solids with cracks. Computational Mechanics Publications, Southampton

Part II
Homogeneous PEM

Part II focuses on the implementation of the proposed in Part I numerical scheme for BIEM solution of time-harmonic anti-plane and in-plane wave propagation problems. Homogeneous anisotropic (Chap. 5) and piezoelectric (Chaps. 6, 7) infinite and finite cracked solids are considered. Effects of the dynamic crack interaction (Chap. 8) plus different crack models for impermeable, permeable, and limited permeable crack (Chap. 9) are studied.

Chapter 5
Steady-State Problems in a Cracked Anisotropic Domain

Abstract We start with the uncoupled homogeneous case, which actually is for a homogeneous elastic anisotropic material. The accuracy and convergence of the numerical BIEM solution for evaluation of the SIFs is studied by comparison with existing solutions for elastic isotropic and orthotropic materials. In addition a parametric study for the wave field sensitivity regarding frequency, crack geometry and material anisotropy is presented.

5.1 Introduction

Studies on crack problems in anisotropic materials have been done since many years. The initial groundwork was laid by Sih et al. [30, 31]. In [15, 16, 29] systematic formulations were presented as a foundation of the anisotropic elasticity. The methods used for the solution of anisotropic crack problems are: (a) semi-analytical, see [7, 8, 12–14, 19, 20, 28]; (b) numerical as finite-difference schemes in Hua et al. [11]; finite-element method in [4, 21, 22]; BIEM in [1–3, 5, 6, 23–27, 32, 36–41] and (c) hybrid methods, see Song and Wolf [34].

In most of the semi-analytical papers, various types of integral equation techniques are used. Fourier or Laplace transforms reduce the boundary-value problem to dual integral equations that are expressed in terms of Fredholm integral equations. Using this approach Ohyoshi [19, 20] solved the anti-plane and the in-plane diffraction problems of waves in a cracked orthotropic plane. Dhawan [7, 8] treated the same problem, but for the transversely-isotropic case. Karim and Kundu [12, 13] considered the dynamic response of a layered anisotropic half-plane with anti-plane interface-cracks and an orthotropic half-plane with a subsurface in-plane crack. Kundu and Bostrom [14] studied wave scattering by a circular crack in a transversely-isotropic solid and the dynamic response of three coplanar cracks in an infinite orthotropic medium has been treated in Sarkar et al. [28].

P. Dineva et al., *Dynamic Fracture of Piezoelectric Materials*,
Solid Mechanics and Its Applications 212, DOI: 10.1007/978-3-319-03961-9_5,

Although BIEM is a very well suited approach for the type of problems considered here, only a few works can be found for dynamic anisotropic crack problems. The main difficulty is the availability of a fundamental solution that can be efficiently evaluated and implemented in a BIEM code.

This chapter is based on the papers by Dineva et al. [9, 10]. The main aim is to solve 2D steady-state elastic in-plane wave scattering problems in plane anisotropic solids by usage of the BIEM discussed in Chap. 4.

The importance of the presented chapter lies in the generality of the proposed methodology and in the parametric study results revealing how the anisotropy of the material, the existence of cracks, the wave parameters as frequency, crack geometry and wave propagation direction influence the dynamic stress concentration fields.

The advantages of the proposed method basing on BIEM include all its important features as the reduction of the dimension of the problem, implicit satisfaction of the radiation condition at infinite, the semi-analytical character of the method, high accuracy of solution of problems with stress gradients. In addition:

- The method is valid for general type of anisotropy. It allows considering the cases, when the coordinate axes do not coincide with the axis of material symmetry.
- The numerical procedure works for arbitrary incident wave angle, while in most cases other methods used for this purpose, as the singular integral method, have been applied only for the normal incident wave.

5.2 Statement of the Problem

We consider an uncoupled problem (2.44), i.e. an infinite, homogeneous, orthotropic and elastic solid containing a finite crack $S_{cr} = S_{cr}^{-} \cup S_{cr}^{+}$, see Fig. 5.1. The solid is subjected to an incident or time-harmonic plane L- or SV- wave, and the deformation of the solid is as in a state of plane strain. The non-zero quantities are the displacement components u_i and the stress components σ_{ij}, $i, j = 1, 3$. The electric field is zero, so $u_4 = 0$. Recall that the BVP is with traction free boundary conditions:

$$\begin{cases} \sigma_{ij,j} + \rho\omega^2 u_i = 0, & \text{in } R^2 \backslash S_{cr}, \\ t_j = 0 \quad \text{on } S_{cr}. \end{cases} \tag{5.1}$$

Here ρ is the mass density, ω is the frequency, the stress-strain low is govern by $\sigma_{ij} = C_{ijkl} u_{k,l}$ and $t_i = \sigma_{ij} n_j$ is the traction, n_i are the components of the unit normal vector on S_{cr}^{+} and C_{ijkl} are the elastic constants that satisfy the conditions (2.20) and (2.21)

$$\begin{aligned} &C_{ijkl} = C_{jikl} = C_{klij}, \quad \text{and} \\ &C_{ijkl} g_{ij} g_{kl} > 0 \quad \text{for every non-zero real symmetric tensor } g_{ij}. \end{aligned} \tag{5.2}$$

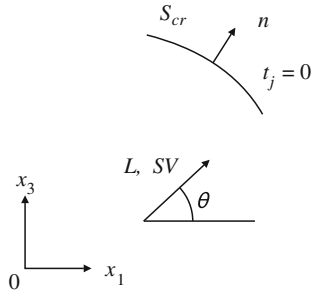

Fig. 5.1 Orthotropic plane with a crack

When the considered case is orthotropic and using the Voigt subscript notations the independent material constants reduce to four: $c_{11}, c_{13}, c_{33}, c_{44}$, see Su and Sun [35], because the coordinate axes and the material axes of symmetry coincide.

The interaction of an incident wave with the crack induces scattered waves. It is assumed in addition that the wave field satisfies the Sommerfeld's radiation condition at infinity, see Sommerfeld [33]. The total wave field is presented as a sum of the incident wave field and the scattered wave field:

$$u_i(x,\omega) = u_i^{in}(x,\omega) + u_i^{sc}(x,\omega), \quad \sigma_{ij}(x,\omega) = \sigma_{ij}^{in}(x,\omega) + \sigma_{ij}^{sc}(x,\omega), \tag{5.3}$$

where $x = (x_1, x_3)$ and ω is the frequency. The functions $u_i^{in}, \sigma_{ij}^{in}$ are the displacement and stress components of the incident wave field in the absence of the crack, while the functions $u_i^{sc}, \sigma_{ij}^{sc}$ are the corresponding displacement and stress of the scattered field due to the interaction of the incident wave with the crack. The incident wave is known, while the scattered wave field is unknown and has to be determined. The scattered wave must satisfy the equation of motion and the boundary condition in Eq. (5.1), which can be rewritten as

$$t_i^{sc} = -t_i^{in} \quad \text{on } S_{cr}. \tag{5.4}$$

The BIDE equation with respect to COD $\Delta u_i = u_i|_{S_{cr}^+} - u_i|_{S_{cr}^-}$ for the orthotropic case consists of the first two equations in Eq. (4.20) and has the form

$$\begin{aligned} t_i^{in}(x,\omega) = {} & C_{ijkl} n_j(x) \int_{S_{cr}^+} \sigma_{p\eta k}^*(x,\xi,\omega) \Delta u_{p,\eta}(\xi,\omega) \delta_{\lambda l} n_\lambda dS \\ & - \rho\omega^2 C_{ijkl} n_j(x) \int_{S_{cr}^+} u_{dk}^*(x,\xi,\omega) \Delta u_d(\xi,\omega) \delta_{\lambda l} n_\lambda dS \\ & - C_{ijkl} n_j(x) \int_{S_{cr}^+} \sigma_{m\lambda k}^*(x,\xi,\omega) \Delta u_{m,l}(\xi,\omega) n_\lambda dS, \quad x \in S_{cr}^+, \end{aligned} \tag{5.5}$$

where $u_{ij}^*(x,\xi,\omega)$ is the fundamental solution, see Eq. (3.58), and $\sigma_{ijk}^*(x,\xi,\omega)$ is its correspondingly stress, see Eq. (3.59).

After solution of BIE (5.5), we have found the scattered displacement $u_i^{sc}(x,\omega)$, and solution of the BVP (5.1) at any point of the considered domain can be found by the boundary integral representation, see Sect. 4.2.2.2

$$u_i^{sc}(x,\omega) = -\int_{S_{cr}^+} \sigma_{kij}^*(x,\xi,\omega)\Delta u_k(\xi,\omega)n_i dS, \quad x \notin S_{cr}^+. \tag{5.6}$$

The stress is obtained by using the Hooke's law and derivatives of Eq. (5.6)

$$\sigma_{pq}^{sc}(x,\omega) = -\int_{S_{cr}^+} \sigma_{ijk,l}^*(x,\xi,\omega)\Delta u_i(\xi,\omega)n_j dS, \quad x \notin S_{cr}^+. \tag{5.7}$$

5.3 Numerical Solution

The numerical procedure for solution of the Eq. (5.5) by BIEM is described in Sect. 4.3. After the discretization of the non-hypersingular traction BIEs, overcoming of the weak and strong singularities in the integrals and satisfaction of the boundary conditions, an algebraic complex system of equations with respect to the crack opening displacement is obtained and solved.

The numerical results are obtained with the program codes based on Mathematica and FORTRAN, see [17, 18].

The above presented formulation is general and it allows to solve dynamic fracture problems for general orthotropic materials. In order to validate the present approach, three test examples for a line crack in an isotropic and orthotropic plane under incident longitudinal time-harmonic waves are analyzed. The results are compared with those obtained by other authors. It should be mentioned that the existing results in the literature, in Ohyoshi [20] and in Dhawan [8] are only for an incidence angle $\theta = \pi/2$.

SIFs computation is obtained directly from the traction values ahead the crack-tip, see Eq. (2.40)

$$K_I = \lim_{r\to 0} t_3\sqrt{2\pi r}, \quad \text{and } K_{II} = \lim_{r\to 0} t_1\sqrt{2\pi r}, \tag{5.8}$$

where t_i is the ith component of the traction at the point along the crack at the distance r from the crack-tip. The SIF is normalized by its static value.

5.3.1 Incident Wave

In order to obtain the incident wave displacement $u_j^{in}(x,\omega)$ and then to find the incident wave traction along the crack line we use the plane wave decomposition method, see Sect. 4.2.2. In the decoupled purely elastic case, the plane wave solution

(4.12) has only 2 components, i.e. $p_4 = 0$ and $p = (p_1, p_3, 0)$. For fixed propagation direction $\eta = (\eta_1, \eta_3)$, $\eta_1 = cos\theta$, $\eta_3 = \sin\theta$, where θ is the incidence angle with respect to Ox_1 axis in the plane Ox_1, x_3, the matrix $D(\eta)$ is

$$D(\eta) = \begin{pmatrix} c_{11}\eta_1^2 + c_{44}\eta_3^2 & (c_{13} + c_{44})\eta_1\eta_3 \\ (c_{13} + c_{44})\eta_1\eta_3 & c_{44}\eta_1^2 + c_{33}\eta_3^2 \end{pmatrix}. \tag{5.9}$$

The positive eigenvalues $a_j(\eta)$ of $D(\eta)$ are shown in Eq. (4.16) and the corresponding unit eigenvectors $p^1(\eta)$, $p^2(\eta)$ are presented in Eq. (4.17), furthermore the wave numbers are $k_j(\eta) = \omega\sqrt{\rho/a_j(\eta)}$. Then the displacement components of the incident wave are

- For L-wave

$$u_1^{1,in}(x,\omega) = p_1^1 e^{-ik_1(\eta)<x,\eta>}, \quad u_3^{1,in}(x,\omega) = p_3^1 e^{-ik_1(\eta)<x,\eta>}. \tag{5.10}$$

- For SV-wave

$$u_1^{2,in}(x,\omega) = p_1^2 e^{-ik_2(\eta)<x,\eta>}, \quad u_3^{2,in}(x,\omega) = p_3^2 e^{-ik_2(\eta)<x,\eta>}. \tag{5.11}$$

The incident wave traction along the crack line is obtained using the expressions

$$t_j^{k,in}(x,\omega) = \sigma_{ij}^{k,in}(x,\omega)n_j(x), \quad \sigma_{ij}^{k,in}(x,\omega) = C_{ijml}u_{m,l}^{k,in}(x,\omega).$$

For example if the crack S_{cr} lies along the Ox_1 axis, then:

- For an incidence L-wave with $\theta = \pi/2$, i.e. $\eta = (0,1)$, $k_1 = \omega\sqrt{\rho/c_{33}}$, the incident wave fields for displacements and tractions are

$$\begin{aligned} &u_1^{1,in}(x,\omega) = 0, \quad u_3^{1,in}(x,\omega) = e^{-ik_1x_2}, \\ &t_1^{1,in}(x,\omega) = 0, \quad t_3^{1,in}(x,\omega) = -i\omega\sqrt{\rho c_{33}} \text{ on } S_{cr}. \end{aligned} \tag{5.12}$$

- For an incident L-wave with $\theta = 0$, i.e. $\eta = (1,0)$, $k_1 = \omega\sqrt{\rho/c_{11}}$, the incident wave fields are

$$\begin{aligned} &u_1^{1,in}(x,\omega) = 0, \quad u_3^{1,in}(x,\omega) = e^{-ik_1x_1}, \\ &t_1^{1,in}(x,\omega) = -i\omega c_{44}\sqrt{\rho/c_{33}}e^{-ik_1x_1}, \quad t_3^{1,in}(x,\omega) = 0 \text{ on } S_{cr}. \end{aligned} \tag{5.13}$$

5.3.2 Numerical Results

In the numerical results following Ohyoshi [20] we characterize the anisotropy of the material by normalizing the stiffness by the coefficient c_{11}. Let us define $c_{ij} = s_{ij}c$, where $c = 6.6495$ GPa and $\rho = 2.4 \times 10^3$ kg/m^3. The following cases with respect to the ratio s_{ij} are considered

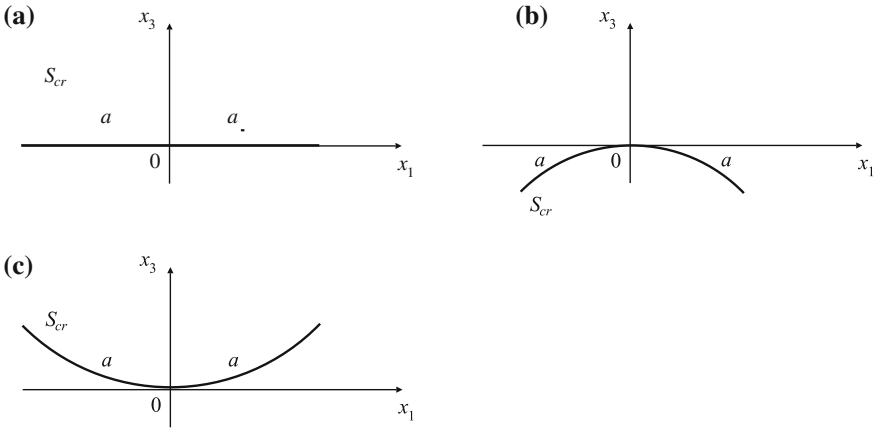

Fig. 5.2 Crack geometry: **a** straight; **b** concave; **c** convex

Case 1: $s_{11} = 1, s_{13} = s_{31} = 1/3, s_{33} = 1, s_{44} = 1/3$;
Case 4: $s_{11} = 1, s_{13} = s_{31} = 1/3, s_{33} = 1, s_{44} = 1/30$;
Case 6: $s_{11} = 1, s_{13} = s_{31} = 1/3, s_{33} = 1, s_{44} = 1/6$;
Case 7: $s_{11} = 1, s_{13} = s_{31} = 1/30, s_{33} = 1, s_{44} = 1/3$.

The material in Case 1 is isotropic, the orthotropic materials in Case 4 and Case 6 have different coefficients only for c_{44}. The material in Case 7 is similar to the material in Case 1, but with different coefficient c_{13}. The dynamic SIFs K_I, K_{II} are normalized by $\sigma\sqrt{\pi a}$, where $\sigma = c_{33}k_1 = \omega\sqrt{\rho c_{33}}$, i.e. $K_I^* = K_I/\sigma$, $K_{II}^* = K_{II}/\sigma$. The normalized frequency is $\Omega = k_1 a = \omega\sqrt{\rho/c_{33}}a$.

For the numerical results in Figs. 5.3, 5.4, 5.5 and 5.6 the crack has a length $2a$ and it lies along Ox_1 axis in the interval $(-a, a)$, see Fig. 5.2a. The number of boundary elements along the crack line is five. The first boundary element is a left QP-BE, the second, the third and the fourth elements are ordinary quadratic boundary elements and the fifth BE is a right QP-BE, see Sect. 4.3.1.1. The corresponding boundary elements lengths are $0.15a$, $0.56a$, $0.58a$, $0.56a$, $0.15a$. The SPM numerical scheme is used, see Sect. 4.3 with shifting of the odd nodes $\xi = 0.05$ on the first and on the second BE, $\xi = -0.05$ on the fourth and fifth BE.

The obtained BIEM results are plotted for normalized SIFs K_I^*, K_{II}^* versus normalized frequency Ω. Figures 5.3 and 5.4 shows the results for normal incident wave, while Figs. 5.5 and 5.6 shows the results for incidence angles $\theta = \pi/4$ and $\theta = 0$ and for different orthotropic elastic constants used in the cases considered by Ohyoshi [20]. In Fig. 5.3 comparison is done for the Cases 6 and 7 with the results of Ohyoshi [20], who solved the problem by Fredholm integral equations of second kind. The Case 1 curve in Fig. 5.4 is for an isotropic solid. The effect of orthotropy at incident angle $\pi/2$ is that with decreasing ratio c_{44}/c_{11}, the point of maximum is shifted to lower frequency region, see Case 4 and Case 6 curves in Fig. 5.4. The effect of c_{13} is small, see Case 1 and Case 7 curves. Figures 5.5 and 5.6 shows new results as the

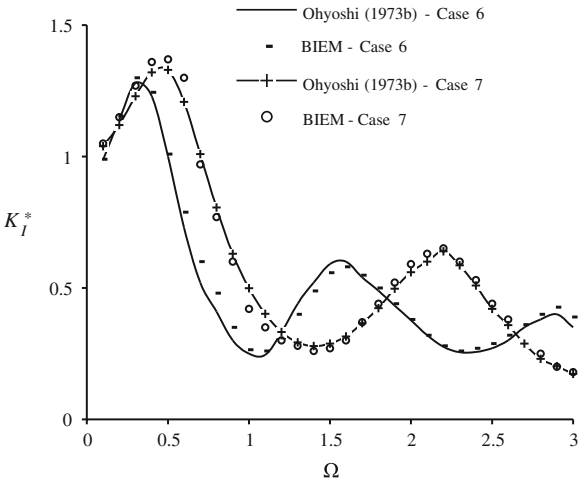

Fig. 5.3 Normalized SIF-I versus normalized frequency for a *line* crack in an infinite orthotropic plane under normal L-*wave*. Comparison with Ohyoshi [20]

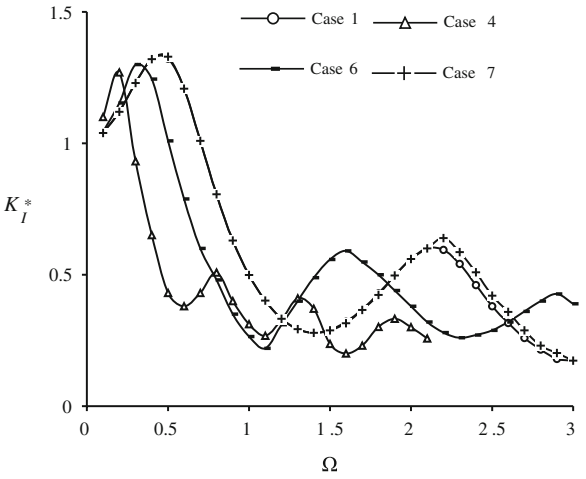

Fig. 5.4 Normalized SIF-I versus normalized frequency for a *line* crack in an infinite orthotropic plane subjected to L-*wave* at incidence angle $\pi/2$

method used in Ohyoshi [20] solves only the case of incident angle $\theta = \pi/2$. The conclusion made in Ohyoshi [20] that the ratio s_{13} does not influence the diffraction is no longer valid for an incidence angle different from $\pi/2$, see Figs. 5.5 and 5.6. It is observed that with decreasing incidence angle, the influence of the ratio c_{13}/c_{11} increases. Figure 5.5b presents the normalized SIF K_{II}^* and it can be seen that Case 4 and 6 curves with smaller value of the ratio c_{44}/c_{11} have smaller values of K_{II}^* in comparison with Cases 1 and 7 curves.

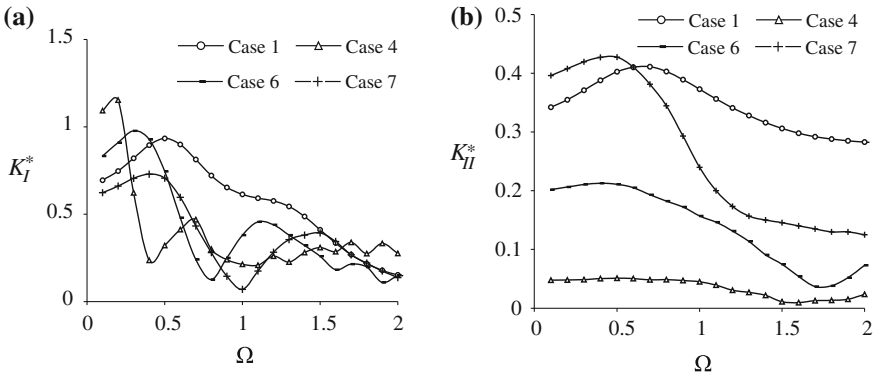

Fig. 5.5 Normalized SIFs versus normalized frequency for a *line* crack in an infinite orthotropic plane subjected to L-*wave* with incidence angle $\pi/4$: **a** SIF-I; **b** SIF-II

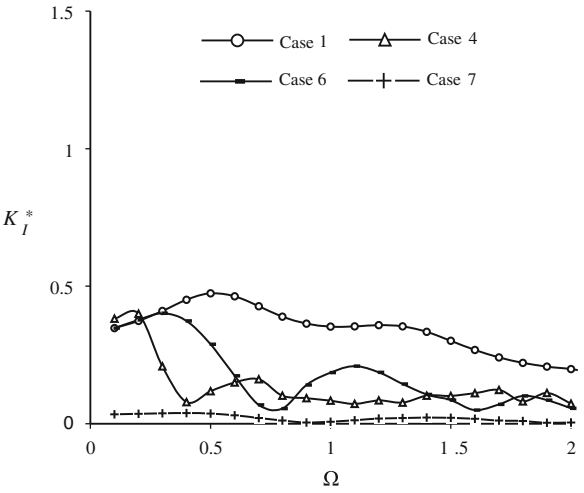

Fig. 5.6 Normalized SIF-I versus normalized frequency for a *line* crack in an infinite orthotropic plane subjected to L-*wave* at incidence angle 0

In Fig. 5.7a, b results for the orthotropic material for Case 3 and for convex and concave cracks (see Fig. 5.2b, c) are depicted. The shape of the crack strongly influences the peaks of the SIFs curves, but it does not change substantially the character of the frequency dependence of the curves. Recall that the length of the curved crack is $2a$. This crack geometry is represented by a broken line with vertices along the arc with an opening angle $\pi/3$ and the radius $R = 3a/\pi$, respectively.

Dynamic normalized SIFs K_I^* and K_{II}^* versus normalized frequency for the isotropic Case 1 and for convex and concave cracks are displayed in Fig. 5.8. At $\Omega = 0.5$ the difference between convex and concave cracks is 17.7 % for SIF K_I^*

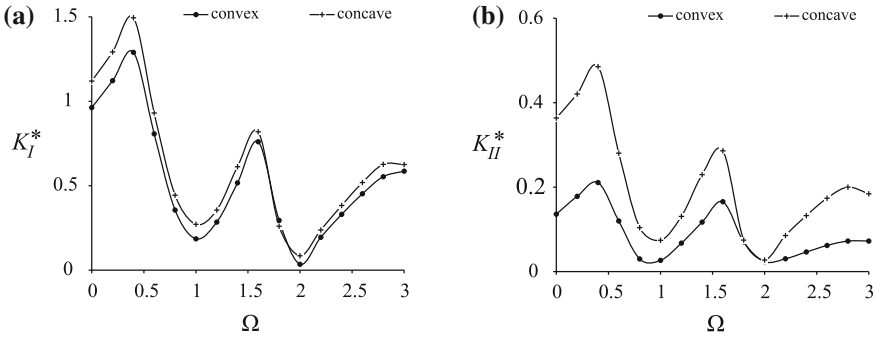

Fig. 5.7 Normalized SIFs versus normalized frequency Ω for an orthotropic cracked plane under normal incident L-*wave* for different crack shapes: **a** SIF-I; **b** SIF-II

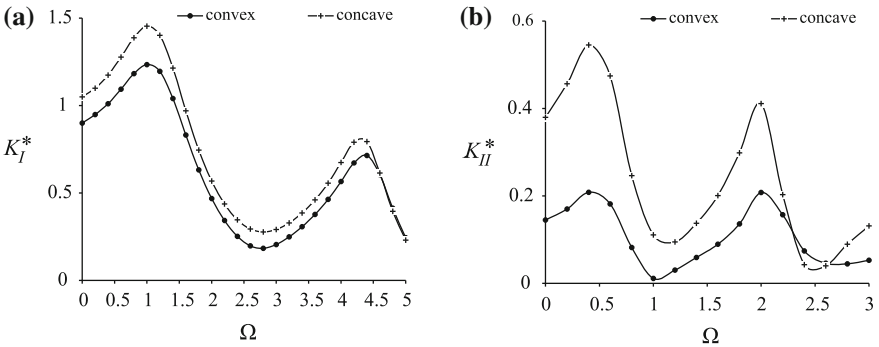

Fig. 5.8 Normalized SIFs versus normalized frequency Ω for an infinite isotropic cracked plane under normal incident L-*wave* for different crack shapes: **a** SIF-I; **b** SIF-II

and 170 % for SIF K_{II}^*. As in the forgoing examples the SIFs for convex cracks are smaller that those for concave cracks.

All Figs. 5.4, 5.5, 5.6, 5.7 and 5.8 demonstrate the combined effect of the anisotropy, crack geometry and of the incident wave direction on the intensity factors.

5.4 Conclusion

2D elastodynamic analysis of in-plane finite crack in an anisotropic plane is presented by non-hypersingular traction BIEM in the frequency domain. The proposed numerical scheme for SIFs calculation is validated by comparison with results achieved by other authors with different methods.

A parametric study for the scattering and diffraction of waves under different incidence angles and for materials with different type of orthotropy is presented.

The numerical results show that the wave-crack interaction in anisotropic continua depends on the combined influence of the incidence wave direction and frequency, crack geometry, the ratio of the wave length to the crack length and type of material anisotropy. The presented numerical scheme and the developed program codes can be used as a base for a solution of dynamic anisotropic problems with more complex geometrical and mechanical properties.

References

1. Abuquerque EL, Sollero P, Aliabadi MH (2002) The Boundary Element Method applied to time dependent problems in anisotropic materials. Int J Solids Struct 39:1405–1422
2. Aliabadi AM, Brebbia CA (eds) (1993) Advances in BEM for fracture mechanics. Computational Mechanics Publications, Southampton
3. Ang WT, Clements DL, Cooke T (1999) A hyper-singular boundary integral equation for anti-plane crack problems for a class of inhomogeneous anisotropic elastic materials. Eng Anal Bound Elem 23:567–572
4. Brebbia CA, Wenturini WS (eds) (1987) Boundary element techniques: applications in stress analysis and heat transfer. Computational Mechanics Publications, Southampton
5. Chan KS, Cruse TA (1986) Stress intensity factors for anisotropic compact-tension specimens with inclined cracks. Eng Fract Mech 23:863–874
6. Chandra A, Hu KX, Huang Y (1995) A hybrid BEM formulation for multiple cracks in orthotropic elastic components. Comput Struct 56:785–797
7. Dhawan GK (1982) Interaction of elastic waves by a Griffith crack in an infinite transversely-isotropic medium. Int J Fract 19:29–37
8. Dhawan GK (1983) Interaction of SV-waves by a Griffith crack in an infinite transversely-isotropic medium. Int J Fract 20:103–110
9. Dineva P, Rangelov T, Gross D (2005) BIEM for 2D steady-state problems in cracked anisotropic materials. Eng Anal Bound Elem 29:689–698
10. Dineva P, Gross D, Rangelov T (2006) Wave scattering in cracked piezoelectric materials—a BIEM approach. J Theor Appl Mech 36(2):65–88
11. Hua Z, Tian YF, Lan QT (1996) Composite materials dynamic fracture studies by generalized Shmuely difference algorithm. Eng Fract Mech 54:869–877
12. Karim MR, Kundu T (1988) Transient surface response of layered isotropic and anisotropic half-spaces with interface-cracks: SH case. Int J Fract 37:245–262
13. Karim MR, Kundu T (1991) Dynamic response of an orthotropic half-space with a subsurface crack: in-plane case. ASME J Appl Mech 58:988–995
14. Kundu T, Boström A (1992) Elastic wave scattering by a circular crack in a transversely isotropic solid. Wave Motion 15:285–300
15. Lekhnitski SG (1963) Theory of elasticity of an anisotropic body. Holden-Day, San Francisco
16. Lekhnitski SG (1968) Anisotropic plates. Gordon and Breach, New York
17. Mathematica 6.0 for MS Windows (2008) Champaign, Illinois
18. MS Visual Studio (2005) Professional edition. Redmond, Washington
19. Ohyoshi T (1973a) Effect of orthotropy on singular stresses produced near a crack tip by incident SH-waves. ZAMM Z Angew Math Mech 53:409–411
20. Ohyoshi T (1973b) Effect of orthotropy on singular stresses for a finite crack. ASME J Appl Mech 40:491–497
21. Pageau SS, Biggers SB (1995) Finite element evaluation of free-edge singular stress fields in anisotropic materials. Int J Solids Struct 38:2225–2239
22. Pageau SS, Joseph PF, Biggers SB (1995) Finite element analysis of anisotropic materials with singular in-plane stress fields. Int J Solids Struct 32:571–591

23. Pan E, Amadei B (1996) Fracture mechanics analysis of cracked 2D anisotropic media with a new formulation of the boundary element method. Int J Fract 77:161–174
24. Saez A, Ariza MP, Dominguez J (1997) Three-dimensional fracture analysis in transversely isotropic solids. Eng Anal Bound Elem 20:287–298
25. Saez A, Dominguez J (1999) BEM analysis of wave scattering in transversely isotropic solids. Int J Numer Meth Eng 44(9):1283–1300
26. Saez A, Dominguez J (2000) Far-field dynamic Green's functions for BEM in transversely isotropic solids. Wave Motion 32:113–123
27. Saez A, Dominguez J (2001) Dynamic crack problems in three-dimensional transversely isotropic solids. Eng Anal Bound Elem 25:203–210
28. Sarkar J, Mandal SC, Ghosh M (1995) Diffraction of elastic waves by three coplanar Griffith cracks in an orthotropic medium. Int J Eng Sci 33(2):163–177
29. Savin GN (1961) Stress concentration around holes. Pergamon Press, New York
30. Sih GC Liebowitz H (eds) (1968) Mathematical theory of brittle fracture. Academic Press, New York
31. Sih GC, Paris PC, Irwin GR (1965) On cracks in rectilinear anisotropic bodies. Int J Fract 1:189–203
32. Snyder MD, Cruse TA (1975) BIE analysis of cracked anisotropy plates. Int J Fract 11:315–328
33. Sommerfeld A (1949) Partial differential equations in physics. Academic Press, New York
34. Song C, Wolf J (2002) Semi-analytical representation of stress singularities as occurring in cracks in anisotropic multimaterials with the scaled boundary finite-element method. Comput Struct 80:183–197
35. Su RKL, Sun HY (2003) Numerical solution of two-dimensional anisotropic crack problems. Int J Solids Struct 40:4615–4635
36. Tan CL, Gao YL (1992) Boundary element analysis of plane anisotropic bodies with stress concentrations and cracks. Comput Struct 20:17–28
37. Wang CY, Achenbach JD (1994) Elastodynamic fundamental solutions for anisotropic solids. Geophys Int J 118:384–392
38. Wang CY, Achenbach JD (1995) Three-dimensional time-harmonic elastodynamic Green's functions for anisotropic solids. Proc R Soc Lond A 449:441–458
39. Wang CY, Achenbach JD (1996) Lamb's problem for solids of general anisotropy. Wave Motion 24:227–242
40. Zhang C (2000) Transient elastodynamic antiplane crack analysis of anisotropic solids. Int J Solids Struct 37:6107–6130
41. Zhao MH, Shen YP, Lin YJ, Liu GN (1988) The method of analysis of cracks in three-dimensional transversely-isotropic media: boundary integral equation approach. Eng Anal Bound Elem 21:169–178

Chapter 6
2D Wave Scattering by Cracks in a Piezoelectric Plane

Abstract Scattering and diffraction of time-harmonic plane waves by a finite crack in a homogeneous piezoelectric plane under plane strain conditions is studied. The BIEM procedure is applied to straight cracks, as well as to curved cracks under incident longitudinal waves and under vertically polarized shear waves. The SIFs results are compared with those available in the literature. Furthermore, their dependence on parameters like frequency, angle of incidence, wave type, crack geometry and material properties is discussed.

6.1 Introduction

During the past decades, many papers on crack problems for piezoelectric materials have been published. They may be divided into the following groups.

- Analytical solutions for simple crack geometry and loading conditions, see e.g. [16, 18, 26, 30].
- Green's function approach and fundamental solution for static and dynamic problems, commented in details in Chap. 3.
- Development of approximate semi-analytical solution methods, see [15, 22, 23, 28, 27].
- Development of numerical methods as the FEM, see [1, 11, 12, 14, 21] and the BIEM, see [2, 4, 5, 9, 10, 13, 17].

Restricting the focus on time-harmonic solutions a few more investigations have to be mentioned. An analytical solution for a simply supported composite plate under harmonic electrical load was given by Ray et al. [20]. A closed form solution for the anti-plane problem of a single crack in an infinite region based on the dual singular integral equations method was presented by [3, 19]. Shindo and Ozawa [22] first investigated the dynamic response of a cracked domain under normal incident longitudinal waves by using Fredholm integral equations. The diffraction of anti-plane shear waves with arbitrary angle of incidence by a crack in an infinite orthotropic

P. Dineva et al., *Dynamic Fracture of Piezoelectric Materials*,
Solid Mechanics and Its Applications 212, DOI: 10.1007/978-3-319-03961-9_6,

piezoelectric ceramic has been investigated by Narita and Shindo [15]. The equivalent two-crack diffraction problem was solved by [28, 29]. Zhao and Meguid [32] investigated the dynamic behavior of a piezoelectric laminate containing multiple interfacial collinear cracks subjected to electro-mechanical loads. Curved and branched cracks in an unbounded piezoelectric solid were studied in Garcia-Sanchez et al. [7] and in Xu and Rajapakse [31] for static problems where the crack is loaded by uniform remote stress or electric displacement.

From this short review can be concluded that the number of papers and results regarding wave diffraction by cracks in piezoelectric continua is still restricted. This fact may be explained by the complexity of the governing equations, the use of different electrical boundary conditions and the mathematical difficulties of developing appropriate solution methods. A well developed solution method for wave diffraction problems is the method of dual singular integral equations and most of the cited results have been obtained by its usage. Because of its relative simplicity there exist more results for the anti-plane case and only a few for the in-plane case which is of higher practical interest.

The aim of this chapter is to show the applicability of the non-hypersingular traction BIEM developed in Chap. 4 for solution of 2D in-plane wave propagation problem in infinite cracked piezoelectric media. The Chapter follows Gross et al. and Dineva et al. [6, 8].

6.2 Problem Statement

We consider an infinite homogeneous piezoelectric plane containing an arbitrary shaped crack S_{cr} and subjected to incident time-harmonic L- or SV- wave, see Fig. 6.1. Using the coordinates x_1, x_3 and assuming plane strain conditions, the non-zero field quantities are the displacement u_i, the stresses σ_{ij}, the electric displacement D_i and the electric field intensity E_i, where $i, j = 1, 3$. Assuming a time-harmonic motion with angular frequency ω the BVP is stated in Sect. 2.6.3. Recall the Eq. (2.44)

$$\begin{cases} \sigma_{iJ,i} + \rho_{JK}\omega^2 u_K = 0 \quad \text{in } R^2 \backslash S_{cr}, \\ t_J|_{S_{cr}} = 0, \end{cases} \tag{6.1}$$

where $u_K = (u_1, u_3, \phi)$, $J, K = 1, 3, 4$ is the generalized displacement, σ_{iJ} is the generalized stress, $\sigma_{iJ} = C_{iJKl}u_{K,l} = C_{iJKl}s_{Kl}$, see Sect. 2.5.1. The generalized traction vector is $t_J = \sigma_{iJ}n_i$, where n_i is the unit normal vector on S_{cr}^+. The kinematical strain–displacement and electric field–potential relations are $s_{ij} = \frac{1}{2}(u_{i,j} + u_{j,i})$, $E_i = -\phi_{,i}$ where s_{ij}, ϕ are the strain tensor and electric potential, ρ is the mass density and $\rho_{JK} = \begin{cases} \rho, & J, K = 1, 3 \\ 0, & J = 4 \text{ or } K = 4 \end{cases}$.

Note that the boundary condition in (6.1) implies that the crack surfaces are free of both mechanical traction and surface charges, i.e. the crack is assumed to be electrically impermeable, see Sect. 2.6. In this case the electric field inside the crack

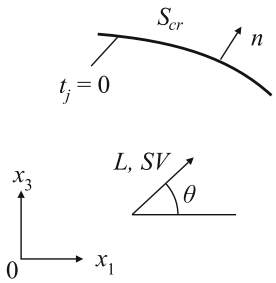

Fig. 6.1 Piezoelectric plane with an arbitrary shaped crack

is ignored and the crack may be thought as a low-capacitance medium with a potential jump $\Delta u_4 = \Delta\phi = \phi^+ - \phi^-$.

The interaction of an incident time-harmonic wave with the crack induces scattered waves. Due to the linearity of the problem the total wave field can be written as a sum of the incident and the scattered wave field:

$$u_J(x,\omega) = u_J^{in}(x,\omega) + u_J^{sc}(x,\omega), \sigma_{iJ}(x,\omega) = \sigma_{iJ}^{in}(x,\omega) + \sigma_{iJ}^{sc}(x,\omega). \tag{6.2}$$

The incident wave is known, while the scattered wave field is unknown. It has to satisfy the BVP (6.1) and Sommerfeld's radiation condition at infinity, see Sommerfeld [25]. The boundary condition in Eq. (6.1), can be re-written as

$$t_J^{sc} = -t_J^{in} \text{ on } S_{cr}. \tag{6.3}$$

As shown in Chap. 4, the BVP (6.1) is transformed to an equivalent BIDE on S_{cr} and Eq. (4.19) now takes the form

$$\begin{aligned} t_J^{in}(x) = &- C_{iJKl} n_l(x) \int_{S_{cr}^+} \Big[(\sigma^*_{\eta PK}(x,\xi)\Delta u_{P,\eta}(\xi) \\ &- \rho_{QK}\omega^2 u^*_{QK}(x,\xi)\Delta u_P(\xi))\delta_{\lambda l} \\ &- \sigma^*_{\lambda PK}(x,\xi)\Delta u_{P,l}(\xi)\Big] n_\lambda(\xi) dS_{cr}, \quad x \in S_{cr}^+. \end{aligned} \tag{6.4}$$

Where u^*_{QK} is the fundamental solution, shown in Sect. 3.4.2, Eqs. (3.83)–(3.87) and $\sigma^*_{iJQ} = C_{iJKl} U^*_{KQ,l}$ is the corresponding stress. Furthermore, $\Delta u_J = u_J|_{S_{cr}^+} - u_J|_{S_{cr}^-}$ is the unknown generalized COD. Once the solution of Eq. (6.4), i.e. Δu_J, is known for a given frequency, the displacements and stress of the scattered field and by this the total field at any point in the whole region can be determined by the integral representation formulae, see Eqs. (4.21) and (4.22):

$$u_J^{sc} = -\int_{S_{cr}^+} \sigma^*_{iMJ}(x,y)\Delta u_M(y) n_i(y) dS_{cr}, \quad x \notin S_{cr}^+, \tag{6.5}$$

$$\sigma_{lJ}^{in}(x) = -\int_{S_{cr}^{+}} \Big[(\sigma_{\eta PK}^{*}(x,\xi)\Delta u_{P,\eta}(\xi) - \rho_{QK}\omega^2 u_{QK}^{*}(x,\xi)\Delta u_P(\xi))\delta_{\lambda l} - \sigma_{\lambda PK}^{*}(x,\xi)\Delta u_{P,l}(\xi)\Big] n_\lambda(\xi) dS_{cr}, \quad x \notin S_{cr}^{+}. \tag{6.6}$$

6.3 Numerical Solution

The numerical solution scheme follows that developed in Sect. 4.3.2. In all numerical examples the crack is divided into seven boundary elements and the shifted points numerical scheme is used. The crack geometry is given by the straight line Ox_1 in the interval $(-a, a)$, and by a convex or concave circular arc with an opening angle $\alpha = \pi/3$ and the radius $R = 3a/\pi$, respectively. The generalized dynamic SIFs are calculated by using the formulae in Eq. (2.40)

$$\begin{aligned} K_I &= \lim_{r\to r_0} t_3\sqrt{2\pi|r-r_0|}, \\ K_{II} &= \lim_{r\to r_0} t_1\sqrt{2\pi|r-r_0|} \\ K_D &= \lim_{r\to r_0} t_4\sqrt{2\pi|r-r_0|} \end{aligned} \tag{6.7}$$

where t_J is the generalized traction at the point r close to the crack-tip r_0. For convenience SIFs are normalized by an appropriate static value. The normalization coefficient for the mechanical SIFs is

$$k = \omega[(c_{33} + e_{33}^2\varepsilon_{33}^{-1})\rho]^{1/2}\sqrt{\pi a}$$

and $K_I^* = |K_I k^{-1}|$, $K_{II}^* = |K_{II}k^{-1}|$. The normalized electric intensity factor is $K_D^* = |c_{33}e_{33}^{-1}K_D k^{-1}|$. The generalized displacement u_J^{in} and generalized stress σ_{iJ}^{in} for an incidence angle θ and correspondingly the traction t_J^{in} at the points on S_{cr} are obtained from Eq. (4.12).

The material constants of different piezoelectric materials which are considered in the following are listed in Table 4.1.

6.3.1 Validation Example

In order to validate the described approach, a straight crack in a transversely-isotropic piezoelectric plane under normal incident L-waves is investigated. The results for the stress intensity factors are compared with those of Shindo and Ozawa [22], who reduced this problem by Fourier transforms to a pair of dual integral equations and finally expressed its solution in terms of a Fredholm integral equation of second kind. For the validation test the material PZT-6B is used.

The normal incident L-wave, according to Eq. (4.12) is

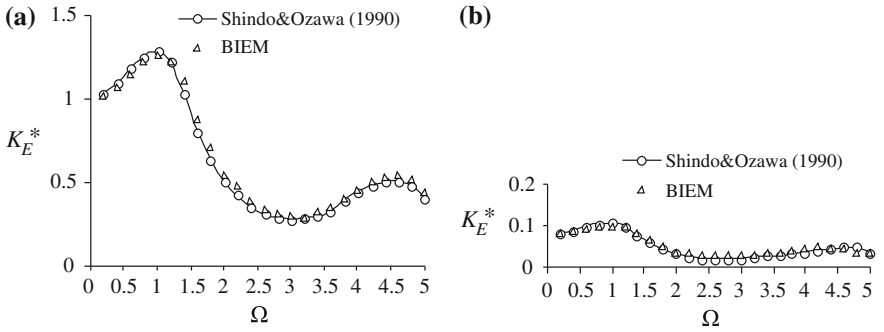

Fig. 6.2 Normalized SIFs versus normalized frequency Ω of normal incident L-wave: **a** mechanical SIF-I; **b** electrical SIF-E

$$u_1^{in} = 0, \quad u_3^{in} = e^{-i\tilde{k}_1 x_3}, \quad u_4^{in} = e_{33}\varepsilon_{33}^{-1} e^{-ik_1 x_3}, \quad k_1 = \omega\sqrt{(c_{33} + e_{33}^2\varepsilon_{33}^{-1})^{-1}\rho}$$
$$t_1^{in} = 0, \quad t_3^{in} = -i\omega\sqrt{(c_{33} + e_{33}^2\varepsilon_{33}^{-1})\rho}, \quad t_4^{in} = 0.$$

In this case $E_1 = 0$ and $u_1 = 0$ holds and E_3 can be obtained at any point along x_1 out of the crack from the constitutive equation (2.16), i.e.

$$\left| \begin{array}{l} t_3 = c_{33}u_{3,3} - e_{33}E_3 \\ t_4 = e_{33}u_{3,3} + \varepsilon_{33}E_3 \end{array} \right. \tag{6.8}$$

from which

$$E_3 = (t_4 c_{33} - t_3 e_{33})(e_{33}c_{33} + e_{33}^2)^{-1} \tag{6.9}$$

Then $K_E = \lim_{x_1 \to a^{\pm}} E_3\sqrt{2\pi(x_1 \mp a)}$, where the electric field E_3 is calculated from Eq. (6.9) at the point close to the crack-tip. Figure 6.2a, b present the variation of the normalized mechanical SIF K_I^* and the normalized electrical field stress intensity factor $K_E^* = |e_{33}K_E k^{-1}|$ versus the normalized frequency $\Omega = a\omega\sqrt{\rho c_{44}^{-1}}$.

Figure 6.2a, b show a very good agreement between the results of Shindo and Ozawa [22] and the used BIEM technique. The maximum differences within the considered frequency domain are 7–8 %. This demonstrates the accuracy and applicability of the non-hypersingular traction based BIEM for solution of 2D in-plane wave problems in piezoelectric materials with cracks.

6.3.2 Parametric Study

In the following, a set of numerical results for a wave loaded straight and curved cracks is presented highlighting the dependence of the stress intensity factors on the frequency, the wave type, the incidence angle and the material constants. Note that

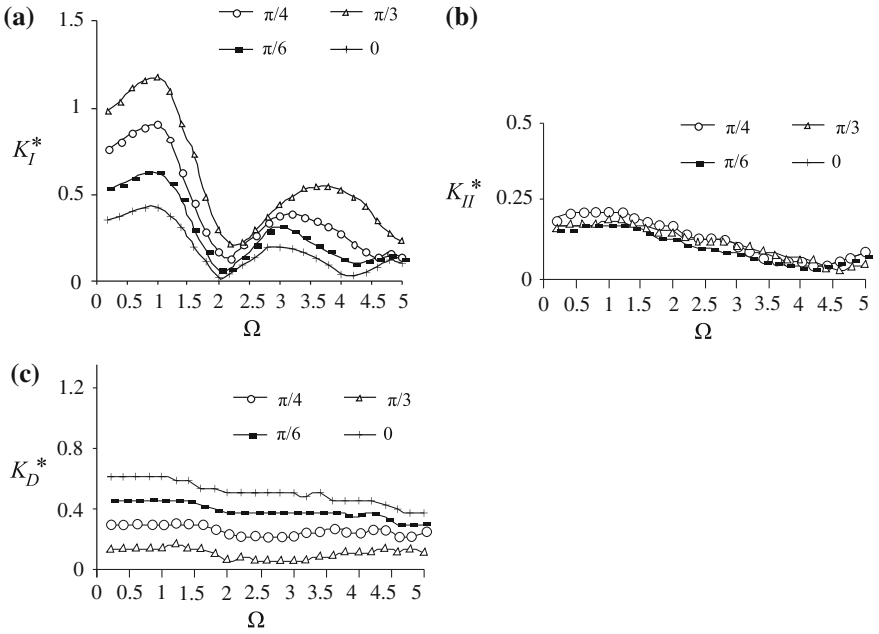

Fig. 6.3 Normalized SIFs versus normalized frequency Ω of L-wave with different incidence angles: **a** mechanical SIF-I; **b** mechanical SIF-II; **c** electrical SIF-D

in Figs. 6.2 and 6.5 (for the incidence angle $\theta = \pi/2$) the normalized mechanical K_I^* and electric field intensity factor K_E^* are displayed, while in Figs. 6.3, 6.4, 6.5, 6.6, 6.7 and 6.8 the normalized mechanical K_I^* and electric displacement intensity factor K_D^* are depicted. Figures 6.3 and 6.4 display the dynamic normalized SIFs versus normalized frequency Ω for different angles of incident L- and SV-waves.

The first maximum of the SIF-I for an incident L-wave, see Fig. 6.3a , appears approximately at $\Omega = 1$ for all considered angles of incidence. Its amplitude, commonly called dynamic amplification, decreases from 1.289 for $\theta = 90°$ and 1.173 for $\theta = 60°$ to 0.429 for $\theta = 0°$ (grazing incidence). The second peak occurs at different frequencies depending on the incidence angle. The SIF-II curves in Fig. 6.3b indicate close results for L-wave incidence angles 30°, 45° and 60°, except where SIF-II is zero. The electrical displacement SIF-D in Fig. 6.3c has its maximal values for an incidence angle $\theta = 0°$ and minimal ones for $\theta = 60°$. The dependence on the frequency is weak.

The first maximum of SIF-I in case of an incident SV-wave, see Fig. 6.4a, appears approximately at $\Omega = 0.8$ for all considered angles of incidence. The dynamic amplification varies here from 0.6592 for $\theta = 30°$, 0.589 for $\theta = 45°$ to 0.383 for $\theta = 60°$. The second peak again occurs at different frequencies depending on the wave incidence angle. The SIF-II curves in Fig. 6.4b show maximal values for SV-waves at an incidence angle $\theta = 0°$, while at $\theta = 45°$ SIF-II is zero. The electrical

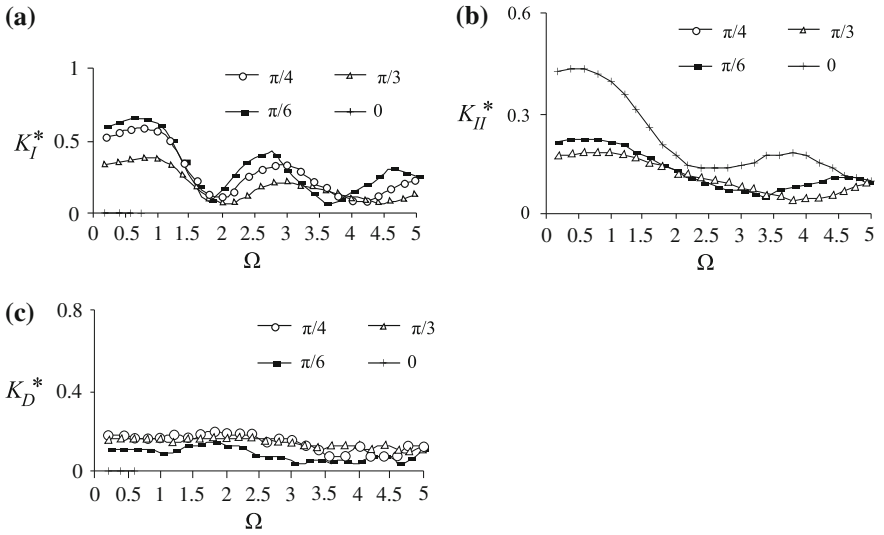

Fig. 6.4 Normalized SIFs versus normalized frequency Ω of SV-wave with different incidence angles: **a** mechanical SIF-I; **b** mechanical SIF-II; **c** electrical SIF-D

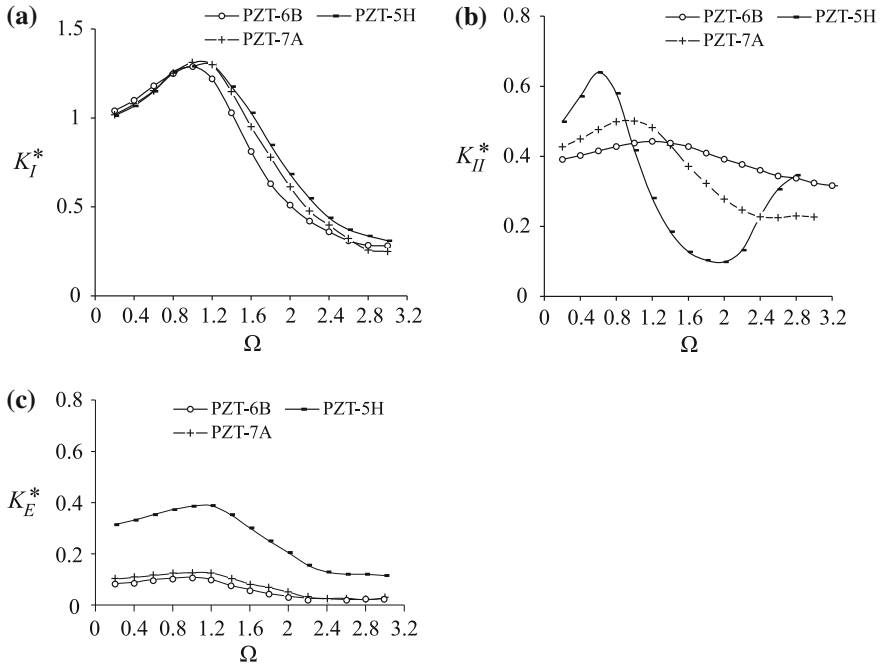

Fig. 6.5 Normalized SIFs versus normalized frequency Ω of normal incident L-waves and three different materials: **a** mechanical SIF-I; **b** mechanical SIF-II; **c** electrical SIF-E

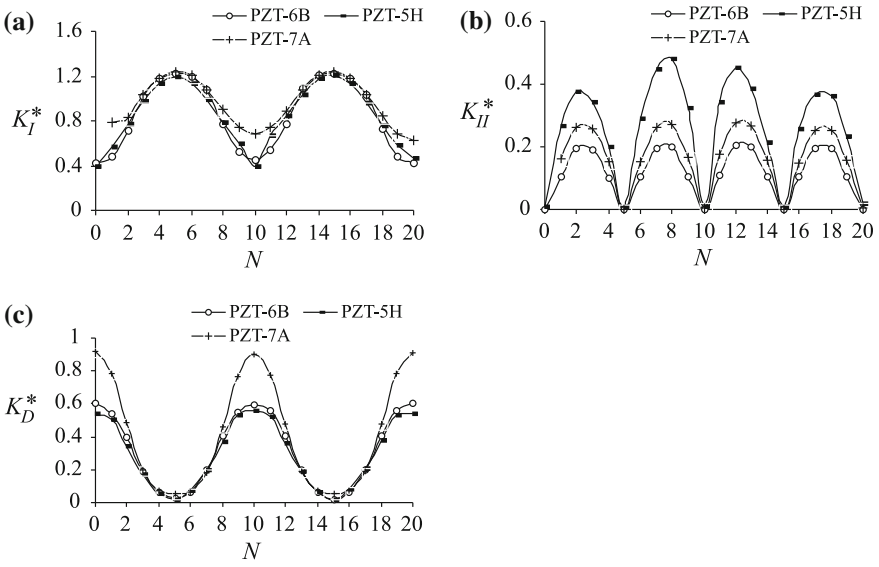

Fig. 6.6 Normalized SIF versus incidence angle of L-wave at fixed normalized frequency $\Omega = 0.8$ for three different materials: **a** mechanical SIF-I; **b** mechanical SIF-II; **c** electrical SIF-D

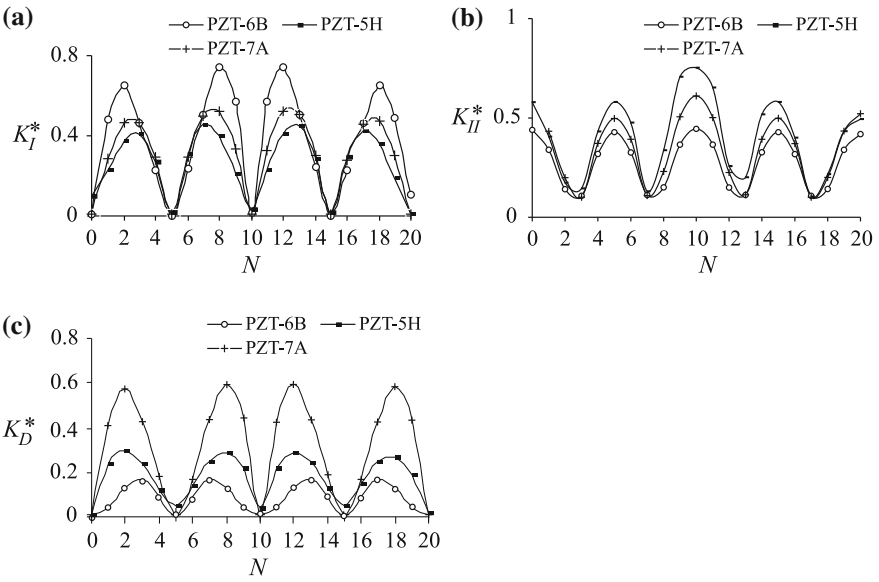

Fig. 6.7 Normalized SIF versus incidence angle of SV-wave loading at fixed normalized frequency $\Omega = 0.8$ for three different materials: **a** mechanical SIF-I; **b** mechanical SIF-II; **c** electrical SIF-D

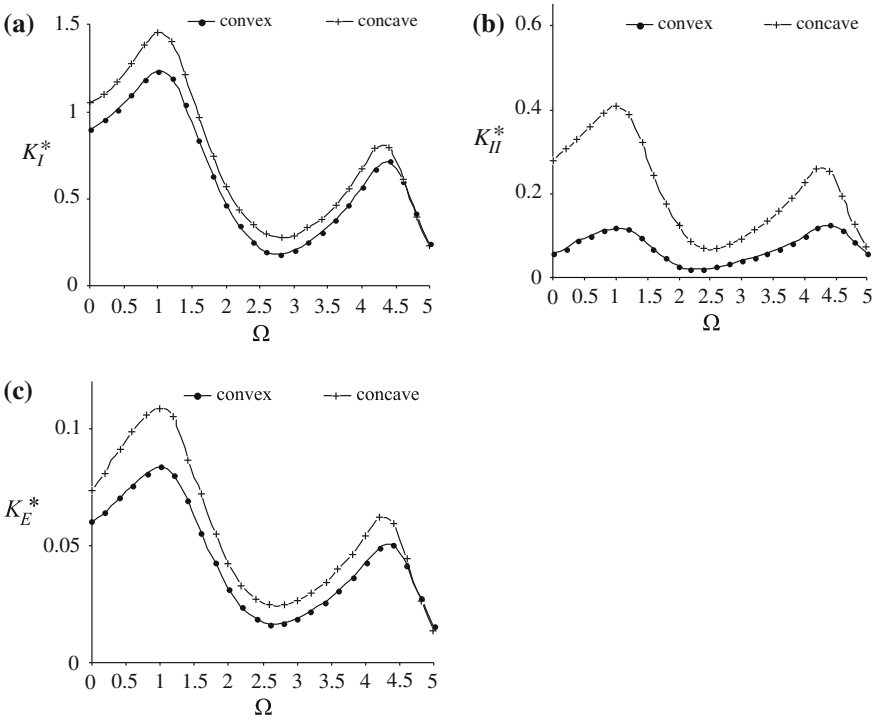

Fig. 6.8 Normalized SIFs versus normalized frequency Ω for a piezoelectric cracked plane under normal incident L-wave for different crack shapes: **a** mechanical SIF-I; **b** mechanical SIF-II; **c** electrical SIF-E

displacement SIF-D in Fig. 6.4c again is weakly dependent on the frequency and displays close results for incidence angles 30°, 45° and 60°; at $\theta = 0°$ SIF-D is zero.

The sensitivity of the stress intensity factors to the material parameters can be seen in Fig. 6.5. It shows the normalized SIF's versus normalized frequency for normal incident L and SV-waves and three different piezoelectric materials. For L-wave loading it can be seen from Fig. 6.5a, b that PZT-5H delivers the highest SIF values followed by PZT-6B. The SIF curves for PZT-7A is in between the SIF curves for PZT-5H and PZT-6B. While the dependence of SIF-I on the material is relatively weak this cannot be said for SIF-E. For SV-wave loading a strong dependence of SIF-II on the material constants can be observed from Fig. 6.5c. PZT-5H again delivers the maximum dynamic amplification followed by PZT-7A.

The influence of the wave type, the incidence angle and the material constants on the amplification effect is depicted in Figs. 6.6 and 6.7, where the normalized SIFs versus incidence angle at fixed frequency $\Omega = 0.8$ are displayed for L and SV-waves and three different piezoelectric ceramics. The SIF-I and SIF-II dependence on the angle of incidence and on the type of the incident wave are qualitatively similar to corresponding curves presented in Sih [24] for a crack in an elastic isotropic medium.

The electrical displacement intensity factors for both wave types are depicted in Fig. 6.6c and 6.7c.

In Fig. 6.8a, b, c the dynamic normalized SIFs for the same situation under normal incident L-wave and material PZT-6B, but now for a crack with convex and concave shape are displayed. The strong geometry effect clearly can be observed. For example, at a fixed frequency $\Omega = 1.0$, the difference between convex and concave cracks is 17.8 % for the SIF-I, 243 % for the SIF-II and 30.8 % for the SIF-E.

Generally, the study reveals that the dynamic mechanical and electrical SIF's are quite sensitive to the type of the wave, its frequency and its angle of incidence, the crack geometry and also to the piezoelectric material properties.

6.4 Conclusion

A 2D analysis of an arbitrarily shaped crack in an infinite transversely isotropic piezoelectric material is presented by non-hypersingular traction BIEM in the frequency domain. A numerical scheme for the solution and determination of generalized SIF's is validated by comparison with results from the literature.

Parametric studies for the scattering and diffraction of longitudinal and shear waves under different angles of incidence, at different frequencies, for different piezoelectric materials and for different crack shapes are presented. The results show that the stress intensity factors strongly depend on the combined influence of the aforementioned parameters.

The presented numerical scheme and the program codes developed are used in the next chapters for the solution of time-harmonic piezoelectric problems with a more complex geometry (e.g. finite cracked solids) and mechanics (e.g. general anisotropy, crack-interaction, existence of material gradient with arbitrary magnitude and direction), and different type of the electrical boundary conditions (impermeable, permeable, limited permeable cracks).

References

1. Benjeddou A (2000) Advances in piezoelectric finite element modeling of adaptive structural elements: a survey. Comput Struct 76(1–3):347–363
2. Chen ZT, Lin FZ (1995) Boundary integral formulations for three-dimensional anisotropic piezoelectric solids. Comput Mech 15(6):485–496
3. Chen ZT, Yu S (1998) Anti-plane vibration of cracked piezoelectric materials. Mech Res Commun 25(3):321–327
4. Davi G, Milazzo A (2001) Multidomain boundary integral formulation for piezoelectric materials fracture mechanics. Int J Solids Struct 38:7065–7078
5. Denda M, Lua J (1999) Development of the boundary element method for 2D piezoelectricity. Compos B 30:699–707
6. Dineva P, Gross D, Rangelov T (2006) Wave scattering in cracked piezoelectric materials—a BIEM approach. J Theor Appl Mech 36(2):65–88

7. Garcia-Sanchez F, Saez A, Dominguez J (2005) Anisotropic and piezoelectric materials fracture analysis by BEM. Comput Struct 83:804–820
8. Gross D, Rangelov T, Dineva P (2005) 2D Wave scattering by a crack in a piezoelectric plane using traction BIEM. Struct Integr Dur 1(1):35–47
9. Hill LR, Farris NT (1998) Three-dimensional piezoelectric boundary element method. AIAA J 36(1):102–108
10. Khutoryansky NM, Sosa H (1995a) Dynamic representation formulas and fundamental solutions for piezoelectricity. Int J Solids Struct 32:3307–3325
11. Kumar S, Singh RN (1997a) Energy release rate and crack propagation in piezoelectric materials: mechanical/electrical load. Acta Mater 45:849–858
12. Kumar S, Singh RN (1997b) Energy release rate and crack propagation in piezoelectric materials: combined mechanical and electrical load. Acta Mater 45:859–868
13. Lee JS (1995) Boundary element method for electroelastic interaction in piezoceramics. Eng Anal Bound Elem 15:321–328
14. McMeeking RM (1999) Crack tip energy relase rate for a piezoelectric compact tension specimen. Eng Fract Mech 64:217–244
15. Narita F, Shindo Y (1998) Dynamic anti-plane shear of a cracked piezoelectric ceramic. Theor Appl Mech 29:169–180
16. Pak YE (1990) Crack extension force in a piezoelectric material. ASME J Appl Mech 57:647–653
17. Pan E (1999) A BEM analysis of fracture mechanics in 2D anisotropic piezoelectric solids. Eng Anal Bound Elem 23:67–76
18. Parton VZ (1976) Fracture mechanics of piezoelectric materials. Acta Astronaut 3:671–683
19. Parton VZ, Kudryavtsev BA (1988) Electromagnetoelasticity. Gordon and Breach, New York
20. Ray MC, Bhattacharya B, Samanta B (1998) Exact solutions for dynamic analysis of composite plates with distributed piezoelectric layers. Comput Struct 66(6):737–743
21. Shang F, Kuna K, Abendroth M (2003) Finite element analysis of three-dimensional crack problems in piezoelectric structures. Eng Fract Mech 70:143–160
22. Shindo Y, Ozawa E (1990) Dynamic analysis of a cracked piezoelectric material. In: Hsieh RKT (ed) Mechanical modeling of new electromagnetic materials. Elsevier, Amsterdam, p 297–304
23. Shindo Y, Katsura H, Yan W (1996) Dynamic stress intensity factor of a cracked dielectric medium in a uniform electric field. Acta Mech 117:1–10
24. Sih GC (1977) Mechanics of fracture 4, elastodynamic crack problems. Noordhoff International Publishing, Leyden
25. Sommerfeld A (1949) Partial differential equations in physics. Academic Press, New York
26. Sosa H (1992) On the fracture mechanics of piezoelectric solids. Int J Solids Struct 29:2613–2622
27. Wang BL, Noda N (2000) A cracked piezoelectric material under generalized plane electromechanical impact. Arch Mech 52(6):933–948
28. Wang XD, Meguid SA (2000a) Effect of electromechanical coupling on the dynamic interaction of cracks in piezoelectric materials. Acta Mech 143:1–15
29. Wang XD, Meguid SA (2000b) Modelling and analysis of the dynamic behaviour of piezoelectric materials containing interfacing cracks. Mech Mater 32:723–737
30. Xu LY, Rajapakse RKND (1998) Boundary element analysis of piezoelectric solids with defects. Eng Fract Mech 29B:655–669
31. Xu LY, Rajapakse RKND (2000) A theoretical study of branched cracks in piezoelectrics. Acta Mater 48:1865–1882
32. Zhao X, Meguid SA (2002) On the dynamic behavior of a piezoelectric laminate with multiple interfacial collinear cracks. Int J Solids Struct 39:2477–2494

Chapter 7
Piezoelectric Cracked Finite Solids Under Time-Harmonic Loading

Abstract The time-harmonic behavior of cracked finite piezoelectric 2D solids is studied. Plane strain and generalized traction free boundary conditions along the crack are assumed. The system may be loaded at the external boundary by arbitrary mechanical and/or electrical loads. As numerical example a center cracked rectangular piezoelectric plate under uniform axial time-harmonic tension and electrical displacement is investigated. The accuracy of the proposed numerical algorithm is checked by comparison with available results obtained by other methods. Parametric studies revealing the sensitivity of the SIFs to the frequency of the applied mechanical and electrical load, to its coupled and uncoupled character and to the piezoelectric properties of the material are presented.

7.1 Introduction

The aim of the chapter is to study the steady-state behavior of a 2D finite cracked piezoelectric solid under in-plane electromechanical load by using BIEM developed in Chap. 4. The accuracy, the efficiency and the convergence of the proposed BIEM are validated by test examples. It is shown that the dynamic stress intensity factors depend on the characteristics of the applied electromechanical load and on the piezoelectric coupling parameters of the material. A parametric study demonstrates these effects. The chapter is based on [3].

7.2 Problem Statement

Consider a finite, homogeneous, transversely-isotropic piezoelectric solid $G \subset R^2$ with boundary S, containing an internal single crack S_{cr} of arbitrary shape, see Fig. 7.1. Let us introduce a rectangular Cartesian coordinate system $Ox_1x_2x_3$ such

P. Dineva et al., *Dynamic Fracture of Piezoelectric Materials*,
Solid Mechanics and Its Applications 212, DOI: 10.1007/978-3-319-03961-9_7,

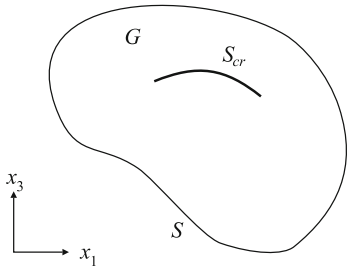

Fig. 7.1 2D cracked piezoelectric solid

that the material symmetry axis, i.e. the poling direction of the material, coincides with the Ox_3 axis and that plane strain deformation is assumed in the plane Ox_1x_3. In this case the non-zero fields are the displacement components u_i, the stresses σ_{ij}, the electric displacements D_i and the electric field components E_i, where $i, j = 1$ or 3. Suppose that $S = S_u \cup S_t$, $S_u \cap S_t = \emptyset$ and that there are given prescribed displacements $\bar{u}_J$ on S_u and prescribed tractions $\bar{t}_J$ on S_t. The following BVP is considered, see Chap. 2, Eq. (2.42).

$$\left|\begin{array}{l} \sigma_{iJ,i} + \rho_{JK}\omega^2 u_K = 0 \quad \text{in } G\backslash S_{cr}, \\ u_J|_{S_u} = \bar{u}_J, \quad t_J|_{S_t} = \bar{t}_J, \\ t_J|_{S_{cr}} = 0, \end{array}\right. \tag{7.1}$$

where $u_K = (u_1, u_3, \phi)$ is the generalized displacement, $J, K = 1, 3, 4$, σ_{iJ} is the generalized stress, $\sigma_{iJ} = C_{iJKl}u_{K,l} = C_{iJKl}s_{Kl}$, see Sect. 2.5.1. The generalized traction vector is $t_J = \sigma_{iJ}n_i$, where n_i is the unit normal vector on S_{cr}^+. The kinematical strain–displacement and electric field-potential relations are $s_{ij} = \frac{1}{2}(u_{i,j} + u_{j,i})$, $E_i = -\phi_{,i}$ where s_{ij}, ϕ are the strain tensor and electric potential, ρ is the mass density and $\rho_{JK} = \begin{cases} \rho, & J, K = 1, 3 \\ 0, & J = 4 \text{ or } K = 4 \end{cases}$.

The boundary condition on the crack means that the crack line is assumed to be free of both mechanical traction and surface charges, i.e. the crack is electrically impermeable.

As special cases the equations of motion for the electrically uncoupled anisotropic and isotropic cases can be obtained from (7.1) by setting the piezoelectric constants to zero:

- If $e_{ij} = 0$ we obtain the orthotropic case;
- If $e_{ij} = 0$ and $c_{11} = c_{33}, c_{11} = c_{13} + 2c_{44}$ we obtain the isotropic case and use the notations $\lambda = c_{13}, \mu = c_{44}$, correspondingly $C_{ijkl} = \lambda\delta_{ij}\delta_{kl} + \mu(\delta_{ik}\delta_{jl} + \delta_{il}\delta_{jk})$.

The BVP (7.1) is transformed as in Sect. 4.2 to the BIDE (4.7) that can be solved with the BIEM.

Here we will proceed in slightly different way and first consider the following two BVPs:

$$\left|\begin{array}{l} L(u^0) = 0 \quad \text{in } G \\ t_J^0 = \bar{t}_J \quad \text{on } S_t \\ u_J^0 = \bar{u}_J \quad \text{on } S_u \end{array}\right. \tag{7.2}$$

$$\left|\begin{array}{l} L(u^c) = 0 \quad \text{in } G \\ t_J^c = -t_J^0 \quad \text{on } S_{cr} \\ u_J^c = 0 \quad \text{on } S_u, \quad t_J^c = 0 \quad \text{on } S_t \end{array}\right. \tag{7.3}$$

Since the BVP (7.1) is linear, its solution is a superposition of the solutions of Eqs. (7.2) and (7.3), i.e. $u_J = u_J^0 + u_J^c$, $t_J = t_J^0 + t_J^c$. The fields: u_J^0, t_J^0 are produced by the dynamic load on S in the crack free body, while u_J^c, t_J^c are produced by the load $t_J^c = -t_J^0$ on S_{cr} and zero boundary conditions on S. As in Sect. 4.2 we derive BIDE for any of the above BVP.

For the problem (7.2) is obtained:

$$\begin{aligned} \frac{1}{2} t_J^0(x) = C_{iJKl} n_i(x) \int_S \Big[\Big(& \sigma^*_{\eta PK}(x,\xi) u^0_{P,\eta}(\xi) \\ & - \rho_{QP}\omega^2 u^*_{QK}(x,\xi) u^0_P \Big) \delta_{\lambda l} - \sigma^*_{\lambda PK}(x,\xi) u^0_{P,l}(\xi) \Big] n_\lambda(\xi) dS \\ & - C_{iJKl} n_i(x) \int_S u^*_{PK,l}(x,\xi) t^0_P dS, \quad x \in S. \end{aligned} \tag{7.4}$$

Here $x = (x_1, x_3)$ denotes the field point and $\xi = (\xi_1, \xi_3)$ is the source point. The function u^*_{IK} is the fundamental solution, see Eqs. (3.83)–(3.87), σ^*_{iJQ} are the corresponding stresses, which are given by $\sigma^*_{iJQ} = C_{iJKl} u^*_{KQ,l}$.

Solving Eq. (7.4) for the displacement u_I^0 and for the traction t_I^0 on S, using Eqs. (4.8) and (4.9) we can find u_K^0 and σ_{jl}^0 on any point inside G. In particular, we can find t_I^0 on the crack line S_{cr}. Proceeding again as in Sect. 4.2 we obtain the equations

$$\begin{aligned} t_J^c(x) = -t_J^0(x) = C_{iJKl} n_i(x) \int_{S_{cr}^+} \Big[\Big(& \sigma^*_{\eta PK}(x,\xi) \Delta u^c_{P,\eta}(\xi) \\ & - \rho_{QP}\omega^2 u^*_{QK}(x,\xi) \Delta u^c_P \Big) \delta_{\lambda l} - \sigma^*_{\lambda PK}(x,\xi) \Delta u^c_{P,l}(\xi) \Big] n_\lambda(\xi) dS_{cr} \\ & + C_{iJKl} n_i(x) \int_S \Big[\Big(\sigma^*_{\eta PK}(x,\xi) u^c_{P,\eta}(\xi) \\ & - \rho_{QP}\omega^2 u^*_{QK}(x,\xi) u^c_P \Big) \delta_{\lambda l} - \sigma^*_{\lambda PK}(x,\xi) u^c_{P,l}(\xi) \Big] n_\lambda(\xi) dS \\ & - C_{iJKl} n_i(x) \int_S u^*_{PK,l}(x,\xi) t^c_P dS, \quad x \in S_{cr}. \end{aligned} \tag{7.5}$$

$$\frac{1}{2}t_J^c(x) = C_{iJKl}n_i(x)\int_{S_{cr}^+}\Big[\Big(\sigma^*_{\eta PK}(x,\xi)\Delta u^c_{P,\eta}(\xi) - \rho_{QP}\omega^2 u^*_{QK}(x,\xi)\Delta u^c_P\Big)\delta_{\lambda l} - \sigma^*_{\lambda PK}(x,\xi)\Delta u^c_{P,l}(\xi)\Big]n_\lambda(\xi)dS_{cr}$$
$$+ C_{iJKl}n_i(x)\int_S\Big[\Big(\sigma^*_{\eta PK}(x,\xi)u^c_{P,\eta}(\xi) - \rho_{QP}\omega^2 u^*_{QK}(x,\xi)u^c_P\Big)\delta_{\lambda l} - \sigma^*_{\lambda PK}(x,\xi)u^c_{P,l}(\xi)\Big]n_\lambda(\xi)dS$$
$$- C_{iJKl}n_i(x)\int_S u^*_{PK,l}(x,\xi)t^c_P dS, \quad x\in S. \tag{7.6}$$

The unknowns here are the generalized crack opening displacement $u_J^c = \Delta u_J^c|_{S_{cr}^+} - \Delta u_J^c|_{S_{cr}^-}$ on S_{cr}, the generalized displacement u_J^c and the generalized traction t_J^c on S.

Equations (7.4)–(7.6) are integro-differential equations for the unknowns u_J^0, t_J^0 and $\Delta u_J^c, u_J^c, t_J^c$, respectively.

7.3 Numerical Solution

The numerical scheme for the solution of the considered problem is described in Sect. 4.3.

In all examples the crack has length $2a$ and lies symmetrically on Ox_1-axis, see Fig. 7.2. Seven boundary elements have been used for the crack in most cases. The first and last elements are QP-BE of length $l_{QP} = 0.15a$, while all other elements are ordinary quadratic BEs.The SIFs are computed directly from the traction nodal values ahead of the crack-tip with the formulae (2.40)

$$\begin{aligned} K_I &= \lim_{x_1\to a^\pm} t_3\sqrt{2\pi(x_1\mp a)},\\ K_{II} &= \lim_{x_1\to a^\pm} t_1\sqrt{2\pi(x_1\mp a)}\\ K_{IV} &= \lim_{x_1\to a^\pm} t_4\sqrt{2\pi(x_1\mp a)} \end{aligned} \tag{7.7}$$

where t_J is the generalized traction at the point $(x_1, 0)$ close to the crack-tip.

7.3.1 Validation Study

In order to test the proposed BIE solution for finite piezoelectric solids and in order to show that the method can be used for both finite elasto-isotropic and elasto-anisotropic solids, that correspond to the uncoupled case, see Sect. 2.6, several test examples are solved. For a single crack in an infinite plane there exist a number of solutions in the literature. A comparison of our results is done with those of: Chen

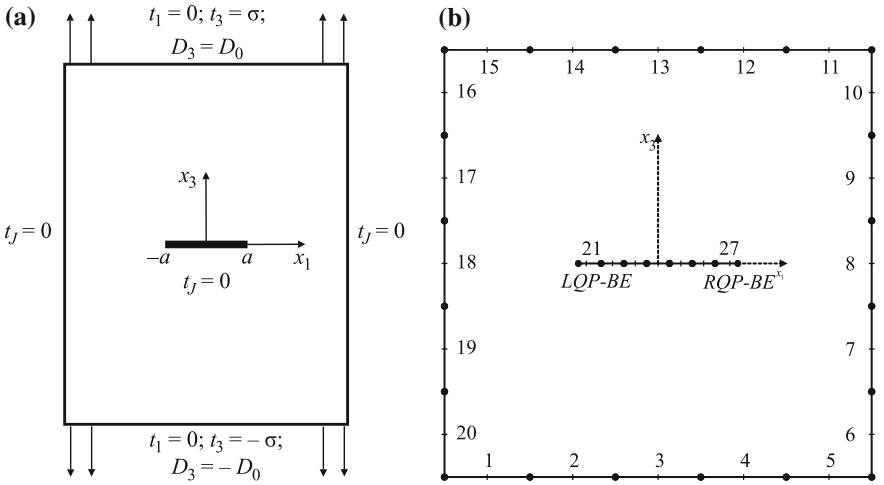

Fig. 7.2 A center cracked piezoelectric plate under uniform uni-axial time-harmonic generalized traction: **a** Plate with boundary conditions; **b** BIEM mesh

and Sih [1] for the isotropic cracked plane; Ohyoshi [4] for the orthotropic cracked plane; Shindo and Ozawa [6] for the piezoelectric cracked plane.

We test our procedure in these cases by representing the infinite domain as a truncated square with a size $b \gg 10a$. For cracked isotropic finite solids there exists an example solved by Chirino and Dominguez [2], which is used for comparison.

7.3.1.1 Cracked Isotropic Plate

Considered is a rectangular plate with the dimensions 20×40 mm and a center crack of length $2a = 5$ mm under time-harmonic tension with an amplitude $\sigma = 400\ \mathrm{N/mm^2}$, see Fig. 7.2. The elastic properties and the density are $\lambda = 0.115385 \times 10^6\ \mathrm{N/mm^2}$, $\mu = 0.76923 \times 10^5\ \mathrm{N/mm^2}$, $\rho = 0.5 \times 10^5\ \mathrm{kg/mm^3}$. A total number of 20 BEs on the external boundary have been used. The normalized by $\sigma\sqrt{\pi a}$ dynamic mode I SIF K_I^* is computed by the traction nodal value ahead the crack-tip, see Eq. (7.7).

The solution of [2] is based on a multi-domain displacement BIEM for a quarter of the rectangular plate and on the fundamental solution expressed by Bessel functions. In contrast, our solution results from single domain traction BIEM and from the Radon transform fundamental solution. The comparison of both solutions methods is depicted in Fig. 7.3 for two different crack discretizations. A good agreement between all these solutions can be observed especially in the low frequency regime. For higher frequency the rough discretization with 5 elements still shows the characteristic features of amplification, but the differences between the other results are higher.

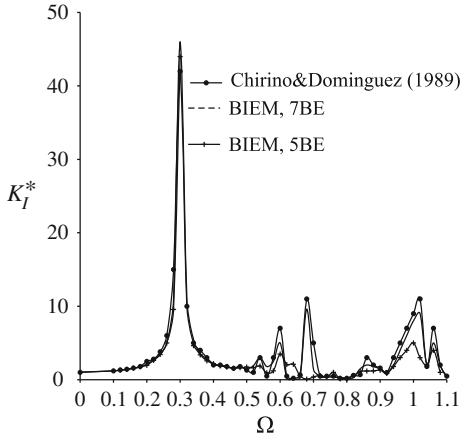

Fig. 7.3 Normalized SIF K_I^* versus normalized frequency Ω for an isotropic plate under uniform uni-axial time-harmonic tension

The solution with 7 boundary elements shows a maximal computational difference with the reference solution of only 7.6 %.

7.3.1.2 A Crack in an Infinite Isotropic Plate Under Incident L-Wave

In what follows two problems are studied: (i) wave scattering by a single crack in an infinite plane and (ii) dynamic behavior of a center cracked plate subjected to an incident L-wave. The infinite domain is represented by a truncated rectangular region with the sizes much bigger than $10a$. The results are compared with those of [2].

The following material data have been chosen: $\lambda = \mu = 2.216 \times 10^{10}\,\mathrm{N/mm^2}$, $\rho = 2.4 \times 10^3\,\mathrm{kg/mm^3}$. The dynamic SIF is normalized by its static value $k_0 = \rho\omega^2\sqrt{\pi a}$. The same problem in the past has been solved by three methods: (a) analytically by Chen and Sih [1]; (b) with multi-domain displacement BIEM by Chirino and Dominguez [2] and (c) with non-hypersingulat traction BIEM by Rangelov et al. [5], where it was shown that all three methods give very close results. Therefore, a comparison with Chirino and Dominguez [2] is sufficient. Figure 7.4 shows the normalized dynamic SIF versus normalized frequency $\Omega = a\omega\sqrt{\rho(3\mu)^{-1}}$ for a normal incident L-wave.

In order to check the numerical algorithm this test example is solved by using truncation approach and solve the problem for a cracked plate with sizes $400 \times 400\,\mathrm{mm}$. In Fig. 7.4 this solution is compared with the solution for a crack in infinite plane obtained by the authors and by Chirino and Dominguez [2].

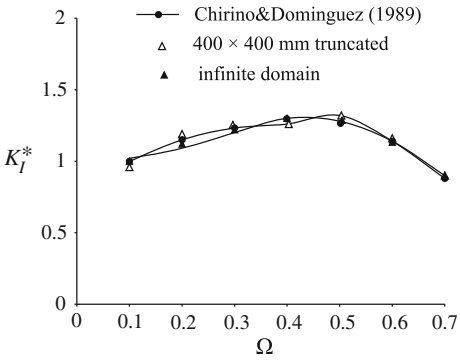

Fig. 7.4 Normalized SIF K_I^* versus normalized frequency Ω for a crack in infinite elasto-isotropic plane under normal incident L-wave

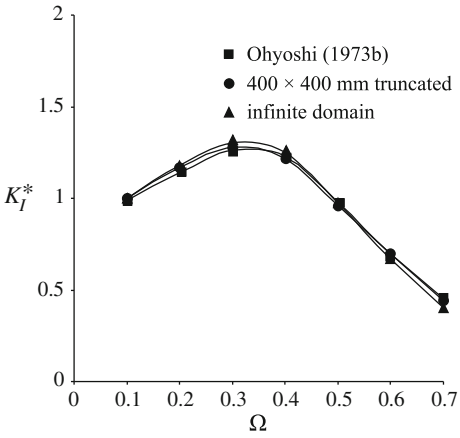

Fig. 7.5 Normalized SIF K_I^* versus normalized frequency Ω for a crack in infinite elasto-anisotropic plane under normal incident L-wave

7.3.1.3 A Crack in an Infinite Orthotropic Plane Under Incident L-Wave

We compare our results for a crack in infinite orthotropic plane and in truncated orthotropic quadratic plate of size $b \gg 10a$ with those of Ohyoshi [4] for an orthotropic plane with a crack under normal incident L-wave. The material constants are chosen as: $c_{11} = c_{33} = 6.649 \times 10^{10}$ N/mm^2, $c_{13} = 2.216 \times 10^{10}$ N/mm^2, $c_{44} = 1.108 \times 10^{10}$ N/mm^2 $\rho = 2.4 \times 10^3$ kg/mm^3. The dynamic SIF normalized by $\omega\sqrt{c_{33}\rho}\sqrt{\pi a}$ versus normalized frequency is depicted in Fig. 7.5. As can be seen, the solutions are very close what shows that the BIEM algorithm works with a good accuracy.

7.3.1.4 A Crack in an Infinite Piezoelectric Plane Under Incident L-Wave

Now our results for an infinite plane and a truncated domain of a size $b \gg 10a$, will be compared with those of Shindo and Ozawa [6] for a crack in infinite piezoelectric plane subjected to normal L-wave. The example is solved for the piezoelectric

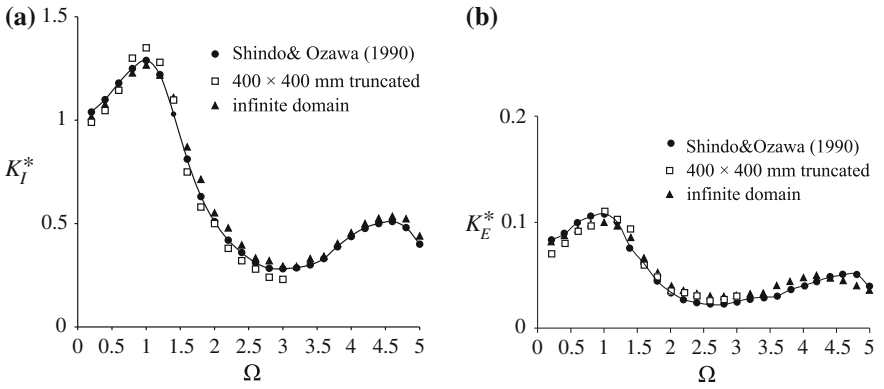

Fig. 7.6 Normalized SIFs versus normalized frequency Ω for a crack in infinite piezoelectric plane under normal incident L-wave: **a** Mechanical SIF K_I^*; **b** Electrical SIF K_E^*

ceramic PZT-6B, see Table 4.1. The incident displacement field is given by

$$u_J^{in} = (0, 1, e_{33}\varepsilon_{33}^{-1})e^{-ik_1 x_3}, \quad k_1 = \omega\sqrt{(c_{33} + e_{33}^2\varepsilon_{33}^{-1})\rho}, \tag{7.8}$$

from which the incident traction on the crack follows as

$$t_J^{in} = (0, -i\omega\sqrt{(c_{33} + e_{33}^2\varepsilon_{33}^{-1})\rho}, 0). \tag{7.9}$$

Figure 7.6a shows the K_I factor normalized by its static value $k = k_1\sqrt{\pi a}$, i.e. K_I^*, versus normalized frequency, while in Fig. 7.6b the normalized dynamic electric field intensity factor $|e_{33}K_{IV}/k|$, i.e., K_E^* versus normalized frequency Ω is plotted. An excellent coincidence between the results obtained by different computational techniques is observed. This demonstrates the good accuracy of the proposed traction based BIEM for the solution of 2D time-harmonic problems in cracked finite and infinite solids.

7.3.2 Parametric Study

Considered is the finite rectangular piezoelectric solid with a center crack as shown in Fig. 7.2. The size of the plate is 40×20 mm, the crack length is $2a = 5$ mm and the material constants are given in Table 4.1. A time-harmonic uniform tension and/or electric displacement is applied along the Ox_3 direction with the amplitudes $t_3 = \sigma = 400 \times 10^6\,\mathrm{N/m^2}$ and $t_4 = D_0 = 0.1\,\mathrm{C/m^2}$. The mechanical SIF K_I is normalized by $\sigma\sqrt{\pi a}$, while the electrical SIF K_{IV} is normalized by $\sigma\sqrt{\pi a}e_{33}/c_{33}$.

The parametric study reveals the following effects:

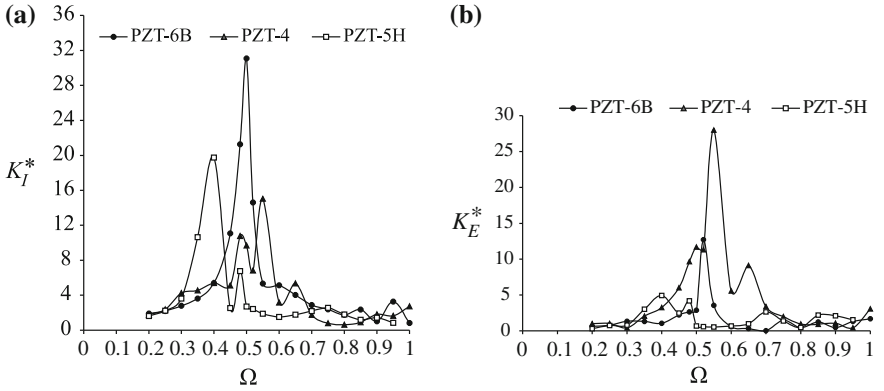

Fig. 7.7 Normalized SIFs versus normalized frequency Ω for different PEM: PZT-6B, PZT-4 and PZT-5H: **a** Mechanical SIF K_I^*; **b** Electrical SIF K_E^*

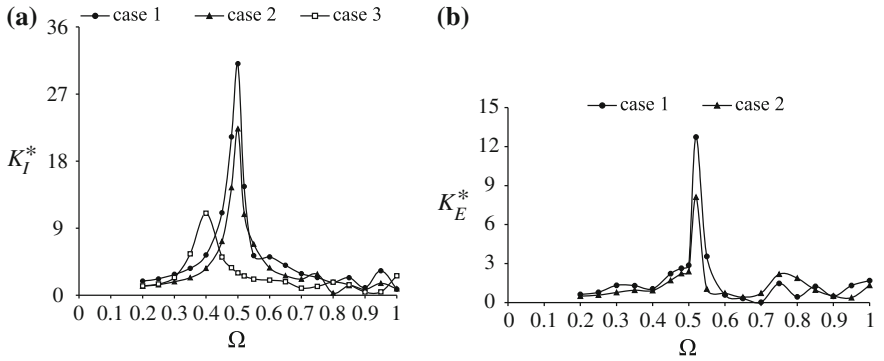

Fig. 7.8 Normalized SIFs versus normalized frequency Ω for PZT-6B at two cases 1 and 2 of dynamical load. Case 3: PZT-6B considered as anisotropic material: **a** Mechanical SIF K_I^*; **b** Electrical SIF K_E^*.

7.3.2.1 Frequency Dependence

Figures 7.7, 7.8, 7.9 and 7.10 show the frequency dependent SIFs curves in the interval $\Omega \in [0.2, 1]$, where $\Omega = a\omega\sqrt{\rho c_{33}^{-1}}$ is the normalized frequency. The frequency of the applied load influences strongly the dynamic response of the cracked solid. The maximum SIFs occur in the frequency interval $\Omega \in [0.4, 0.55]$ for the considered three types of piezoelectric materials. Nevertheless, the resonance frequencies are different for different piezoelectric materials. Figure 7.8a shows that when the material PZT-6B is considered as a pure anisotropic material (without taking the electromechanical coupling into account) subjected to uniform tension, the resonance peak is shifted to the left, i.e. to lower frequencies.

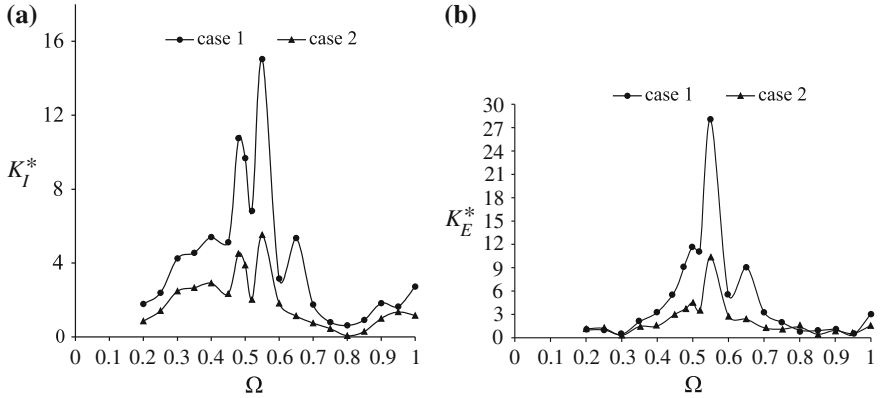

Fig. 7.9 Normalized SIFs versus normalized frequency Ω for PZT-4 at two cases 1 and 2 of dynamical load: **a** Mechanical SIF K_I^*; **b** Electrical SIF K_E^*

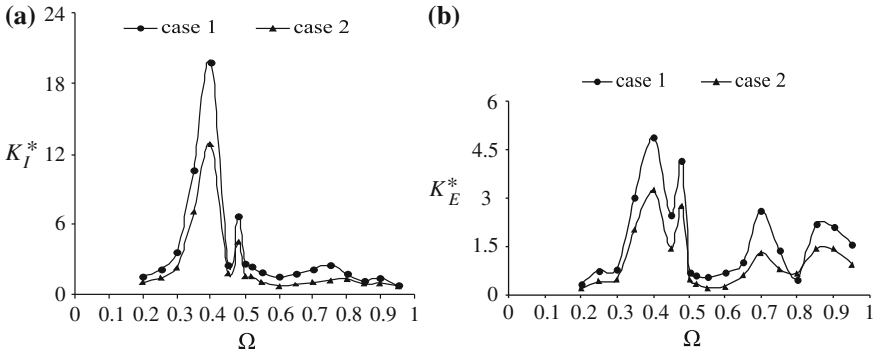

Fig. 7.10 Normalized SIFs versus normalized frequency Ω for PZT-5H at two cases 1 and 2 of dynamical load: **a** Mechanical SIF K_I^*; **b** Electrical SIF K_E^*

7.3.2.2 Effect of the Piezoelectric Material Properties

Figure 7.7a, b present the normalized SIFs for three different piezoelectric materials—PZT-6B, PZT-4 and PZT-5H, see Table 4.1. It clearly can be seen that the mechanical constants strongly influence the character of the SIFs curve. The piezoelectric material PZT-6B has only one resonance peak in the interval, while the other two materials have more than one peak. The resonance peak of the SIFs occurs for PZT-5H at lower and for PZT-4 at higher frequencies. A comparison between SIF-I for PZT-6B and PZT-4 materials shows that the difference in their maximum values is about 106 %. The difference in the peaks of SIF-IV for PZT-4 and PZT-5H is about 460 %.

7.3.2.3 Effect of the Electromechanical Coupling

Figures 7.8, 7.9 and 7.10 demonstrate the influence of the coupling properties on the generalized SIFs. The figures show the SIFs curves for two different cases of the applied loads.

case 1: a combined electro-mechanical load is applied, i.e. $t_3 = 400 \times 10^6 M/m^2$ and $t_4 = D_3 = 0.1C/m^2$;
case 2: the load is pure mechanical tension, i.e. $t_3 = 400 \times 10^6 M/m^2$ and $t_4 = D_3 = 0$.

One can see that the dynamic response is strongly electro-mechanical even when solely a mechanical tension is applied, see Figs. 7.8b and 7.10b, case 2. The profiles of the SIFs curves are similar in the both cases, but the SIFs in case 1 is rather higher than that in case 2. For example, the differences between the peak values in cases 1 and 2 for the different materials are as follows:

- For PZT-6B:39 % for SIF-I and 57 % for SIF-IV;
- For PZT-4: 172 % for SIF-I and 174 % for SIF-IV;
- For PZT-5H: 55 % for SIF-I and 52 % for SIF-IV.

As a resume, the parametric study convincingly demonstrates the sensitivity of the K-factor to the frequency of the applied electro-mechanical load, to the coupled character of the electromechanical field and to the specific properties of the different piezoelectric materials.

7.4 Concluding Remarks

The 2D dynamic in-plane problem of a cracked finite piezoelectric solid is solved in the frequency domain by means of non-hypersingular traction BIEM. Numerical examples for a center crack in a finite rectangular plate under uniform electro-mechanical load are solved. Parametric studies show the dependence of the dynamic response on the excitation frequency, on the coupled/uncoupled character of the electro-mechanical field and on the properties of different piezoelectric materials.

References

1. Chen EP, Sih GC (1977) Scattering waves about stationary and moving cracks. In: Sih GC (ed), Mechanics of fracture 4, elastodynamic crack problems. Nordhoff International Publishing, Leyden, pp 119–212
2. Chirino F, Dominguez J (1989) Dynamic analysis of cracks using BEM. Eng Fract Mech 34:1051–1061
3. Gross D, Dineva P, Rangelov T (2007) BIEM solution of piezoelectric cracked finite solids under time-harmonic loading. Eng Anal Bound Elem 31(2):152–162

4. Ohyoshi T (1973) Effect of orthotropy on singular stresses for a finite crack. ASME. J Appl Mech 40:491–497
5. Rangelov T, Dineva P, Gross D (2003) A hyper-singular traction BIEM for stress intensity factor computation in a finite cracked body. Eng Anal Bound Elem 27:9–21
6. Shindo Y, Ozawa E (1990) Dynamic analysis of a cracked piezoelectric material. In: Hsieh RKT (ed) Mechanical modeling of new electromagnetic materials. Elsevier, Amsterdam, pp 297–304

Chapter 8
Dynamic Crack Interaction in Piezoelectric and Anisotropic Solids

Abstract Multiple in-plane cracks in a piezoelectric or anisotropic plane loaded by time-harmonic waves is treated. Simulations for different crack configurations such as coplanar, collinear or cracks in arbitrary position to each other are presented and discussed. They demonstrate among others the strong effect of electromechanical coupling, show the frequency dependent shielding and amplification resulting from crack interaction and reveal the sensitivity of the K-factors to the complex influence of both the wave–crack and crack–crack interaction.

8.1 Introduction

While in the past mostly single cracks in piezoelectric materials were in the focus of interest, the behaviour of multiple cracks, i.e. crack interaction, recently attracted increasing attention. One reason for that is the observation that a precursor of final failure often is the formation of interacting micro cracks, which subsequently coalesce to a macro crack.

Crack systems under static loading have been studied by several authors. Without claiming completeness we mention Sun, Zhou and Wang, and Zhou et al. [18, 25, 26] who studied a symmetric system of parallel permeable cracks under anti-plane shear loading by pairs of triple integral equations. Closed-form solutions for the in-plane problem of collinear permeable cracks have been presented by Gao and Fan [4] who used the complex potential method, while Han and Chen [7] considered parallel impermeable cracks.

There is a limited number of papers for crack systems under dynamic load, transient or time-harmonic. This refers to piezoelectric as well as to uncoupled, i.e. anisotropic solids. It was Itou, Itou and Haliding [9, 10] who first computed SIFs for collinear and coplanar in-plane cracks in an infinite orthotropic plane subjected to time-harmonic plane wave by the method of dual integral equations.

P. Dineva et al., *Dynamic Fracture of Piezoelectric Materials*,
Solid Mechanics and Its Applications 212, DOI: 10.1007/978-3-319-03961-9_8,

A comprehensive treatment of the interaction between two cracks in a piezoelectric plane under steady state in-plane electrical and anti-plane mechanical loads was provided in Wang and Meguid [21, 22]. Their analysis was based on singular integral equations coupled with a so-called pseudo-incident wave method, see Wang and Meguid [20]. With the same method Wang [23] solved the wave scattering of multiple permeable cracks in the interface between two infinite piezoelectric media. A similar problem was solved by Zhao and Meguid [24]. Meguid and Chen [12] studied the transient response of a finite piezoelectric strip with coplanar impermeable anti-plane cracks under electro-mechanical impact. Hankel [8] analyzed the dynamic interaction between permeable multiple cracks in a strip under anti-plane shear waves. The transient response of two coplanar cracks in a piezoelectric region under anti-plane mechanical and in-plane electric impact loads was investigated in Chen, Chen and Worswick [1, 2]. As further works shall be mentioned those of Sun et al. [19] on unequal parallel permeable interface cracks in a layer bonded to two piezoelectric half planes, Li and Lee [11] on two surface cracks and Su et al. [17] on coplanar interface cracks between two dissimilar piezoelectric strips. All these papers use the singular integral equation method and they are restricted to anti-plane problems and relatively simple crack and loading geometries.

Garcia-Sanchez, Garcia-Sanchez et al. and Saez et al. [5, 6, 15] presented results for more involved in-plane problems of cracks in a piezoelectric or uncoupled anisotropic plane subjected to incident plane waves. In these works the hypersingular mixed (dual) BIEM formulation is developed, validated and applied, where the displacement BIE is used over one of the crack surfaces, while the hypersingular traction BIE is applied over the other crack surface. The treatment of the hypersingular integrals is carried out by means of variable change that transforms the boundary to the complex plane in conjunction with the singularity subtraction method.

The present chapter follows Dineva et al. [3] and its aim is threefold. First, as an alternative to the just mentioned hypersingular mixed BIEM formulation the use of non-hypersingular traction BIEM for the treatment of crack systems shall be discussed. Thus the chapter is a continuation of Chap. 6. Secondly, the flexibility, efficiency and accuracy of the method shall be demonstrated. These properties rely on the fundamental solution, which is obtained by Radon transform and evaluated semi-analytically in Chap. 3. By this means an anisotropic material may be considered as a simplified case of a piezoelectric material, which needs no specific treatment, see Chap. 5. Finally, as examples of crack systems, various configurations of interacting in-plane cracks loaded by plane waves of different incident angles are considered. Parametric studies for the SIFs reveal the influence of the crack geometry, the incident wave's frequency and angle.

8.2 Problem Statement

Consider an infinite, transversely isotropic piezoelectric domain containing N straight cracks $\Gamma_k = \Gamma_k^+ \cup \Gamma_k^-$, $k = 1, \ldots, N$ of prescribed length $2a_k$, subjected to incident time-harmonic L- or SV- waves with angular frequency ω and incident

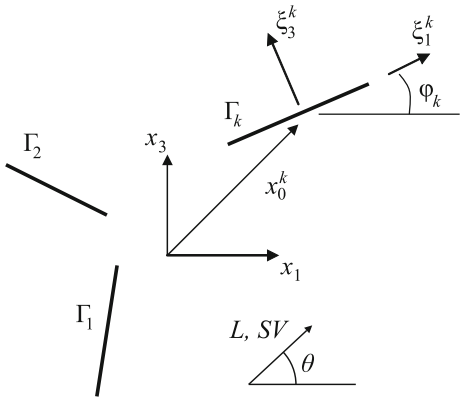

Fig. 8.1 Crack system under harmonic wave loading

angle θ with respect to x_1, see Fig. 8.1. The material symmetry axis, i.e. the poling direction coincides with the Ox_3 -axis and plane strain deformation is assumed in the Ox_1x_3-plane. The non-zero field quantities then are the displacement u_i, the stress σ_{ij}, the dielectric displacement D_i and the electric field E_i, where $i, j = 1, 2$.

The location of the kth crack with respect to the global Ox_1x_3 coordinate system can be described by the position vector $x_0^k = (x_{01}^k, x_{03}^k)$ of the crack center and the crack angle φ_k. With the local coordinates (ξ_1^k, ξ_3^k) and the accompanying unit vectors n^k, e^k the points along the cracks are given by the position vector

$$x_i^k = x_{0i}^k + \xi_i^k e_i^k; \quad |\xi_i^k| \le a_k. \tag{8.1}$$

The scattering problem in absence of volume forces and charges is described by the BVP (2.44) and for the considered multiple crack's system with a notation $S_{cr} = \cup_1^N \Gamma_k$ it is

$$\left| \begin{array}{l} \sigma_{iJ,i} + \rho_{JK}\omega^2 u_K = 0 \quad \text{in } R^2 \backslash S_{cr}, \\ t_J|_{S_{cr}} = 0, \end{array} \right. \tag{8.2}$$

where $u_K = (u_1, u_3, \phi)$ is the generalized displacement , $J, K = 1, 3, 4$, σ_{iJ} is the generalized stress, $\sigma_{iJ} = C_{iJKl}u_{K,l} = C_{iJKl}s_{Kl}$, see Sect. 2.5.1. The generalized traction vector is $t_J = \sigma_{iJ}n_i$, where n_i is the unit normal vector on S_{cr}^+. The strain-displacement and electric field-potential relations are $s_{ij} = \frac{1}{2}(u_{i,j} + u_{j,i})$, $E_i = -\phi_{,i}$ where s_{ij}, ϕ are the strain tensor and electric potential, ρ is the mass density and $\rho_{JK} = \begin{cases} \rho, & J, K = 1, 3 \\ 0, & J = 4 \text{ or } K = 4. \end{cases}$

All cracks, for simplicity, are assumed to be free of mechanical traction and surface charges, i.e. in the BVP (8.2) impermeable cracks are assumed. In addition Sommerfeld's radiation condition at infinity holds. It is further assumed that the cracks are separated, i.e. the direction of incident waves is such that a proper scattering occurs.

As mentioned in Sect. 6.2, in the special case when the piezoelectric constants vanish, i.e. $e_{ij} = 0$, the BVP described by the Eq. (8.2) degenerate to the uncoupled anisotropic case. As further specialization the mechanical isotropic case will be described when the stiffness are chosen as $C_{ijkl} = \lambda\delta_{ij}\delta_{kl} + \mu(\delta_{ik}\delta_{jl} + \delta_{il}\delta_{jk})$, where $\mu = c_{44}$, $\lambda = c_{13}$ and $c_{11} = c_{33} = \lambda + 2\mu$.

The total wave field is again written as a sum of the incident and the scattered wave field

$$u_J(x,\omega) = u_J^{in}(x,\omega) + u_J^{sc}(x,\omega) \quad \sigma_{iJ}(x,\omega) = \sigma_{iJ}^{in}(x,\omega) + \sigma_{iJ}^{sc}(x,\omega), \tag{8.3}$$

where u_J^{in}, t_J^{in} and u_J^{sc}, t_J^{sc} are the incident and scattered generalized displacements and tractions, respectively, while $x = (x_1, x_3)$. The incident wave is prescribed as a plane time-harmonic L- or SV- wave. Its generalized displacement u_J^{in} and stress σ_{iJ}^{in} are given in Sect. 4.2. The scattered wave field is unknown and has to be determined. It has to satisfy the BVP (8.2) and Sommerfeld's radiation condition at infinity. The boundary conditions in (8.2) can be rewritten as

$$t_J^{sc} = -t_J^{in}, \quad \text{on } \Gamma_k, \quad k = 1, \ldots, N. \tag{8.4}$$

The representation formula for the scattered wave field can be expressed by the superposition principle and Eq. (4.21) as

$$u_J^{sc}(x,\omega) = -\sum_{k=1}^{N} \int_{\Gamma_k^+} \sigma_{iMJ}^*(x,\xi,\omega)\Delta u_M^k(\xi,\omega) n_i^k(\xi) d\xi, \quad x \notin S_{cr}, \tag{8.5}$$

where $x = (x_1, x_3)$ is the source point, $\xi = (\xi_1, \xi_3)$ is the observation point, $\sigma_{iJQ}^* = C_{iJKl}U_{KQ,l}^*$ is the stress derived from the fundamental solution u_{QK}^*, see Eqs. (3.83)–(3.87). Furthermore, $\Delta u_J^k = u_J^k|_{\Gamma_k^+} - u_J^k|_{\Gamma_k^-}$ is the unknown generalized COD on the crack Γ_k and n_i^k is the outward normal vector at the observation point along the kth-crack Γ_k^+. The non-hypersingular traction boundary integral equation is obtained by Eq. (4.20):

$$\begin{aligned} t_J^{in}(x,\omega) = &- C_{iJKl} n_i(x) \\ &\times \sum_{k=1}^{N} \int_{\Gamma_k} \Big[\Big(\sigma_{\eta PK}^*(x,\xi,\omega)\Delta u_{P,\eta}^k(\xi,\omega) - \rho_{QK}\omega^2 U_{QK}^*(x,\xi,\omega)\Delta u_P^k(\xi,\omega) \Big) \delta_{\lambda l} \\ &- \sigma_{\lambda PK}^*(x,\xi,\omega)\Delta u_{P,l}^k(\xi,\omega) \Big] n_\lambda(\xi) d\xi, \quad x \in S_{cr}. \end{aligned} \tag{8.6}$$

Equation (8.6) forms, strictly speaking, a system of integro–differential equations with respect to the unknowns Δu_J^k along the cracks.

The numerical treatment of Eq. (8.6) follows the procedure developed in Chap. 4 and is realized within a FORTRAN code, see [13].

Knowing the traction, the generalized dynamic SIFs at the tips of the kth crack are calculated by using the formulae, see Eq. (2.40)

$$\begin{aligned} K_I^k &= \lim_{r^k \to 0} t_3^k \sqrt{2\pi r^k}, \\ K_{II}^k &= \lim_{r^k \to 0} t_1^k \sqrt{2\pi r^k}, \\ K_{IV}^k &= \lim_{r^k \to 0} t_4^k \sqrt{2\pi r^k}, \end{aligned} \tag{8.7}$$

where t_J^k, $J = 1, 3, 4$ is the generalized traction ahead of the crack-tips of the kth crack, r^k is the corresponding distance to the crack-tip. Regarding the electrical SIFs, the electric field SIF K_E^k with

$$K_E^k = \lim_{r^k \to 0} E_3^k \sqrt{2\pi r^k} \quad \text{and } E_3^k = (c_{33} t_4^k - e_{33} t_3^k)(e_{33} c_{33} + e_{33}^2)^{-1}$$

or the electric displacement SIF K_D^k with $K_D^k = K_{IV}^k$ can be determined. In all calculations an appropriate normalization has been used. For the mechanical SIFs it is given by

$$K_{I,II}^{*,k} = K_{I,II}^k / m, \quad \text{with } m = |\bar{t}_3^{in} \sqrt{\pi a}| = \omega \sqrt{(c_{33} + e_{33}^2 \varepsilon_{33}^{-1})\rho} \sqrt{\pi a},$$

where $\bar{t}_3^{in}$ is the mechanical traction of the normal incident wave. The normalized electrical SIFs are defined as

$$K_E^{*,k} = e_{33} m^{-1} |K_E^k| \quad \text{and } K_D^{*,k} = c_{33} e_{33} m^{-1} |K_D^k|,$$

while the normalized frequency is introduced through $\Omega = a\omega \sqrt{\rho c_{44}^{-1}}$.

8.3 Numerical Results

In the following, SIFs results are presented for a single crack and for different two-crack configurations, see Fig. 8.2. For simplicity all cracks are of length $2a = 5\,\text{mm}$. Numerical studies showed that seven boundary elements for each crack are sufficient to achieve a satisfying accuracy within the considered frequency range. The first and the last element are QP-BE, while the remaining elements are ordinary quadratic elements. Their lengths have been chosen as $l_1 = l_7 = 0.375\,\text{mm}$, $l_2 = l_6 = 0.5\,\text{mm}$, $l_3 = l_5 = 1.0\,\text{mm}$, $l_4 = 1.25\,\text{mm}$.

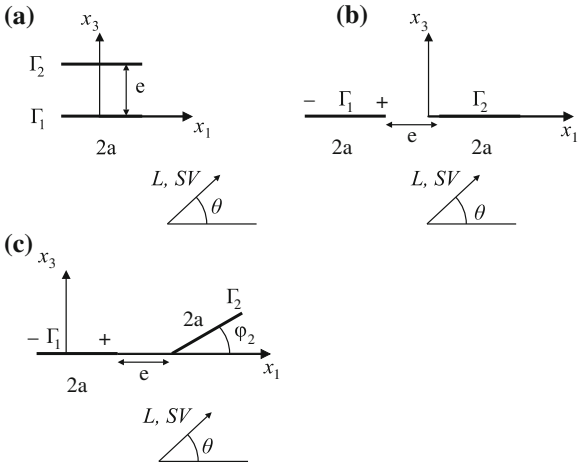

Fig. 8.2 Three-crack systems: **a** stacked cracks; **b** collinear cracks; **c** inclined cracks

8.3.1 Piezoelectric Solids

Two different piezoelectric materials have been considered to make comparisons with available in the literature results. The first one is PZT-6B, the second material is PZT-5H, see Table 4.1.

Figure 8.3 shows the authors' SIFs results, here denoted as BIEM, for a single crack under normal incident L-waves, which have already been presented in Chap. 6. A comparison with those of Garcia-Sanchez, Shindo and Ozawa [5, 16] leads to computational differences less than 8 %. This indicates that the numerical scheme works satisfactory albeit the low number of chosen elements. The results are additionally compared with those of collinear and stacked cracks, respectively, which are far away from each of other. For this case SIFs as for a single crack can be expected since the interaction between the two cracks is negligible on account of their large distance. This fact is properly reflected by the results, which verify again the applicability of the numerical scheme. Finally, by comparison of Fig. 8.3a and c, it can be observed that the shape of the SIF versus frequency curves is slightly different, i.e. the specific material properties have a noticeable influence.

In Fig. 8.4 dynamic SIFs K_I^{*+} and K_E^{*+} for the inner crack tips of two collinear cracks under a normal incident L-wave are depicted. First, a comparison of our K_I^{*+} -results with those of Garcia-Sanchez [5] for the crack-tip distance $e = a$ in Fig. 8.4a shows again an excellent agreement. Secondly, a significant influence of the material properties and the crack distance is noticeable. For $e = a$ the so-called dynamic overshoot, i.e. the maximum of K_I^{*+} and its location, is different for PZT-5H and PZT-6B (Fig. 8.4a, b). Unexpectedly, for PZT-6B this maximum is below that for a single crack, which also appears for the electric SIF K_E^{*+}. When the crack-tips

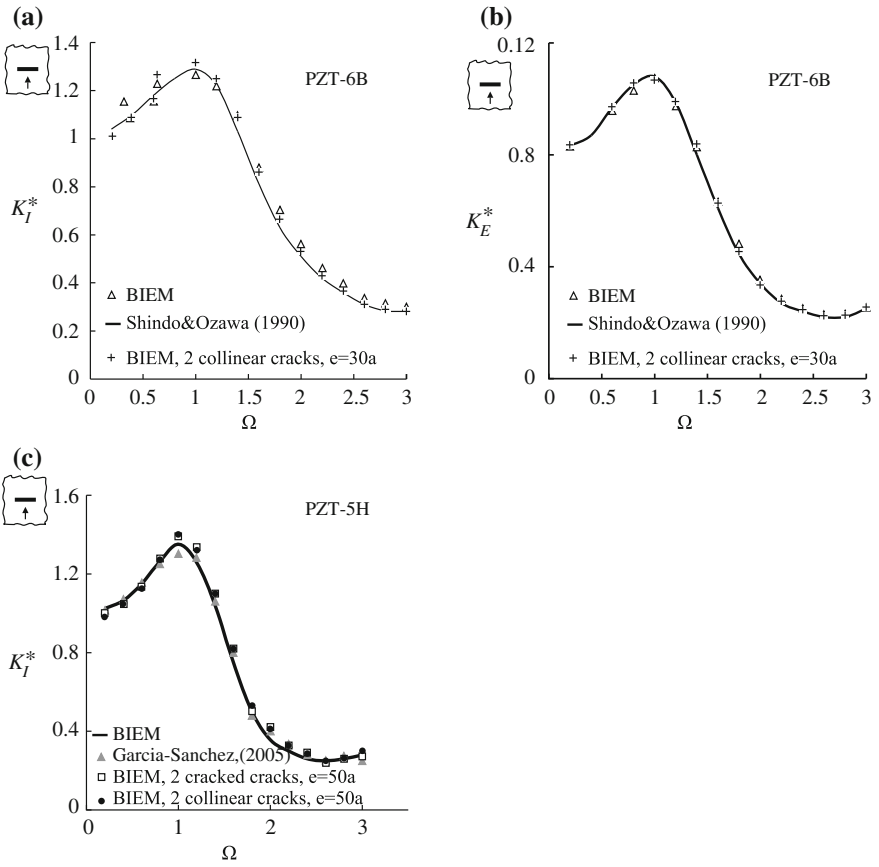

Fig. 8.3 K-factors versus frequency of normal incident L wave for a single crack in a piezoelectric plane—comparison with results in Garcia-Sanchez, Shindo and Ozawa [5, 16] and with the authors' results for two-crack systems: **a** normalized SIF-I for PZT-6B; **b** normalized SIF-E for PZT-6B; **c** normalized SIF-I for PZT-5H

approach each other the maximum SIFs in general increase. This clearly can be seen in Fig. 8.4b, c for $e = a/4$.

Stress intensity factors versus frequency for the lower crack of two stacked cracks under normal incident L-waves are plotted in Fig. 8.5. Because this problem is non-symmetric with respect to the wave-cracks-configuration, a mode-II SIF K_{II}^{*+} appears. The dynamic overshoot for all SIFs of this configuration increases significantly with decreasing crack distance e. For the small crack distance $e = 2a/3$ a sharp resonance peak at $\Omega = 1.1$ can be observed, but in general the strength of the crack interaction depends on the frequency. Comparing the peak values with those for collinear cracks in Fig. 8.4, it can be concluded that the crack interaction effect is much stronger for stacked cracks than for collinear cracks.

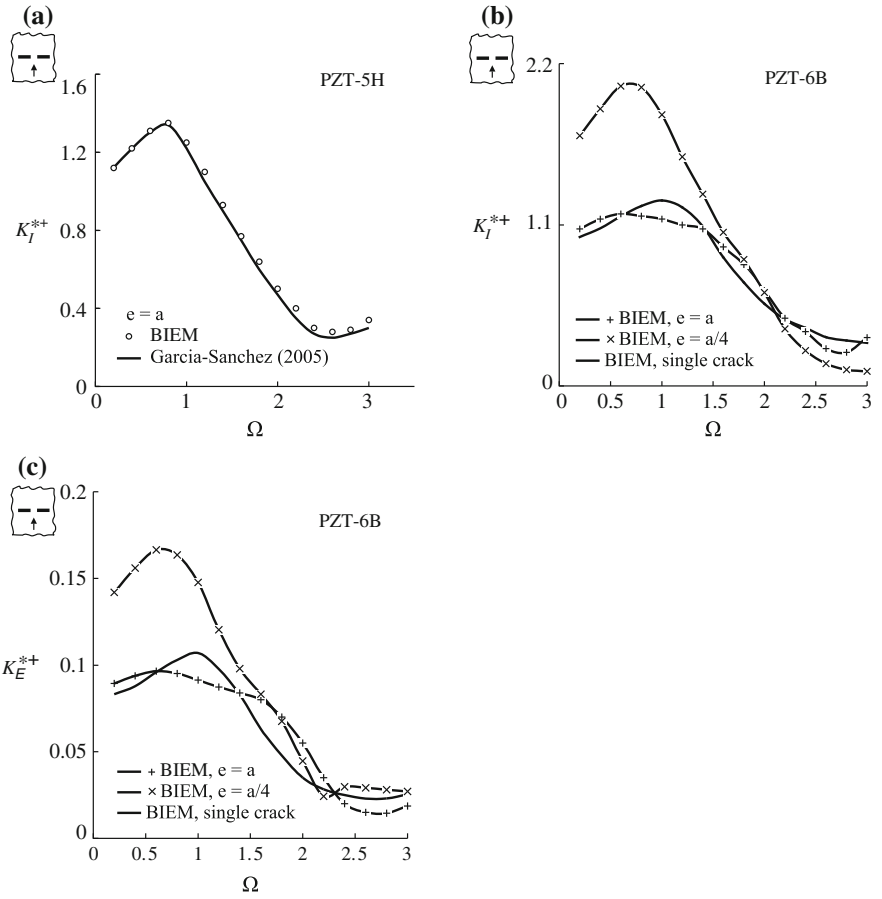

Fig. 8.4 K-factors versus frequency of normal incident L- wave for two collinear cracks (Fig. 8.2b) with separate distance e in a piezoelectric plane—comparison with results of Garcia-Sanchez [5]: **a** normalized SIF-I at internal crack-tip for PZT-5H; **b** normalized SIF-I at internal crack-tip for PZT-6B; **c** normalized SIF-E at internal crack-tip for PZT-6B

The influence of an oblique wave incidence is shown for collinear cracks in Fig. 8.6. Considered are SIFs at the inner crack tip of the left crack for L- and SV-waves with an incidence angle $\theta = \pi/4$. By comparison of Figs. 8.6a and 8.4b for a L-wave it can be seen that the mode-I SIFs for all crack distances are significantly smaller than for a normal incident angle. But now in addition a mode-II SIF appears, see Fig. 8.6b, which is not present for normal incidence. The mode-I SIFs for the SV-wave in Fig. 8.6c are smaller than for the L-wave. However, the influence of the inclined second crack on the SIFs of the first crack loaded by normal incident L-waves is shown in Fig. 8.7 for two different inclination angles and the crack tip distance $e = a/24$. For the higher inclination angle $\varphi_2 = \pi/3$, the interaction leads

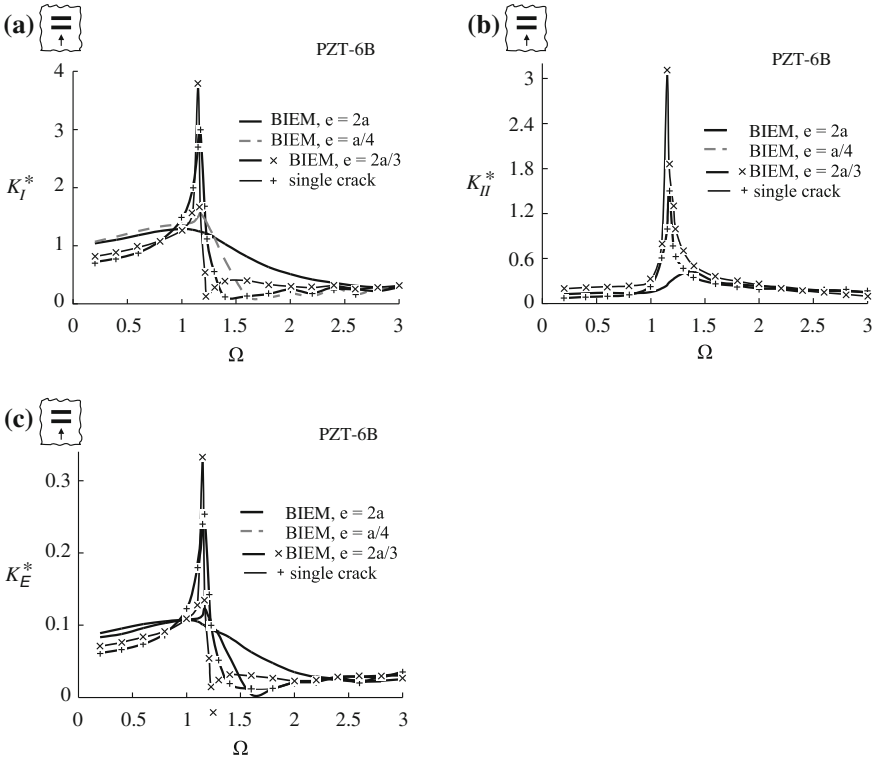

Fig. 8.5 K-factors at crack Γ_1 versus frequency of normal incident L-wave for two stacked cracks (Fig. 8.2a) at a separate distance e in a piezoelectric plane: **a** normalized SIF-I; **b** normalized SIF-II; **c** normalized SIF-E

to higher peak values of both the mode-I and the electric SIF compared with the results of a single crack. For the smaller inclination angle $\varphi_2 = \pi/20$ the opposite is visible, i.e. through interaction with the second crack, the first crack is shielded in the frequency region of the peak. On account of the non-symmetry of the configuration, again a mode-II SIF is present which is not shown here.

8.3.2 Anisotropic Solids

The illustrative numerical examples presented in this section are restricted to cracks in orthotropic materials with a symmetry axis parallel to Ox_3 axis, i.e. the effect of material alignment is not considered. The numerical scheme follows exactly those described in Chap. 5. A detailed validation study for a single crack in an isotropic, orthotropic and transversely-isotropic material subjected to normal incident L-waves has already been presented in Chap. 5, comparing the BIEM results with those of

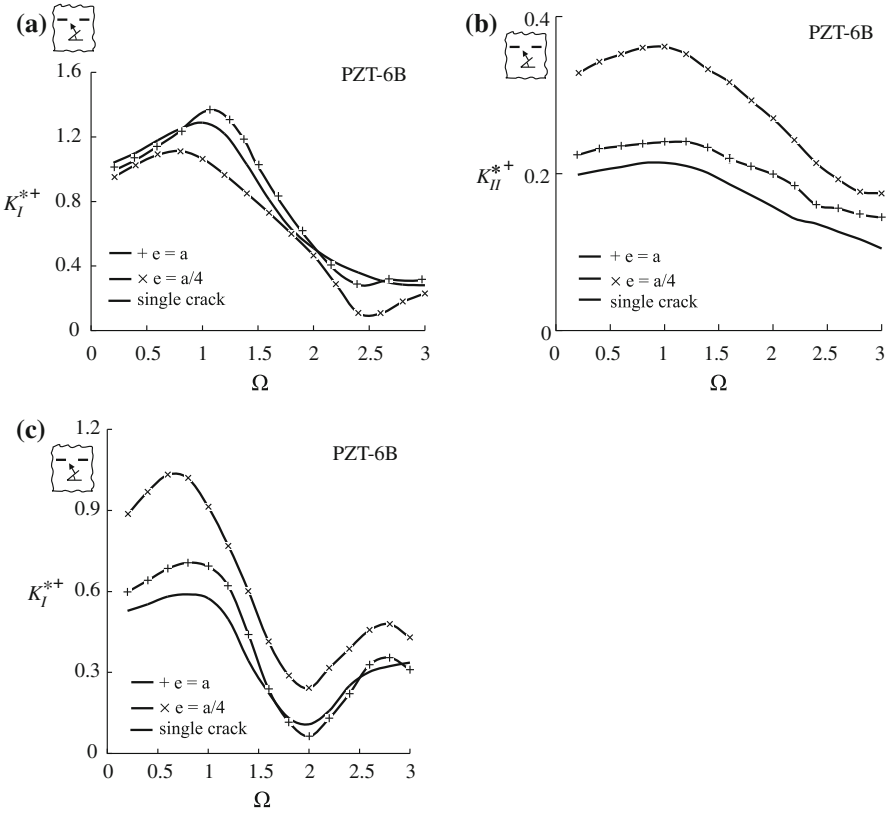

Fig. 8.6 K-factors versus normalized frequency at the internal crack-tip of two collinear cracks (Fig. 8.2b) in a piezoelectric plane under oblique L- and SV-wave at incident angle $\theta = \pi/4$: **a** normalized SIF-I for incident L-wave; **b** normalized SIF-II for incident L-wave; **c** normalized SIF-I for incident SV-wave

Ohyoshi [14]. Regarding two-crack systems, the SIFs results for large distances between two interacting cracks recover the solutions of a single crack.

In Figs. 8.8 and 8.9 the results for SIFs are compared with those of Itou and Haliding [10] for stacked cracks and of Itou [9] for collinear cracks under normal incident L-wave. The orthotropic material in Figs. 8.8a and 8.9a, b is a Boron-Epoxy composite with the properties $E_1 = 224.06\,\text{GPa}$; $E_3 = 12.69\,\text{GPa}$; $\mu_{13} = 4.43\,\text{GPa}$; $\nu_{13} = 0.256$. Graphite-Epoxy composite is considered in Fig. 8.8b with following properties $E_1 = 158.06\,\text{GPa}$; $E_3 = 15.3\,\text{GPa}$; $\mu_{13} = 5.52\,\text{GPa}$; $\nu_{13} = 0.34$. The dynamic SIFs are normalized by $\sigma_0\sqrt{a}$ in Itou and Haliding [10] and by $\sigma_0\sqrt{\pi a}$ in Itou [9], where $\sigma_0 = i\omega c_{33}/c_T$ and $c_T = \sqrt{c_{44}/\rho}$ is the shear wave velocity. Plotted are the normalized SIFs K^* for both cracks of the stacked crack configuration in Fig. 8.8 and for the inner $(+)$ and outer $(-)$ tips of the collinear crack configuration in Fig. 8.9 versus normalized frequency $\Omega = a\omega/c_T = a\omega\sqrt{\rho c_{44}^{-1}}$. Figures 8.8 and

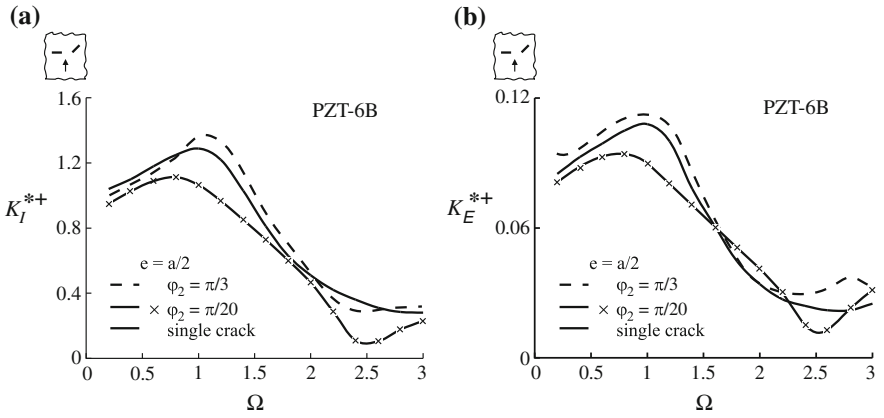

Fig. 8.7 K-factors versus normalized frequency at internal crack-tip of two inclined cracks (Fig. 8.2c) in a piezoelectric plane under normal incidence L-wave: **a** normalized SIF-I; **b** normalized SIF-E

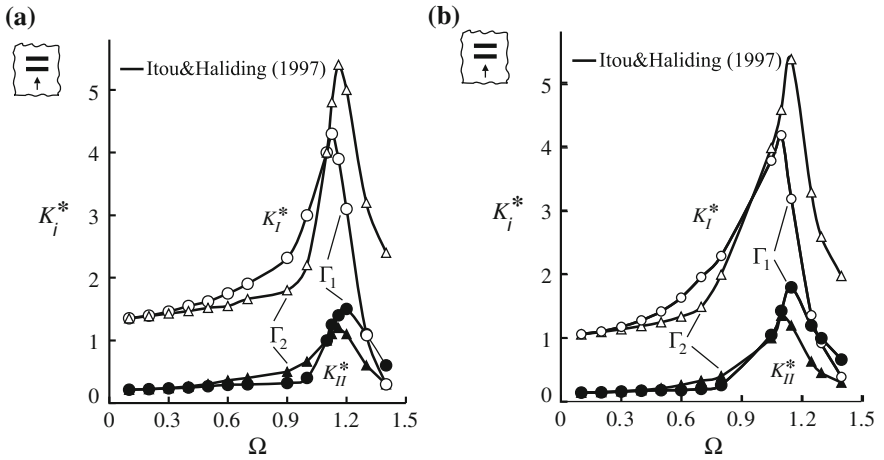

Fig. 8.8 Normalized SIF-I versus normalized frequency for stacked cracks (Fig. 8.2a) in an orthotropic plane under normal L-wave: **a** Boron-Epoxy, **b** Graphite-Epoxy

8.9 demonstrate that the results obtained by the different computation techniques are very close.

In the following we consider anisotropic materials with properties defined in Ohyoshi [14], where $c_{ij} = s_{ij}C$ with $C = 6.6495\,\text{GPa}$ and $\rho = 2.4 \times 10^3\,\text{kg/m}^3$. Following the notation in Chap. 5, the so-called case 6 material is given by $s_{11} = 1$, $s_{13} = s_{31} = 1/3$, $s_{33} = 1$, $s_{44} = 1/6$, while the case 7 material has the properties $s_{11} = 1, s_{13} = s_{31} = 1/30$, $s_{33} = 1$, $s_{44} = 1/3$. The dynamic SIFs are now normalized by $\omega d_{33}^{-1/2}\sqrt{\pi a}$, where $d_{33} = c_{33}/\rho$ and plotted versus the normalized

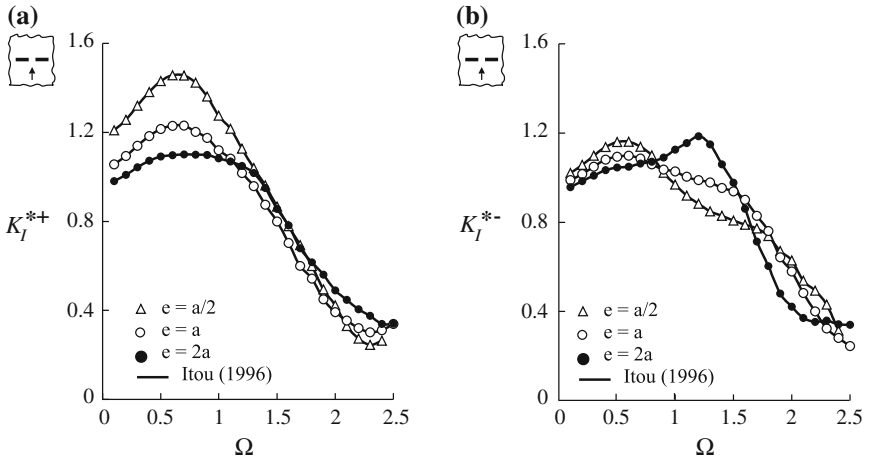

Fig. 8.9 Normalized SIF-I versus normalized frequency of two collinear cracks (Fig. 8.2b) in an orthotropic Boron-Epoxy plane under normal L-wave: **a** at the internal crack-tip; **b** at the outer crack-tip

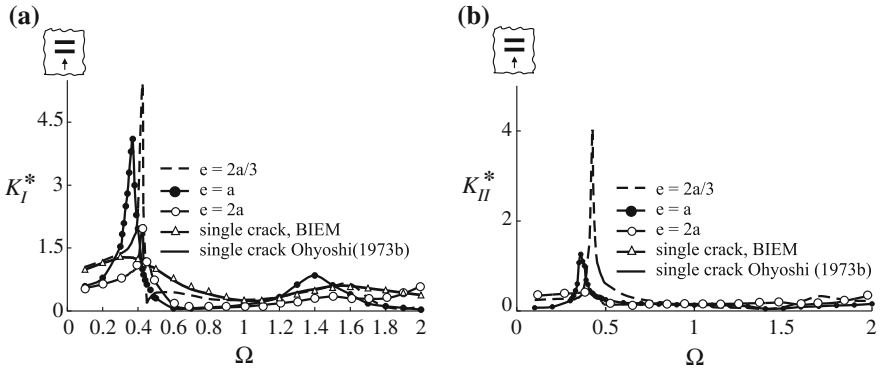

Fig. 8.10 K-factors at crack Γ_1 of two stacked cracks (Fig. 8.2a) in an orthotropic material of "case 6" under normal L-wave: **a** normalized SIF-I; **b** normalized SIF-II

frequency $\Omega = a\omega/c_L = a\omega\sqrt{\rho c_{33}^{-1}}$, which is different from that used in Figs. 8.8 and 8.9.

Results for stacked cracks in a case 6 material subjected to normal incident L-waves are depicted in Fig. 8.10. The peak values of both the mode-I and mode-II SIFs increase with decreasing crack distance. This tendency and the formation of sharp resonance peaks are similar as in the piezoelectric case, see Fig. 8.5. Furthermore, it can be observed that compared with the single crack, the peaks are shifted slightly to higher frequencies. It also should be noted that in case of a single crack no mode-II SIF is present. All these effects are clearly induced by crack interaction.

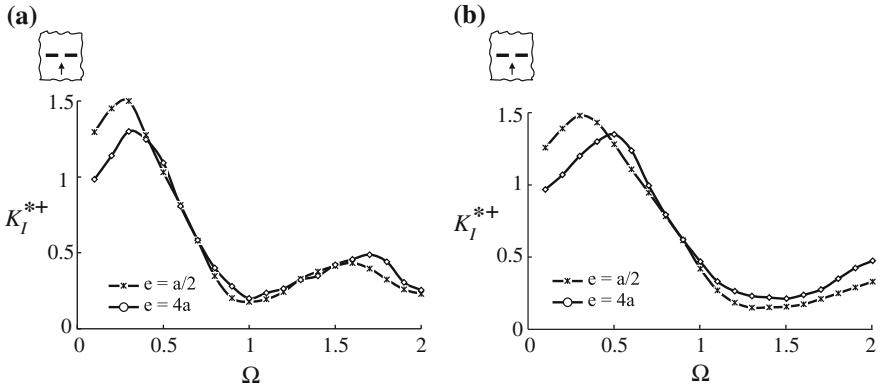

Fig. 8.11 K-factors at two collinear cracks (Fig. 8.2b) under normal L-wave loading: comparison of two different orthotropic materials: **a** material of type "case 6"; **b** material of type "case 7"

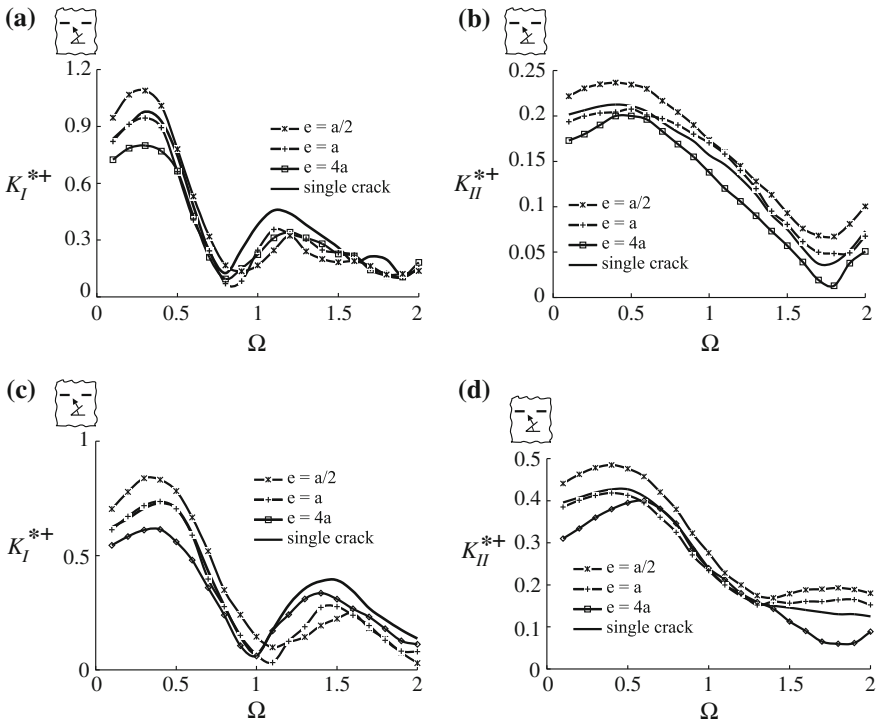

Fig. 8.12 K-factors at two collinear cracks (Fig. 8.2b) in an orthotropic plane under oblique L-wave loading at incident angle $\theta = \pi/4$: **a** and **b** material of type "case 6"; **c** and **d** material of type "case 7"

The dynamic mode-I SIFs versus frequency are plotted for the inner crack tips of collinear cracks under normal incident L-wave loading in Fig. 8.11. Compared are results for two different crack distances and the two different materials: material type "case 6" in Fig. 8.11a and material type "case 7" in Fig. 8.11b. As expected, the peak value increases with decreasing distance for both materials, but the influence of different material parameters is significant. Mentioned in this context shall only be the differences in the shapes of the SIF-curves, in the location of the peaks and their shift to lower frequencies for decreasing distance e. Similar phenomena can be observed in Fig. 8.12, where again results for collinear cracks in two different materials are shown, but now for an oblique L-wave loading under $\theta = \pi/4$. Here the mode-I SIFs for the case-6 material are generally higher than for case-7, while the opposite is true for the mode-II SIFs. Figure 8.12c clearly reveals the frequency character of both the shielding and amplification phenomena. In the frequency interval $\Omega \in [0.1, 1]$ an amplification effect for the shortest crack distance $e = a/2$ is visible, while in the higher frequency interval $\Omega \in [1.2, 2]$ a shielding effect is present.

8.4 Conclusion

2D wave scattering by in-plane impermeable cracks in piezoelectric plane is considered. The solution procedure is based on non-hypersingular traction BIEM. Both the SIFs and the scattered wave field can be evaluated and used for application in dynamic fracture mechanics and non-destructive testing correspondingly. The elastic anisotropic problem is considered as a special uncoupled case of the piezoelectric case. Numerical simulations reveal typical crack interaction phenomena such like amplification and shielding effects. Parametric studies for wave scattering by different crack systems show that the local crack tip fields, expressed by the SIFs, are a complex result of many interacting factors as the crack configuration, material properties, wave type and its characteristics, coupled character of the dynamic load and the crack–crack and wave–crack interaction phenomena.

References

1. Chen ZT, Yu SH (1999) Transient response of a piezoelectric ceramic with two coplanar cracks under electromechanical impact. Acta Mech Sin 15(4):326–333
2. Chen ZT, Worswick MJ (2000) Anti-plane mechanical and inplane electric time-dependent load applied to two coplanar cracks in piezoelectric ceramic material. Theoret Appl Fract Mech 33:173–184
3. Dineva P, Gross D, Rangelov T (2008) Dynamic interaction of cracks in piezoelectric and anisotropic solids: a non-hypersingular BIEM approach. Theoret Appl Mech (Belgrade) 35(1–3):73–91
4. Gao C, Fan W (1999) A general solution for the plane problem in piezoelectric media with collinear cracks. Int J Eng Sci 37:347–363

5. Garcia-Sanchez F (2005) Numerical study of fracture problems in elastic anisotropic and piezoeleztric solids. Ph.D. thesis, Engineering High School, University of Sevilla, Sevilla, Spain
6. Garcia-Sanchez F, Saez A, Dominguez J (2006) Two-dimensional time-harmonic BEM for cracked anisotropic solids. Eng Anal Boundary Elem 30:88–99
7. Han JJ, Chen YH (1999) Multiple parallel cracks interaction problem in piezoelectric ceramics. Int J Solids Struct 36:3375–3390
8. Hankel WG (2002) Multi-cracks problem for piezoelectric materials strip subjected to dynamic loading. Mech Res Commun 29:413–424
9. Itou S (1996) Dynamic stress intensity factors of two collinear cracks in orthptropic medium subjected to time-harmonic disturbance. Theoret Appl Fract Mech 25:155–166
10. Itou S, Haliding H (1997) Dynamic stress intensity factors around two parallel cracks in an infinite-orthptropic plane subjected to incident harmonic stress waves. Int J Solids Struct 34:1145–1165
11. Li XF, Lee KY (2004) Dynamic behaviour of a piezoelectric ceramic layer with two surface cracks. Int J Solids Struct 41:3193–3209
12. Meguid SA, Chen ZT (2001) Transient response of a finite piezoelectric strip containing coplanar insulating cracks under electromechanical impact. Mech Mater 33:85–96
13. MS Visual Studio, Professional Edition (2005). Redmond, Washington
14. Ohyoshi T (1973b) Effect of orthotropy on singular stresses for a finite crack. ASME J Appl Mech 40:491–497
15. Saez A, Garcia-Sanchez F, Dominguez J (2006) Hypersingular BEM for dynamic fracture in 2- D piezoelectric solids. Comput Methods Appl Mech Eng 196:235–246
16. Shindo Y, Ozawa E (1990) Dynamic analysis of a cracked piezoelectric material. In: Hsieh RKT (ed) Mechanical modeling of new electromagnetic materials. Elsevier, Amsterdam, pp 297–304
17. Su RKL, Wemjie F, Jinxi L, Zhenzhu Z (2003) Transient response of coplanar interfacial cracks between two dissimilar piezoelectric strips under anti-plane mechanical and in-plane electrical impacts. Acta Mech Solida Sin 16(4):300–312
18. Sun Y (2003) Multi-interface cracks in a piezoelectric layer bonded to two half-piezoelectric spaces under anti-plane shear loading. Mech Res Commun 30:443–454
19. Sun JL, Zhou ZG, Wang B (2004) Dynamic behaviour of uneaqual parallel permeable interface multi-cracks in a piezoelectric layer bonded to two piezoelectric materials half planes. Eur J Mech A Solids 23:993–1005
20. Wang XD, Meguid SA (1997) Diffraction of SH waves by interacting matrix crack and an inhomogeneity. ASME J Appl Mech 64:568–575
21. Wang XD, Meguid SA (2000a) Effect of electromechanical coupling on the dynamic interaction of cracks in piezoelectric materials. Acta Mech 143:1–15
22. Wang XD, Meguid SA (2000b) Modelling and analysis of the dynamic behaviour of piezoelectric materials containing interfacing cracks. Mech Mater 32:723–737
23. Wang XD (2001) On the dynamic behaviour of interacting interfacial cracks in piezoelectric media. Int J Solids Struct 38:815–831
24. Zhao X, Meguid SA (2002) On the dynamic behavior of a piezoelectric laminate with multiple interfacial collinear cracks. Int J Solids Struct 39:2477–2494
25. Zhou Z, Wang B (2002) The behaviour of two parallel symmetry permeable interface cracks in a piezoelectric layer bonded to two half piezoelectric materials planes. Int J Solids Struct 39:4485–4500
26. Zhou Z, Wang B, Cao M (2003) The behaviour of permeable multi-cracks in a piezoelectric material. Mech Res Commun 30:395–402

Chapter 9
Different Electric Boundary Conditions

Abstract Dynamic SIFs for a straight crack in a piezoelectric material under time-harmonic L- or SV- and SH- wave are determined for different electric boundary conditions. Compared are impermeable, permeable and limited permeable cracks. A parametric study in the frequency domain shows the dependence of the SIFs on the choice of the electrical boundary conditions at the crack faces.

9.1 Introduction

Among other open problems in piezoelectric fracture mechanics, the issue of how to impose the electric boundary conditions along the crack faces is a controversial one. The difficulty arises from the fact that there are not yet sufficient experimental data available, which clarify the detailed conditions at the crack faces and within the open crack. Therefore, in many cases idealized electrical boundary conditions along the crack faces are employed.

Special interest has been devoted in the last decade to a realistic modeling of the dielectric medium inside the crack because its properties influence the electro-mechanical fields around the crack tip. Depending on the ratio between the dielectric permittivities of the medium inside the open crack ε_{cr} and of the piezoelectric solid ε, two extreme cases can be distinguished. The *impermeable crack* is obtained for the limiting case $\varepsilon_{cr}/\varepsilon = 0$, which leads to zero surface charges or mechanically and electrically to traction free boundary conditions, respectively. In contrast, completely *permeable crack* conditions are attained for $\varepsilon_{cr}/\varepsilon \to \infty$. In this case the crack is not "visible" for the electric field, i.e. the crack faces are mechanically traction free, while the electrical displacement has no jump across the crack.

Impermeable boundary conditions along the crack faces are given by $D_n^+ = D_n^- = 0$ with the consequence $\triangle\Phi = \Phi^+ - \Phi^- \neq 0$ on S_{cr}. Here $D^{\pm}$, $\Phi^{\pm}$ and $S_{cr} = S_{cr}^+ \cup S_{cr}^-$ are the normal component of the electrical displacement, the electrical potential and the crack boundary, respectively. The impermeable assumption is based

P. Dineva et al., *Dynamic Fracture of Piezoelectric Materials*,
Solid Mechanics and Its Applications 212, DOI: 10.1007/978-3-319-03961-9_9,

on the fact that the permittivity of piezoceramics is three orders higher than that of air or vacuum inside the crack. This type of ideal electrical condition is extensively used in the literature. Deeg [2] first introduced the impermeable crack model. It became popular in the early 1990s, see Pak [14, 15], Park [16], Park and Sun [17], Sosa [24], Suo et al. [25], Wang [26], Zhu [33]. They found that solutions based on the impermeable crack assumption can be applied with a reasonable degree of confidence to the fracture prediction of PEM, see Wang and Mai [27]. Based on the impermeable crack assumption Fulton and Gao [4], Wang and Mai [28], Wang et al. [29], predicted qualitatively the failure strength of a piezoelectric material under combined electric-mechanical load. However, it is clear that the impermeable condition physically is not fully correct because a non-zero value of the electric displacement is present even if the dielectric constant of the crack's interior is much smaller than the dielectric constant around it.

The permeable crack model assumes that the crack does not perturb the electrical fields directly, i.e. there is no potential jump $\Phi^+ = \Phi^-$ on S_{cr} with the consequence $D_n^+ = D_n^- \neq 0$. This implies that the crack electrically is treated as if it remains closed in its undeformed configuration. This model was used by Parton [18] and later by McMeeking [10, 12], Ou and Chen [13], Shindo and Ozawa [21], Shindo et al. [22]. They concluded that physically the permeable crack model is more adequate than the impermeable one, since the crack opening in piezoelectric materials is always very small and the electric field could generally permeate the interior without substantial change. On the other hand Wan et al. [29], Wang and Meguid [31] pointed out some disadvantages of the permeable crack model. Their numerical results showed that for the permeable crack model, the applied electric loads would contribute nothing to the fracture load what contradicts available experimental observations.

McMeeking [11] compared both the impermeable and permeable models by calculating the static electroelastic field in a 2D isotropic dielectric body with dielectric constant ε_m, containing a flat elliptic flaw with a dielectric constant ε_{cr} and a semi-axes ratio $b/a \ll 1$. He concluded that the impermeable crack solution is good as long as $(\varepsilon_{cr}/\varepsilon_m) < 0.1(b/a)$, while for $(b/a) \approx (\varepsilon_{cr}/\varepsilon_m)$ the permeable crack solution is better. Thus the question of whether the impermeable or permeable model should be applied would be decided on a case-by-case basis.

Since both idealized models have their drawbacks, the real situation is better described by taking into account the electric field inside the crack and the electric jump across the crack faces. When the crack is deformed, the thickness of the dielectric medium filling the crack changes will influence the overall dielectric property of the crack. As a result, the electric boundary conditions along the crack surfaces will be deformation-dependent. Among others, Hao and shen [7], Wang and Mai [28], Wang and Jiang [30] proposed simplified deformation dependent electrical boundary condition. Kuna [8] used this approximation for the solution of 2D and 3D static and dynamic crack problems by the finite element method. The model which first has been introduced by Parton and Kudryavtsev [19] can be formulated as $D_n^+ = D_n^- = D_{cr}$ and $D_{cr}(u_n^+ - u_n^-) = \varepsilon_{cr}(\Phi^+ - \Phi^-)$ on S_{cr}. These relations are based on the analogy with a slit capacitor filled by a medium with a prescribed permittivity. As limiting cases for $\varepsilon_{cr} \to 0$ and $\varepsilon_{cr} \to \infty$ they include the impermeable and permeable

crack, respectively. The *limited permeable* condition is deformation dependent and, therefore leads to solution of nonlinear problem.

Calculating the jump of the normal displacements $\triangle u_n$ and electric potential $\triangle \Phi$ for a given external load, the electrical displacement D_{cr} is determined according to the condition for limited permeable crack. Since $\triangle u_n$ and $\triangle \Phi$ themselves depend on D_{cr}, an equilibrium of the three fields must be sought iteratively. Wippler et al. [32] described the correct implementation of the "capacitor analogy" and found by finite element calculations that this approach reflects the real situation very well. Recently Landis [9] formulated energetically consistent boundary conditions, in which also the mechanical traction at the crack faces are directly coupled with the electrical field. This consequently leads to the solution of a nonlinear problem. Although the physically correct boundary conditions are still an issue of debate, the capacitor analogy qualitatively seems to reflect the most essential properties along the crack faces.

Almost all available solutions of crack problems with different type of boundary condition are for static problems. Here a BIEM solution for crack problems is presented using the permeable or limited permeable electrical boundary conditions. Time-harmonic problems of anti-plane cracks have been solved in the past only for impermeable and permeable cracks. For in–plane permeable cracks there are papers concerning transient dynamic problems, see Shindo et al. [23] and for permeable and limited permeable cracks, see Enderlein et al. [3]. But there are no results for time–harmonic wave scattering by permeable or limited permeable in-plane cracks.

The chapter follows Rangelov et al. [20] and its main aim is to discuss, based on an BIEM formulation, the influence of the impermeable, permeable and limited permeable assumptions on the SIFs of in-plane and anti-plane cracks loaded by time-harmonic plane waves.

9.2 Formulation of the Problem

Poled synthetic piezoelectric materials as e.g. barium titanate $BaTiO_3$ or lead zirconate titanate PZT are transversely-isotropic with the material symmetry axis in poling direction. Consider a rectangular Cartesian coordinate system $Ox_1x_2x_3$ and assume that the poling direction is along the Ox_3 -axis and the plane Ox_1x_2 is the isotropic plane. The electromechanical interaction depends strongly on the orientation of the crack $S_{cr} = S_{cr}^{+} \bigcup S_{cr}^{-}$ and the type of the wave loading, see Fig. 9.1.

Let us consider the in–plane crack subjected to a plane time-harmonic incident L- or SV- wave and the anti–plane crack under SH-wave. The wave incident angle with respect to the Ox_1 -axis is denoted by θ. Furthermore, it is assumed that all field quantities are harmonic with frequency ω, which allows to omit the common time function $e^{i\omega t}$. This is correct in the limiting cases of a permeable or an impermeable crack, when the boundary value problem is linear. In the case of a limited permeable crack, when the boundary value problem becomes nonlinear, this is an approximation. Since the problem in any case remains time-periodic with a periodicity given by

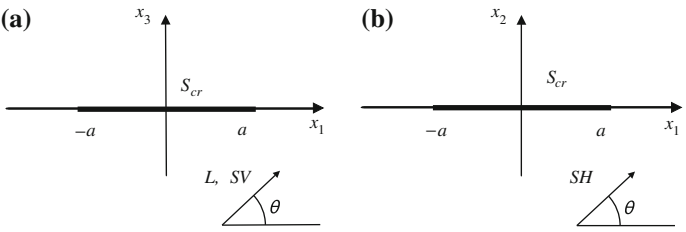

Fig. 9.1 Crack under incident plane wave: **a** in-plane; **b** anti-plane

frequency ω, the approximation by a time-harmonic function is acceptable as it simplifies the problem considerably.

According to Fig. 9.1 the analysis is carried out for two plane problems. In the in-plane case the non-zero field quantities are the displacements u_1, u_3, stresses σ_{11}, σ_{33}, σ_{13}, electrical displacements D_1, D_3, electrical field components E_1, E_3 and electric potential Φ which depend on x_1, x_3. In contrast, the non-zero quantities in the anti-plane case are the displacement u_3, stresses σ_{13}, σ_{23}, electrical displacements D_1, D_2, electrical field components E_1, E_2 and electrical potential Φ which now depend on x_1, x_2. The field equations and boundary conditions for both cases will be formulated separately following Sect. 2.6, where BVPs are formulated only for impermeable and for permeable boundary conditions.

9.2.1 In-plane Crack Problem

The mechanical and electrical balance equation for time-harmonic processes in absence of body forces and electric charges can be written in the compact form, see Chap. 2.

$$\sigma_{iJ,i} + \rho_{JK}\omega^2 u_K = 0, \qquad \rho_{JK} = \begin{cases} \rho, & J, K = 1, 3 \\ 0, & J = 4 \text{ or } K = 4 \end{cases} \tag{9.1}$$

where $u_K = (u_1, u_3, \phi)$ is the generalized displacement, $J, K = 1, 3, 4$, σ_{iJ} is the generalized stress, $\sigma_{iJ} = C_{iJKl}u_{K,l} = C_{iJKl}s_{Kl}$, see Sect. 2.5.1. The generalized traction vector is $t_J = \sigma_{iJ}n_i$, where n_i is the unit normal vector on S_{cr}^+. The strain–displacement and electric field–potential relations are $s_{ij} = \frac{1}{2}(u_{i,j}+u_{j,i})$, $E_i = -\phi_{,i}$ where s_{ij}, ϕ are the strain tensor and electric potential and ρ is the mass density.

The interaction of an incident wave with the crack induces scattered waves. The total wave field at a given field point $x = (x_1, x_3)$ can be written as a sum of the incident (in) and the scattered (sc) wave field, which both must fulfill the field Eq. (9.1). The decomposition

$$u_J(x, \omega) = u_J^{in}(x, \omega) + u_J^{sc}(x, \omega) \tag{9.2}$$

for the generalized displacement holds analogously for all field quantities. The incident wave is known, while the scattered wave field has to be determined such that Sommerfeld's radiation condition at infinity and the boundary conditions along the crack are fulfilled. The latter are discussed in what follows.

9.2.1.1 Impermeable Crack

In this case the crack is free of mechanical tractions and surface charges, i.e.

$$t_J = t_J^{in} + t_J^{sc} = 0 \quad \text{or} \quad t_J^{sc} = -t_J^{in} \ \text{ on } \ S_{cr}, \tag{9.3}$$

where $t_J = \sigma_{Ji} n_i = (t_1, t_3, D_n)$ is the generalized traction vector and n_i is the unit normal vector on Γ. Furthermore, t_J^{in}, t_J^{sc}, t_J^{cr} are the traction of the incident wave field, the scattered wave field and the traction field inside the crack, respectively.

9.2.1.2 Permeable Crack

The permeable crack is free of mechanical traction, but continuity of the electrical potential and the normal component of the electrical displacement are assumed:

$$t_1 = t_3 = 0, \quad \triangle\Phi = 0, \quad D_n^+ = D_n^- = D_n^{cr} \ \text{ on } \ S_{cr}. \tag{9.4}$$

Here D_n^{cr} is the normal component of the electrical displacement inside the crack and $D_n^{sc} = D_n^{cr} - D_n^{in}$ since $D_n^{in} + D_n^{sc} = D_n^{cr}$ on S_{cr}. Therefore, the boundary condition on S_{cr} can be written as

$$t_J^{sc} = -t_J^{in}, \quad J = 1, 3, \qquad t_4^{sc} = D^{cr} - t_4^{in}. \tag{9.5}$$

9.2.1.3 Limited Permeable Crack

The crack faces again are free of mechanical traction and for the electrical part the "capacitor analogy" is applied, see Wippler et al. [32]. In this model, using the potential jump $\Delta\Phi = \Phi^+ - \Phi^-$ and the crack opening in normal direction $\Delta u_n = u_n^+ - u_n^-$, the electric field inside the crack is expressed by $E_n = -\Delta\Phi/\Delta u_n$. For the electric displacement this leads to

$$D_n^{cr} = \varepsilon_{cr} E_n = -\varepsilon_{cr}(\triangle\Phi/\triangle u_n) \ \text{ on } \ S_{cr}, \tag{9.6}$$

where ε_{cr} is the dielectric constant of the medium inside the crack. As the normal component of the scattered electrical displacement is $D_n^{sc} = -D_n^{in} + D_n^{cr} = -D_n^{in} - \varepsilon_{cr}(\triangle\Phi/\triangle u_n)$ because of $D_n^{in} + D_n^{sc} = D_n^{cr}$ on S_{cr}, the boundary condition takes the form

$$t_J^{sc} = -t_J^{in}, \quad J = 1, 3, \qquad t_4^{sc} = -t_4^{in} - \varepsilon_{cr}(\triangle\Phi/\triangle u_n). \tag{9.7}$$

Because it contains the initially unknown potential and displacement jumps, the problem in this case becomes nonlinear and the solution has to be sought iteratively.

9.2.2 Anti-plane Crack Problem

In this case the balance equations in absence of body forces and electric charges are given by

$$\sigma_{iJ,i} + \rho_{JK}\omega^2 u_K = 0, \qquad \rho_{JK} = \begin{cases} \rho, & J = K = 3 \\ 0, & J = 4 \text{ or } K = 4 \end{cases} \tag{9.8}$$

where $u_K = (u_3, \phi)$ is the generalized displacement, $J, K = 3, 4$, σ_{iJ} is the generalized stress, $\sigma_{iJ} = C_{iJKl}u_{K,l} = C_{iJKl}s_{Kl}$, see Sect. 2.5.1. The generalized traction vector is $t_J = \sigma_{iJ}n_i$, where n_i is the unit normal vector on S_{cr}^+. The strain–displacement and electric field–potential relations are $s_{ij} = \frac{1}{2}(u_{i,j} + u_{j,i})$, $E_i = -\phi_{,i}$ where s_{ij}, ϕ are the strain tensor and electric potential and ρ is the mass density.

The boundary conditions for the anti-plane crack are formulated in analogy to the in-plane case. In this context it shall be noted that the anti-plane case shall only be considered as a model case, whose physical relevance is doubtful.

9.2.2.1 Impermeable Crack

$$t_J^{sc} = -t_J^{in}, \quad J = 3, 4. \tag{9.9}$$

9.2.2.2 Permeable Crack

$$t_3^{sc} = -t_3^{in}, \quad t_4^{sc} = D^{cr} - t_4^{in}. \tag{9.10}$$

9.2.2.3 Limited Permeable Crack

$$t_3^{sc} = -t_3^{in}, \quad t_4^{sc} = -t_4^{in} - \varepsilon_{cr}(\triangle\Phi/\triangle u_n). \tag{9.11}$$

9.3 Numerical Realization

For the numerical solution of the formulated BVPs we will use the non-hypersingular traction BIE, see Sect. 4.2

$$
\begin{aligned}
t_J^{sc}(x) = -C_{iJKl} n_i(x) \int_{S_{cr}^+} \Big[& (\sigma^*_{\eta PK}(x,\xi)\Delta u_{P,\eta}(\xi) \\
& - \rho_{QP}\omega^2 u^*_{QK}(x,\xi)\Delta u_P(\xi))\delta_{\lambda l} \\
& - \sigma^*_{\lambda PK}(x,\xi)\Delta u_{P,l}(\xi)\Big] n_\lambda(\xi) dS, \quad x \in S_{cr}.
\end{aligned}
\tag{9.12}
$$

Here $\Delta u_J = u_J|_{S_{cr}^+} - u_J|_{S_{cr}^-}$ is the generalized COD along the crack S_{cr}, $n_i(x)$ and $n_\lambda(\xi)$ are the outward normal vectors on S_{cr}^+ at the observation point x and the collocation point ξ, respectively. The quantity u^*_{KQ} is the fundamental solutions, see Eqs. (3.83)–(3.87) for the in-plane case and Eq. (3.43) for the anti-plane case, respectively, and $\sigma^*_{iJQ} = C_{iJKl} u^*_{KQ,l}$ is the associated stresses. Finally, the left hand side of Eq. (9.12) is prescribed by the boundary conditions.

The solution of the integro-differential Eq. (9.12) is described in Sect. 4.3 for impermeable and permeable boundary conditions, see also Chaps. 6, 7, 8 for numerical results. The limited permeable case needs more explanations. In this case the electric field inside the crack is affected by the crack profile. Thus, a nonlinear analysis is required to determine the fields associated with the deformed crack. Following the lines of Balke et al. [1], Govorukhla and Kamlah [5], Gruebner [6] an iteration scheme is used for this purpose. The iteration scheme $(D_n^{cr})_{(k+1)} = -\varepsilon_{cr}(\triangle\Phi/\triangle u_n)_{(k)}$ starts with an impermeable crack, i.e. $(D_n^{cr})_{(0)} = 0$ and determines in the zero step a solution for the crack opening displacement. Using this COD the electrical displacement for the first iteration step is calculated next: $(D_n^{cr})_{(1)} = -\varepsilon_{cr}(\triangle\Phi/\triangle u_n)_{(0)}$. The scheme continues with the usage of $(D_n^{cr})_{(1)}$ in order to find the solution for the generalized COD $(\triangle u_J)_{(1)}$ and so forth. The iteration process stops when a prescribed accuracy is achieved. Here, for the in-plane case, the condition

$$
\max\left[\sum_{l=1}^{N} \frac{|\Delta(u_n^l)_{(k)} - \Delta(u_n^l)_{(k+1)}|}{|\Delta(u_n^l)_{(k)}|}, \sum_{l=1}^{N} \frac{|\Delta(\Phi^l)_{(k)} - \Delta(\Phi^l)_{(k+1)}|}{|\Delta(\Phi^l)_{(k)}|}\right] \leq 0.01,
\tag{9.13}
$$

has been chosen where N is the number of the boundary nodes and k the number of iterations. The analogous procedure is applied for anti-plane crack problem. It is obvious that the number of necessary iterations depends on the permittivity of the medium inside the crack.

9.4 Numerical Results

We consider a straight crack of length $2a = 10\,\text{mm}$, which lies on the x_1-axis in the interval $(-a, a)$ under normally incident wave loading. The crack is discretized into seven boundary elements, where the first and the last element are QP-crack tip

elements of length $l_{QP} = 0.15a$. The properties of the piezoelectric materials are given in Table 4.1.

The SIFs are obtained directly from the traction nodal values ahead of the crack-tip according to Eq. (2.40) for the in-plane case and Eq. (2.41) for the anti-plane case. For a straight crack of length $2a$ the relations read for in-plane case

$$\begin{aligned} K_I &= \lim_{x_1 \to \pm a} t_3 \sqrt{2\pi(x_1 \mp a)}, \quad K_{II} = \lim_{x_1 \to \pm a} t_1 \sqrt{2\pi(x_1 \mp a)}, \\ K_D &= \lim_{x_1 \to \pm a} t_4 \sqrt{2\pi(x_1 \mp a)}, \quad K_E = \lim_{x_1 \to \pm a} E_3 \sqrt{2\pi(x_1 \mp a)}, \end{aligned} \tag{9.14}$$

and for anti-plane case

$$K_{III} = \lim_{x_1 \to \pm a} t_3 \sqrt{2\pi(x_1 \mp a)}, \quad K_D = \lim_{x_1 \to \pm a} t_4 \sqrt{2\pi(x_1 \mp a)}, \tag{9.15}$$

where t_J is the traction at the point $(x_1, 0)$ close to the crack-tip.

As usual it is useful to normalize the stress intensity factors and the frequency. This is done in the in-plane case for the mechanical SIFs in Eq. (9.14) K_I and K_{II} through the normalization coefficient $\overline{k} = t_3^{in}\sqrt{\pi a} = \omega[(c_{33} + e_{33}^2/\varepsilon_{33})\rho]^{1/2}\sqrt{\pi a}$ and are denoted by K_I^* and K_{II}^* respectively. The associated normalized electrical stress intensity factors are given by $K_E^* = |e_{33}\overline{k}^{-1} K_E|$ and $K_D^* = |(e_{33}/\varepsilon_{33})\overline{k}^{-1} K_D|$, while the normalized frequency is defined as $\Omega = a\omega\sqrt{\rho c_{44}^{-1}}$. In the anti–plane case the dynamic SIFs K_{III} and K_D in Eq. (9.15) are normalized by the terms $\tau\sqrt{\pi a}$ and $\tau(\varepsilon_{11}/e_{15}\sqrt{\pi a})$ and denoted by K_{III}^* and K_D^* respectively. The wave number and the shear stress amplitude of the incident SH-wave are given by $k = \omega[(c_{44} + e_{15}^2/\varepsilon_{11})^{-1}\rho]^{1/2}$ and $\tau = (c_{44} + e_{15}^2/\varepsilon_{11})k$, respectively.

First, the in–plane case is considered, where the crack is subjected to normal incident L-wave and/or an additional electrical load. The mechanical part is given by $t_3 = t_3^{in}$ with $t_3 = \sigma_0 = 5\,\text{MPa}$, while the electrical part is prescribed by $t_4 = D_3 = s\, t_3^{in}(\varepsilon_{33}/e_{33})$ with $D_3 = D_0 = 0.01\text{C/m}^2$. The parameter s is a loading parameter, which in case of a combined loading is chosen as $s = 0.5, 1.0, 2.0$. For a pure mechanical load s is zero and a pure electrical load is characterized by $s = 1$ and $t_3 = 0$. For limited permeable cracks relative permittivities of $\varepsilon_r = 10, 30, 50$ have been chosen.

Figure 9.2 shows the normalized K_I^* factor versus normalized frequency Ω for different electrical boundary conditions, different materials and different loading. For a pure mechanical load ($s = 0$) K_I^* starts at $\Omega = 0$ with $K_I^* = 1$ (the statical value), increases slightly with increasing frequency and shows a maximum in some cases (dynamic overshoot). It is interesting to note that for all three materials the limited permeable crack shows a somewhat higher response than the other electrical boundary conditions. For the pure electrical load K_I^* staring from zero increases considerably with frequency Ω.

The dependence of the K_I^* versus frequency Ω curves on the load factor s, for combined electromechanical loading is displayed in Fig. 9.3. For the impermeable

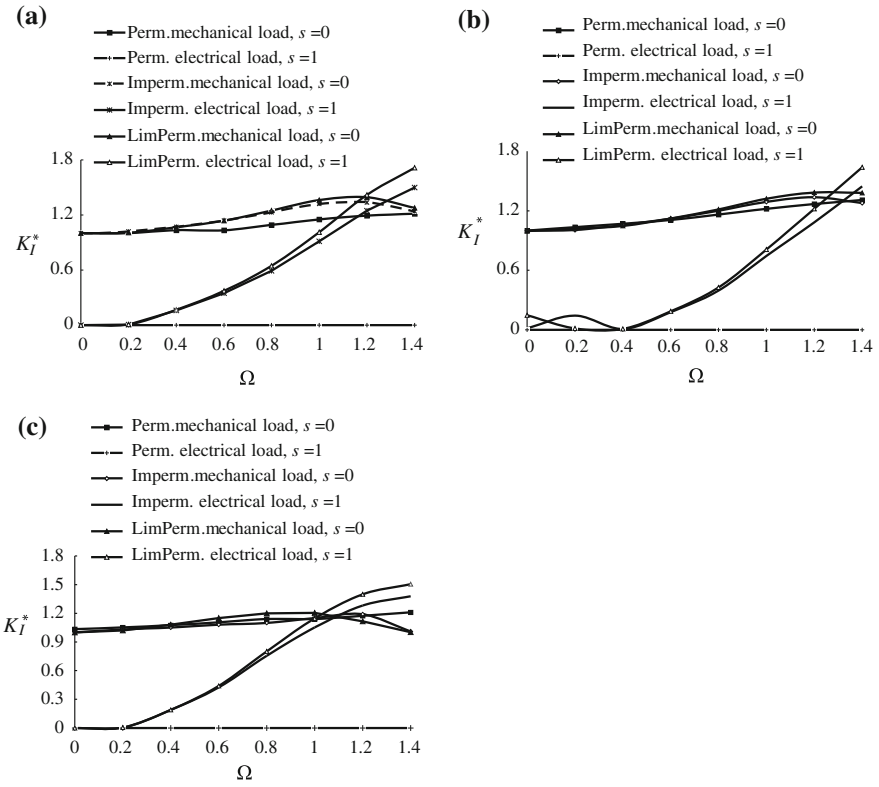

Fig. 9.2 Normalized SIF-I for different type of load and different electrical boundary conditions: **a** PZT 5H; **b** PZT 4; **c** $BaTiO_3$

and the limited permeable crack K_I^* increases with s, where the limited permeable crack shows higher effects. Only for the permeable crack the response is independent of s because the crack is not visible for the electric field. That the normalized electric SIF K_D^* for a permeable and an impermeable crack is independent on the frequency can be seen from Fig. 9.4. Since the electric field does not see a permeable crack, $K_D^* = 0$ for a pure electrical loading. For a mixed electromechanical load such a crack sees only the mechanical part, so that K_D^* is independent on the load factor s. For the impermeable crack K_D^* increases with the load factor s, but is still independent on Ω.

The influence of the relative permittivity of the medium inside the crack on the frequency dependent curves of K_I^* and K_E^* is shown in Fig. 9.5. For frequencies $\Omega < 0.8$, the permeable and impermeable boundary conditions form a lower and upper bound. In between, K_I^* increases with decreasing ε_r. The opposite tendency in the entire frequency range can be observed for K_E^*.

Results for the anti-plane case are depicted in Figs. 9.6 and 9.7. Figure 9.6 shows the dependence of K_{III}^* on the boundary conditions for a pure mechanical and a pure

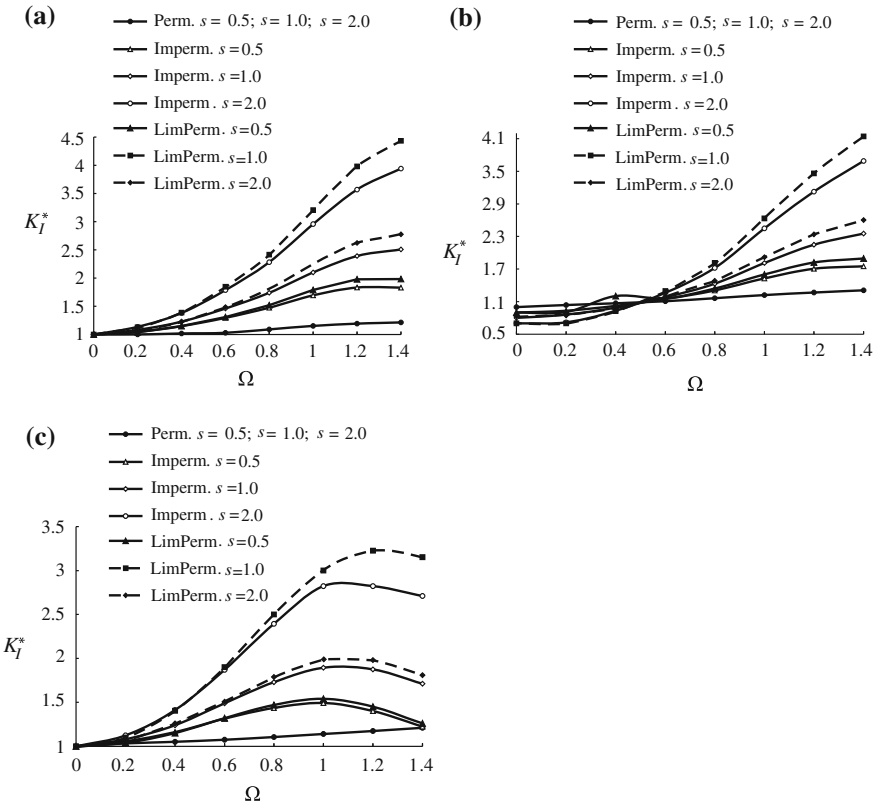

Fig. 9.3 Normalized SIF-I for different types of electromechanical loads and different electrical boundary conditions: **a** PZT 5H; **b** PZT 4; **c** $BaTiO_3$

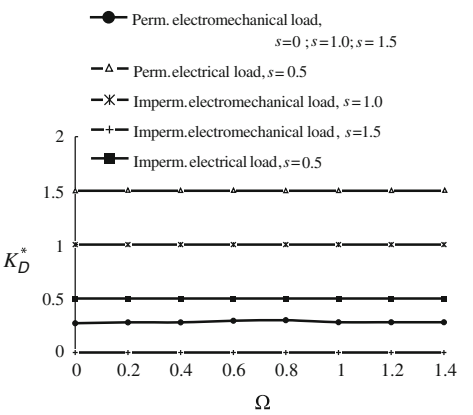

Fig. 9.4 Normalized SIF-D for different types of electromechanical loading and different electrical boundary conditions

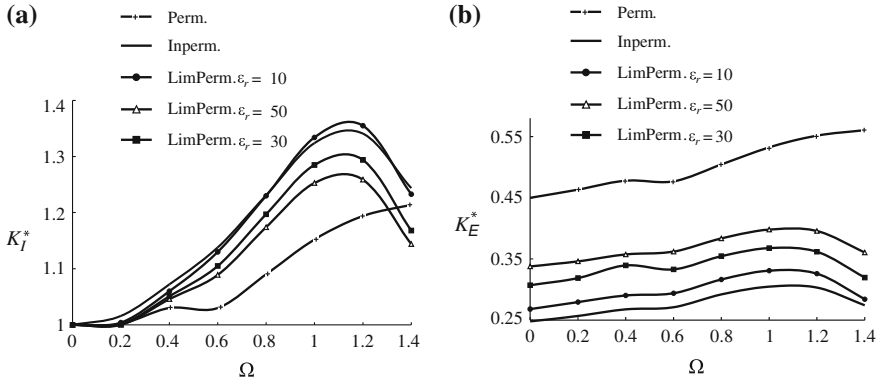

Fig. 9.5 The influence of the permeability of the crack on K_I^* and K_E^*

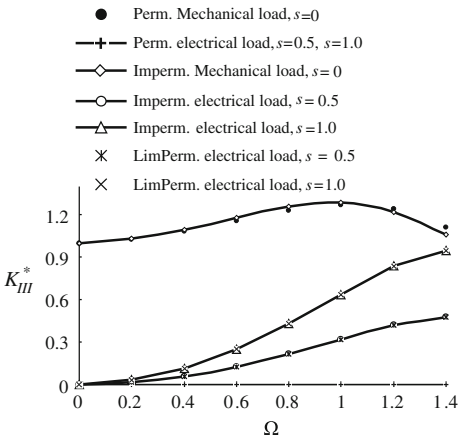

Fig. 9.6 K_{III}^* versus Ω for pure mechanical or electrical loading

electrical load. It is interesting to note that for the pure electrical load the limited permeable case delivers practically the same results as the impermeable case. For such a load, a permeable crack again is invisible.

The frequency dependent curve of the stress intensity factor K_{III}^* is sensitive also to the load factor s of the electromechanical loading and the type of the boundary conditions, see Fig. 9.7. As can be expected, except for the permeable case, K_{III}^* increases with increasing load factor.

In summary the following conclusions can be drawn from the results:

- SIFs obtained for the permeable crack do not depend on the amplitude of the applied electrical load, while SIFs obtained for impermeable and limited permeable crack are sensitive to the amplitude of the applied electrical load, see Figs. 9.3 and 9.7.

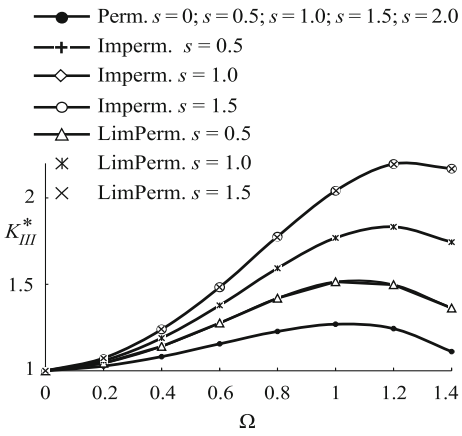

Fig. 9.7 K^*_{III} versus Ω in dependence of s and the electrical boundary conditions

- The applied electrical displacement results in additional deformation, which may significantly affect the stress concentration near the crack-tip. This effect appears only at impermeable and limited permeable cracks.
- The results obtained for the limited permeable crack are more close to the solutions for an impermeable crack. It is worth to note that the differences between both models increase with increasing of the applied electrical load, see Fig. 9.3. This figure also shows that the SIFs for impermeable and limited permeable cracks depend on the applied electrical load in a different way.
- There is an influence of the crack permeability on SIFs K^*_I and K^*_E, see Fig. 9.5. It shows that higher values of crack permittivity lead to an increase of the electrical SIF K^*_E, approaching the results of the permeable crack. Consequently, the dielectric properties of the media inside the crack have an influence on the SIF solutions. Numerical results prove the physical picture that the impermeable and permeable assumptions are two extreme cases of the real situation represented by the limited permeable crack model.
- In the case of pure mechanical load the impermeable crack shows zero electrical displacement SIF K^*_D, while permeable and limited‘permeable cracks have nonzero SIFs K^*_I and K^*_D. In the case of pure electrical load impermeable and limited permeable cracks have nonzero SIFs, while a permeable crack shows zero SIFs.
- The material properties of different PEM have a considerable influence on the SIFs, independent on the used boundary conditions.
- The frequency and the amplitude of the applied electromechanical load have a significant influence on the SIFs. The electrical SIF K^*_D is independent of the frequency and of the applied stress amplitude. It depends only on the applied electrical displacement.

9.5 Concluding Remarks

The present chapter focuses on the influence of the boundary conditions on the dynamic stress intensity factors for in-plane and anti-plane cracks under time-harmonic loading. Compared are the ideal impermeable and permeable electrical boundary conditions with the more realistic deformation dependent electrical boundary condition. The parametric study illustrates that significant differences can occur, when using different boundary conditions.

References

1. Balke H, Kemmer G, Drescher J (1997) Some remarks on fracture mechanics of piezoelectric solids. In: Michel B, Winkler T (eds) Proceedings of the micro materials conference, pp 398–401
2. Deeg WF (1980) The analysis of dislocation, cracks and inclusion problems in piezoelectric solids. Ph.D. thesis, Stanford University, Stanford, California
3. Enderlein M, Ricoeur A, Kuna M (2005) Finite element technique for dynamic crack analysis in piezoelectrics. Int J Fract 134:191–208
4. Fulton CC, Gao H (2001) Effect of local polarization switching on piezoelectric fracture. J Mech Phys Solids 49:927–952
5. Govorukhla V, Kamlah M (2005) Investigation of an interface crack with a contact zone in a piezoelectric bimatirial under limited permeable electric boundary conditions. Acta Mech 178:85–99
6. Gruebner O, Kamlah M, Munz D (2003) Finite element analysis of cracks in piezoelectric materials taking into account the permittivity of the crack medium. Eng Fract Mech 70:1399–1413
7. Hao TH, Shen ZY (1994) A new electric boundary condition of electric fracture mechanics and its applications. Eng Fract Mech 47:793–802
8. Kuna M (2006) Finite element analyses of cracks in piezoelectric structures: a survey. Arch Appl Mech 76:725–745
9. Landis CM (2004) Energetically consistent boundary conditions for electromechanical fracture. Int J Solids Struct 41:6241–6315
10. McMeeking RM (1989) Electrostrictive stresses near crack-like flaws. J Appl Math Phys 40:615–627
11. McMeeking RM (1999) Crack tip energy relase rate for a piezoelectric compact tension specimen. Eng Fract Mech 64:217–244
12. McMeeking RM (2004) The energy release rate for a Griffith crack in a piezoelectric material. Eng Fract Mech 71:1149–1163
13. Ou ZS, Chen ZH (2003) Discussion of the crack faces electric boundary condition in piezoelectric fracture mechanics. Int J Fract 123:L151–L155
14. Pak YE (1990) Crack extension force in a piezoelectric material. ASME J Appl Mech 57:647–653
15. Pak YE (1992b) Linear electro-elastic fracture mechanics of piezoelectric materials. Int J Fract 54:79–100
16. Park SB (1994) Fracture behaviour of piezoelectric materials. Ph.D. thesis, Purdue University, Purdue, USA
17. Park SB, Sun CT (1995) Effect of electric field on fracture of piezoelectric ceramics. Int J Fract 70(3):203–216
18. Parton VZ (1976) Fracture Mechanics of piezoelectric materials. Acta Astronautica 3:671–683

19. Parton VZ, Kudryavtsev BA (1988) Electromagnetoelasticity. Gordon and Breach Sci. Publ, New York
20. Rangelov T, Dineva P, Gross D (2010) On the influence of electric boundary conditions on dynamic SIFs in piezoelectric materials. Arch Apl Mech 80:985–996
21. Shindo Y, Ozawa E (1990) Dynamic analysis of a cracked piezoelectric material. In: Hsieh RKT (ed) Mechanical modeling of new electromagnetic materials, pp 297–304
22. Shindo Y, Ozawa E, Nowacki J (1990) Singular stress and electric fields of a cracked piezoelectric strip. Int J Appl Elect Mech 1:77–87
23. Shindo Y, Narita F, Ozawa E (1999) Impact response of a finite crack in an orthotropic piezoelectric ceramic. Acta Mech 137:99–107
24. Sosa H (1992) On the fracture mechanics of piezoelectric solids. Int J Solids Str 29:2613–2622
25. Suo Z, Kuo C, Barnett D, Willis J (1992) Fracture mechanics for piezoelectric ceramics. J Mech Phys Solids 40:739–765
26. Wang BL (1992) Three-dimensional analysis on an ellipsoidal inclusion in a piezoelectric material. Int J Solids Struct 29:293–308
27. Wang BL, Mai YW (2002) A piezoelectric material strip with a crack perpendicular to its boundary surfaces. Int J Solids Struct 39:4501–4524
28. Wang BL, Mai YW (2003) On the electrical boundary conditions on the crack surfaces in piezoelectric ceramics. Int J Solids Struct 41:633–652
29. Wang BL, Han JC, Du SY (2000) New considerations for the fracture of piezoelectric materials under electromechanical loading. Mech Res Commun 27:435–444
30. Wang XD, Jiang LY (2002) Fracture behaviour of cracks in piezoelectric media with electromechanically coupled boundary conditions. Proc Royal Soc London A458:2545–2560
31. Wang XD, Meguid SA (2000a) Effect of electromechanical coupling on the dynamic interaction of cracks in piezoelectric materials. Acta Mech 143:1–15
32. Wippler K, Recoeur A, Kuna M (2004) Towards the computation of electrically permeable cracks in piezoelectrics. Eng Fract Mech 71:2567–2587
33. Zhu H (1992) A method to evaluate three-dimanesional time-harmonic elastodynamic Green's function in transversely isotropic media. ASME. J Appl Mech 59:587–590

Part III
Functionally Graded PEM

Part III addresses the dynamic behavior of 2D functionally graded piezoelectric infinite and finite solids with cracks (Chaps. 10–13) and/or holes (Chaps. 14, 15) subjected to time-harmonic horizontally polarized shear waves, longitudinal waves, and vertically polarized shear waves. The computational tool is a non-hypersingular traction BIEM based on fundamental solutions derived in a closed form by Radon transform for a restricted class of inhomogeneous materials. All stages of work, presented by the BIEM modeling, the numerical solution scheme as well its validation, and a considerable number of simulations are discussed.

Chapter 10
In-plane Crack Problems in Functionally Graded Piezoelectric Solids

Abstract In-plane crack analysis of functionally graded piezoelectric solids under time-harmonic loading is performed by using a non-hypersingular traction BIEM. The material parameters are assumed to vary quadratically with both spatial variables. Numerical results for the SIFs are discussed for different examples. Investigated are the effects of the inhomogeneity parameters, the frequency of the applied electromechanical load and the geometry of the crack scenario on the K-factors.

10.1 Introduction

Piezoelectric functionally graded materials are composites with continuously varying properties that have significant advantages over discretely layered materials. The most used piezoelectric devices as bimorphs and monomorphs usually consist of two long and thin piezoelectric elements, which are bonded along their long faces by adhesive epoxy resin, and suitable covered with electrodes. The well-known drawback is that the bonding agent may crack during the fabrication process or in-service loading conditions. The advantage of using devices made of FGMs or its usage as a transit layer instead of the bonding agent is that failure from internal debonding or from stress peaks in conventional bimorphs can be avoided. The gradual variation of material properties in piezoelectric is quite effective to decrease the thermal and residual stresses and to increase the bonding strength and toughness. In principle, by controlling the material gradation during the manufacturing process, the desired electromechanical response may be attained. The special feature of graded spatial compositions provides some freedom in the design of novel smart structures.

On the other hand, FGMs are challenging regarding modeling and numerical simulation of their inhomogeneous structure. The mathematical background of models describing the mechanical behavior of these materials involves the solution of partial differential equations with spatially varying coefficients. The number of works devoted to dynamically loaded cracks in inhomogeneous piezoelectric materials is

P. Dineva et al., *Dynamic Fracture of Piezoelectric Materials*,
Solid Mechanics and Its Applications 212, DOI: 10.1007/978-3-319-03961-9_10,

rather small. Most of them are focused on the anti-plane case, see Chen et al. [4], Chue and Ou [7], Ding and Li [10], Keqiang et al. [13], Li and Weng [15], Ma et al. [17, 18], Rangelov et al. [22], Wang and Zhang [32]. The method used therein is mainly the singular integral equation method. There are only a few papers dealing with the respective in-plane case. The dynamic piezoelectric Mode-I problem was treated in Chen et al. [5] where the material properties were assumed to vary continuously only along one coordinate axis. Using the singular integral equation method the influence of the inhomogeneity on the K-factors for an impact loading was studied. In Chen and Liu [3] crack interaction was investigated based on the same method. The dynamic response of an exponentially graded piezoelectric finite plate containing a crack perpendicular to the free boundaries under the action of normal impact was considered in Ueda [29]. The same author in Ueda [28, 30] studied the problem of a finite crack in a graded piezoelectric strip by using the singular integral equation method after applying integral transform technique. As an alternative numerical tool the meshless formulation in recent years has been successfully applied to homogeneous and inhomogeneous piezoelectric problems, see Sladek et al. [24, 26, 27]. In Sladek et al. [26] this method was used for the solution of central and edge crack problems in strips subjected to pure static mechanical and/or electrical loads. The same configurations under Heaviside impact loadings were considered in Sladek et al. [27] for impermeable and permeable cracks.

The application of the BIEM to dynamic problems in inhomogeneous piezoelectric solids meets serious difficulties because the method requires the fundamental solution for the corresponding FGM. In general, partial differential equations with variable coefficients do not possess explicit fundamental solutions that can easily be implemented in the existed BIEM software. This prevents the reduction of a BVP to a system of IDE which can be treated by standard numerical quadrature techniques. The key role of the fundamental solution in a BIEM formulation is to reduce a given BVP into a system of BIEs by using the reciprocal theorem. For this reason the representation of the fundamental solutions in analytical form is so important.

In elastodynamics, the following ways have been proposed to obtain BIEM solutions for inhomogeneous elastic continua:

(i) Use of available fundamental solutions for homogeneous material see Manolis and Shaw [19]. Here, by applying suitable algebraic transformations the partial differential equation with variable coefficients is reduced to one with constant coefficients;
(ii) Use of the dual-reciprocity BIEM based on the fundamental solution for the homogeneous case, see Park and Ang [20] and Ang et al. [1]. Fundamental solutions for restricted cases of quadratic and exponential inhomogeneous piezoelectric material have been derived in Rangelov and Dineva [21] by using an appropriate algebraic transformation and the properties of the Radon transform.

The literature review shows that there exist only a few results for dynamic in-plane crack problems in inhomogeneous piezoelectric solids.

The chapter follows Dineva et al. [9], Rangelov and Dineva [21] and the aim is to develop a non-hypersingular traction BIEM for SIFs computation of in-plane cracked

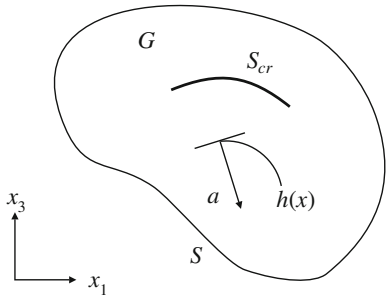

Fig. 10.1 Cracked inhomogeneous finite piezoelectric solid

functionally graded piezoelectric materials based on the frequency dependent fundamental solution. The applicability of the method is demonstrated by numerical examples for the GaN (Gallium Nitride) piezoelectric material. The chapter is connected with the Chap. 11 where anti-plane cracked piezoelectric solids are considered. It is shown in both chapters that stress concentration fields near the crack–tips in piezoelectric solids depend not only on different factors discussed separately, but also depend on the polarization phenomenon which is extremely significant in the areas of the smart structures and multifunctional materials.

10.2 Formulation of the BVP

Consider the 2D problem of a finite inhomogeneous piezoelectric solid G with a smooth boundary S and an internal crack—an open arc S_{cr}, subjected to time-harmonic electromechanical loading with a prescribed frequency ω, see Fig. 10.1. Let the poling direction coincide with the x_3-axis of the coordinate system and assume plane-strain conditions in the x_1, x_3-plane. The mechanical and electrical loading is assumed to be such that the only non-zero field quantities are the displacement u_i, the stress σ_{ij}, the electric field E_i and the electric displacement D_i, where $i, j = 1, 3$. In this case the governing equations in the absence of volume forces consist of the mechanical and electrical balance equations in the frequency domain and are as follows:

$$\sigma_{iJ,i} + \rho_{JK}\omega^2 u_K = 0, \tag{10.1}$$

where $u_K = (u_1, u_3, \phi)$ is the generalized displacement, $J, K = 1, 3, 4$ and σ_{iJ} is the generalized stress, $\sigma_{iJ} = C_{iJKl}u_{K,l} = C_{iJKl}s_{Kl}$, see Sect. 2.5.1. The generalized traction vector is $t_J = \sigma_{iJ}n_i$, where n_i is the unit normal vector on S_{cr}^+. The strain–displacement and electric field–potential relations are $s_{ij} = \frac{1}{2}(u_{i,j}+u_{j,i})$, $E_i = -\phi_{,i}$ where s_{ij}, ϕ are the strain tensor and electric potential, ρ is the mass density and $\rho_{JK} = \begin{cases} \rho, & J, K = 1, 3 \\ 0, & J = 4 \text{ or } K = 4 \end{cases}$.

In difference with the homogeneous case considered in Chaps. 6–9, we assume that the mass density and the material parameters vary in the same manner with $x = (x_1, x_3)$, i.e. there exists a function

$$h(x) = (a_1 x_1 + a_3 x_3 + 1)^2, \quad h(x) > 0 \text{ in } G,$$

such that $C_{iJKl}(x) = C^0_{iJKl} h(x)$ and $\rho_{JK}(x) = \rho^0_{JK} h(x)$. The constant vector $a = (a_1, a_3)$ is such that

$$\overline{G} \cap \{(x_1, x_3) : a_1 x_1 + a_3 x_3 + 1 = 0\} = \emptyset.$$

The main inhomogeneity parameter, the vector a, can be written in polar coordinates as $a = (r \cos\alpha, r \sin\alpha)$, where $\alpha \in [0, \pi]$ and $r = \sqrt{a_1^2 + a_3^2}$ are the direction and the magnitude of the inhomogeneity gradient respectively. Furthermore, regarding the reference material tensor, the following restrictions are assumed:

$$c^0_{13} = c^0_{44} \qquad \text{and} \qquad e^0_{31} = e^0_{15} \tag{10.2}$$

These equalities are approximately fulfilled for example for the piezoelectric material GaN, see Bykhovski et al. [2], Levinshtein et al. [14] and Table 4.1.

The problem statement is completed by the boundary conditions. They are given on the outer boundary S by a prescribed displacement $\overline{u}_J$ on the part of the boundary S_u and a prescribed traction $\overline{t}_J$ on the complementary part S_t, $S = S_u \cup S_t$, $S_u \cap S_t = \emptyset$. The finite crack S_{cr} here is assumed to be impermeable and mechanical traction free:

$$u_J|_{S_u} = \overline{u}_J, \qquad t_J|_{S_t} = \overline{t}_J, \qquad t_J|_{S_{cr}} = 0, \tag{10.3}$$

but also other electrical boundary conditions could have been used.

Our aim is to solve the BVP (10.1), (10.3), which is the same as formulated in Chap. 4, but now for the inhomogeneous solid. For this purpose, using an appropriate fundamental solution, the BVP must be formulated as an equivalent boundary integro–differential equation along the crack line S_{cr} and the solid's boundary S and solved numerically by BIEM.

10.3 Numerical Procedure

10.3.1 Fundamental Solution

The fundamental solution of Eq. (10.1) is defined as solution of the equation

$$\sigma^*_{iJM,i} + \rho_{JK}\omega^2 u^*_{KM} = -\delta_{JM}\delta(x - \xi) \tag{10.4}$$

where $\sigma^*_{iJM} = C_{iJKl}u^*_{KM,l}$, $x = (x_1, x_3)$, $\xi = (\xi_1, \xi_3)$, δ is Dirac's distribution and δ_{JM} the Kronecker symbol. The fundamental solution is derived in Rangelov and Dineva [21] transforming Eq. (10.4) into an equation with constant coefficients and then proceeding as in Sect. 3.4 with Radon transform.

Applying the smooth transformation of u^*_{KM} in G as

$$u^*_{KM} = h^{-1/2}U^*_{KM}, \tag{10.5}$$

Eq. (10.4) becomes an equation for U^*_{KM} with constant coefficients. Indeed,

$$\begin{aligned}\sigma^*_{iJM,i} &+ \rho_{JK}\omega^2 u^*_{KM} \\ &= h^{1/2}\{C^0_{iJKl}[U^*_{KM,il} + h^{-1/2}(h^{1/2}_{,i}U^*_{KM,l} - h^{1/2}_{,l}U^*_{KM,i} - h^{1/2}_{,il}U^*_{KM})] \\ &\quad + \rho^0_{JK}\omega^2 U^*_{KM}\} \\ &= h^{1/2}[C^0_{iJKl}U^*_{KM,il} + \rho^0_{JK}\omega^2 U^*_{KM}],\end{aligned}$$

since $h^{1/2}_{,il} = 0$ and due to restriction (10.2),

$$C^0_{iJKl}(h^{1/2}_{,i}U^*_{KM,l} - h^{1/2}_{,l}U^*_{KM,i}) = 0$$

is satisfied. Dividing Eq. (10.4) by $h^{1/2}$ and having in mind that $h^{-1/2}(x)\delta(x,\xi) = h^{-1/2}(\xi)\delta(x,\xi)$ we obtain

$$[M_{JK}(\partial) + \Gamma_{JK}]U^*_{KM} = -h^{-1/2}(\xi)\delta_{JM}\delta(x-\xi), \quad (x,\xi) \in G \times G \tag{10.6}$$

where $M_{JK}(\partial) = C^0_{iJKl}\partial_i\partial_l$, $\Gamma_{JK} = \rho^0_{JK}\omega^2$. Equation (10.6) represents three systems of linear partial differential equations of second order with constant coefficients. The solution U^{*0}_{JK} is found with Radon transform as is shown in Sect. 3.4, so from (10.5) we obtain

$$u^*_{JK}(x,\xi) = h^{-1/2}(\xi)h^{-1/2}(x)U^*_{JK}(x,\xi) \tag{10.7}$$

The stress, associated to the fundamental solution, is

$$\sigma^*_{iJM} = C_{iJKl}[h^{-1/2}_{,l}(\xi)h^{-1/2}(x)U^{*0}_{KM} + h^{-1/2}(x)h^{-1/2}(\xi)U^{*0}_{KM,l}] \tag{10.8}$$

Equations (10.7) and (10.8) for the fundamental solution and for the associated stress show their dependence on the mechanical properties of the reference material, on the location and distance between the source and observation point, on the frequency of the applied load and on the inhomogeneity function and it's derivatives. Using the asymptotic behavior of $U^*_{JK}(x,\xi)$ for $x \to \xi$, see Eq. (3.89) we obtain

$$\begin{aligned}u^{*as}_{JK} &= h^{-1}(\xi)b_{JK}\ln|x-\xi|, \\ \sigma^{*as}_{iJM} &= h^{-1/2}(\xi)h_{,l}(\xi)p_{iJMl}\ln|x-\xi| + q_{iJM}\frac{1}{|x-\xi|},\end{aligned} \tag{10.9}$$

where b_{JK}, p_{iJMl} and q_{iJM} depend on the elastic, dielectric, piezoelectric constants and the density, but not on the frequency. Though, the term with $1/|x-\xi|$ dominated in σ^{*as}_{iJM}, for the numerical approximation it is better for the accuracy to use both terms.

10.3.2 Non-hypersingular Traction BIEM

Following the method in Chap. 4 for homogeneous piezoelectric materials, the non-hypersingular BIE formulation on the boundaries $S \cup S_{cr}$ is derived. For the considered linear BVP (10.1), (10.3), the superposition principle is valid, see Wang et al. [31], Zhang et al. [35]. As in Sect. 7.2, Eqs. 7.2 and 7.3, the displacement and traction are written as $u_J = u^0_J + u^c_J, t_J = t^0_J + t^c_J$. Here u^0_J, t^0_J are the fields due to the external load on the boundary S of the crack free body, while the fields u^c_J, t^c_J are induced by the load $t^c_J = -t^0_J$ on the crack S_{cr} with zero boundary conditions on the boundary S. Using the representation formula for the generalized displacement gradients $u_{K,l}$ and taking the limit $x \to S \cup S_{cr}$, the following system of non-hypersingular traction BIEs for the posed problem is obtained:

$$\begin{aligned}\frac{1}{2}t^0_J(x) = {} & C_{iJKl}(x)n_i(x)\int_S [(\sigma^*_{\eta PK}(x,\xi)u^0_{P,\eta}(\xi) \\ & - \rho_{QP}\omega^2 u^*_{QK}(x,\xi)u^0_P(\xi))\delta_{\lambda l} - \sigma^*_{\lambda PK}(x,\xi)u^0_{P,l}(\xi)]n_\lambda(\xi)dS \\ & - C_{iJKl}(x)n_i(x)\int_S u^*_{PK,l}(x,\xi)t^0_P(\xi)dS, \quad x \in S,\end{aligned} \tag{10.10}$$

$$\begin{aligned}t_J(x) = {} & C_{iJKl}(x)n_i(x)\int_{S^+_{cr}} [(\sigma^*_{\eta PK}(x,\xi)\Delta u^c_{P,\eta}(\xi) \\ & - \rho_{QP}\omega^2 u^*_{QK}(x,\xi)\Delta u^c_P(\xi))\delta_{\lambda l} - \sigma^*_{\lambda PK}(x,\xi)\Delta u^c_{P,l}(\xi)]n_\lambda(\xi)dS_{cr} \\ & + C_{iJKl}(x)n_i(x)\int_S [(\sigma^*_{\eta PK}(x,\xi)u^c_{P,\eta}(\xi) - \rho_{QP}\omega^2 u^*_{QK}(x,\xi)u^c_P(\xi))\delta_\lambda \\ & - \sigma^*_{\lambda PK}(x,\xi)u^c_{P,l}(\xi)]n_\lambda(\xi)dS \\ & - C_{iJKl}(x)n_i(x)\int_S u^*_{PK,l}(x,\xi)t^c_P(\xi)dS, \quad x \in S \cup S_{cr}\end{aligned} \tag{10.11}$$

where

$$t_J = \begin{cases} t^c_J/2 & \text{on} \quad S, \\ -t^0_J & \text{on} \quad S_{cr}, \end{cases}$$

and $\Delta u^c_J = u^c_J|_{S^+_{cr}} - u^c_J|_{S^-_{cr}}$ is the generalized crack opening displacement. Furthermore, $x = (x_1, x_3)$ and $y = (y_1, y_3)$ denote the position vector of the observation point and source point, respectively. Equations (10.10) and (10.11) constitute a sys-

tem of integro-differential equations for the unknowns Δu_J^c on S_{cr} and u_J^0, t_J^0, u_J^c, t_J^c on S. From its solution the generalized displacement u_J and traction t_J at each internal point can be determined by using the corresponding representation formulae, see Sect. 4.2.1, Eqs. 4.8 and 4.9.

10.4 Numerical Results

The solution procedure follows the numerical algorithm developed and validated in Chap. 4. The only difference is that in the Eqs. (10.10) and (10.11) there appear as multipliers smooth functions on S coming from the inhomogeneity. For their numerical solution with BIEM, a FORTRAN code has been developed.

The displacement and stress at the crack-tip in the inhomogeneous material have the same asymptotic behavior as those in the homogeneous one, see Sladek et al. [25] and Zhang et al. [33, 34]. Although the structure of the asymptotic crack–tip fields is not influenced by the material gradient, the SIFs are dependent on inhomogeneity type and properties through the solution of the BVP.

Knowing the traction, the generalized dynamic SIFs at the crack–tips are calculated, see Eq. (2.40). For example, in case of a straight crack along the interval $(-c, c)$ on the x_1-axis, the respective formulae are given by

$$\begin{aligned} K_I &= \lim_{x_1 \to \pm c} t_3 \sqrt{2\pi (x_1 \mp c)}, \\ K_{II} &= \lim_{x_1 \to \pm c} t_1 \sqrt{2\pi (x_1 \mp c)}, \\ K_{IV} &= \lim_{x_1 \to \pm c} t_4 \sqrt{2\pi (x_1 \mp c)}, \end{aligned} \tag{10.12}$$

where t_J is the generalized traction at the point $(x_1, 0)$ close to the crack-tip. Regarding the electrical SIFs, the electric field SIF K_E is given by

$$K_E = \lim_{x_1 \to \pm c} E_3 \sqrt{2\pi (x_1 \mp c)}, \quad E_3 = (c_{33} t_4 - e_{33} t_3)(e_{33} c_{33} + e_{33}^2)^{-1} \tag{10.13}$$

and the electric displacement SIF $K_D = K_{IV}$ can also be determined. Equations (10.12) and (10.13) are based on the fact known in the literature, see Li and Weng [16], that stresses and electric displacements at the crack-tip in functionally graded materials still posses the inverse square root singularity in terms of a local coordinate at the crack-tip and that the angular distribution functions are the same as in the cases of a homogeneous piezoelectric solid.

The numerical study aims to illustrate the sensitivity of the mechanical and electrical SIFs to the frequency of the applied electro-mechanical load, to the direction and magnitude of the material gradient and to the geometry of the crack configuration.

In all examples a straight crack of length $2c = 5\,\text{mm}$ is considered which is discretized by seven boundary elements, see Fig. 10.2b. The numerical studies showed that this number is sufficient to achieve a satisfying accuracy within the considered frequency range. The first and the last element are quarter point quadratic BEs while

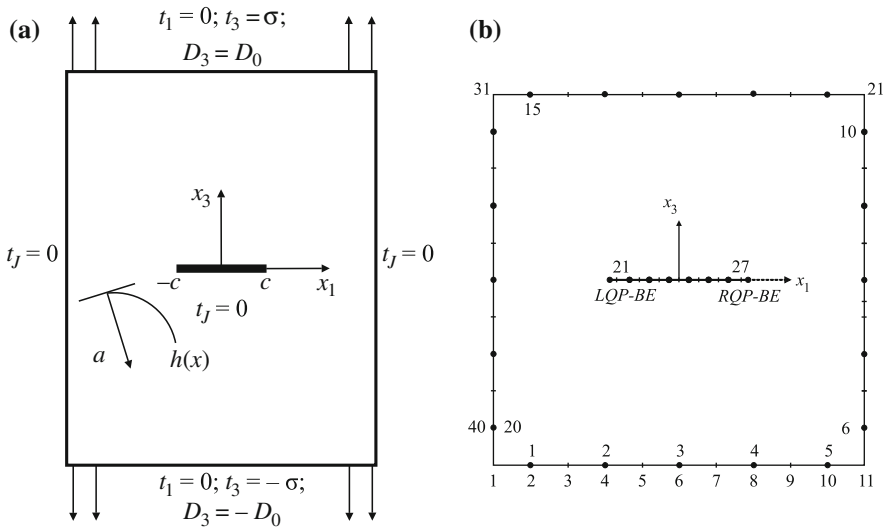

Fig. 10.2 Inhomogeneous rectangular plate (**a**), discretization (**b**)

the remaining elements are ordinary quadratic BEs. Their lengths have been chosen as $l_1 = l_7 = 0.375\,\text{mm}$, $l_2 = l_6 = 0.5\,\text{mm}$ $l_3 = l_5 = 1.0\,\text{mm}$, $l_4 = 1.25\,\text{mm}$. As reference piezoelectric material GaN is taken with properties shown in Table 4.1. The crack is centered in a rectangular plate with the dimensions $20 \times 40\,\text{mm}$ which is loaded by an uniform time-harmonic electromechanical tension along the x_3-axis at the opposite sides with amplitudes $\sigma_0 = 400 \times 10^6\,\text{N/m}^2$ and $D_0 = 0.1\,\text{C/m}^2$, see Fig. 10.2a, b. A normalized frequency is introduced through $\Omega = c\,\omega\sqrt{\rho_0/c_{44}^0}$, where $\omega[1/s]$ is the angular frequency. The mechanical SIFs K_I and K_{II} are normalized by $\sigma_0\sqrt{\pi c}$, denoted by K_I^* and K_{II}^*, respectively. The electrical SIF K_D is normalized by $D_0\sqrt{\pi c}$, and the electric field SIF K_E is normalized by $|\sigma_0|\sqrt{\pi c}/e_{33}$, denoted by K_D^* and K_E^*, respectively. A total number of 20 quadratic BEs on the external boundary S have been used, see Fig. 10.2b.

A detailed validation study of the proposed numerical scheme for the homogeneous crack problem in an infinite region is presented in Sect. 6.3 and therefore is omitted here.

For cracks in finite homogeneous piezoelectric regions under time-harmonic loading the results are presented in Chap. 6 . However, a solution for a cracked anisotropic rectangular plate under time-harmonic load has been published by Garcia-Sanchez et al. [12]. Figure 10.3 shows a comparison of the authors BIEM results: (a) with results of Chirino and Dominguez [6] for a homogeneous elastic isotropic material and (b) with results of Garcia-Sanchez et al. [12] for a homogeneous elastic anisotropic Boron-epoxy (type I) composite with the following properties: Young's moduli $E_1 = 224.06\,\text{GPa}$, $E_3 = 12.69\,\text{GPa}$, shear modulus $G_{13} = 4.43\,\text{GPa}$ and Poisson's ratio $\nu_{13} = 0.256$. It is a peak observed for the normalized frequency

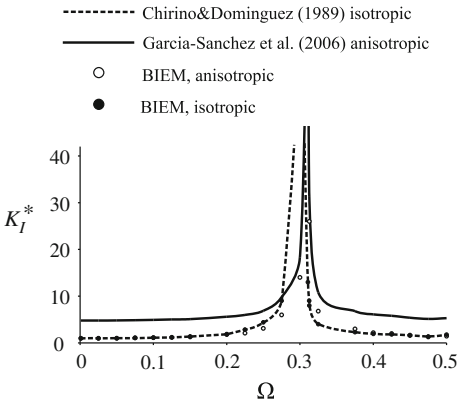

Fig. 10.3 Normalized SIF-I versus normalized frequency Ω for a center cracked isotropic/anisotropic homogeneous plate

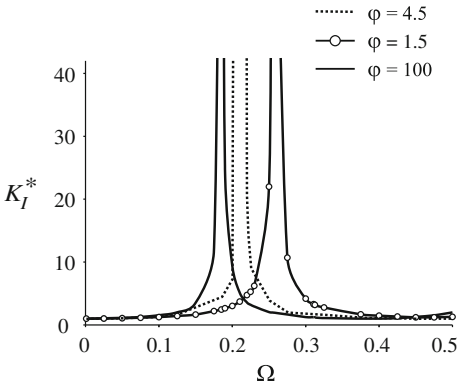

Fig. 10.4 Normalized SIF-I versus normalized frequency Ω for a center cracked anisotropic homogeneous Boron-epoxy I composite at different orthotropy ratios

around 0.3 which is considered as a resonance value of the SIF. The existence of this resonance effect is described and discussed by several authors as for the isotropic cracked domains, see Chirino and Dominguez [6], so for the anisotropic cracked domains, see Garcia-Sanchez et al. [12]. As can be seen, the results are in excellent agreement, although very different computational techniques are used in Chirino and Dominguez [6], Garcia-Sanchez et al. [12] and in the present investigation. To the author's knowledge there are no available results for SIF computation for finite cracked piezoelectric solids with quadratic inhomogeneity subjected to in-plane time-harmonic mechanical and electrical load. Due to this reason the validation is based on the comparison of the author's BIEM results with the results of other authors for the homogeneous case. Using the developed program code for inhomogeneous case and replacing the inhomogeneity function $h(x)$ with 1 we show the validation.

For the same homogeneous material, Fig. 10.4 shows BIEM results revealing the influence of the orthotropy ratio $\varphi = E_1/E_3$ on the SIFs. Here, the shear modulus has been defined as $G_{13} = E_1/(\varphi + 2\nu_{13} + 1)$, see Garcia-Sanchez et al. [11]. Figure 10.4 shows that with increasing φ the resonance peak is shifted to lower frequencies and this effect is the same as that shown in Garcia-Sanchez et al. [12].

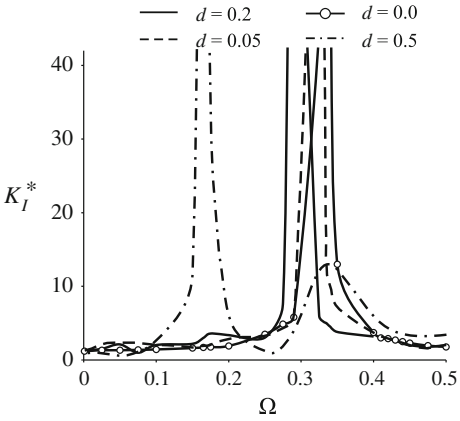

Fig. 10.5 Normalized SIF-I versus normalized frequency Ω for a center cracked inhomogeneous anisotropic plate. Material gradient direction $\alpha = \pi/2$

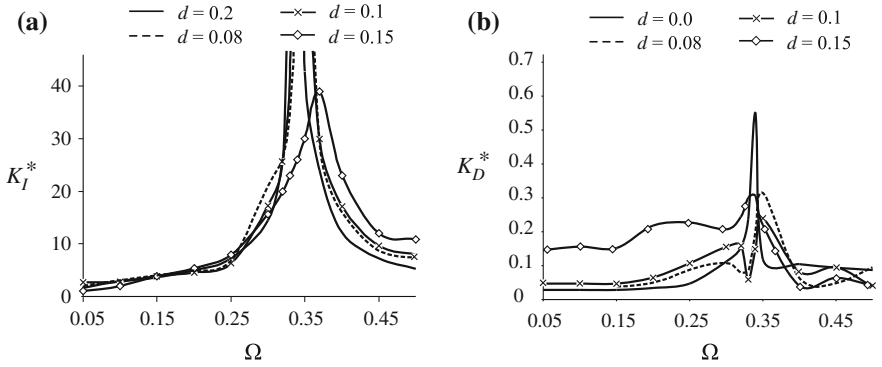

Fig. 10.6 Normalized SIFs versus normalized frequency Ω for a center cracked inhomogeneous piezoelectric plate. Material gradient direction $\alpha = \pi/2$. **a** K_I^*; **b** K_D^*

Following Zhang et al. [35, 36] the dimensionless magnitude $d = r.c$ and the direction α of the inhomogeneity gradient are defined, where the magnitude of the inhomogeneity gradient r is defined in Sect. 10.2 and c is the half-length of the crack. In Figs. 10.5–10.10 the inhomogeneity effects are evaluated with respect to d and α. First, by setting the piezoelectric constants of GaN to zero, the purely elastic anisotropic case is studied. For an inhomogeneity direction perpendicular to the crack, Fig. 10.5 shows the normalized K_I versus frequency Ω for different inhomogeneity magnitude d. With increasing d the resonance peak is shifted to lower frequencies. All further results are devoted to inhomogeneous piezoelectric materials.

In Fig. 10.6a, b the SIFs at the right crack tip for different inhomogeneity magnitudes d and inhomogeneity direction $\alpha = \pi/2$ are plotted. The following observations can be made: (a) Generally, the inhomogeneity effect is clearly visible; (b)

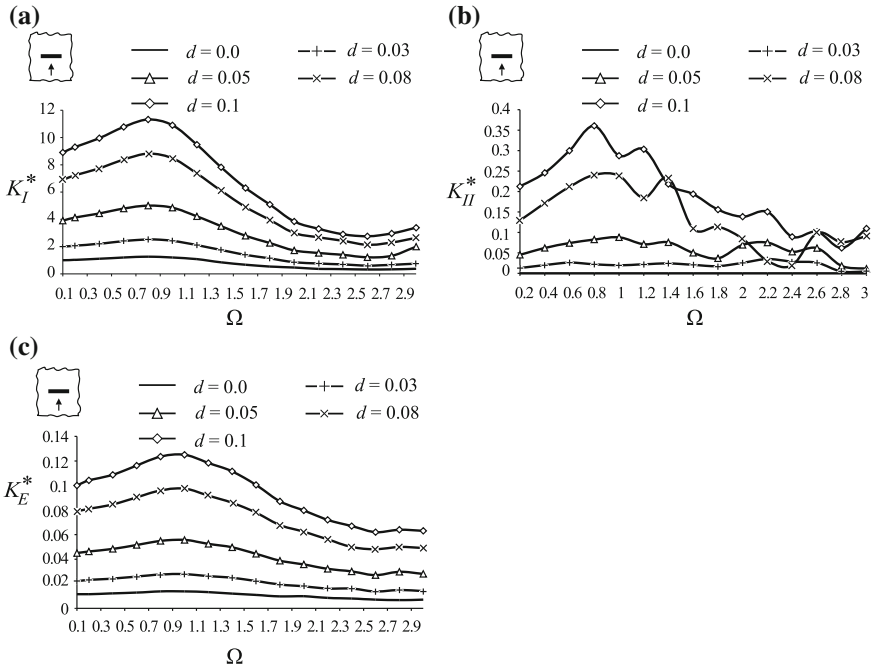

Fig. 10.7 Normalized SIFs versus normalized frequency Ω of normal incident L-wave at the right crack-tip for a piezoelectric inhomogeneous plane: **a** K_I^*; **b** K_{II}^*; **c** K_E^*

The inhomogeneity effect is more pronounced for the electrical SIFs; (c) The FGM with $d = 0.15$ reduces the resonance amplitude, see Fig. 10.6a due to the material inhomogeneity; (d) A mode K_{II} factor appears under periodic uniaxial tension on account of the non-symmetry if the inhomogeneity direction is not perpendicular to the crack plane. This effect has been investigated for general FGMs recently by Dineva et al. [8] and Zhang et al. [35, 36]. It will also be shown in the following examples where the external boundary has a minor influence on the complex wave field inside the solid so that the inhomogeneity effects can be demonstrated more clear.

In the following examples, in order to decrease the disturbing wave reflection at the external boundary and to compare the present results with those for a finite crack in an infinite plane, the edge-length W of the square plate with the crack is taken sufficiently large, say $W = 7c$, as in Sladek et al. [23]. For the case of normal incident L-wave Fig. 10.7 demonstrates the influence of the magnitude of the material gradient d on K_I^*, K_{II}^* and K_E^* in the case the material properties vary normal to the crack line, i.e. the direction of the material gradient is $\alpha = \pi/2$. Figures 10.8 and 10.9 show the same quantities but now for the inhomogeneity directions $\alpha = \pi/4$ and $\alpha = \pi/9$, respectively. In Fig. 10.10, for the inhomogeneity direction $\alpha = \pi/6$ and two different d, the K-factors at the right and the left crack-tips are compared. It

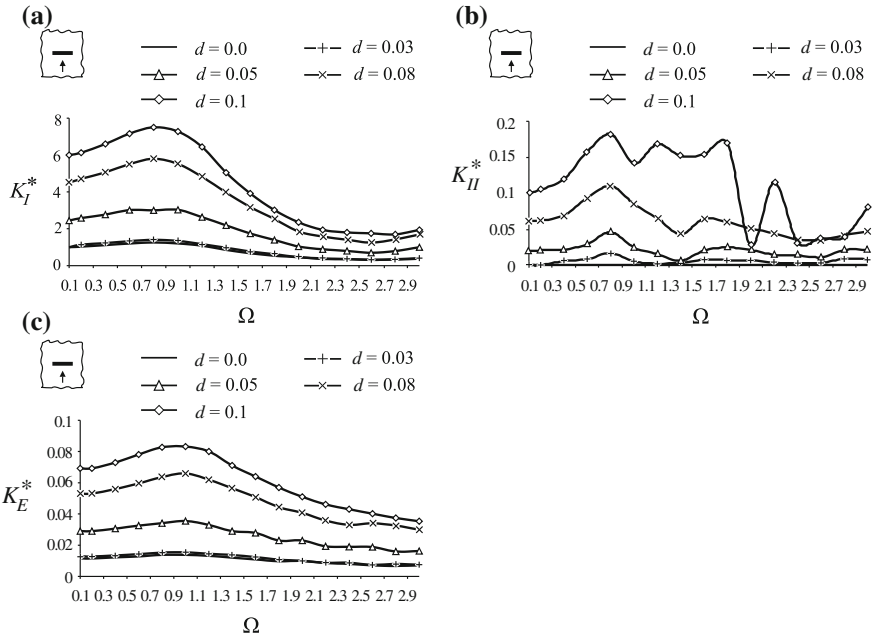

Fig. 10.8 Normalized SIFs versus normalized frequency Ω of normal incident L-wave at the *right* crack-tip of a crack in piezoelectric inhomogeneous plane: **a** K_I^*; **b** K_{II}^*; **c** K_E^*. Inhomogeneity direction is $\alpha = \pi/4$

can be seen, as could be expected, that the difference between K factors at left and right crack-tips increase with increasing inhomogeneity magnitude d.

The numerical study clearly shows that the inhomogeneity has a strong influence on the SIFs, i.e. the dynamic stress concentration at the crack-tips. Because the dynamic crack-tip field is a complex result of the influence of the different parameters like geometry, loading, electromechanical coupling, anisotropy strength, inhomogeneity strength and direction, the picture is not as clear as in the simple uncoupled static case. The results demonstrate that the SIFs are sensitive to the direction and magnitude of the material inhomogeneity and they depend on the frequency of the applied load and on the relation between the magnitude of the gradient parameter and the crack size. The comparison of the results in Fig. 10.6 with those in Figs. 10.8–10.10 reveals the role of the reflected waves from the external boundaries of the finite piezoelectric solid and the influence of the geometry of the crack scenario on the obtained dynamic stress concentration field. It is important to note that the K_{II}^* factor is not zero in the inhomogeneous case under pure tension which is in contrast to the homogeneous case.

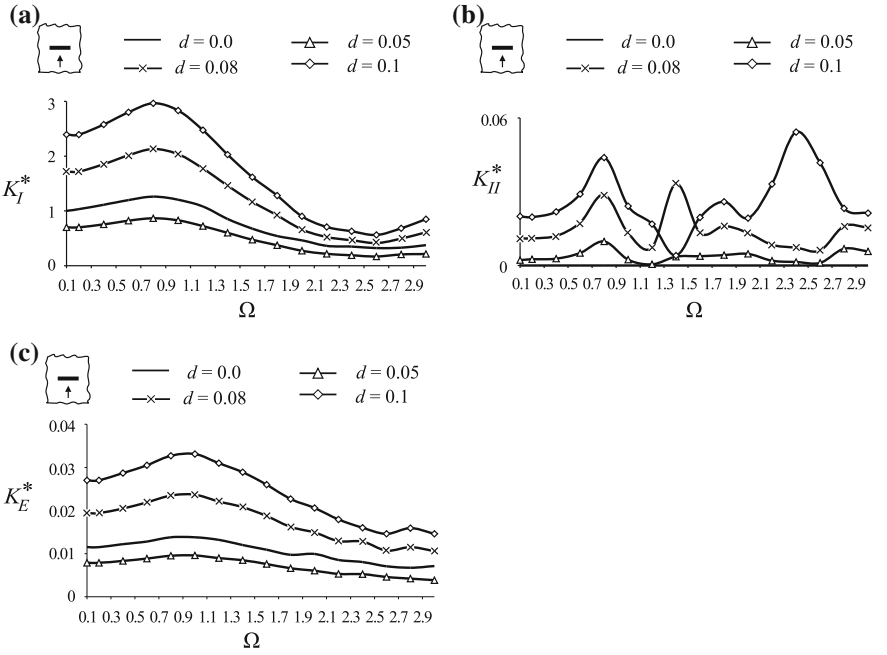

Fig. 10.9 Normalized SIFs versus normalized frequency Ω of normal incident L wave at the *right* crack-tip of a crack in piezoelectric inhomogeneous plane under normal time-harmonic uniform tension: **a** K_I^*; **b** K_{II}^*; **c** K_E^*. Inhomogeneity direction is $\alpha = \pi/9$

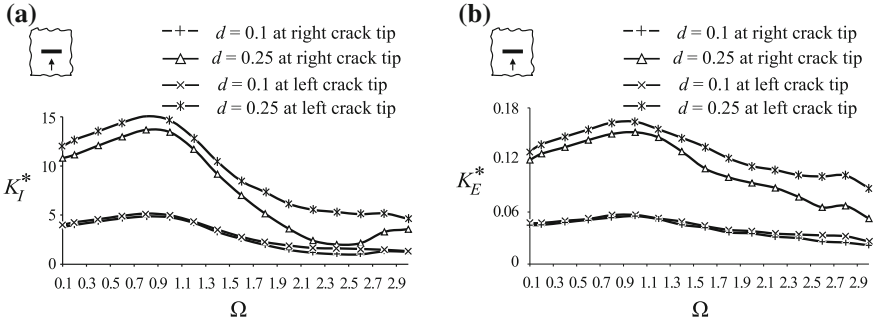

Fig. 10.10 Normalized SIFs versus normalized frequency Ω of normal incident L-wave at the *right* and at the *left* crack-tips of a crack in a piezoelectric inhomogeneous plane under normal time-harmonic uniform tension: **a** K_I^*; **b** K_E^*. Inhomogeneity direction is $\alpha = \pi/6$

10.5 Conclusion

Presented is an analytical methodology that derives the fundamental solutions for wave equations of a specific class of inhomogeneous piezoelectric materials with quadratic variation of the material characteristics. The non-hypersingular traction

based BIE formulation of the dynamic problem for a cracked finite inhomogeneous solid subjected to in-plane mechanical and/or in-plane electrical load is presented. Using the derived fundamental solutions and accurate numerical procedure, an efficient BIEM software is developed and validated. Numerical examples for SIFs computation in cracked piezoelectric functionally graded GaN materials and solids are presented. Conclusion from the simulations is that the coupled crack-tip field is sensitive to the magnitude and direction of the material inhomogeneity gradient, to the frequency of the applied dynamic load, to the crack geometry and to the electro-mechanical coupling.

References

1. Ang WT, Clements DL, Vahdati N (2003) A dual-reciprocity boundary element method for a class of elliptic boundary value problems for non-homogeneous anisotropic media. Engng Anal Bound Elem 27:49–55
2. Bykhovski AD, Gelmond BL, Shur MS (1997) Elastic strain relaxation and piezoeffect in Ga N- AIN, Ga N- Al Ga N and Ga N- In Ga N superlattices. Appl Phys 81(9):6332–6338
3. Chen J, Liu ZX (2005) On the dynamic behavior of a functionally graded piezoelectric strip with periodic cracks vertical to the boundary. Int J Solids Struct 42:3133–3146
4. Chen J, Liu ZX, Zou ZZ (2003a) The central crack problem for a functionally graded piezoelectric strip. Int J Fract 121:81–94
5. Chen J, Liu ZX, Zou ZZ (2003b) Electromechanical impact of a crack in functionally graded piezoelectric medium. Theoret Appl Fract Mech 39:47–60
6. Chirino F, Dominguez J (1989) Dynamic analysis of cracks using BEM. Engng Fract Mech 34:1051–1061
7. Chue CH, Ou YL (2005) Mode III crack problems for two bonded functionally graded piezoelectric materials. Int J Solids Struct 42:3321–3337
8. Dineva P, Rangelov T, Manolis G (2007) Elastic wave propagation in a class of cracked functionally graded materials by BIEM. Comput Mech 39:293–308
9. Dineva P, Gross D, Müller R, Rangelov T (2010a) Time-harmonic crack problems in functionally graded piezoelectric solids via BIEM. Eng Fract Mech 77:73–91
10. Ding SH, Li X (2008) Periodic cracks in functionally graded piezoelectric layer bonded to a piezoelectric half-plane. Theor Appl Fract Mech 49(3):313–320
11. Garcia-Sanchez F, Saez A, Dominguez J (2004) Traction boundary elements for cracks in anisotropic solids. Engng Anal Bound Elem 28:667–676
12. Garcia-Sanchez F, Saez A, Dominguez J (2006) Two-dimensional time-harmonic BEM for cracked anisotropic solids. Engng Anal Bound Elem 30:88–99
13. Keqiang H, Zheng Z, Bo J (2003) Electroelastic intensification near anti-plane crack in a functionally gradient piezoelectric ceramic strip. Acta Mech Solida Sinica 16(3):197–204
14. Levinshtein ME, Rumyantsev SL, Shur MS (2001) Properties of advanced semiconductor materials GaN, AIN, InN, BN and SiGe. John Wiley and Sons, London
15. Li C, Weng G (2002) Antiplane crack problem in functionally graded piezoelectric materials. J Appl Mech T ASME 69:481–488
16. Li C, Weng G (2002a) Antiplane crack problem in functionally graded piezoelectric materials. ASME. J Appl Mech 69:481–488
17. Ma L, Wu LZ, Zhou ZJ, Guo LC, Shi LP (2004) Scattering of the harmonic anti-plane share waves by two collinear cracks in functionally graded piezoelectric materials. Europ J Mech /A Solids 23:633–643
18. Ma L, Wu LZ, Zhou ZJ, Guo LC (2005) Scattering of the harmonic anti-plane share waves by a crack in functionally graded piezoelectric materials. Composite Str 69:436–441

19. Manolis G, Shaw R (1996) Green's function for a vector wave equation in mildly heterogeneous continuum. Wave Motion 24:59–83
20. Park S, Ang W (2000) A complex variable boundary element method for an elliptic partial differential equation with variable coefficients. Commun Numer Meth Eng 16:697–703
21. Rangelov T, Dineva P (2007a) Dynamic behaviour of a cracked inhomogeneous piezoelectric solid. In-plane case. Comptes Rendus Acad Bulg Sci 60(2), 141–148.
22. Rangelov T, Dineva P, Gross D (2008) Effect of material inhomogeneity on the dynamic behavior of cracked piezoelectric solids: a BIEM approach. ZAMM-Z Angew Math Mech 88:86–99
23. Sladek J, Sladek V, Zhang C (2005) A meshless local boundary integral equation method for dynamic anti-plane shear crack problem in functionally graded materials. Engng Anal Bound Elem 29:334–342
24. Sladek J, Sladek V, Zhang C, Garcia-Sanchez F, Wunsche M (2006) Meshless local Petrov-Galerkin method for plane piezoelectricity. CMC: computers. Mater Continua 4:109–118
25. Sladek J, Sladek V, Zhang C, Solek P, Pan E (2007a) Evaluation of fracture parameters in continuously non-homogeneous piezoelectric solids. Int J Fract 145:313–326
26. Sladek J, Sladek V, Zhang C, Solek P, Starek L (2007b) Fracture analysis in continuously nonhomogeneous piezoelectric solids by the MLPG. Comput Methods Eng Sci 19(3):247–262
27. Sladek J, Sladek V, Zhang C (2007c) A local integral equation method for dynamic analysis in functionally graded piezoelectric materials. In: Minutoto V, Aliabadi MH (eds) Advances in boundary element technique VIII, pp 141–148
28. Ueda S (2003) Crack in functionally graded piezoelectric strip bonded to elastic surface layers under electromechanical loading. Theor Appl Fract Mech 40:325–336
29. Ueda S (2005a) Impact response of a functionally graded piezoelectric plate with a vertical crack. Theor Appl Fract Mech 44:239–342
30. Ueda S (2005b) Electromechanical response of a cnter crack in a functionally graded piezoelectric strip. Smart Mater Struct 14:1133–1138
31. Wang BL, Du SY, Han JC (1998) Dynamic fracture mechanics analysis for anti-plane cracks in non-homogeneous composite material. Acta Mater Comp Sinica 15(4):66–75
32. Wang CY, Zhang Ch (2005) 2 D and 3 D dynamic Green's functions and time-domain BIE formulations for piezoelectric solids. Eng Anal Bound Elem 29:454–465
33. Zhang C, Savidis A, Zhu H (2001) A time domain BIEM for crack analysis in functionally graded materials under impact loading. In: Denda M (ed) Advances in boumdary element techniques II, pp 405–412
34. Zhang C, Savidis A, Savidis G, Zhu H (2003) Transient dynamic analysis of a cracked functionally graded material by a BIEM. Comput Mater Sci 26:167–174
35. Zhang C, Sladek J, Sladek V (2003b) Numerical analysis of cracked functionally graded materials. Key Eng Mater 251(252):463–471
36. Zhang C, Sladek J, Sladek V (2004) Crack analysis in unidirectionally and bidimensionally functionally graded materials. Int J Fract 129:385–406

Chapter 11
Functionally Graded Piezoelectric Media with a Single Anti-plane Crack

Abstract Treated is an arbitrarily shaped anti-plane shear crack in a finite inhomogeneous piezoelectric domain under time-harmonic loading. Within a unified scheme different types of inhomogeneity are considered for which the material parameters may vary in arbitrary directions. The problem is solved by using a numerically efficient non-hypersingular traction BIEM. The fundamental solutions for the different inhomogeneity types are derived in closed form. Numerical results for the SIFs are discussed. They show the effect of the material inhomogeneity type and characteristics and the efficiency of the computational method.

11.1 Introduction

Elastodynamic problems in inhomogeneous media are usually treated mainly by two models. The multilayer model considers the solid as composed by piecewise homogeneous layers where scattering arises from sequences of reflections and refractions. In contrast, in the smooth model where the material properties are assumed to be continuous functions of the spatial coordinates.

The second approach, describing the material properties as continuous functions, has been often used for purely elastic materials in the last years. Applying analytical methods, cracked inhomogeneous materials under static conditions have been studied e.g. by Delale and Erdogan [7], Oztruk and Erdogan [21], Erdogan [9]. Finite element methods were applied by Kim and Paulino [14], Gu et al. [10], and BIEM has been used by Pan and Amadei [22] and Yu and Xiao [28]. Equivalent dynamic problems have been treated by Zhang et al. [29–31]. In all mentioned papers the spatial variation of the material parameters is described by an exponential law, where a symmetrical material graduation with respect to the crack-plane is assumed.

The number of works devoted to cracks in inhomogeneous piezoelectric materials is rather small. The static problem of an anti-plane crack located in a functionally gradient piezoelectric interlayer between two dissimilar homogeneous piezoelectric

P. Dineva et al., *Dynamic Fracture of Piezoelectric Materials*,
Solid Mechanics and Its Applications 212, DOI: 10.1007/978-3-319-03961-9_11,

half-planes was solved in Hu et al. [11]. A mode III crack in a functionally graded piezoelectric material was considered in Wang [26], where the mechanical and the electrical properties of the medium were assumed to take a specific functional form for which the dynamic equation had an analytic solution. The relevant problem subsequently was solved by means of the singular integral equation technique. The anti-plane problem of an exponentially functionally gradient piezoelectric strip with a finite crack parallel to the edges has been analyzed in Keqiang et al. [13] by using the Fourier transform and formulating by this two pairs of dual integral equations. The same method of singular integral equations has been used by Chen et al. [3] for the problem for an anti-plane crack in a functionally graded piezoelectric layer bonded between two elastic layers under combined anti-plane mechanical shear and in-plane electric impacts. Scattering of harmonic anti-plane shear waves by cracks in functionally graded piezoelectric materials was investigated by Ma et al. [17, 18] who assumed the exponential variation of the material properties. An anti-plane loaded crack located within one of two bonded functionally graded piezoelectric materials has been studied by Chue and Ou [5]. Chen et al. [2] discussed results for the dynamic anti-plane problem of an inhomogeneous piezoelectric strip containing a periodic array of parallel cracks arranged perpendicular to the strip boundary. Although there are some specific solutions available, the number of investigations of dynamic crack problems in inhomogeneous piezoelectric materials is very limited. In particular there is a lack of an efficient numerical BIEM tool for the solution of such problems.

The aim of the present chapter is to derive fundamental solutions for different types of inhomogeneous piezoelectric materials and to implement them into efficient BIEM software for the solution of the anti-plane time-harmonic problem in a cracked finite solid. The chapter follows [23, 25].

11.2 Formulation of the BVP

We consider a piezoelectric domain G with an arbitrary shaped internal crack S_{cr} and a smooth boundary S, poled in x_3 - direction and subjected to time-harmonic loading, see Fig. 11.1. The mechanical and electrical loading is assumed to be such that the only nonvanishing displacements are the anti-plane mechanical displacement $u_3(x_1, x_2)$ and the in-plane electrical displacements $D_i = D_i(x_1, x_2)$, $i = 1, 2$. For such a case, assuming quasi-static approximation of piezoelectricity, the field equations in absence of body forces are given by the balance equation

$$\sigma_{iJ,i} + \rho_{JK}\omega^2 u_K = 0, \quad J, K = 3, 4, \tag{11.1}$$

where $u_K = (u_3, \phi)$ is the generalized displacement $J, K = 3, 4$ and σ_{iJ} is the generalized stress, $\sigma_{iJ} = C_{iJKl}u_{K,l} = C_{iJKl}s_{Kl}$, see Sect. 2.5.2, where

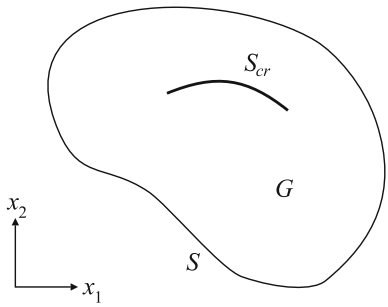

Fig. 11.1 2D cracked piezoelectric solid

$$C_{i33l} = \begin{cases} c_{44}, i = l \\ 0, \quad i \neq l \end{cases}; \quad C_{i34l} = \begin{cases} e_{15}, i = l \\ 0 \quad i \neq l \end{cases}; \quad C_{i44l} = \begin{cases} -\varepsilon_{11}, i = l \\ 0, \qquad i \neq l \end{cases}.$$

The strain-displacement and electric field-potential relations are $s_{i3} = u_{3,i}$, $E_i = -\phi_{,i}$ where s_{ij}, ϕ are the strain tensor and electric potential, $s_{iJ} = (u_{3,i}, E_i)$ and ρ is the mass density, $\rho_{JK} = \begin{cases} \rho, J = K = 3 \\ 0, J = 4 \text{ or } K = 4 \end{cases}$.

The boundary conditions on the outer boundary S are given by a prescribed displacement $\bar{u}_J$ on the part of the boundary S_u and prescribed traction $\bar{t}_J$ on the complementary part S_t, $S = S_u \cup S_t$, $S_u \cap S_t = \emptyset$ i.e.

$$u_J(x) = \bar{u}_J(x) \quad \text{on } S_u, \quad t_J(x) = \bar{t}_J(x) \quad \text{on } S_t. \tag{11.2}$$

The boundary condition along the crack is given by

$$t_J = 0 \quad \text{on } S_{cr}, \tag{11.3}$$

where the generalized traction vector is $t_J = \sigma_{iJ} n_i$ and n_i is the unit normal vector on S_{cr}^+. Condition (11.3) means that the crack faces are free of mechanical traction as well as of surface charges, i.e. the crack is electrically impermeable. It is well known that this assumption is only a rough approximation since real cracks are partially permeable. But because the boundary conditions have no influence on the fundamental solution and subsequent implementation into the BIEM, (11.3) has been chosen for simplicity.

We further assume that the mass density and material parameters vary in the same manner with x, i.e. there exists a function $h(x) \in C^2(G)$, $h(x) > h_0 > 0$, such that

$$c_{44}(x) = c_{44}^0 h(x), \quad e_{15}(x) = e_{15}^0 h(x), \quad \varepsilon_{11}(x) = \varepsilon_{11}^0 h(x), \quad \rho(x) = \rho^0 h(x). \tag{11.4}$$

Following Akamatsu and Nakamura [1] it can be proved that the BVP (11.1)–(11.3) admits a continuous differentiable solution, if the usual smoothness and compatibility requirements for the boundary data are satisfied.

We will solve the BVP (11.1)–(11.3) numerically transforming it into the equivalent integro-differential equation along the boundaries $S \cup S_{cr}$ as in the homogeneous case, see Chap. 4. This can be done if we are able to use an appropriate fundamental solution for the wave Eq. (11.1). Our aim is to specify classes of nonhomogeneity functions $h(x)$ for which the fundamental solution can be derived in closed form and subsequently be used to solve the boundary value problem within the framework of a non-hypersingular traction BIEM.

11.3 Inhomogeneity and Fundamental Solution

The fundamental solution of Eq. (11.1) is defined as solution of the equation

$$\sigma^*_{iJM,i} + \rho_{JK}\omega^2 u^*_{KM} = -\delta_{JM}\delta(x,\xi), \tag{11.5}$$

where $\sigma^*_{iJM} = C_{iJMl}u^*_{KM,l}$, $J, K, M = 3, 4$, $i, l = 1, 2$, $x = (x_1, x_2)$ and $\xi = (\xi_1, \xi_2)$. It is well known, see John [12], that if $h(x)$ is an analytical function in G the solution of Eq. (11.5) exists. In order to derive it we first transform Eq. (11.5) by a suitable change of functions to an equation with constant coefficients. This can be done if certain restrictions on function $h(x)$ are supposed. In a second step we apply Radon transform, as in Chap. 3, which allows the construction of a set of fundamental solutions depending on the roots of the characteristic equation of the obtained ODE-system. Finally, using both the inverse Radon transform and the inverse change of functions, the fundamental solutions of Eq. (11.1) is obtained for specific types of piezoelectric materials. In the first step we use a method which successfully was applied by Manolis and Shaw [19] for elastic continua. The smooth transformation

$$u_K = h^{-1/2}(x)U_K, \tag{11.6}$$

leads to a wave equation with constant coefficients, having in mind that

$$\begin{aligned} u_{K,l} &= -\tfrac{1}{2}h^{-3/2}h_{,l}U_K + h^{-1/2}U_{K,l}, \\ \sigma_{iJ} &= C^0_{iJKl}hu_{K,l} = C^0_{iJKl}[-(h^{1/2})_{,l}U_K + h^{1/2}U_{K,l}], \text{ and} \\ \sigma_{iJ,q} &= C^0_{iJKl}[-(h^{1/2})_{,lq}U_K - (h^{1/2})_{,l}U_{K,q} + (h^{1/2})_{,q}U_{K,l} + h^{1/2}U_{K,lq}], \end{aligned}$$

where $C_{iJKl} = h(x)C^0_{iJKl}$. Since for $q = i = l$ the terms with the first derivatives of U_K vanish, Eq. (11.1) after dividing it by $h^{1/2}$ takes the form

$$C^0_{iJKi}U_{K,ii} + [\rho^0_{JK}\omega^2 - C^0_{iJKi}h^{-1/2}(h^{1/2})_{,ii}]U_K = 0, \tag{11.7}$$

Correspondingly, using the property $h^{-1/2}(x)\delta(x,\xi) = h^{-1/2}(\xi)\delta(x,\xi)$ of the Dirac function, Eq. (11.5) with the transformation

$$u^*_{KM} = h^{-1/2}(x)U^*_{KM} \tag{11.8}$$

yields

$$C^0_{iJKi}U^*_{KM,ii} + [\rho^0_{JK}\omega^2 - C^0_{iJKi}h^{-1/2}(h^{1/2})_{,ii}]U^*_{KM} = h^{-1/2}(\xi)\delta_{JM}\delta(x,\xi). \tag{11.9}$$

Equations (11.7) and (11.9) are equations with constant coefficients, if the condition

$$C^0_{iJKi}h^{-1/2}(h^{1/2})_{,ii} = p_{JK} = const, \quad x \in G, \tag{11.10}$$

is fulfilled, what constitutes certain restrictions for the inhomogeneity function $h(x)$.

Following the presented method in Sect. 3.3, we can solve the system of equations with constant coefficients (11.9) for U^*_{KM} and consequently obtain the fundamental solution of Eq. (11.5) with inverse Radon transform and transformation (11.8)

Before continuing with the derivation of the fundamental solution let us consider three types of inhomogeneous piezoelectric materials for which condition (11.10) is fulfilled. Note that the notations $a = (a_1, a_2)$ and $|a| = \sqrt{\langle a, a\rangle}$ are used below.

Type A: For $p_{JK} = 0$ the inhomogeneity function $h(x)$ is of the type $h(x) = (dx_1x_2 + \langle a, x\rangle + b)^2$ in the domain $G \subset R^2$ and $G \cap \{x : dx_1x_2 + \langle a, x\rangle + b \le 0\} = \emptyset$.

Type B: For $p_{JK} = C^0_{iJKi}a_i^2$ the inhomogeneity function $h(x)$ is of the type $h(x) = e^{2(\langle a,x\rangle+b)}$ or $h(x) = \cosh^2(\langle a, x\rangle + b)$ in the domain $G \subseteq R^2$ and $h(x) = \sinh^2(\langle a, x\rangle + b)$ in the domain $G \subset R^2 \cap \{x : \langle a, x\rangle + b \neq 0\}$.

Type C: For $p_{JK} = -C^0_{iJKi}a_i^2$ the inhomogeneity function $h(x)$ is of the type $h(x) = \sin^2(\langle a, x\rangle + b)$ in the domain $G \subset R^2$, $G \subset \{x : 0 < \langle a, x\rangle + b < \pi\}$, $h(x) = \cos^2(\langle a, x\rangle + b)$ in the domain $G \subset R^2$, $G \subset \{x : -\frac{\pi}{2} < \langle a, x\rangle + b < \frac{\pi}{2}\}$ and $h(x) = [\sin(a_1x_1)\sin(a_2x_2)]^2$ in the domain $G \subset (0, \pi/a_1) \times (0, \pi/a_2), a_1 > 0, a_2 > 0$.

Exponential inhomogeneity functions $h(x)$ of type B were studied in Ma et al. [2, 17], Cheng et al. [18] and Wang [26], while in Li and weng [16] functions $h(x)$ of type A were used. Fundamental solutions for inhomogeneous purely elastic materials of type A–C have been derived by Rangelov et al. [24]. Several BVPs with BIEM for isotropic and anisotropic inhomogeneous materials of types A and B, respectively were solved in Manolis et al. [8] and Dineva et al. [20].

It shall be noted that beside the above mentioned inhomogeneity types, for which the fundamental solution can be derived in a closed form, there exists another class of functions $h(x)$ fulfilling the condition (11.10). Let's assume the solid G is a bounded simple connected domain and let $G \subset \text{int}(G_1)$, where the simple connected domain G_1 has a smooth boundary ∂G_1. There exists a function $g(x)$ that is the first eigenfunction of the Dirichlet problem for the Laplacian in G_1:

$$\begin{cases} -\triangle g = \lambda_g g, x \in G_1, \\ g = 0 \text{ on } \partial G_1. \end{cases} \tag{11.11}$$

Moreover, $g(x) > 0$ in $int(G_1)$ and the function $g(x)$ is convex and unique with respect to a positive constant multiplier, see Courant and Hilbert [6]. It is obvious that $h^{1/2}(x) = g(x)$ satisfies the condition (11.10). Since in the derivation of the fundamental solution only these conditions are used, it follows that if the inhomogeneity is defined by the function $h(x) = g^2(x)$, the fundamental solution of Eq. (11.1) exists in a closed form.

In the numerical examples we consider and compare the homogeneous case (0): $h = 1$ and the following three types of inhomogeneous material behaviour: (q) quadratic, type A: $h_q(x) = (a_1x_1 + a_2x_2 + 1)^2$; (e) exponential, type B: $h_e(x) = e^{2(a_1x_1+a_2x_2)}$; (s) sinusoidal, type C: $h_s(x) = \sin^2(a_1x_1 + a_2x_2 + 1)$.

Let us shortly show the difference between the three inhomogeneous types on the level of fundamental solutions.

To derive the fundamental solution we apply the Radon transform to both sides of Eq. (11.9), and with $|m| = 1$ we obtain

$$[C^0_{iJKi}m_i^2\partial_s^2 + (\rho^0_{JK}\omega^2 - p_{JK})]\hat{U}^*_{KM} = -h^{-1/2}(\xi)\delta_{JM}\delta(s - \langle\xi, m\rangle). \quad (11.12)$$

Let us denote $p_{JK} = C^0_{iJKi}p$, then $p = 0$ for h_q, $p = |a|^2$ for h_e and $p = -|a|^2$ for h_s and the Eq. (11.12) in compact matrix form can be written

$$(M\partial_s^2 + \Gamma)\hat{U}^* = F, \quad (11.13)$$

where $\hat{U}^* = \{\hat{U}^*_{JK}\}$, $F = \{f_{JM}\} = -\{h^{-1/2}(\xi)\delta_{JM}\delta(s - \langle\xi, m\rangle)\}$,

$$M = \{C^0_{iJKi}m_i^2\} = \begin{pmatrix} c^0_{44} & e^0_{15} \\ e^0_{15} & -\varepsilon^0_{11} \end{pmatrix},$$
$$\Gamma = \{\rho^0_{JK}\omega^2 - C^0_{iJKi}p\} = \begin{pmatrix} \rho^0\omega^2 - c^0_{44}p & -e^0_{15}p \\ -e^0_{15}p & \varepsilon^0_{11}p \end{pmatrix}.$$

The difference between the three inhomogeneity types A–C consists in the sign of p_{JK} and in the domain G where $h(x)$ is defined.

The matrix Eq. (11.13) represents two systems of second order ODEs. Multiplying the second equation in Eq. (11.13) by $\frac{e^0_{15}}{\varepsilon^0_{11}}$ and adding it to the first one we obtain a new equivalent system of equations. Its first equation contains now only the functions $\hat{U}^*_{3J}$ and can be written as

$$(\partial_s^2 + \gamma)w = g\delta(s - \tau), \quad (11.14)$$

where $\gamma = (\rho^0\omega^2 - a_0p)a_0^{-1}$, $a_0 = c^0_{44} + \frac{e^{02}_{15}}{\varepsilon^0_{11}}$, and $w = \hat{U}^*_{33}$, $g = -h^{-1/2}(\xi)a_0^{-1}$ for $J = 3$ and $w = \hat{U}^*_{34}$, $g = -h^{-1/2}(\xi)\frac{e^0_{15}}{\varepsilon^0_{11}}a_0^{-1}$ for $J = 4$. The second equation remains unchanged. The solutions of (11.14) are shown in Sect. 3.2 and their type

can be exponential, trigonometric or polynomial depending on the value of the key parameter γ which can be positive, zero or negative. In the examples we have

For h_q: $\gamma = \rho^0\omega^2 a_0^{-1}$ and the solution is given by trigonometric functions;

For h_e: $\gamma = (\rho^0\omega^2 - a_0|a|)a_0^{-1}$ and with notation $\omega_0 = |a|\sqrt{a_0/\rho^0}$ the solution isgiven by exponential functions for $\omega < \omega_0$, by first order polynomial function for $\omega = \omega_0$ and by trigonometric functions for $\omega > \omega_0$;

For h_s: $\gamma = (\rho^0\omega^2 + a_0|a|)a_0^{-1}$ and the solution is given by exponential functions.

After solving also the second equation in (11.13) we obtain that $\hat{U}^*_{JK}$ is a linear combination of functions of the types $e^{i\beta|s-\tau|}$, $|s-\tau|$, $e^{i\alpha|s-\tau|}$. More precisely, for considered inhomogeneity functions h we have:

For h_q: With $k = \omega\sqrt{\rho^0/a_0}$ functions $\hat{U}^*_{JK}$ are already given in the homogeneous case, Eqs. (3.40), (3.42), where constants are with subscribes 0.

For h_e: With respect to the frequency ω there are the following three cases: For

$\omega < \omega_0, i.e. \gamma < 0$ with the notation $k = \sqrt{|\gamma|}$:

$$\hat{U}^*_{33} = -h^{-1/2}(\xi)\frac{1}{2ka_0}e^{k|s-\tau|},$$

$$\hat{U}^*_{34} = \hat{U}^*_{43} = -h^{-1/2}(\xi)\frac{1}{2ka_0}\frac{e^0_{15}}{\varepsilon^0_{11}}e^{k|s-\tau|},$$

$$\hat{U}^*_{44} = -h^{-1/2}(\xi)\left[\frac{1}{2ka_0}\left(\frac{e^0_{15}}{\varepsilon^0_{11}}\right)^2 e^{k|s-\tau|} - \frac{1}{\varepsilon^0_{11}}\frac{1}{2|a|}e^{|a||s-\tau|}\right]. \quad (11.15)$$

For $\omega = \omega_0$, i.e. $\gamma = 0$:

$$\hat{U}^*_{33} = -h^{-1/2}(\xi)\frac{1}{2a_0}|s-\tau|,$$

$$\hat{U}^*_{34} = \hat{U}^*_{43} = -h^{-1/2}(\xi)\frac{1}{2a_0}\frac{e^0_{15}}{\varepsilon^0_{11}}|s-\tau|,$$

$$\hat{U}^*_{44} = \frac{h^{-1/2}(\xi)}{2|a|}\left(\frac{1}{\varepsilon^0_{11}} - \frac{e^0_{15}}{a_0\varepsilon^0_{11}} + \frac{e^{02}_{15}}{a_0\varepsilon^0_{11}}\right)e^{|a||s-\tau|} - \frac{h^{-1/2}(\xi)}{2a_0}\left(\frac{e^0_{15}}{\varepsilon^0_{11}}\right)^2|s-\tau|. \quad (11.16)$$

For $\omega > \omega_0$, i.e. $\gamma > 0$ with the notation $k = \sqrt{\gamma}$:

$$\hat{U}^*_{33} = h^{-1/2}(\xi)\frac{i}{2ka_0}e^{ik|s-\tau|},$$

$$\hat{U}^*_{34} = \hat{U}^*_{43} = h^{-1/2}(\xi)\frac{i}{2ka_0}\frac{e^0_{15}}{\varepsilon^0_{11}}e^{ik|s-\tau|} \quad (11.17)$$

$$\hat{U}^*_{44} = h^{-1/2}(\xi)\left[\frac{i}{2ka_0}\left(\frac{e^0_{15}}{\varepsilon^0_{11}}\right)^2 e^{ik|s-\tau|} + \frac{1}{\varepsilon^0_{11}}\frac{1}{2|a|}e^{|a||s-\tau|}\right];$$

For h_s: With notation $k = \sqrt{\gamma}$:

$$\hat{U}^*_{33} = h^{-1/2}(\xi)\frac{i}{2ka_0}e^{ik|s-\tau|},$$
$$\hat{U}^*_{34} = \hat{U}^*_{43} = h^{-1/2}(\xi)\frac{i}{2ka_0}\frac{e^0_{15}}{\varepsilon^0_{11}}e^{ik|s-\tau|}$$
$$\hat{U}^*_{44} = h^{-1/2}(\xi)\left[\frac{i}{2ka_0}\left(\frac{e^0_{15}}{\varepsilon^0_{11}}\right)^2 e^{ik|s-\tau|}\right] - \frac{i}{2|a|\varepsilon^0_{11}}\left[1 - \frac{e^0_{15}}{\varepsilon^0_{11}} + \frac{ke^{02}_{15}}{a_0}\right]e^{i|a||s-\tau|}]; \tag{11.18}$$

Regarding the inverse Radon transform we use the corresponding formulae (3.20) for K and (3.15) for R^*.

11.4 Numerical Realization

Following the method presented in Chap. 4 for homogeneous piezoelectric materials, the non-hypersingular BIE formulation on the considered boundaries $S \cup S_{cr}$ is derived. For this purpose the displacements and the tractions are written as $u_J = u^0_J + u^c_J$, $t_J = t^0_J + t^c_J$, where u^0_J, t^0_J are the fields due to the external load on the boundary S of the crack free body, while the fields u^c_J, t^c_J are induced by the load $t^c_J = -t^0_J$ on the crack boundary S_{cr} with zero boundary conditions on the boundary S. The following system of non-hypersingular traction BIE for the problem (11.1)–(11.3) is obtained

$$\begin{aligned} t_J(x) = C_{iJKl}n_i(x)\int_{S^+_{cr}}[(\sigma^*_{\eta PK}(x,\xi)\Delta u^c_{P,\eta}(\xi) - \rho_{QP}\omega^2 u^*_{QK}(x,\xi)\Delta u^c_P(\xi))\delta_{\lambda l} \\ - \sigma^*_{\lambda PK}(x,\xi)\Delta u^c_{P,l}(\xi)]n_\lambda(\xi)dS_{cr} + C_{iJKl}n_i(x)\int_S[(\sigma^*_{\eta PK}(x,\xi)u^c_{P,\eta}(\xi) \\ - \rho_{QP}\omega^2 u^*_{QK}(x,\xi)u^c_P(\xi))\delta_{\lambda l} - \sigma^*_{\lambda PK}(x,\xi)u^c_{P,l}(\xi)]n_\lambda(\xi)dS \\ - C_{iJKl}n_i(x)\int_S u^*_{PK,l}(x,\xi)t^c_P(\xi)dS, \quad x \in S \cup S_{cr}. \end{aligned} \tag{11.19}$$

Here u^*_{KQ} is the fundamental solution of (11.5), $\sigma^*_{iJQ} = C_{iJKl}u^*_{KQ,l}$ is the corresponding stress, $t_J = \begin{cases} \frac{1}{2}t^c_J & \text{on } S \\ -t^0_J & \text{on } S_{cr} \end{cases}$ and $\Delta u^c_J = u^c_J|_{S^+_{cr}} - u^c_J|_{S^-_{cr}}$ is the generalized crack opening displacement. Furthermore, $x = (x_1, x_2)$ and $\xi = (\xi_1, \xi_2)$ denote the position vector of the observation point and source point, respectively.

Equation (11.19) constitute an integro-differential equation system for the unknowns Δu^c_J on S_{cr} and u^c_J, t^c_J on S. From its solution the generalized displacement u^c_J and traction t^c_J at each internal point can be determined by using the corresponding representation formulae, see Sect. 4.2.1.

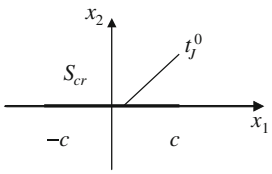

Fig. 11.2 Finite crack in an inhomogeneous plane under time-harmonic load t_J^0

The numerical solution scheme of Eq. (11.19) follows the procedure developed in Sect. 4.2.1 for homogeneous cracked piezoelectric solids, subjected to anti-plane electromechanical loading. The program code based on Mathematica and FORTRAN has been created following the above described procedure.

The mechanical dynamic stress intensity factor K_{III}^{σ} and the electrical displacement intensity factor K_{III}^{D} are obtained directly from the traction nodal values ahead of the crack-tip, see Eq. (2.41) e.g. for a straight crack of length $2c$, see Fig. 11.2 the relations read:

$$K_{III}^{\sigma} = \lim_{x_1 \to \pm c} t_3 \sqrt{2\pi(x_1 \mp c)}, \quad K_{III}^{D} = \lim_{x_1 \to \pm c} t_4 \sqrt{2\pi(x_1 \mp c)}, \tag{11.20}$$

where t_J is the generalized traction at the point $(x_1, 0)$ close to the crack-tip, see Sect. 2.6.2.

The BIEM formulation of the boundary value problem is valid for a finite cracked piezoelectric domain. However, in order to show more clearly the influence of the material inhomogeneity on the dynamic SIFs, the numerical study is done for a straight finite crack in an infinite domain. In this case disturbing wave reflections at the external boundary S do not occur.

11.4.1 Incident SH-Waves

Let us assume that the crack S_{cr} is described by the segment $(-c, c)$ on the axis Ox_1, see Fig. 11.2. Considered are normal incident time harmonic SH-waves leading along the crack S_{cr} to an anti-plane mechanical traction and in-plane electric displacement. The incoming wave for the different inhomogeneity types is given by

$$\text{For } h_q\text{: } u_J^0 = (a_1 x_1 + a_2 x_2 + 1)^{-1} \begin{pmatrix} 1 \\ \dfrac{e_{15}^0}{\varepsilon_{11}^0} \end{pmatrix} e^{ik_0 x_2}, \quad k_0 = \sqrt{\frac{\rho_0}{a_0}}\omega,$$

$$t_J^0|_{x_2=0} = a_0[-a_2 + ik_0(a_1 x_1 + 1)] \begin{pmatrix} 1 \\ 0 \end{pmatrix};$$

For h_e: $u_J^0 = e^{-(a_1 x_1 + a^2 x_2)} \begin{pmatrix} 1 \\ \frac{e_{15}^0}{\varepsilon_{11}^0} \end{pmatrix} e^{ik_e x_2}$, $k_e = \sqrt{\frac{\rho_0 \omega^2}{a_0} - |a|^2}$;

$$t_J^0|_{x_2=0} = a_0[-a_2 + ik_e] \begin{pmatrix} 1 \\ 0 \end{pmatrix};$$

For h_s: $u_J^0 = \sin^{-1}(a_1 x_1 + a_2 x_2 + 1) \begin{pmatrix} 1 \\ \frac{e_{15}^0}{\varepsilon_{11}^0} \end{pmatrix} e^{ik_s x_2}$, $k_s = \sqrt{\frac{\rho_0 \omega^2}{a_0} + |a|^2}$,

$$t_J^0|_{x_2=0} = a_0[-a_2 + ik_s \sin(a_1 x_1 + 1) + ik_s \cos(a_1 x_1 + 1)] \begin{pmatrix} 1 \\ 0 \end{pmatrix}.$$

The main inhomogeneity parameter, the vector $a = (a_1, a_2)$, can be written in polar coordinates as $(a_1, a_2) = r(\cos\alpha, \sin\alpha)$, where α and r are the direction and the magnitude of the inhomogeneity gradient. The cases $\alpha = 0$ and $\alpha = \pi/2$ correspond to the scenarios, where the material gradient is parallel or normal to the crack. At arbitrary angle α the direction of the material gradient is arbitrarily oriented to the crack, i.e. the material properties vary in both the vertical and lateral directions.

11.4.2 Validation Example

In order to validate the proposed solution method, the obtained BIEM results are compared with those of Wang and Meguid [27], who studied the homogeneous case, i.e. $r = 0$ by using the singular integral equation method. The respective material data of PZT-4 are given in Table 4.1. The absolute values of the normalized DSIF $K_{III}^* = \frac{K_{III}^\sigma}{\tau\sqrt{\pi c}}$, $\tau = t_3^0$ versus normalized frequency $\Omega = ck_0 \in [0.1, 1.4]$, are presented in Fig. 11.3. The following cases are considered : pure mechanical load: $t_3^0 = \tau, t_4^0 = 0$; electromechanicl load: $t_3^0 = \tau, t_4^0 = sd, d = \frac{\varepsilon_{11}^0}{e_{15}^0}\tau$, for $s = 0.5, 1.0$. The comparison shows that the maximum difference between the results is about 8–10 %. This figure shows also the effect of the frequency and the magnitude of the applied electromechanical load upon the normalized DSIF. The applied electrical displacement results in additional deformation, which may significantly affect the stress concentration at the crack-tip.

Regarding the difference it is worth mentioning that the used BIEM mesh in both the validation and parametric study is given by only five quadratic boundary elements along S_{cr}, where two of them are quarter point elements. Their lengths have been chosen as, $l_1 = l_5 = 0.15c$, $l_2 = l_4 = 0.56c$ and $l_3 = 0.58c$.

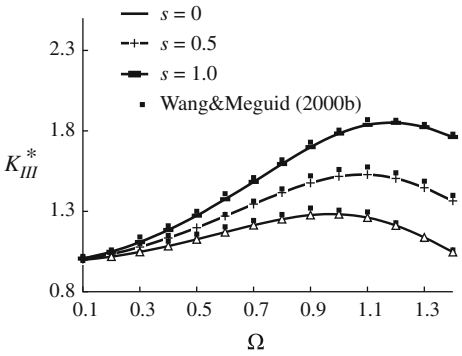

Fig. 11.3 Normalized DSIF K^*_{III} of a finite crack in a piezoelectric homogeneous plane

11.4.3 Parametric Study

The parametric study aims showing the sensitivity of the SIFs to the type (A, B or C) and characteristics (α, r) of the material inhomogeneity. The material used in the simulation study is PZT-6B whose data for the homogeneous case are given in Table 4.1. Note that for the considered cases (A)–(C) the fundamental solutions derived in Sect. 11.3 are composed by different types of special functions. In all figures curve (0) refers to the homogeneous material, while curves (q), (e) and (s) present solutions for material inhomogeneity of type A, B and C correspondingly. In addition, the sensitivity of the SIFs to the normalized frequency $\Omega = ck$ is evaluated where $k = k_0$ for (0) and (q) curves, $k = k_e$ for (e) curve and $k = k_s$ for (s)curve. The half-crack length is $c = 5$ mm and calculated is in most cases the normalized DSIF K^*_{III} and the normalized EDIF K^*_D, where $K^*_D = \dfrac{K^D_{III}}{d\sqrt{\pi c}}$, $d = \dfrac{\varepsilon^0_{11}}{e^0_{15}}\tau$, versus normalized frequency Ω in the interval [0.1, 1.4].

Figures 11.4, 11.5, 11.6, 11.7 and 11.8 show results for pure anti-plane mechanical loading, while Figs. 11.9 and 11.10 present solutions for combined electro-mechanical loading consisting of anti-plane time-harmonic mechanical and in-plane electrical load. Figure 11.11 concerns the case of pure electrical load.

Figure 11.4a, b displays K^*_{III} versus Ω at the left crack-tip (Fig. 11.4a) and the right crack-tip (Fig. 11.4b) for the different inhomogeneity types and the parameters $rc = 0.2$ and $\alpha = 0$, i.e. the material parameters vary continuously parallel to the crack. It can be seen that K^*_{III} is strongly dependent on the type of inhomogeneity. The homogeneous material (0) at both tips shows high stress intensity factors, but they are slightly exceeded at the left tip by the material types A and B. Material type C at both tips leads to relatively low K^*_{III}-values. Generally, the K^*_{III}-factors at the left crack-tip are higher than at the right tip.

In Fig. 11.5 K^*_{III} is again depicted for the same data, except the gradient direction, which is now $\alpha = \pi/2$, i.e. the material parameters vary continuously normal to the crack. Due to the symmetry the stress intensity factors are equal at both tips: $K^{*,L}_{III} = K^{*,R}_{III}$. The results for the homogeneous material and the types A and B

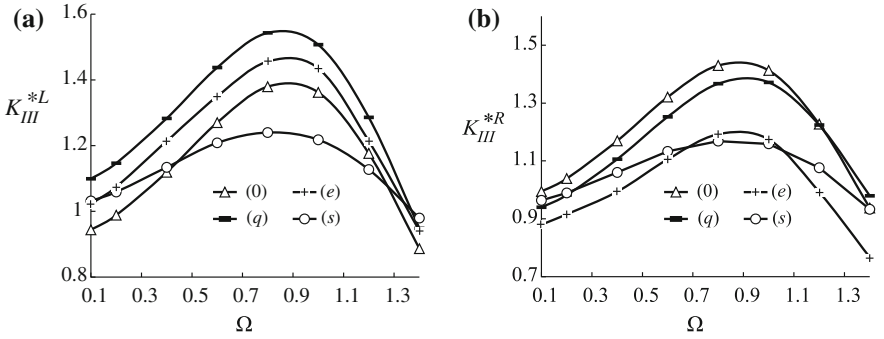

Fig. 11.4 Normalized DSIF K_{III}^{*} versus normalized frequency Ω for a material gradient parallel to the crack-plane ($\alpha = 0$) and the gradient parameter $rc = 0.2$: **a** *left* crack-tip; **b** *right* crack-tip

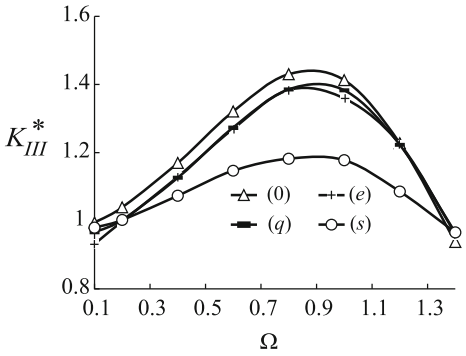

Fig. 11.5 Normalized DSIF K_{III}^{*} versus normalized frequency Ω for a material gradient normal to the crack plane ($\alpha = \pi/2$) and the gradient parameter $rc = 0.2$

show only slight differences while material type C again leads to considerable lower K_{III}^{*}-values.

Results for the gradient direction $\alpha = \pi/4$ are shown in Fig. 11.6a, b. The behaviour in this case is very similar to that for $\alpha = 0$. The dependence of K_{III}^{*} and K_{D}^{*} at both tips on the gradient direction $\alpha \in [0, \pi]$, $\alpha = m\dfrac{\pi}{12}$, $m = 0, 1, 2, ..., 12$ can be seen in Figs. 11.7, 11.9 and 11.10 for the fixed frequency $\Omega = 1.2$ and at $rc = 1.0$. Figure 11.8 compares K_{III}^{*}—values for the homogeneous case ($rc = 0$) and exponential type B of inhomogeneity at $rc = 0.2$ and $\alpha = 0$. The results show very clear the influence of the inhomogeneity on the dynamic stress concentration field.

Normalized DSIF K_{III}^{*} and normalized EDIF K_{D}^{*} at both crack-tips are displayed in Fig. 11.9 for different gradient directions, when the crack is loaded by a normal incident shear wave with $t_3^0 = \tau$ and in-plane electrical displacement $t_4^0 = d$ at $rc = 1.0$ and $\Omega = 1.2$. The material inhomogeneity is of quadratic type A. It is interesting to note that for the homogeneous material the EDIF K_{D}^{*} does not depend

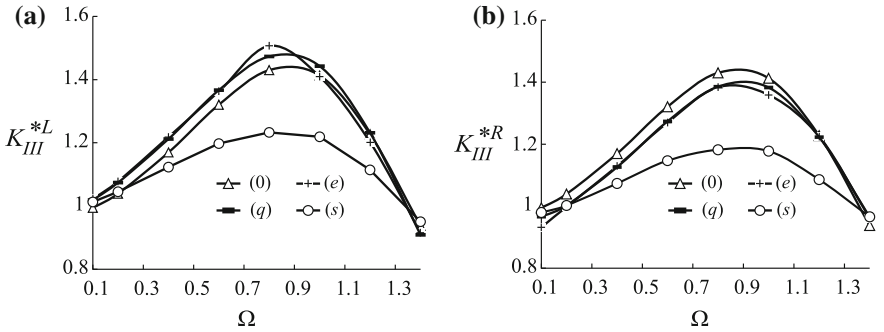

Fig. 11.6 Normalized DSIF K_{III}^{*} versus normalized frequency Ω for a gradient direction $\alpha = \pi/4$ and the gradient parameter $rc = 0.2$: **a** *left* crack-tip; **b** *right* crack-tip

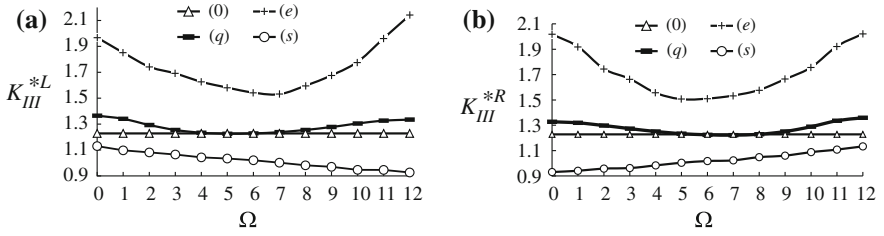

Fig. 11.7 Normalized DSIF K_{III}^{*} versus the angle of the material gradient at normalized frequency $\Omega = 1.2$, gradient parameter $rc = 1.0$: **a** *left* crack-tip; **b** *right* crack-tip

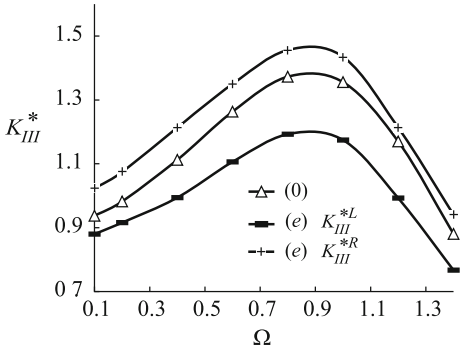

Fig. 11.8 Comparison of the DSIF K_{III}^{*} for $\alpha = 0$ and $rc = 0.0$, $rc = 0.2$, material inhomogeneity type B

on both the mechanical load and the frequency, see Wang and Meguid [27]. In the inhomogeneous case K_D^{*} depends strongly on the direction of the material gradient.

Figure 11.10a, b shows normalized SIFs vs. material gradient direction for quadratic type of inhomogeneity at fixed $rc = 1.0$ and $\Omega = 1.2$ for the electro-

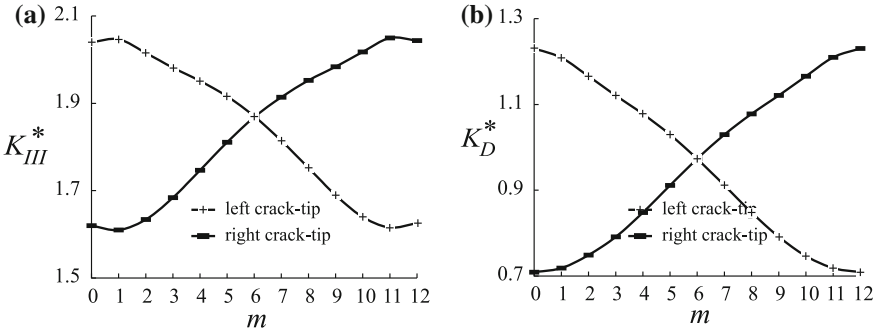

Fig. 11.9 Normalized DSIF K^*_{III} and EDIF K^*_D versus angle of material gradient for (q) case at normalized frequency $\Omega = 1.2$ of electromechanical load $t^0_3 = \tau$ and $t^0_4 = d$ at gradient parameter $rc = 1.0$: **a** K^*_{III}; **b** K^*_D

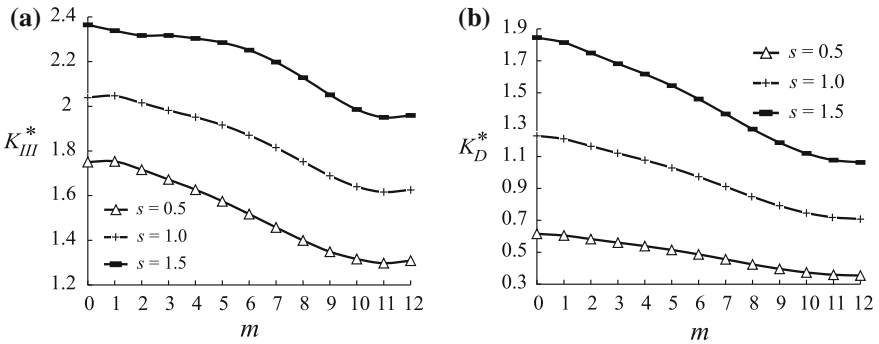

Fig. 11.10 Normalized DSIF K^*_{III} and EDIF K^*_D versus angle of material gradient for (q) inhomogeneity at normalized frequency $\Omega = 1.2$ and $rc = 1.0$ and combined electromechanical load $t^0_3 = \tau$ and $t^0_4 = sd$: **a** K^*_{III}; **b** K_D

mechanical loads $t^0_3 = \tau$, $t^0_4 = sd$ at $s = 0.5, 1.0, 1.5$. These figures demonstrate that the dynamic singular stress field around the crack-tip is governed not only by the applied stress and the applied electrical displacement, but also by the gradient of the piezoelectric material properties. The case of pure electrical load $t^0_3 = 0$, $t^0_4 = sd$ at $s = 0.5, 1.0, 1.5$ is presented in Fig. 11.11a, b. DSIF K^*_{III}, normalized by $\frac{e^0_{15}}{\varepsilon^0_{11}} d\sqrt{\pi c}$ is plotted in Fig. 11.11a, where it is shown that $K^*_{III} \neq 0$. The normalized EDIF K^*_D in Fig. 11.11b shows identical behaviour as in Fig. 11.10b. This is because, as in the homogeneous case (see [4, 15]) the dynamic singular electrical displacement field around the impermeable crack is independent of the applied mechanical stress but depends on the inhomogeneity of the piezoelectric materials and on the applied electrical load.

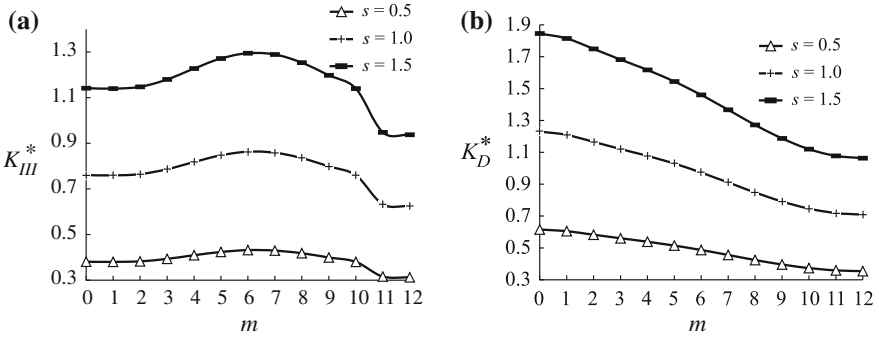

Fig. 11.11 Normalized DSIF K^*_{III} and EDIF K^*_D versus angle of material gradient for (q) inhomogenity at normalized frequency $\Omega = 1.2$ and $rc = 1.0$ and pure electrical load $t^0_3 = 0$ and $t^0_4 = sd$: **a** K^*_{III}; **b** K^*_D

The general conclusion from the results in Figs. 11.4, 11.5, 11.6, 11.7, 11.8, 11.9, 11.10 and 11.11 is that the dynamic crack-tip field is a complex result of the interaction between the dynamic electro-mechanical load and the piezoelectric material with its specific peculiarities like anisotropy, inhomogeneity and internal connectivity between mechanical and electrical fields. The numerical simulations demonstrate that the normalized SIF is sensitive to:

(i) the type of the material inhomogeneity;
(ii) the direction of the material gradient with respect to the crack;
(iii) the frequency of the applied dynamic load;
(iv) the magnitude of both mechanical and electrical dynamic load;
(v) the magnitude of the gradient parameter rc and its relation with the crack size.

11.5 Conclusions

The BIE formulation of the dynamic problem for a single-cracked finite inhomogeneous solid subjected to anti-plane mechanical and in-plane electrical loads is derived. Presented is an analytical methodology that derives the fundamental solutions for wave equations of certain classes of inhomogeneous piezoelectric materials. Using the obtained fundamental solutions an accurate numerical procedure and efficient BIEM software is developed for solving the problem in the frequency domain. The parametric study reveals the sensitivity of the coupled crack-tip fields to the type and magnitude of the material inhomogeneity, on the frequency and magnitude of the applied dynamic load and on the coupled electro-mechanical field.

References

1. Akamatsu M, Nakamura G (2002) Well-posedness of initial-boundary value problems for piezoelectric equations. Appl Anal 81:129–141
2. Chen J, Liu ZX, Zou ZZ (2003a) The central crack problem for a functionally graded piezoelectric strip. Int J Fract 121:81–94
3. Chen J, Soh AK, Liu J, Liu ZX (2004) Transient anti-plane crack problem of a func-tionally graded piezoelectric strip bonded to elastic layers. Acta Mech 169:87–100
4. Chen ZT (2006) Dynamic fracture mechanics study of an electrically impermeable mode III crack in a transversely isotropic piezoelectric material under pure electrical load. Int J Fract 141:395–402
5. Chue CH, Ou YL (2005) Mode III crack problems for two bonded functionally graded piezoelectric materials. Int J Solids Struct 42:3321–3337
6. Courant R, Hilbert D (1962) Methods of mathematical physics, vol II. Willey, New York
7. Delale F, Erdogan F (1983) The crack problem for a nonhomogeneous plane. J Appl Mech 50:609–614
8. Dineva P, Rangelov T, Manolis G (2007) Elastic wave propagation in a class of cracked functionally graded materials by BIEM. Comput Mech 39:293–308
9. Erdogan F (2000) Finite element technique for dynamic crack analysis in piezoelectrics. Int J Solids Struct 37:171–183
10. Gu P, Dao M, Asaro R (1999) A simplified method for calculating the crack-tip field of functionally graded materials using the domain integral. ASME J Appl Mech 66:101–108
11. Hu K, Zhong Z, Jin B (2005) Anti-plane shear crack in a functionally gradient piezoelectric layer bonded to dissimilar half spaces. Int J Mech Sci 47:82–93
12. John F (1955) Plane waves and spherical means applied to partial differential equations. Wiley International Science, New York
13. Keqiang H, Zheng Z, Bo J (2003) Electroelastic intensification near anti-plane crack in a functionally gradient piezoelectric ceramic strip. Acta Mech Solida Sinica 16(3):197–204
14. Kim JH, Paulino GH (2002) Finite element evaluation of mixed mode stress intensity factors in functionally graded materials. Int J Numer Meth Eng 53:1903–1935
15. Kuna M (2006) Finite element analyses of cracks in piezoelectric structures: a survey. Arch Appl Mech 76:725–745
16. Li C, Weng G (2002) Antiplane crack problem in functionally graded piezoelectric materials. J Appl Mech T ASME 69:481–488
17. Ma L, Wu LZ, Zhou ZJ, Guo LC, Shi LP (2004) Scattering of the harmonic anti-plane share waves by two collinear cracks in functionally graded piezoelectric materials. Eur J Mech A Solids 23:633–643
18. Ma L, Wu LZ, Zhou ZJ, Guo LC (2005) Scattering of the harmonic anti-plane share waves by a crack in functionally graded piezoelectric materials. Compos Struct 69:436–441
19. Manolis G, Shaw R (1996) Green's function for a vector wave equation in mildly heterogeneous continuum. Wave Motion 24:59–83
20. Manolis G, Dineva P, Rangelov T (2004) Wave scattering by cracks in inhomogeneous continua using BIEM. Int J Solids Struct 41:3905–3927
21. Oztruk M, Erdogan F (1996) Axisymetric crack problem in bonded materials with a graded interfacial region. Int J Solids Struct 33:193–219
22. Pan E, Amadei B (1999) Boundary element analysis of fracture mechanics in anisotropic bimaterials. Eng Anal Bound Elem 23:683–691
23. Rangelov T, Dineva P (2007) Dynamic behaviour of a cracked inhomogeneous piezoelectric solid. Anti-plane case. C R Acad Bulg Sci 60(3):231–238
24. Rangelov T, Manolis G, Dineva P (2005) Elastodynamic fundamental solutions for 2 D inhomogeneous anisotropic domains: basic derivations. Eur J Mech A Solids 24:820–836
25. Rangelov T, Dineva P, Gross D (2008) Effect of material inhomogeneity on the dynamic behavior of cracked piezoelectric solids: a BIEM approach. ZAMM-Z Angew Math Mech 88:86–99

26. Wang BL (2003) A mode III crack in functionally graded piezoelectric materials. Mech Res Commun 30:151–159
27. Wang XD, Meguid SA (2000b) Modelling and analysis of the dynamic behaviour of piezoelectric materials containing interfacing cracks. Mech Mater 32:723–737
28. Yue ZQ, Xiao HT (2002) Generalized Kelvin solution based boundary element method for crack problems in multilayered solids. Eng Anal Bound Elem 26:691–705
29. Zhang C, Savidis A, Zhu H (2001) A time domain BIEM for crack analysis in functionally graded materials under impact loading. In: Denda M, Aliabadi MH, Charafi A (eds) Advances in boundary element techniques II. Hoggar Press, Plan-les-Ouates, pp 405–415
30. Zhang C, Savidis A, Savidis G, Zhu H (2003) Transient dynamic analysis of a cracked functionally graded material by a BIEM. Comput Mater Sci 26:167–174
31. Zhang C, Sladek J, Sladek V (2003a) Effects of material gradients on transient dynamic mode-III stress intensity factors in a FGM. Int J Solids Struct 40:5251–5270

Chapter 12
Multiple Anti-plane Cracks in Quadratically Inhomogeneous Piezoelectric Finite Solids

Abstract Anti-plane cracks in finite functionally graded piezoelectric solids under time-harmonic loading are studied. The formulation allows for a quadratic variation of the material properties in arbitrary direction. The numerical solution provides the displacements and traction on the external boundary as well as the crack opening displacements from which the mechanical SIF and the EDIF are determined. Several examples for single and multiple straight and curved cracks show the influence of the different system parameters.

12.1 Introduction

The work is an extension of previous Chaps. 8, 10 and 11. In Chap. 11 fundamental solutions have been derived analytically for the anti-plane dynamic case concerning certain classes of FGPM including variable material characteristics of quadratic, exponential and sinusoidal type. A BIE formulation was presented for a cracked inhomogeneous solid subjected to anti-plane mechanical and in-plane electrical loads. In Chap. 11 crack interaction and the influence of external boundaries was not taken into consideration. This was done in Chap. 8 were multiple in-plane crack interaction in infinite domains has been studied, but it did not account for the material inhomogeneity and did not consider finite piezoelectric anti-plane cracked solids. In-plane crack analysis of functionally graded piezoelectric solids under time-harmonic loads was considered in Chap. 10, where an investigation of the combined effect of the material inhomogeneity, the frequency and the geometry of the crack scenario was presented and discussed. Based on the results in Chaps. 8, 10 and 11 and following Dineva et al. [5], the present chapter aims to evaluate the dynamic stress concentration field in a finite functionally graded piezoelectric solid with anti-plane cracks as a complex result from the mutual influence of the key factors like:

- the type and characteristics of the dynamic electromechanical load,

P. Dineva et al., *Dynamic Fracture of Piezoelectric Materials*,
Solid Mechanics and Its Applications 212, DOI: 10.1007/978-3-319-03961-9_12,

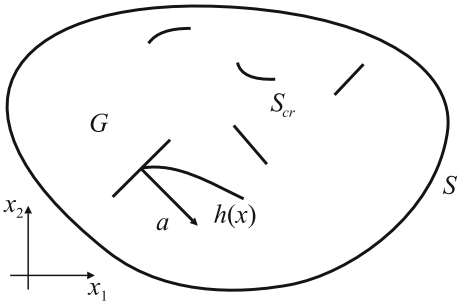

Fig. 12.1 2D inhomogeneous finite anti-plane cracked piezoelectric solid

- the piezoelectric material with its specific peculiarities as electro-mechanical coupling, anisotropy and quadratically varying inhomogeneity in arbitrary direction,
- the geometry of the crack scenario including multiple cracks interaction and the influence of the the external boundary.

For this aim a numerical scheme based on the non-hypersingular traction based BIEM is developed, validated and applied.

12.2 Statement of the Problem

Although some parts of the problem statement can be found in Chap. 11 they are repeated here in order to make the text to be self-contained. In a Cartesian coordinate system $Ox_1x_2x_3$ in R^3 consider a finite transversely isotropic functionally graded piezoelectric solid G with a smooth boundary S, poled in Ox_3 direction containing N internal finite arbitrary shaped cracks $S_{cr}^k = S_{cr}^{k+} \cup S_{cr}^{k-}, k = 1, \cdots N$, of arc length $2c_k$, see Fig. 12.1. Let G be subjected to a time-harmonic anti-plane mechanical and in-plane electrical load with a frequency ω. The only non-vanishing displacements are the anti-plane mechanical displacement $u_3(x_1, x_2)$ and the in-plane electrical displacements $D_i(x_1, x_2)$. Since all fields are time-harmonic with the frequency ω, the common multiplier $e^{i\omega t}$ is suppressed here and in the following. For such a case, assuming quasi-static approximation of piezoelectricity, the field equations in absence of body forces are given by the balance equations

$$\sigma_{i3,i} + \rho\omega^2 u_3 = 0, \qquad D_{i,i} = 0, \tag{12.1}$$

the strain-displacement and electric field-potential relations

$$s_{i3} = u_{3,i}, \qquad E_i = -\phi_{,i} \tag{12.2}$$

and the constitutive relations, see Sect. 2.5.2

$$\begin{aligned} \sigma_{i3} &= c_{44} s_{i3} - e_{15} E_i, \\ D_i &= e_{15} s_{i3} + \varepsilon_{11} E_i. \end{aligned} \tag{12.3}$$

Here $\sigma_{i3}, s_{i3}, E_i, \phi$ are the stress tensor, strain tensor, electric field vector and the electric potential, respectively, $i = 1, 2$, subscript commas denote partial differentiation and the summation convention for repeated indices is applied. Furthermore, $\rho, c_{44}, e_{15}, \varepsilon_{11}$ are the mass density, the shear stiffness, the piezoelectric and the dielectric permittivity.

Suppose that the mass density and the material parameters vary in the same manner with $x = (x_1, x_2)$ through the function $h(x) = (a_1 x_1 + a_2 x_2 + 1)^2$, i.e.

$$c_{44} = c_{44}^0 h(x), \quad e_{15} = e_{15}^0 h(x), \quad \varepsilon_{11} = \varepsilon_{11}^0 h(x), \quad \rho = \rho^0 h(x). \tag{12.4}$$

Restrictions on the inhomogeneity function $h(x)$ are due to the nondegeneracy of the Eq. (12.1), i.e.

$$\overline{G} \cap \{(x_1, x_2) : a_1 x_1 + a_2 x_2 + 1 = 0\} = \emptyset. \tag{12.5}$$

The Poisson's ratio can be assumed to be constant, see Delale and Erdogan [3, 4] owing to the fact that its variation within a practical range has a rather insignificant influence on the magnitude of the crack-tip driving force. So, in our case of the anti-plane crack the only elastic module—the shear modulus (resp. Young's modulus) will vary, but the Poisson ratio is a constant. The same approach for anti-plane crack problem is used by Li and Weng [6, 7], Wang [12], Chen and Liu [1], Singh et al. [10, 11], Collet et al. [2]. The assumption that the elastic, piezoelectric and dielectric properties vary in one and the same manner is a necessary idealization to avoid the mathematical complexity of the considered problem. However, even in this case it is worth to do such a research as far as it reveals the complex character of the dynamic stress and electric field concentrations around cracks. Also the obtained results can be used as benchmark problem solutions.

The inhomogeneity parameter, the vector $a = (a_1, a_2)$, can be written in polar coordinates as $a = r(\cos\alpha, \sin\alpha)$, where α and r are the direction and the magnitude of the inhomogeneity gradient.

The basic Eqs. (12.2) and (12.3) can be written in a more compact form if the notation of the generalized displacement $u_J = (u_3, \phi)$ is introduced. The constitutive Eq. (12.3) then takes the form

$$\sigma_{iJ} = C_{iJKl} u_{K,l} \quad i, l = 1, 2, \quad J, K = 3, 4, \tag{12.6}$$

where $C_{iJKl} = h(x) C_{iJKl}^0$,

$$C_{i33l}^0 = \begin{cases} c_{44}^0, & i = l \\ 0, & i \neq l \end{cases}, \quad C_{i43l}^0 = C_{i34l}^0 = \begin{cases} e_{15}^0, & i = l \\ 0, & i \neq l \end{cases}, \quad C_{i44l}^0 = \begin{cases} -\varepsilon_{11}^0, & i = l \\ 0, & i \neq l \end{cases}$$

and Eq. (12.1) reduces to

$$\sigma_{iJ,i} + \rho_{JK}\omega^2 u_K = 0, \quad J, K = 3, 4, \tag{12.7}$$

with the generalized mass density $\rho_{JK} = \begin{cases} \rho, J = K = 3 \\ 0, J = 4 \text{ or } K = 4 \end{cases}$.

Note that Eq. (12.7) in conjunction with Eq. (12.6) must be regarded as a system with non-constant coefficients since the material parameters depend on x.

The boundary condition on the outer boundary S are given by a prescribed displacement $\bar{u}_J$ on the part of the boundary S_u and prescribed traction $\bar{t}_J$ on the complementary part S_t, $S = S_u \cup S_t$, $S_u \cap S_t = \emptyset$ i.e.

$$u_J(x) = \bar{u}_J(x) \quad \text{on } S_u, \quad t_J(x) = \bar{t}_J(x) \quad \text{on } S_t. \tag{12.8}$$

The boundary condition along each crack is

$$t_J = 0 \quad \text{on} \quad S_{cr} = \cup_1^N S_{cr}^k. \tag{12.9}$$

This means that the cracks are assumed to be free of mechanical traction as well as of surface charges, i.e. all cracks are electrically impermeable.

12.3 Numerical Procedure

One way to solve the boundary value problem presented by the Eqs. (12.7–12.9) numerically is to transform it into equivalent integro-differential equation along the boundaries $S \cup S_{cr}$. Our aim is to solve the BVP within the framework of a non-hypersingular traction BIEM and to determine the stress intensity factors occurring in the cracked solid.

The non-hypersingular traction based BIE is derived in Chap. 4 following the procedure given by Wang and Zhang [13] and Rangelov et al. [9] for the homogeneous case and shown in Chap. 11 for the considered inhomogeneous case. Using superposition principle the displacements and the stresses are represented as $u_J = u_J^0 + u_J^c$, $\sigma_{iJ} = \sigma_{iJ}^0 + \sigma_{iJ}^c$, where u_J^0, σ_{iJ}^0 are the fields due to the load on the external boundary S of the crack free body, while the fields u_J^c, σ_{iJ}^c are induced by the load $t_J^c = -t_J^0$ on the k-th crack line S_{cr}^k with zero boundary conditions on the external boundary S. Here $t_J = \sigma_{iJ} n_i$, n_i is the outward normal vector on S_{cr}^{k+}. The following system of BIE describes the posed boundary value problem

$$\frac{1}{2} t_J^0(x) = C_{iJKl} n_i(x) \int_S [(\sigma_{\eta PK}^*(x,\xi) u_{P,\eta}^0(\xi) - \rho_{QP}\omega^2 u_{QK}^*(x,\xi) u_P^0(\xi))\delta_{\lambda l} - \sigma_{\lambda PK}^*(x,\xi) u_{P,l}^0(\xi)] n_\lambda(\xi) dS - C_{iJKl} n_i(x) \int_S u_{PK,l}^*(x,\xi) t_P^0(\xi) dS, \quad x \in S, \tag{12.10}$$

$$
\begin{aligned}
t_J(x) = C_{iJKl} n_i(x) \sum_{k=1}^{N} \int_{S_{cr}^{k+}} [(\sigma^*_{\eta PK}(x,\xi) \Delta u^{c,k}_{P,\eta}(\xi) \\
- \rho_{QP}\omega^2 u^*_{QK}(x,\xi)\Delta u^{c,k}_{P}(\xi))\delta_{\lambda l} - \sigma^*_{\lambda PK}(x,\xi)\Delta u^{c,k}_{P,l}(\xi)]n_\lambda(\xi) dS^k_{cr} \\
+ C_{iJKl} n_i(x) \int_S [(\sigma^*_{\eta PK}(x,\xi) u^c_{P,\eta}(\xi) - \rho_{QP}\omega^2 u^*_{QK}(x,\xi)\Delta u^c_P(\xi))\delta_{\lambda l} \\
- \sigma^*_{\lambda PK}(x,\xi) u^c_{P,l}(\xi)]n_\lambda(\xi) dS - C_{iJKl} n_i(x) \int_S u^*_{PK,l}(x,\xi) t^c_P(\xi) dS, \; x \in S \cup S^+_{cr}.
\end{aligned}
\tag{12.11}
$$

Here, u^*_{JK} is the fundamental solution of Eq. (12.7), $\sigma^*_{iJQ} = C_{iJKl} u^*_{KQ,l}$ is the corresponding stress, $t_J = \begin{cases} t^c_J & \text{on } S \\ -t^{0,k}_J & \text{on } S^k_{cr} \end{cases}$ and $\Delta u^{c,k}_J = u^{c,k}_J|_{S^{+k}_{cr}} - u^{c,k}_J|_{S^{-k}_{cr}}$ is the generalized COD on the k-th crack S^k_{cr}. Furthermore, $x = (x_1, x_2)$ and $\xi = (\xi_1, \xi_2)$ denote the position vector of the observation and source point, respectively. The functions $u_J, t_J, u^*_{JK}, \sigma^*_{iJQ}$ additionally depend on the frequency ω, which is omitted in the list of arguments for simplicity. Equations (12.10) and (12.11) constitute a system of integro-differential equations for the unknowns $\Delta u^{c,k}_J$ on the line S^k_{cr} of each crack and u^c_J, t^c_J on the external boundary S of the piezoelectric solid. From its solution the generalized displacement u_J at every internal point of G can be determined by using the corresponding representation formulae, see Sect. 4.2.1.

In order to solve the system of Eqs. (12.10) and (12.11), it is necessary to know the fundamental solution u^*_{JK} and its stress σ^*_{lQK} in a closed form. The fundamental solution of Eq. (12.7) is defined as solution of the equation

$$
\sigma^*_{iJM,i} + \rho_{JK}\omega^2 u^*_{KM} = -\delta_{JM}\delta(x,\xi), \tag{12.12}
$$

where δ is the Dirac distribution and δ_{JM} is the Kronecker symbol. The fundamental solution for the inhomogeneous solid under anti-plane mechanical and in-plane electrical loading is derived in Sect. 11.3 and we shortly present it here for the aim of completeness.

First, with a suitable change of functions, see Manolis and Shaw [8], Eq. (12.12) is transformed into an equation with constant coefficients. The smooth transformation $u^*_{JK} = h^{-1/2}(x) U^*_{JK}$ in G leads to an equation with constant coefficients for U^*_{JK}. The second step is to apply the Radon transform, see Zayed [15], and to obtain a system of ordinary differential equations. This system is decoupled via linear algebra tools. The third step is to apply the inverse Radon transform and to find the fundamental solution in the form

$$
u^*_{JK} = h^{-1/2}(x) U^*_{JK}(x,\xi) h^{-1/2}(\xi). \tag{12.13}
$$

Here the generalized function $U^*_{JK}(x,\xi)$ is the fundamental solution for the homogeneous anti-plane case, see Sect. 3.2 with the reference material constants C^0_{iJKl}. This fundamental solution and its associated stress are implemented in the FORTRAN program code for the numerical solution of the boundary-value problem.

The numerical procedure for the solution of the BVP follows the numerical algorithm developed in Chap. 4 and validated in Chap. 11.

The mechanical dynamic SIF K_{III} and the electrical displacement intensity factor K_D are obtained directly from the traction nodal values ahead of the crack-tip, (2.41). For example, in case of a straight crack, the interval $(-c, c)$ on the Ox_1 axis, the expressions are

$$K_{III} = \lim_{x_1 \to \pm c} t_3 \sqrt{2\pi(x_1 \mp c)}, \quad K_D = \lim_{x_1 \to \pm c} t_4 \sqrt{2\pi(x_1 \mp c)}, \tag{12.14}$$

where t_J is the generalized traction at the point $(x_1, 0)$ close to the crack-tip. Note that the asymptotic behaviour of stresses and electric displacements at the crack-tip is the same as for the homogeneous material, see Li and Weng [6] and Sect. 10.4.

12.4 Numerical Results

In all examples cracks are of length $2c = 5$ mm and they are discretisized by 7 BEs, while a total number of 20 ordinary quadratic BEs on the external boundary are used. Numerical studies showed that this number of BEs is sufficient to achieve an satisfactorily accuracy within the considered frequency range. The first and the last BEs on the cracks are quarter point BEs, while the remaining elements are ordinary quadratic BEs. Their lengths l_j are chosen as follows: $l_1 = l_7 = 0.375$ mm, $l_2 = l_6 = 0.5$ mm, $l_3 = l_5 = 1.0$ mm, $l_4 = 1.25$ mm. Considered is a piezoelectric cracked rectangular plate with dimensions 20×40 mm loaded by uniform time-harmonic electromechanical tension in x_2 direction with amplitudes $\sigma_0 = 400 \times 10^6$ N/m^2 and $D_0 = 0.1$ C/m^2, see Fig. 12.2. The electro-mechanical properties of the reference piezoelectric ceramic PZT 4 are shown in Table 4.1.

Since there are no SIF results available for finite cracked piezoelectric solids with quadratically varying material properties subjected to time-harmonic anti-plane mechanical and in-plane electrical loading, the validation of the numerical scheme is possible only by comparing the BIEM results with results of other authors for the homogeneous case. For this purpose the inhomogeneity function $h(x)$ in the developed program code for the inhomogeneous case must simply be set to one.

In the following the BIEM results are compared with the results of Wang and Meguid [14], who used the singular integral equation method. They studied a single crack in an infinite homogeneous plane subjected to a mechanical load $t^0_3 = \tau = a_0 k$, $a_0 = c^0_{44} + \dfrac{e^{02}_{15}}{\varepsilon^0_{11}}$, $k = \sqrt{\rho^0 / a_0}$ of a normal incident SH-wave and an additional

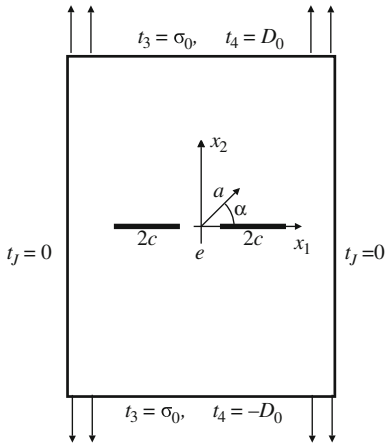

Fig. 12.2 Cracked rectangular inhomogeneous finite plate

electrical load $t_4^0 = sd$, $d = \dfrac{\varepsilon_{11}^0}{e_{15}^0}\tau$. A detailed discussion of a similar comparison is given in Chap. 11, which is restricted to infinite domains. In order to test the new BIE solution for finite piezoelectric solids, the results of Wang and Meguid [14] are now compared with the BIEM results for a center cracked square domain of size $w > 10c$ with $2w$ being the side length of the square. Figure 12.3a shows the normalized dynamic SIF $K_{III}^* = K_{III}/\tau\sqrt{\pi c}$ versus normalized frequency $\Omega = kc$ of the applied electro-mechanical load. An excellent coincidence between the results obtained by the different computational techniques can be observed. This underlines the good accuracy of the proposed traction based BIEM approach for the solution of 2D time-harmonic problems. This example also shows that remote external boundaries do not influence the results significantly in the considered frequency range. In Fig. 12.3b the results of Wang and Meguid [14] for $s = 0.5$ are compared with those of two collinear cracks with distance $e = 10c$ in an infinite plane. Because of the big distance the SIF K_{III}^* are expected to take nearly the same values as for as single crack since crack interaction is weak. The case of a cracked square plate of size $w > 10c$ (referred below as an infinite plate), with two cracks at distance $e = 7c$ subjected by the same time-harmonic load as in the previous example with $s = 0$ is also validated. As can be seen from Fig. 12.3b that the solution recovers again the results of Wang and Meguid [14]. The difference is not bigger than 8 % what indicates that the proposed method works for multiple cracks in a finite solid with high accuracy.

We now will discuss numerical results, which provide some insight in the effect of various system parameters on the SIFs as they are:

(a) the frequency of the applied load,
(b) the direction and magnitude of the material inhomogeneity,
(c) the electro-mechanical coupling,

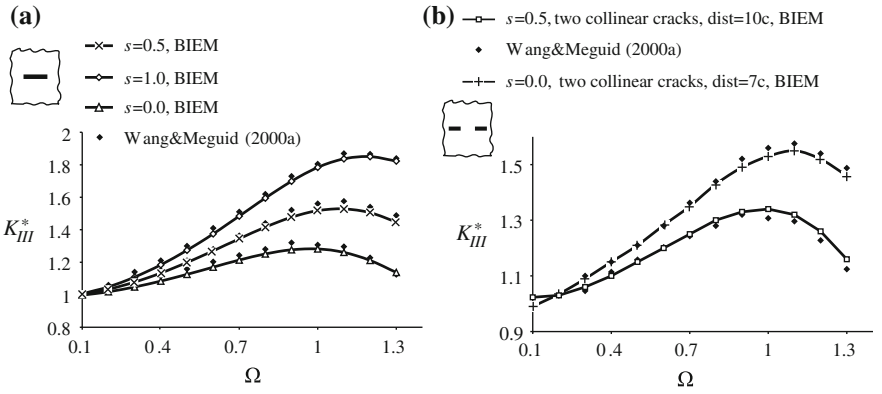

Fig. 12.3 Normalized SIF versus normalized frequency for a homogeneous infinite plate under electro-mechanical load: **a** single crack; **b** two collinear cracks

(d) the wave-crack, wave-material, crack-crack and crack-external boundary interaction,
(e) the geometry of the crack scenario.

The first series of numerical results concern a finite rectangular center cracked plate of PZT 4 having quadratically varying material properties with a prescribed magnitude and direction. The straight crack has the half-length c and the plate is loaded by a mechanical time-harmonic load with the amplitude $\sigma_0 = 400 \times 10^6\ \mathrm{N/m^2}$ and/or an in-plane electrical displacement with the amplitude $D_0 = 0.1\ \mathrm{C/m^2}$. Figure 12.4a, b, c show for a pure mechanical load how the normalized mechanical SIF K^*_{III} values depend on the frequency and on the direction and magnitude of the material inhomogeneity. For $\alpha = 90°$ the magnitude of the first peak at $\Omega \approx 0.15$ is highest for the homogeneous case ($rc = 0$) and lowest for the strongest inhomogeneity ($rc = 0.1$), see Fig. 12.4a. This tendency changes significantly with Ω and α. For example, at $\alpha = 20°$ the second peak at $\Omega \approx 0.45$ is highest for the strongest inhomogeneity ($rc = 0.1$) and lowest for the homogeneous case ($rc = 0$). In Fig. 12.5a, b, c for three different combinations of electromechanical loading, K^*_{III} curves for different inhomogeneity strengths rc at a fixed inhomogeneity direction $\alpha = 90°$ are compared. Figure 12.5b, c shows the results for pure mechanical and pure electrical loading, respectively. The necessary additional normalization in the latter figure is done by $D_0(e^0_{15}/\varepsilon^0_{11})$. As can be seen from the figures, for all three loading conditions the first peak is highest for the homogeneous case and lowest for the strongest inhomogeneity. The reversed tendency can be observed at the second peak. The height of the peaks strongly depends on the loading.

Figures 12.4 and 12.5 reveal that the stress field is a result of different physical phenomena and their mutual internal interaction. These physical phenomena are:

- wave-crack-external solid's boundary interaction that leads to more complex character of the SIFs curve;

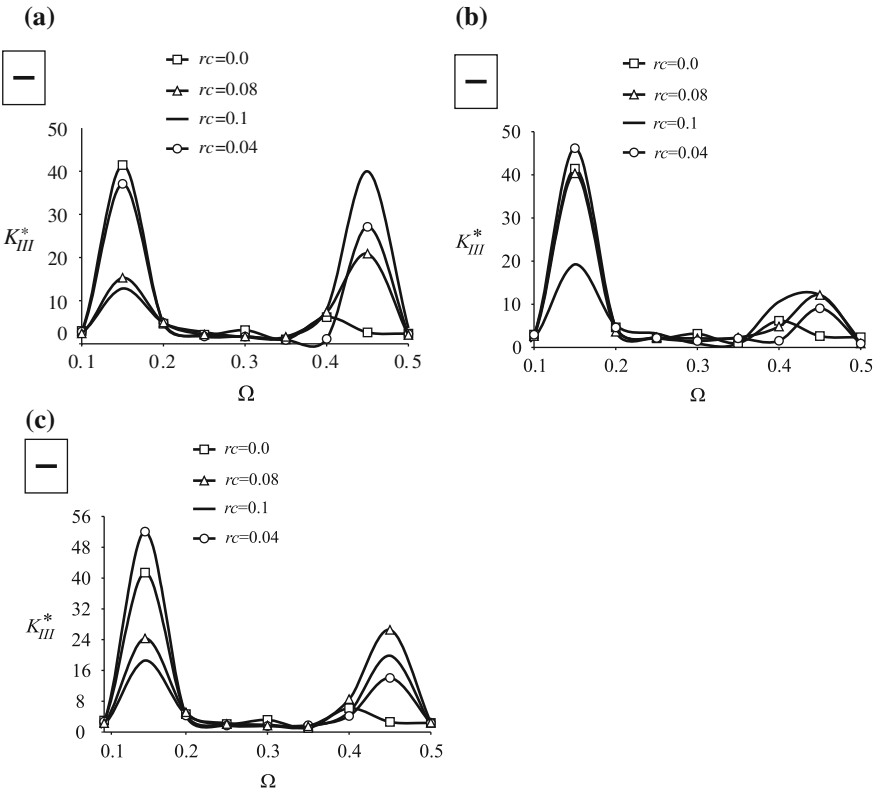

Fig. 12.4 Normalized SIF versus normalized frequency at the right crack-tip for an inhomogeneous finite plate under mechanical load for different inhomogeneity directions: **a** $\alpha = 90°$; **b** $\alpha = 45°$; **c** $\alpha = 20°$

- wave-material with its anisotropic, inhomogeneous coupled properties interaction that leads to the appearance and shifting of the resonance frequencies;
- type and characteristics of the applied electromechanical load (pure mechanical, pure electrical and hybrid electro-mechanical).

The second series of simulations concern two collinear cracks in a rectangular inhomogeneous plate. In Fig. 12.6a, b the normalized mechanical SIF K^*_{III} at the right crack-tip of the crack S^1_{cr} left from the origin of the coordinate system (see Fig. 12.2) is plotted versus normalized frequency Ω of the applied electro-mechanical load for two different crack distances and $\alpha = 90°$. For comparison the result for a single crack in a homogeneous plate is also displayed. As expected, the interaction effect of the collinear cracks increase with decreasing crack distance. Remarkable is also the frequency shift of the first peak between the collinear cracks and the single crack system. For the same loading conditions K^*_{III} curves for the right crack-tip of the crack S^1_{cr} are presented in Fig. 12.6a, b for the fixed crack distance $e = c/4$

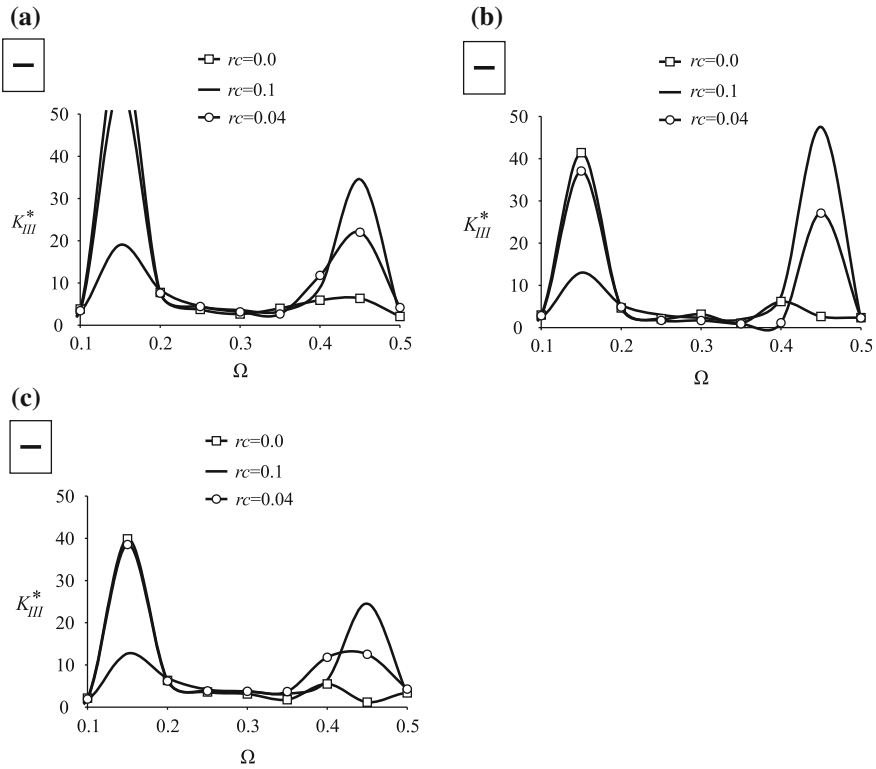

Fig. 12.5 Normalized SIF versus normalized frequency for an inhomogeneous finite plate under different mechanical and/or electrical loads for inhomogeneity direction $\alpha = 90°$: **a** $\sigma_0 = 400 \times 10^6$ N/m^2, $D_0 = 0.1$ C/m^2; **b** $\sigma_0 = 400 \times 10^6$ N/m^2, $D_0 = 0.0$ C/m^2; **c** $\sigma_0 = 0.0$ N/m^2, $D_0 = 0.1$ C/m^2

but for different inhomogeneity directions. Again, for comparison, the results for the homogeneous single crack and collinear crack configuration are displayed. It can be seen that the inhomogeneity direction as well as its strength influence the results significantly.

Figure 12.6 demonstrates convincingly that to the mutual internal play of the physical mechanisms of the wave-crack, the wave-material, the wave-solid's boundaries and the electro-mechanical interaction we must add the dynamic crack-crack interaction and as a whole the crack scenario with all its peculiarities.

The third group of examples concentrates on the results in an infinite plane, when there is no effect of the external boundary. For this purpose two collinear cracks under pure mechanical loading in an infinite domain with different inhomogeneity strength and direction are considered, see Figs. 12.7 and 12.8. Shown are K^*_{III} curves for the right crack-tip of the left crack S^1_{cr} for two different crack distances $e = 2c$ and $e = c/4$, respectively. A comparison with the results in Fig. 12.4 reveals the role

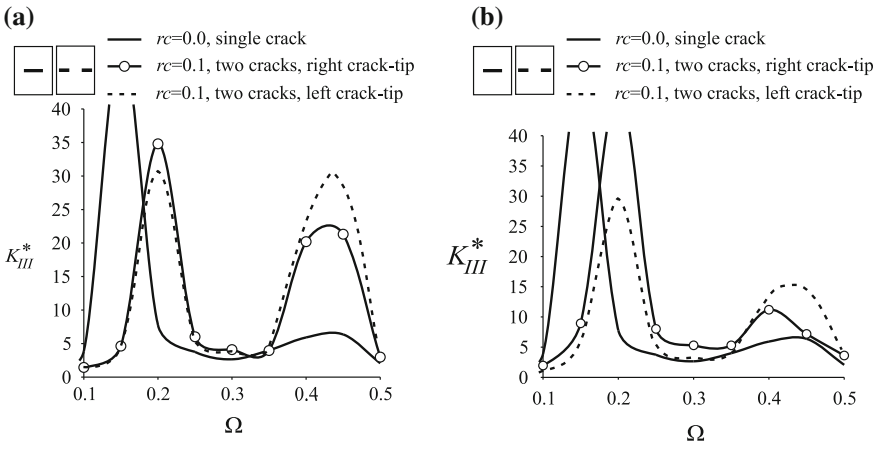

Fig. 12.6 Normalized SIF versus normalized frequency for an inhomogeneous finite plate with two collinear cracks under mechanical load $\sigma_0 = 400 \times 10^6$ N/m^2 and electrical load $D_0 = 0.1$ C/m^2 for the inhomogeneity direction $\alpha = 90°$: **a** $e = c/2$; **b** $e = c/4$

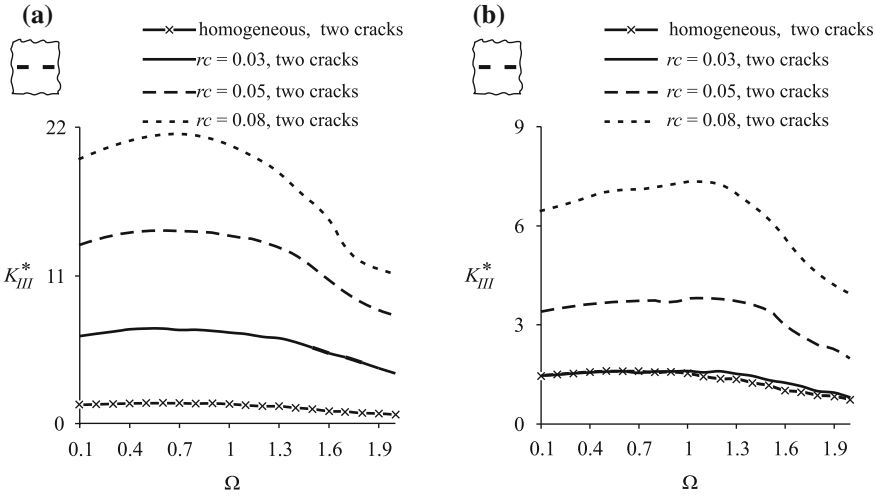

Fig. 12.7 Normalized SIF versus normalized frequency at the inner tip of the left crack of two collinear cracks at distance $e = 2c$ in an inhomogeneous infinite plane under mechanical load: **a** $\alpha = 90°$; **b** $\alpha = 20°$

of the reflected waves from the external boundary of the finite piezoelectric solid. Their interaction with the waves scattered by the crack shows the influence of the geometry of the crack scenario.

The fourth group of simulations covers results obtained for curvilinear cracks under pure mechanical loading in an infinite domain. Considered are convex and concave circular arcs with an opening angle $\beta = \pi/2$ and the radius $R = c\sqrt{2}$.

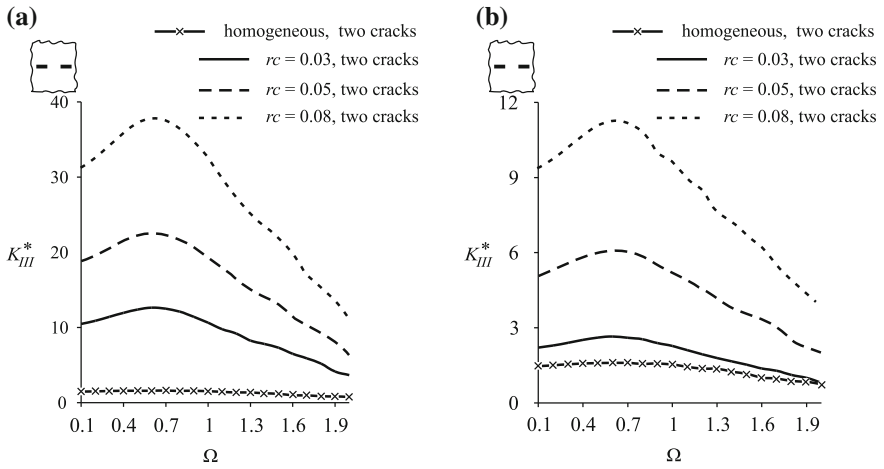

Fig. 12.8 Normalized SIF versus normalized frequency at the inner tip of the left crack of two collinear cracks at distance $e = c/4$ in an inhomogeneous infinite plane under mechanical load: **a** $\alpha = 90°$; **b** $\alpha = 20°$

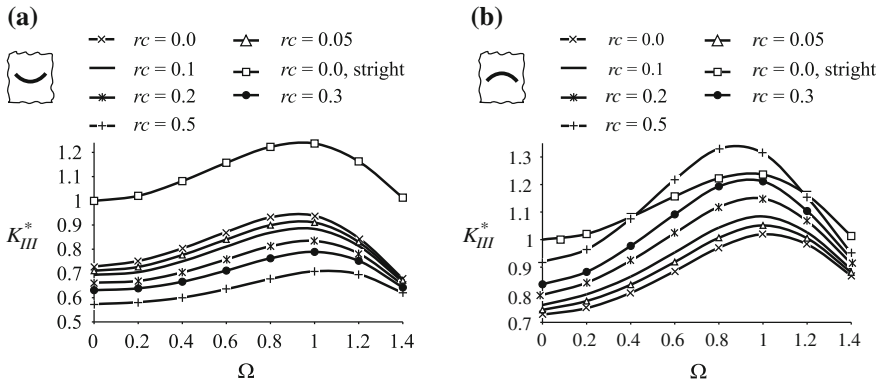

Fig. 12.9 Normalized SIF versus normalized frequency for an infinite inhomogeneous plane under mechanical load: **a** convex crack; **b** concave crack

Figure 12.9a, b shows for single arc cracks normalized K^*_{III} factors versus normalized frequency Ω for the inhomogeneity direction $\alpha = 90°$ and different inhomogeneity strengths rc. For comparison also the result for a straight crack in a homogeneous material is shown. For the convex crack K^*_{III} decreases with increasing inhomogeneity strength while the opposite tendency is observed for the concave crack. This simply can be explained by the local stiffness increase or decrease, respectively, at the crack-tip. The effect coming solely from the crack type can be seen more clearly in Fig. 12.10a, where K-factors for the convex and concave crack in a homogeneous material are compared. The deviation of both results increases with increasing frequency. The effect coming solely from the material inho-

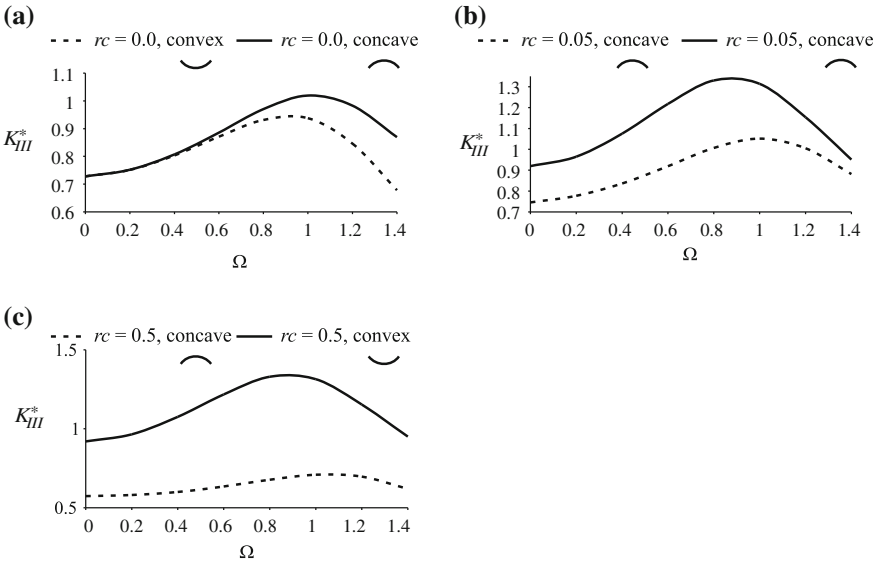

Fig. 12.10 Comparison of normalized SIF curves for the right crack-tip of a curvilinear crack in an inhomogeneous infinite plane under mechanical load (inhomogeneity direction $\alpha = 90°$): **a** convex and concave crack, $rc = 0.0$; **b** concave crack, $rc = 0.05$ and $rc = 0.5$; **c** convex and concave crack, $rc = 0.5$

mogeneity is shown in Fig 12.10b, where K^*_{III} curves for a concave crack for two different inhomogeneity strengths are depicted. Since the local stiffness is higher at the crack-tips for $rc = 0.5$ the K factors are higher than for $rc = 0.05$. The same explanation holds for Fig. 12.10c, where for a fixed inhomogeneity strength K curves for a convex and a concave crack are compared.

The wave-material interaction and the associated s resonance phenomena can be seen in Figs. 12.4, 12.5 and 12.6. It is clear that the value of the resonance is sensitive to the excitation frequency, to the properties of the material, like anisotropy, inhomogeneity and to the electro-mechanical coupling. The obtained simulation results reveal that the direction and the magnitude of material gradient have strong influence on the place of the resonance frequencies. The frequency dependence of the SIFs is more complex in the cases of two cracks in a finite plate, see Fig. 12.6. But even in the case of a single crack in an infinite inhomogeneous plane the wave-inhomogeneous material interaction is observed through the shift of the frequencies where the maximal values of the SIFs occur, see Fig. 12.10b.

All the curves in Figs. 12.8 and 12.9 reach a peak and then oscillate about the static value. It can be seen that the peak values are less than that for the homogeneous material. So, the conclusion is that the crack driving force can be reduced by using the concept for the FGPM and the idea to replace the homogeneous materials by smoothly inhomogeneous ones in the new smart structure technologies may work successfully. Taking all results together, the simulations show that:

(i) the inhomogeneity direction and strength may induce strong differences between the local fields at the left and right crack-tips;
(ii) the mechanical SIF and EDIF are frequency dependent and resonance phenomena occur;
(iii) the wave-crack, wave-material and crack-crack interaction effects play an important role;
(iv) the external boundary plays an equally important role since it is a source of reflected waves making the dynamic stress field more complex;
(v) the electro-mechanical coupling is essential for effects in piezoelectric materials;
(vi) the applied electrical loads affect the local stress field at the crack-tips;
(vii) the crack geometry is an important factor;
(viii) the material inhomogeneity-crack-tip interaction depends on the location of the crack-tip (left or right) and on its disposition in the overall cracks-solid configuration and geometry.

The proposed mechanical model combined with the validated numerical scheme has the potential to reveal and to study all these phenomena.

12.5 Conclusion

The two dimensional dynamic anti-plane crack problem of a functionally graded piezoelectric solid is solved in the frequency domain by means of non-hypersingular traction BIEM. The material properties vary quadratically in an arbitrary direction. Numerical examples for straight and curved center cracks and two collinear cracks in a rectangular plate under uniform electromechanical load are solved. The general conclusion from the simulations is that the dynamic stress field is a complex result of the dynamic electromechanical load (its type and characteristics), the piezoelectric material with its specific peculiarities like anisotropy, inhomogeneity, electro-mechanical coupling and the geometry of the crack scenario (multiple cracks, external boundary, crack-tip position, relation between crack length and sizes of the cracked solid, etc.). Numerical results demonstrate that the mechanical SIF and EDIF are sensitive to the direction and magnitude of the material inhomogeneity, dependent on the frequency of the applied load and on the relation between the magnitude of the gradient parameter and the crack size and that they are influenced strongly by the crack interaction and geometry of the crack system.

References

1. Chen J, Liu ZX (2005) On the dynamic behavior of a functionally graded piezoelectric strip with periodic cracks vertical to the boundary. Int J Solids Struct 42:3133–3146
2. Collet B, Destrade M, Maugin G (2006) Bleustein–Gulyaev waves in some functionally graded materials. Eur J Mech A Solids 25:695–706

3. Delale F, Erdogan F (1983) The crack problem for a nonhomogeneous plane. J Appl Mech 50:609–614
4. Delale F, Erdogan F (1988) On the mechanical modeling of the interfacial region in bonded half-planes. J Appl Mech 55:317–324
5. Dineva P, Gross D, Müller R, Rangelov T (2010b) BIEM analysis of dynamically loaded anti-plane cracks in graded piezoelectric finite solids. Int J Solids Struct 47:3150–3165
6. Li C, Weng G (2002a) Antiplane crack problem in functionally graded piezoelectric materials. ASME J Appl Mech 69:481–488
7. Li C, Weng GJ (2002b) Yoffe-type moving crack in a functionally graded piezoelectric material. Proc R Soc Lond A 458:381–399
8. Manolis G, Shaw R (1996) Green's function for a vector wave equation in mildly heterogeneous continuum. Wave Motion 24:59–83
9. Rangelov T, Dineva P, Gross D (2008) Effect of material inhomogeneity on the dynamic behavior of cracked piezoelectric solids: a BIEM approach. ZAMM-Z Angew Math Mech 88:86–99
10. Singh BM, Rokne J, Dhaliwal RS (2007) The study of dynamic behaviour of functionally graded piezoelectric materials and an application to a contact problem. Q Appl Math 65(1):155–162
11. Singh BM, Rokne J, Dhaliwal RS, Vrbik J (2009) Scattering of anti-plane shear wave by an interface crack between two bonded dissimilar functionally graded piezoelectric materials. Proc R Soc A 465:1249–1269
12. Wang BL (2003) A mode III crack in functionally graded piezoelectric materials. Mech Res Commun 30:151–159
13. Wang CY, Zhang Ch (2005) 2 D and 3 D dynamic Green's functions and time-domain BIE formulations for piezoelectric solids. Eng Anal Bound Elem 29:454–465
14. Wang XD, Meguid SA (2000a) Effect of electromechanical coupling on the dynamic interaction of cracks in piezoelectric materials. Acta Mech 143:1–15
15. Zayed A (1996) Handbook of generalized function transformations. CRC Press, Boca Raton

Chapter 13
Anti-plane Cracks in Exponentially Inhomogeneous Finite Piezoelectric Solid

Abstract Anti-plane cracked functionally graded finite piezoelectric solids under time-harmonic elecro-mechanical load are studied by a non-hypersingular traction boundary integral equation method. Exponentially varying material properties are considered. Numerical solutions are obtained by using Mathematica. The dependence of the mechanical stress intensity factor and electrical field intensity factor on the inhomogeneous material parameters, on the type and frequency of the dynamic load and on the crack position are numerically analyzed by illustrative examples.

13.1 Introduction

Mathematical modeling of finite cracked solids of FGPM leads to a boundary value problem for a coupled electro-mechanical system of partial differential equations with non-constant coefficients.

The solution of problems for inhomogeneous piezoelectric solids requires advanced numerical methods because of the high mathematical complexity. The dual integral equations approach used in the most of the papers is restricted to the problems with simple geometry and boundary conditions. This method is developed in [4, 5, 16, 17, 22] for investigating anti-plane cracks in a plane or in a strip with varying exponentially properties in a direction parallel or perpendicular to the crack line. Transforming the BVP to dual integral equations along the crack, the SIF is evaluated solving Fredholm integral equation. Modern computational techniques like finite element method and BIEM are applied for more general fracture analysis of piezoelectric solids. So far, most commercial software is available mainly for a static piezoelectric analysis and mostly it is based on FEM. FEM results for a solution of crack problems of piezoelectric solids are shown in [1, 12, 13, 25]. The application of FEM for the solution of dynamic fracture problems of PEM is discussed in [8–10]. A survey of FEM results for cracks in piezoelectric structures is presented in Kuna [14]. Most of the results concern cracks in infinite homogeneous piezoelectric solids and

P. Dineva et al., *Dynamic Fracture of Piezoelectric Materials*,
Solid Mechanics and Its Applications 212, DOI: 10.1007/978-3-319-03961-9_13,

only a few papers consider finite bounded solids. A numerical example for a finite rectangular in-plane cracked plate under transient loading conditions is solved by FEM in Enderlein et al. [10]. However, numerical techniques for 2D and 3D cracked finite piezoelectric solids are still under development, as it is concluded by Kuna [14]. This is even more true for inhomogeneous bounded cracked solids subjected to dynamic electro-mechanical loading. Here the BIEM is an efficient alternative method. The main difficulty in application of the BIEM to this type of materials is the derivation of the fundamental solution of the governing equation describing wave propagation in piezoelectric inhomogeneous media. The difficulty steams from the combination of the material anisotropy, the coupled character of the field variables, the quasi-static approximation of the electric field and the dependence of the material properties on the space variables. Additionally, when cracks are considered, the conventional displacement BIEM degenerates. Therefore, alternative techniques proposed for the elastic case as sub-region technique, established by Blandford et al. [3], dual BIEM [23], hypersingular [29] and non-hypersingular traction BIEM [28] should be applied. The elastodynamic fundamental solution for the general inhomogeneous transversely-isotropic piezoelectric solid is still not available. In Rangelov et al. [21], see Chap. 11, elastodynamic fundamental solutions for certain classes of FGPM, of quadratic, exponential and sinusoidal type, have been derived by the Radon transform. The results are mainly for cracks in infinite inhomogeneous solids. The dynamic behaviour of a cracked finite solid for the quadratic type of material gradient is studied in Dineva et al. [7], see Chap. 12. When the BIEM formulation is applied, the BVP is transformed to an equivalent integro-differential equation along the crack line and along the external boundary of the considered solid. After obtaining the numerical solution at every point of the domain, the SIF can be evaluated, i.e., the leading coefficient in the asymptotic of the generalized displacement and stress solutions near the crack tips.

To our knowledge, there are no results for a finite cracked transversely isotropic piezoelectric exponentially inhomogeneous solid subjected to anti-plane mechanical and/or in-plane electrical dynamic time-harmonic loading. This is the motivation to propose an efficient non-hypersingular traction BIEM for the solution of anti-plane dynamic fracture problems concerning piezoelectric transversely isotropic exponentially inhomogeneous finite solid. The chapter follows Marinov and Rangelov [18, 19] and Dineva et al. [7].

The essential items in the current chapter are:

(i) an efficient numerical BIEM scheme is proposed for solving the anti-plane dynamic problem of a finite cracked exponentially inhomogeneous transversely isotropic piezoelectric solid;
(ii) the material gradient has an arbitrary direction with respect to the crack line, while in the most published cases the material properties vary along or perpendicular to the crack line;
(iii) the dynamic behaviour of the cracked solid depends on the frequency of the applied load, on the reference material properties and on the magnitude of the material gradient. Two types of solutions are considered, namely the first

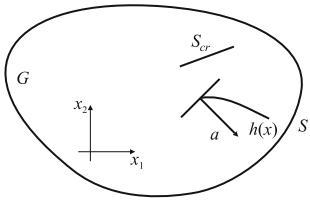

Fig. 13.1 Cracked inhomogeneous finite solid

for frequencies higher than the defined critical frequency, where the dynamic behaviour is described by a wave propagation process, and the second for frequencies lower than the defined critical frequency, where only simple vibrations occurs.

13.2 Statement of the Problem

In a Cartesian coordinate system Ox in R^3 consider a finite transversally isotropic piezoelectric solid $G \in R^2$, with boundary S and poled in Ox_3 direction. Let $S_{cr} = S_{cr}^+ \cup S_{cr}^-$, $S_{cr} \subset \Omega$ is an internal straight crack—an open segment, see Fig. 13.1.

Assume that G is subjected to anti-plane mechanical and in-plane electrical time-harmonic load. The only non-vanishing displacements are the anti-plane mechanical displacement $u_3(x,t)$ and the in-plane electrical displacement $D_i(x,t), i = 1,2$, $x = (x_1, x_2)$. Since all fields are time-harmonic with frequency ω, the common multiplier $e^{i\omega t}$ is suppressed here and in the following. Assuming the quasi-static approximation of piezoelectricity, the field equation in absence of a body force and an electric charge is presented by the balance equations

$$\sigma_{i3,i} + \rho\omega^2 u_3 = 0, \quad D_{i,i} = 0, \tag{13.1}$$

where the summation convention over repeated indices is applied. The strain—displacement and electric field—potential relations are

$$s_{i3} = u_{3,i}, \quad E_i = -\Phi_{,i}, \tag{13.2}$$

and the constitutive relations, see Landau and Lifshitz [15] are

$$\begin{aligned} \sigma_{i3} &= c_{44} s_{i3} - e_{15} E_i, \\ D_i &= e_{15} s_{i3} + \varepsilon_{11} E_i. \end{aligned} \tag{13.3}$$

where $i = 1,2$ and a comma denotes partial differentiation. Here σ_{i3}, s_{i3}, E_i, Φ are the stress tensor, strain tensor, electric field vector and electric potential, respectively. Furthermore, $\rho(x) > 0, c_{44}(x) > 0, e_{15}(x), \varepsilon_{11}(x) > 0$ are the inhomogeneous mass density, the shear stiffness, piezoelectric and dielectric permittivity characteristics.

We assume that the mass density and material parameters vary in the same manner with x, through the function $h(x) = e^{2\langle a,x\rangle}$, where $\langle .,. \rangle$ means the scalar product in R^2, and $a = (a_1, a_2)$, such that

$$c_{44}(x) = c_{44}^0 h(x), \quad e_{15}(x) = e_{15}^0 h(x), \quad \varepsilon_{11}(x) = \varepsilon_{11}^0 h(x), \quad \rho(x) = \rho^0 h(x). \tag{13.4}$$

Introducing Eqs. (13.2) and (13.3) into Eq. (13.1) leads to the coupled system

$$\begin{aligned} &(c_{44}u_{3,i})_{,i} + (e_{15}\Phi_{,i})_{,i} + \rho\omega^2 u_3 = 0, \\ &(e_{15}u_{3,i})_{,i} - (\varepsilon_{11}\Phi_{,i})_{,i} = 0. \end{aligned} \tag{13.5}$$

The basic equations can be written in a more compact form if the notation $u_J = (u_3, \Phi)$, $J = 3, 4$ is introduced. Then the constitutive Eq. (13.3) take the form

$$\sigma_{iJ} = C_{iJKl} u_{K,l}, \quad i, l = 1, 2, \tag{13.6}$$

where $C_{iJKl} = C_{iJKl}^0 h(x)$ and $C_{i33l}^0 = \begin{cases} c_{44}^0, i = l \\ 0, \quad i \neq l \end{cases}$, $C_{i34l}^0 = C_{i43l}^0 \begin{cases} e_{15}^0, i = l \\ 0, \quad i \neq l \end{cases}$, $C_{i44l}^0 = \begin{cases} -\varepsilon_{11}^0, i = l \\ 0, \quad i \neq l \end{cases}$ and Eq. (13.5) is reduced to

$$L(u) \equiv \sigma_{iJ,i} + \rho_{JK}\omega^2 u_K = 0, \quad J, K = 3, 4, \tag{13.7}$$

where $\rho_{JK} = \begin{cases} \rho, J = K = 3 \\ 0, J = 4 \text{ or } K = 4 \end{cases}$.

The boundary conditions on the outer boundary S shall be given by a prescribed traction $\bar{t}_J$

$$t_J = \bar{t}_J \text{ on } S, \tag{13.8}$$

where $t_J = \sigma_{iJ} n_i$ and $n = (n_1, n_2)$ is the outer normal vector. The boundary condition along the crack reads

$$t_J = 0 \text{ on } S_{cr}^+. \tag{13.9}$$

It means that the crack is free of mechanical traction as well as of surface charge, i.e. the crack is electrically impermeable.

Following Akamatsu and Nakamura [2] can be proved that the BVP (13.7)–(13.9) admits a continuously differentiable solution if the usual smoothness and compatibility requirements for the boundary data are satisfied. Consider the following BVPs

$$\left| \begin{aligned} &L(u^1) = 0 \quad \text{in } G, \\ &t_J^1 = \bar{t}_J \quad \text{on } S, \end{aligned} \right. \tag{13.10}$$

$$\left|\begin{array}{l} L(u^2) = 0 \quad \text{in } G\backslash S_{cr}, \\ t_J^2 = -t_J^1 \quad \text{on } S_{cr}^+ \\ t_J^2 = 0 \quad \text{on } S. \end{array}\right. \tag{13.11}$$

Since the BVP (13.7)–(13.9) is linear its solution is a superposition of the BVPs (13.10) and (13.11), so that $u_J = u_J^1 + u_J^2$ and $t_J = t_J^1 + t_J^2$. The fields u_J^1, t_J^1 are obtained by the dynamic load on S in the crack free domain G, while u_J^2, t_J^2 are produced by the load $t^2 = -t_J^1$ on S_{cr}^+ and zero boundary conditions on S.

13.3 Non-hypersingular BIEM

Following [21, 27] the system of BVPs (13.10) and (13.11) is transformed into an equivalent system of integro-differential equations on $S \cup S_{cr}$, see Chap. 4.

$$\begin{aligned} \frac{1}{2}t_J^1(x) = C_{iJKl}n_i(x) \int_S [(\sigma^*_{\eta PK}(x,y)u^1_{P,\eta}(y) - \rho_{QP}\omega^2 u^*_{QK}(x,y)u^1_P(y))\delta_{\lambda l} \\ - \sigma^*_{\lambda PK}(x,y)u^1_{P,l}(y)]n_\lambda(y)dS - C_{iJKl}n_i(x)\int_S u^*_{PK,l}(x,y)t^1_P(y)dS, \quad x \in S, \end{aligned} \tag{13.12}$$

$$\begin{aligned} t_J^c(x) = C_{iJKl}n_i(x) \int_{S_{cr}^+} [(\sigma^*_{\eta PK}(x,y)\Delta u^2_{P,\eta}(y) \\ - \rho_{QP}\omega^2 u^*_{QK}(x,y)\Delta u^2_P(y))\delta_{\lambda l} - \sigma^*_{\lambda PK}(x,y)\Delta u^2_{P,l}(y)]n_\lambda(y)dS_{cr} \\ + C_{iJKl}n_i(x)\int_S [(\sigma^*_{\eta PK}(x,y)u^2_{P,\eta}(y) - \rho_{QP}\omega^2 u^*_{QK}(x,y)u^2_P(y))\delta_{\lambda l} \\ - \sigma^*_{\lambda PK}(x,y)u^2_{P,l}(y)]n_\lambda(y)dS, \quad x \in S \cup S_{cr}. \end{aligned} \tag{13.13}$$

Here $t_J^c(x) = \begin{cases} -t_J^1(x), & x \in S_{cr}^+ \\ 0, & x \in S \end{cases}$, u^*_{JK} is the fundamental solution of Eq. (13.7), $\sigma^*_{iJQ} = C_{iJKl}u^*_{KQ,l}$ is the corresponding stress, and $\Delta u_J^2 = u_J^2|_{S_{cr}^+} - u_J^2|_{S_{cr}^-}$ is the generalized COD on the crack S_{cr}. Finally, $x = (x_1, x_2)$ and $y = (y_1, y_2)$ denote the position vector of the observation and source point, respectively. The functions $u_J, t_J, u^*_{JK}, \sigma^*_{iJQ}$ additionally depend on the frequency ω, which is omitted in the list of arguments for simplicity. Equations (13.12) and (13.13) constitute a system of integro-differential equations for the unknown Δu_J^2 on the line S_{cr}, t_J^1 on S_{cr}^+ and u_J^1, u_J^2 on the external boundary S of the piezoelectric solid G. From its solution the generalized displacement u_J at every internal point of G can be determined by using the corresponding representation formulae, see [11, 27].

For the solution of the system of Eqs. (13.12) and (13.13) we will use the fundamental solution u^*_{JK} and the corresponding stress σ^*_{lQK} presented in Sect. 11.3, Eqs. (11.15)–(11.17).

These fundamental solutions show clearly that the dynamic behaviour of an exponentially inhomogeneous piezoelectric material are governed by the frequency of the dynamic load. More precisely, denote $\omega_0 = \sqrt{\frac{a_0}{\rho^0}}|a|$, where $a_0 = c^0_{44} + \frac{e^{02}_{15}}{\varepsilon^0_{11}}$ and $|a| = \sqrt{a_1^2 + a_2^2}$ then: (a) at frequency $\omega > \omega_0$, the fundamental solution is expressed by oscillating functions presenting a wave propagation process; (b) at frequency $\omega < \omega_0$, the fundamental solution loses its wave nature and shows simple vibration with decreasing amplitudes; (c) at frequency $\omega = \omega_0$, the fundamental solution corresponds to that of the static case.

13.4 Numerical Solution and Results

13.4.1 Numerical Solution

The numerical procedure for the solution of the defined BVP follows the numerical algorithm developed and validated in Chaps. 11 and 12.

The program code based on Mathematica, see MAT [20] has been created following the above outlined procedure. The mechanical dynamic SIF K_{III}, the electrical displacement intensity factor K_D and the electric intensity factor K_E are obtained directly from the traction nodal values ahead of the crack-tip, see Suo et al. [24]. In a local polar coordinate system (r, φ) with the origin at the crack-tip the formulae read correspondingly

$$K_{III} = \lim_{r\to\pm 0} t_3\sqrt{2\pi r}, \quad K_D = \lim_{r\to\pm 0} t_4\sqrt{2\pi r},$$
$$K_E = \lim_{r\to\pm 0} E_3\sqrt{2\pi r}, \quad E_3 = \frac{1}{e^2_{15} + c_{44}\varepsilon_{11}}(-e_{15}t_3 + c_{44}t_4), \tag{13.14}$$

where t_J is the generalized traction at the point (r, φ) close to the crack-tip, see Sect. 2.6.2. Note that, although the structure of the asymptotic crack-tip fields is not influenced by the material gradient, see Li and Weng [16] and Sect. 10.4, the SIFs depend on the material gradient through the solution of the BVP.

13.4.2 Numerical Results

The material used in the numerical examples is PZT-4, see Table 4.1. The crack S_{cr} is a segment with a length $2c = 5$ mm and its position is determined by the center point (x_1, x_2) and inclination angle ψ with respect to Ox_1 axis. The rectangular domain

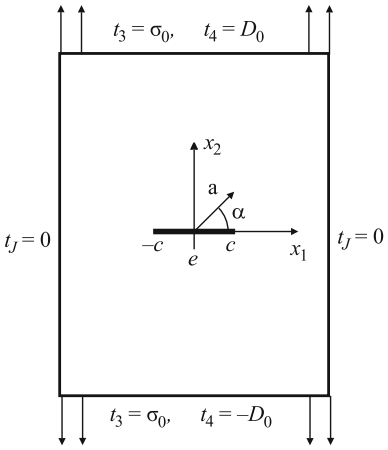

Fig. 13.2 Rectangular inhomogeneous finite solid with a central crack

G has the dimension 20×40 mm. The crack is discretized by 7 BE with lengths l_j: $l_1 = l_7 = 0.375$, $l_2 = l_6 = 0.5$, $l_3 = l_5 = 1.0$, $l_4 = 1.25$ mm. The boundary S is discretized by 20 BE. Time-harmonic load is uniform uniaxial electro-mechanical tension in Ox_2 direction with amplitudes σ_0 in N/m^2 and D_0 in C/m^2, see Fig. 13.2.

Concerning the frequency interval used for simulations the proposed method has no computational limitations. However the size of the discretization mesh should satisfy the well known accuracy condition $\lambda > 10l$ where λ is the wave length and l is the maximal size of the boundary elements. The aim of the simulations is to consider scattering and diffraction processes in finite exponentially inhomogeneous piezoelectric solids with internal cracks around the critical frequency ω_0, that depends on the variable material properties.

Denote $a_1 = |a| \cos\alpha, a_2 = |a| \sin\alpha$, where α is the direction and $|a|$ is the magnitude of the material inhomogeneity. As mentioned in Daros [6] and Marinov and Rangelov [18] for the whole FGPM plane, the behaviour of SIF for exponential inhomogeneity depends strongly on the critical frequency ω_0, defined in Sect. 13.3. For $\omega < \omega_0$ the dynamic behaviour is simple vibration; for $\omega = \omega_0$ it is static and for $\omega > \omega_0$ it is wave propagation. These effects are shown by the results of the numerical examples in Figs. 13.4, 13.5, 13.6, 13.7 and 13.8.

In the presented examples the normalized frequency is $\Omega = c\sqrt{\rho^0/a_0}\omega$. Denote the amplitude of the mechanical load by $\sigma = 400 \times 10^6$ N/m^2. We consider the following types of loads: mechanical with $\sigma_0 = \sigma$, $D_0 = 10^{-5}$ C/m^2; electro-mechanical with $\sigma_0 = \sigma$, $D_0 = 0.1\dfrac{\varepsilon^0_{11}}{e^0_{15}}\sigma$; electrical with $\sigma_0 = 10^{-3}$ N/m^2, $D_0 = 0.1\dfrac{\varepsilon^0_{11}}{e^0_{15}}\sigma$.

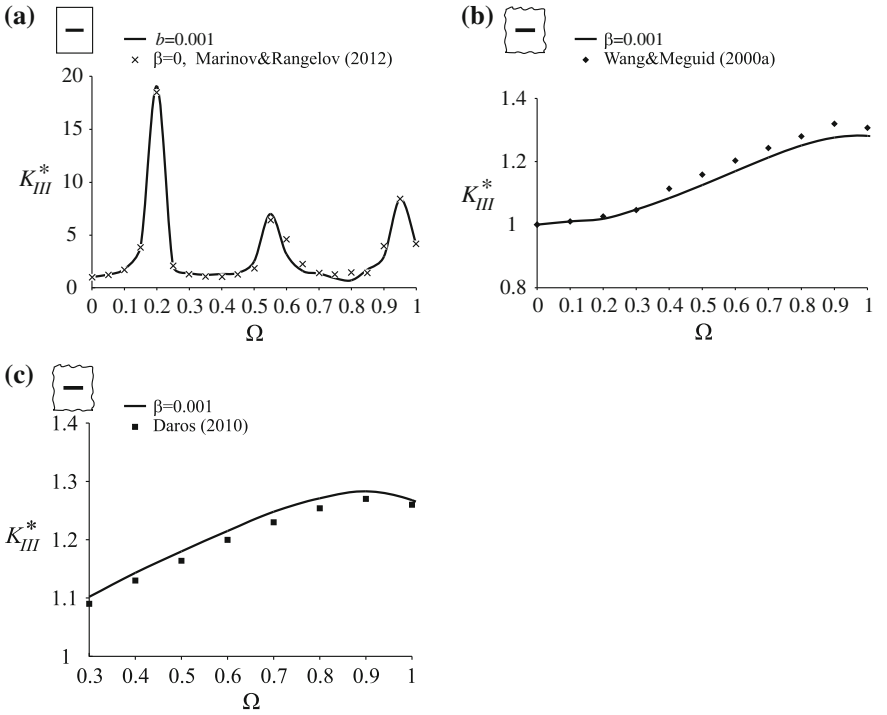

Fig. 13.3 Comparison of SIF K^*_{III} versus frequency Ω between: **a** the authors' results and Marinov and Rangelov [19] result; **b** the authors' results based on truncation approach and Wang and Meguid [26] result; **c** the authors' results based on truncation approach, for $\beta = 0.4$ and with Daros [6] for $\beta = 0.4$

In the figure is plotted the absolute value of the normalized SIF $K^*_{III} = \dfrac{K_{III}}{\sigma\sqrt{\pi c}}$ and normalized EFIF $K^*_E = \dfrac{K_E}{\sigma\sqrt{\pi c}}$ versus nondimensional frequency Ω for different values of the normalized inhomogeneity amplitude $\beta = 2|a|c$, the direction of the material inhomogeneity α and the crack location expressed by the crack center (x_1, x_2) and the crack inclination angle ψ.

The validation is based on the comparison of the BIEM results with the available ones from the literature for the homogeneous case. The reason is that there are no available results for mechanical SIF and EFIF of finite anti-plane cracked piezoelectric solids with exponentially varying properties in both frequency intervals before and after the critical frequency ω_0, where the cracked solid changes its dynamic behaviour. It is used the developed software for the inhomogeneous case where the inhomogeneity amplitude is set to $\beta = 0.001$. In this homogeneous case a comparison is made with the results obtained in Dineva et al. [7] and Marinov and Rangelov [19] for a finite rectangular anti-plane cracked solid under uniform uniaxial time-harmonic traction. The maximum difference is smaller than 7 %, see Fig. 13.3a.

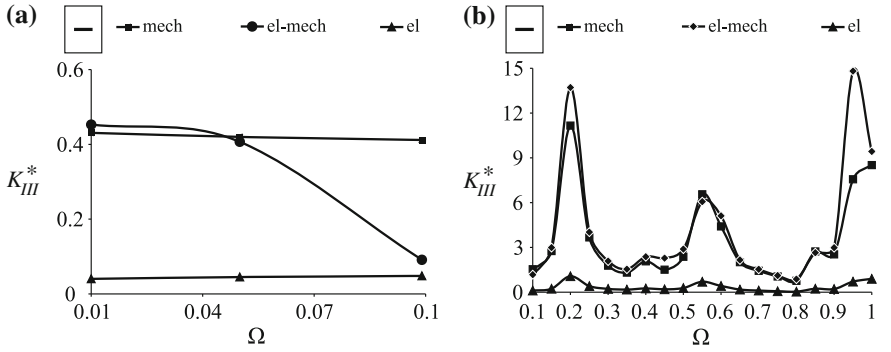

Fig. 13.4 SIF K^*_{III} versus frequency Ω for different types of applied load: **a** $\Omega \in (0, 0.1)$; **b** $\Omega \in (0.1, 1.0)$

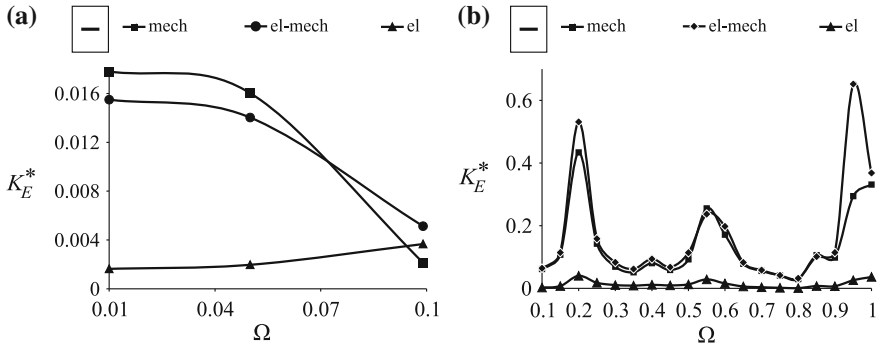

Fig. 13.5 EFIF K^*_E versus frequency Ω for different types of load: **a** $\Omega \in (0, 0.1)$; **b** $\Omega \in (0.1, 1.0)$

Additionally, in order to test the here proposed new BIEM for a finite piezoelectric solid, the results are also compared with those of Wang and Meguid [26] for an anti-plane crack in a homogeneous plane using the truncation approach where the size of the square plate is 10 times greater than the half-length of the crack, see Fig. 13.3b. The same truncation technique is used here in order to compare the BIEM results with the results obtained by Daros [6], see Fig. 13.3c where an anti-plane crack in an elastic anisotropic exponentially inhomogeneous plane under time-harmonic load is considered. In both cases the difference between BIEM results and the results obtained in Wang and Meguid [26] and in Daros [6] is not more than 7 %. Note that Wang and Meguid [26] used the dual integral equation method, while Daros [6] used the non-hypersingular traction BIEM based on the frequency dependent fundamental solution, obtained by Fourier transform.

In the first group of figures (Figs. 13.4 and 13.5) the mechanical SIF K^*_{III} and EFIF K^*_E versus frequency Ω for three types of loads: mechanical, electro-mechanical and electrical are plotted. The inhomogeneity has the magnitude $\beta = 0.2$, so the normalized critical frequency is $\Omega = 0.1$. The direction of material inhomogeneity is $\alpha = \pi/2$ and the crack is a segment $(-c, c)$ on Ox_1 axis, i.e. $(x_1, x_2) = (0, 0)$

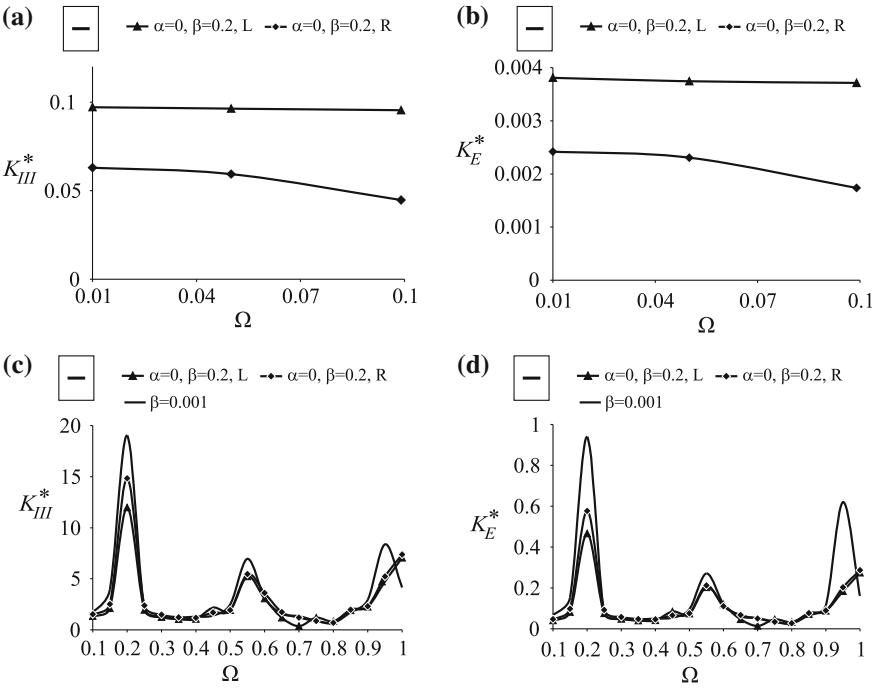

Fig. 13.6 SIF K^*_{III} and EFIF K^*_E versus Ω for $\beta = 0.2$, $\alpha = 0$: **a** K^*_{III}, $\Omega \in (0.0, 0.1)$; **b** K^*_E, $\Omega \in (0.0, 0.1)$; **c** K^*_{III}, $\Omega \in (0.1, 1.0)$; **d** K^*_E, $\Omega \in (0.1, 1.0)$

and $\psi = 0$. Figures 13.4a, b and 13.5a, b demonstrate clearly the sensitivity of the stress and electric field concentrations to the type of the applied load and to the coupled character of the electro-mechanical continuum. As could be expected the behavior of both SIFs strongly differs in two considered frequency intervals before and after the critical frequency ω_0. The oscillating character and the appearance of the resonance frequencies when $\omega > \omega_0$ is visible when Figs. 13.4a and 13.5a with Figs. 13.4b and 13.5b are compared. The normalized mechanical SIF K^*_{III} in the frequency interval $\omega < \omega_0$ shows a different behavior with respect to the frequency when an electro-mechanical load is applied. At very low frequencies this behavior approaches the corresponding one for the case of pure mechanical load, while for frequencies near the critical frequency the values of K^*_{III} are close to those obtained in the case of pure electrical load, see Fig. 13.4a. Figure 13.4b reveals that the frequency dependent curves of K^*_{III} almost repeat the places of the resonance frequencies, but the maximal values are obtained for an electro-mechanical loads. Figures 13.4 and 13.5 confirm that the coupled character of the exponentially inhomogeneous piezoelectric material leads to a quite different dynamic stress and electric field concentrations with respect to the prescribed frequency, i.e. there exists different near-field behavior if the frequency is lower or higher than the critical one.

The second group of figures (Figs. 13.6, 13.7 and 13.8) aims to show the dependence of the mechanical SIF and the EFIF on the magnitude of the inhomogeneity for

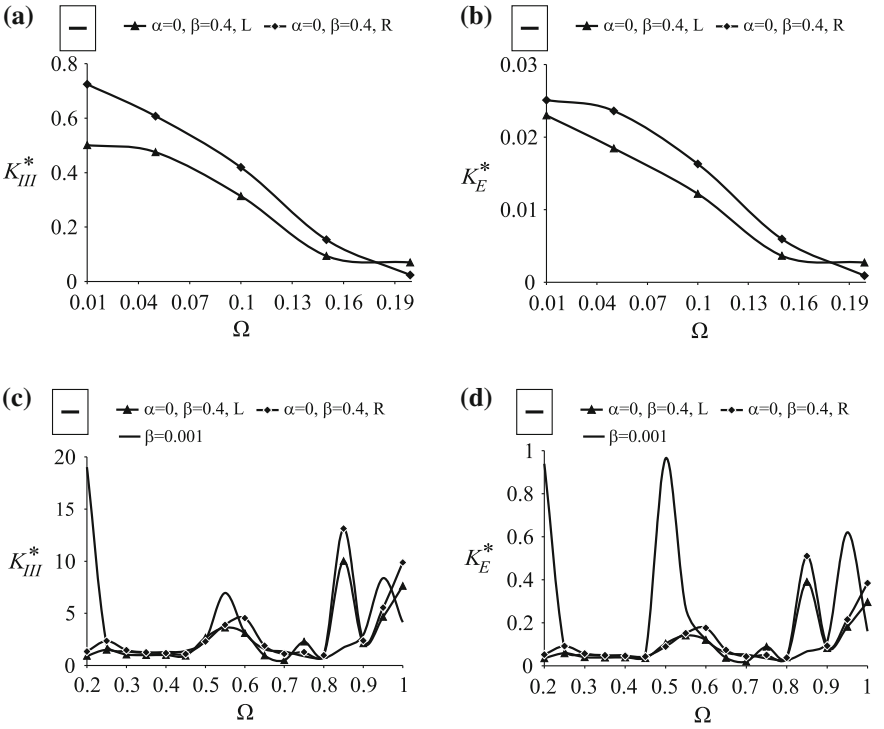

Fig. 13.7 SIF K^*_{III} and EFIF K^*_E versus Ω for $\beta = 0.4$, $\alpha = 0$: **a** K^*_{III}, $\Omega \in (0.0, 0.1)$; **b** K^*_E, $\Omega \in (0.0, 0.1)$; **c** K^*_{III}, $\Omega \in (0.1, 1.0)$; **d** K^*_E, $\Omega \in (0.1, 1.0)$

a fixed inhomogeneity direction $\alpha = 0$. Three cases for β are considered: $\beta = 0.2$ in Fig. 13.6; $\beta = 0.4$ in Fig. 13.7 and $\beta = 0.8$ in Fig. 13.8. The crack is situated as in the first group of examples and both intensity factors (SIF and EFIF) at the left and at the right crack-tip are shown in the figures.

Figures 13.6, 13.7 and 13.8 visualize the following effects: (a) near the critical frequency ω_0, where the character of the dynamic behavior is changed the value of the SIF and EFIF have a jump; (b) there is a different stress and electric field concentration behavior at a fixed magnitude at the left and at the right crack tips; (c) with increasing the inhomogeneity magnitude the difference in the near stress fields at left and right crack-tips increases and while in Fig. 13.6a the higher values are for the left crack-tip, in Figs. 13.7a and 13.8a the right crack-tip values are higher; (d) with increasing inhomogeneity magnitude, K^*_{III} and K^*_E decrease, see and compare Fig. 13.6c, d and Fig. 13.8c, d. This is only true for the frequencies $\omega > \omega_0$, while the opposite behavior is observed for the frequencies $\omega < \omega_0$; (e) with changing the magnitude of the material gradient the places of the resonance phenomena are also changed and these changes are different for both crack-tips.

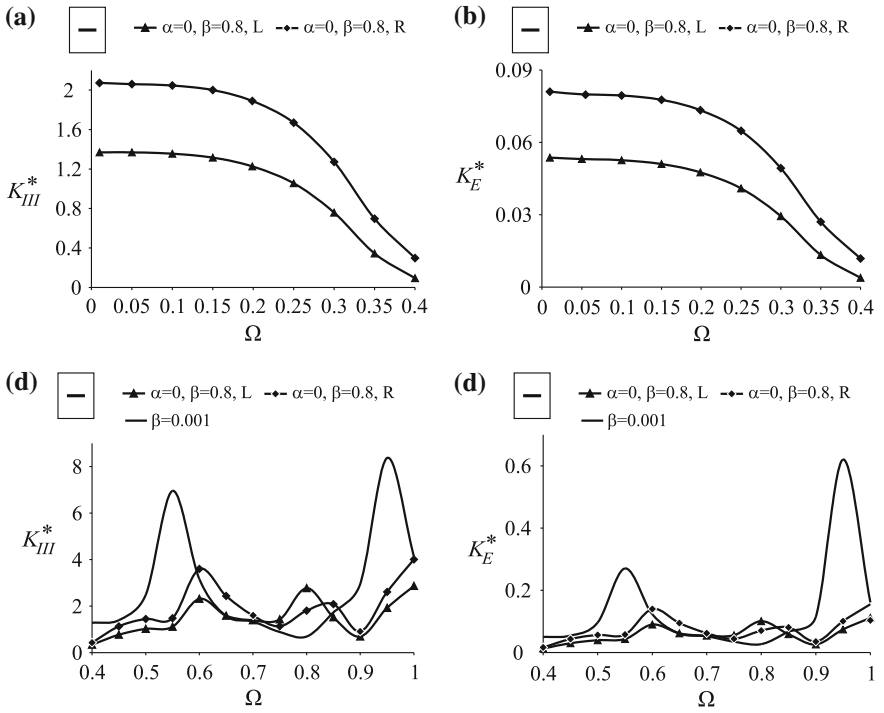

Fig. 13.8 SIF K^*_{III} and EFIF K^*_E versus Ω for $\beta = 0.8$, $\alpha = 0$: **a** K^*_{III}, $\Omega \in (0.0, 0.1)$; **b** K^*_E, $\Omega \in (0.0, 0.1)$; **c** K^*_{III}, $\Omega \in (0.1, 1.0)$; **d** K^*_E, $\Omega \in (0.1, 1.0)$

The effect of the crack location presented by the inclination angle ψ and the coordinates of the crack center on the SIF K^*_{III} is presented in Fig. 13.9 for a fixed inhomogeneity magnitude $\beta = 0.2$ and inhomogeneity direction $\alpha = 0$. Three positions of the crack are considered: a) $\psi_1 = \pi/3$, $(x_1^1, x_2^1) = (0, 0)$; b) $\psi_2 = \pi/4$, $(x_1^2, x_2^2) = (5.17 \cdot 10^{-4}, -3.97 \cdot 10^{-4})$; c) $\psi_3 = \pi/6$, $(x_1^3, x_2^3) = (9.15 \cdot 10^{-4}, -9.15 \cdot 10^{-4})$.

Figure 13.9 shows that with decreasing angle of the crack inclination the values of the SIF increase. There is also not big difference between the behavior at both crack-tips excluding the resonance values at higher frequencies.

The last group of figures (Figs. 13.10 and 13.11) presents the combined effect of both load types: mechanical (Fig. 13.10) or electrical (Fig. 13.11) and the crack position on the non-uniform stress and the electric field distribution in a finite solid. The magnitude of the material inhomogeneity is $\beta = 0.4$, the fixed frequency $\Omega = 0.6$ and dynamic stress concentration field for different directions of the material gradient $\alpha = m\dfrac{\pi}{10}$, $m = 0, \ldots, 9$ is shown. The crack has the fixed angle $\psi = \pi/3$ with respect to Ox_1 axis and two cases for the crack center: $(x_1^1, x_2^1) = (0, 0)$ and $(x_1^4, x_2^4) = (-7.75 \cdot 10^{-3}, -1.583 \cdot 10^{-2})$ are considered.

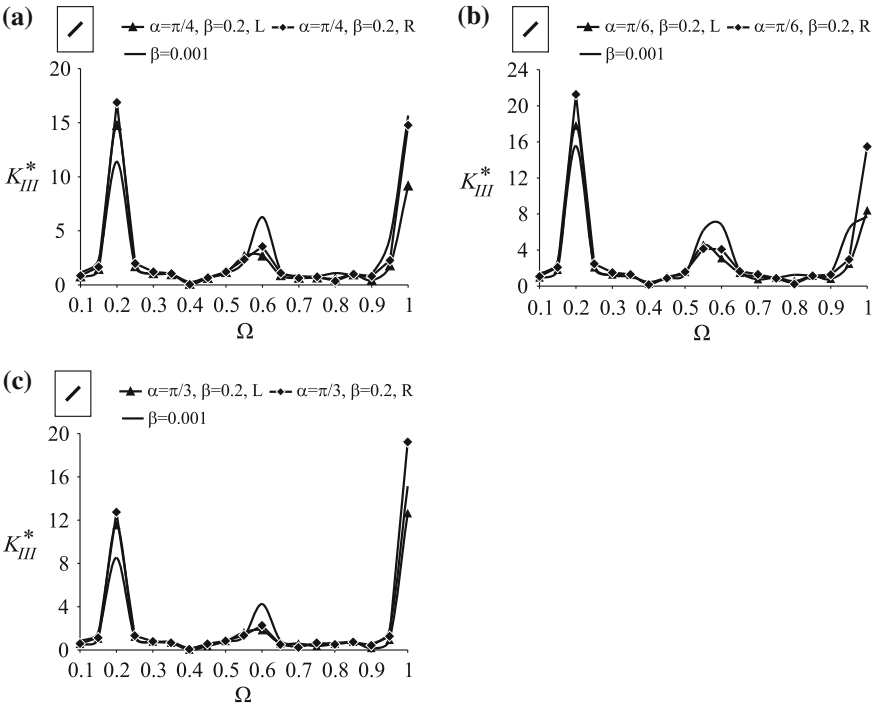

Fig. 13.9 SIF K^*_{III} versus frequency $\Omega \in (0.1, 1.0)$ for $\beta = 0.2$, $\alpha = 0$, and inclined crack: **a** ψ_1, (x_1^1, x_2^1); **b** ψ_2, (x_1^2, x_2^2); **c** ψ_3, (x_1^3, x_2^3)

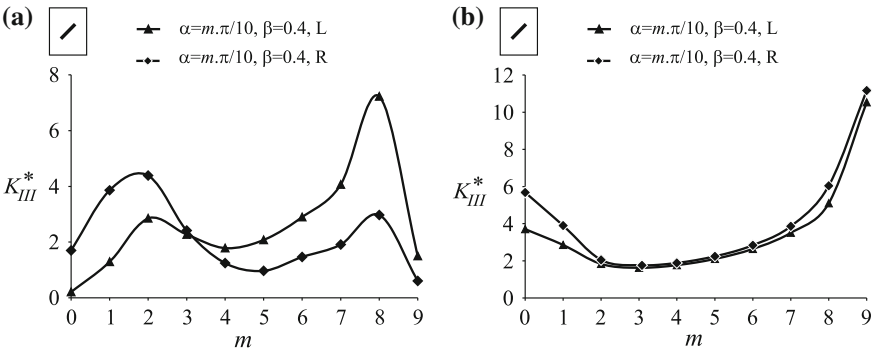

Fig. 13.10 SIF K^*_{III} for fixed frequency $\Omega = 0.6$, $\beta = 0.4$ versus $\alpha = m\frac{\pi}{10}$, $m = 0, \ldots, 9$ under mechanical load for crack angel $\psi = \pi/3$ and crack center: **a** (x_1^1, x_2^1); **b** (x_1^4, x_2^4)

The following effects are visible comparing Figs. 13.10 and 13.11: (a) the coupled material properties provoke the coupled reaction in the obtained stress concentration fields, when mechanical or electrical load are applied. These fields are different at both crack-tips due to the material inhomogeneity; (b) the crack location is an

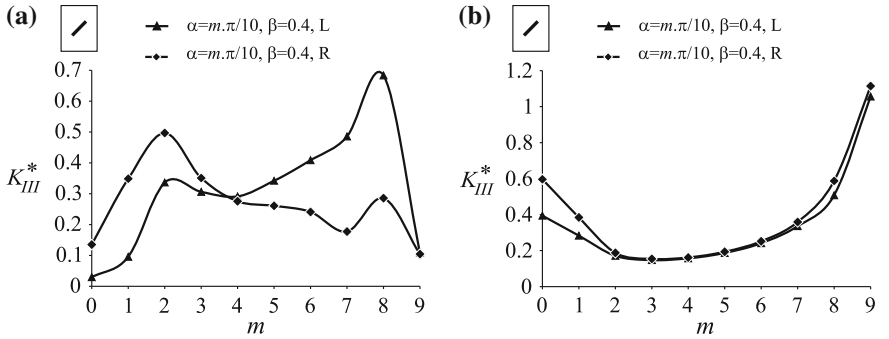

Fig. 13.11 SIF K^*_{III} for fixed frequency $\Omega = 0.6$, $\beta = 0.4$ versus $\alpha = m\frac{\pi}{10}$, $m = 0, \ldots, 9$ under electrical load for crack angel $\psi = \pi/3$ and crack center: **a** (x_1^1, x_2^1); **b** (x_1^4, x_2^4)

important key factor and it can change the amplitude of the SIF as can be seen in Figs. 13.10b and 13.11b, where higher values are obtained due to the interaction between the crack and the external boundary of the finite solid; (c) the direction of the material gradient is also key factor and its influence is different for the stress fields at the left and the right crack tip.

The following conclusions can be made: (i) In most obtained results the IFs for the inhomogeneity case is lower than for the homogeneous one but this effect is frequency dependent; (ii) For the inhomogeneity direction $\alpha = \pi/2$, the SIF is equal at both crack-tips; (iii) For the inhomogeneity direction $\alpha = 0$, the magnitude of the SIF at the left crack-tip is greater than at the right crack-tip for frequencies below the critical frequency and vice-versa for frequencies above the critical one. Note that in the case of the infinite exponentially inhomogeneous piezoelectric plane, see Marinov and Rangelov [18] the order of the magnitudes of the SIF at the left and at the right crack-tips with increasing inhomogeneity magnitude is opposite to those obtained for the case of finite solids. The reason of changing the order in the case of finite domain can be explained by the influence of the external boundary of the considered finite solid, where additional scattering and reflections of the propagating wave occur and where the scattered waves from both the external boundary and the existing crack interact. The numerical results show that the influence of the external boundary strongly decreases for $d > 10c$.

13.5 Conclusion

The time-harmonic crack problem for an anti-plane cracked finite solid of FGPM is solved numerically by means of a non-hypersingular traction BIEM which is developed and validated by Mathematica code. The BIEM computational tool is based on the fundamental solution derived in a closed form by Radon transform. Presented and

discussed are illustrative examples for mechanical SIF and EFIF computation. The simulations reveal that the dynamic non-uniform stress and the electric field distribution in a finite inhomogeneous piezoelectric cracked solid is a complex result of the mutual play of different key factors as: the type and the characteristics of the applied load; the type of material gradient and its magnitude and direction; the crack location and its interaction with the external boundary of the finite solid. The proposed methodology can be applied further for the solution of dynamic crack problems in finite FGPM solids with multiple cracks. The proposed approach has the potential to be used as a foundation for formulation and solution of inverse problems for identification of cracks shape, sizes and locations as well as for the evaluation of the fracture state of different structural elements with a different type of defects as cracks, holes and inclusions.

References

1. Abendroth M, Groh U, Kuna M, Ricoeur A (2002) Finite element-computation of the electromechanical J-integral for 2- D and 3- D crack analysis. Int J Fract 114:359–378
2. Akamatsu M, Nakamura G (2002) Well-posedness of initial-boundary value problems for piezoelectric equations. Appl Anal 81:129–141
3. Blandford GE, Ingrafea AR, Ligget JA (1981) Two-dimensional stress intensity factor computations using the boundary element method. Int J Numer Meth Eng 17:387–404
4. Chan Y-S, Paulino GH, Fannjiang AC (2001) The crack problem for nonhomogeneous materials under anti-plane shear loading—a displacement based formulation. Int J Solids Struct 38:2989–3005
5. Chen J, Liu Z, Zou Z (2003) The central crack problem for functionally graded piezoelectric strip. Int J Fract 121:81–94
6. Daros CH (2010) On modelling SH-waves in a class of inhomogeneous anisotropic media via the Boundary Element Method. ZAMM - Z Angew Math Mech 90:113–121
7. Dineva P, Gross D, Müller R, Rangelov T (2010b) BIEM analysis of dynamically loaded anti-plane cracks in graded piezoelectric finite solids. Int J Solids Struct 47:3150–3165
8. Enderlein M (2004) FEM-analysis of cracks in piezoelectric structures under dynamic electromechanical loading. In: Nilsson F (ed) Proceedings of the 15th european conference on fracture (ECF 15)
9. Enderlein M, Ricoeur A, Kuna M (2003) Comparison of finite element technique for 2 D and 3 D analysis under impact loading. Int J Solids Struct 40:3425–3437
10. Enderlein M, Ricoeur A, Kuna M (2005) Finite element technique for dynamic crack analysis in piezoelectrics. Int J Fract 134:191–208
11. Gross D, Dineva P, Rangelov T (2007) BIEM solution of piezoelectric cracked finite solids under time-harmonic loading. Eng Anal Boundary Elem 31(2):152–162
12. Gruebner O, Kamlah M, Munz D (2003) Finite element analysis of cracks in piezoelectric materials taking into account the permittivity of the crack medium. Eng Fract Mech 70:1399–1413
13. Kuna M (1998) Finite element analyses of crack problems in piezoelectric structures. Comput Mater Sci 13:67–80
14. Kuna M (2006) Finite element analyses of cracks in piezoelectric structures: a survey. Arch Appl Mech 76:725–745
15. Landau DL, Lifshitz EM (1960) Electrodynamics of continuous media. Pergamon Press, Oxford
16. Li C, Weng G (2002) Antiplane crack problem in functionally graded piezoelectric materials. J Appl Mech T ASME 69:481–488

17. Ma L, Wu LZ, Zhou ZJ, Guo LC, Shi LP (2004) Scattering of the harmonic anti-plane share waves by two collinear cracks in functionally graded piezoelectric materials. Europ J Mech A Solids 23:633–643
18. Marinov M, Rangelov T (2011) Integro-differential equations for anti-plane cracks in inhomogeneous piezoelectric plane. C R Acad Bulg Sci 64(12):1669–1678
19. Marinov M, Rangelov T (2012) Time-harmonic behaviour of cracked piezoelectric solid by BIEM. Serdica J Comput 6(2):185–194
20. Mathematica 6.0 for MS Windows (2007) Wolfram Research, Champaign, Illinois
21. Rangelov T, Dineva P, Gross D (2008) Effect of material inhomogeneity on the dynamic behavior of cracked piezoelectric solids: a BIEM approach. ZAMM-Z Angew Math Mech 88:86–99
22. Singh BM, Dhaliwal RS, Vrbik J (2009) Scattering of anti-plane shear wave by an interface crack between two bonded dissimilar functionally graded piezoelectric materials. Proc R Soc A 465:1249–1269
23. Sollero P, Aliabadi MH (1995) Anisotropic analysis of cracks in composite laminates using the dual boundary element method. Compos Struct 31:229–233
24. Suo Z, Kuo C, Barnett D, Willis J (1992) Fracture mechanics for piezoelectric ceramics. J Mech Phys Solids 40:739–765
25. Wang CY, Zhang C, Hirose S (2004) Finite element dual analysis for piezoelectric crack. In: Zhong ZH, Yao MW, Yuan WX (ed) Computational mechanics. WCCM VI in Conjunction with APCOM'04. Tsinghua University Press & Springer, Beijing
26. Wang XD, Meguid SA (2000a) Effect of electromechanical coupling on the dynamic interaction of cracks in piezoelectric materials. Acta Mechanica 143:1–15
27. Wang CY, Zhang Ch (2005) 2 D and 3 D dynamic Green's functions and time-domain BIE formulations for piezoelectric solids. Eng Anal Boundary Elem 29:454–465
28. Zhang C, Gross D (1998) On wave propagation in elastic solids with cracks. Computational Mechanics Publications, Southampton
29. Zhang C, Sladek J, Sladek V (2003a) Effects of material gradients on transient dynamic mode-III stress intensity factors in a FGM. Int J Solids Struct 40:5251–5270

Chapter 14
Exponentially Inhomogeneous Piezoelectric Solid with a Circular Anti-plane Hole

Abstract This chapter addresses the evaluation of the stress and electric field concentrations around a circular hole in a functionally graded piezoelectric plane subjected to anti-plane elastic SH-wave and in-plane time-harmonic electric load. All material parameters vary exponentially along a line of arbitrary orientation in the plane of the piezoelectric material under consideration. Numerical solutions with non-hypersingular traction BIEM for the stress and electric field concentration factors (SCF and EFCF, respectively) around the perimeter of the hole are obtained. Presented are results showing the dependence on various system parameters as e.g. the electro-mechanical coupling, the type of the dynamic load and its characteristics, the wave-hole and wave-material interaction and the magnitude and direction of the material inhomogeneity.

14.1 Introduction

Analytical solutions for static problems of piezoelectric solids with defects have been presented in [2, 4, 18, 19, 24, 25]. The problem of piezoelectric solid with an elliptic cavity was considered in Sosa and Khutoryansky [25]. A circular and elliptic piezoelectric inclusion embedded in an infinite piezoelectric matrix was analyzed in Pak [18, 19], where a closed form solution was obtained for the anti-plane case. Various authors have solved the static anti-plane piezoelectric elliptic inclusion problem, see [2, 12, 17]. A general static solution was provided in Sosa [24] in terms of complex potentials, with emphasis on stress concentrations in the vicinity of circular and elliptical holes. The interactions of electro-elastic fields with voids and cracks contained in a piezoelectric solid under static load were addressed both in closed form and numerically in Perez-Aparicio et al. [21]. In the work by Wang [26] a solution was developed for an infinite, piezoelectric medium containing a piezoelectric ellipsoidal inclusion. In Shindo et al. [22] the dynamic theory of linear anti-plane piezoelectricity was applied to investigate the scattering of horizontally polarized shear waves

P. Dineva et al., *Dynamic Fracture of Piezoelectric Materials*,
Solid Mechanics and Its Applications 212, DOI: 10.1007/978-3-319-03961-9_14,

by a circular piezoelectric inclusion in an infinite piezoelectric matrix subjected to an in-plane electric load. More recently, Fang et al. [8, 9] and Fang [7] studied the dynamic stresses induced by a circular cavity in a semi-infinite functionally graded material. In specific, in Fang [7] the electro-elastic field and dynamic stress around a cavity embedded in a graded piezoelectric layer bonded to a homogeneous piezoelectric substrate were investigated by analytical methods. Generally, the most used analytical and semi-analytical methods for stress concentration factor calculations are the wave function expansion, matched asymptotic expansion, integral transforms and singular integral equation methods. However, the application of analytical methods for the analysis of piezoelectric solids with defects suffers from a number of drawbacks. The most important is the inflexibility since by analytical methods only a very restricted class of problems can be treated (e.g. an elliptic void/inclusion with an axis parallel to the polarization, infinite domains, single void/inclusion, homogeneous materials, etc.).

It is well known that among numerical methods the BIEM has many advantages for problems which are discussed here. However, due to the lack of fundamental solutions for anisotropic, coupled and inhomogeneous solids, the BIEM results in the field are very scarce. Lee [13], Xu and Rajapakse [28] and Liu and Fan [14] applied the BIEM to treat the static problem for a homogeneous piezoelectric solid with a hole. The paper of Xu and Rajapakse [28] considered coupled elastic and electric fields in piezoelectric solids with different types of defects. The stress concentration induced by the existence of multiple holes, cracks and inclusions and their mutual interactions was studied by Hwu and Liao [11].

Most of the references discussed above are for the static problems and for homogeneous piezoelectrics, see [2, 14, 19, 21, 25, 28]. There is still a lack of results for dynamic problems, see [15, 23, 24] and Fang [7] and more specifically for dynamic problems of functionally graded piezoelectric solids with holes.

The present chapter aims to study numerically the stress and electric field distribution around a hole in an inhomogeneous piezoelectric plane under incident SH-wave and in-plane time-harmonic electrical loading. The analysis is an extension of Chaps. 10 and 11 , where the in-plane and anti-plane crack problem in functionally graded piezoelectric solids have been analyzed by using the BIEM. This chapter follows the work in Dineva et al. [6].

14.2 Statement of the Problem

Consider an infinite transversely isotropic functionally graded piezoelectric material with its axis of symmetry and poling axis both along the x_3 axis of an Cartesian coordinate system $Ox_1x_2x_3$. A single circular hole H of radius c and center $(0, 0)$ is embedded in the plane $x_3 = 0$. The mechanical load is given by (shear) SH-waves with a circular frequency ω, polarized in Ox_3 direction and propagating in the plane $x_3 = 0$ under the incident angle θ with respect to the x_1 axis, see Fig. 14.1. Additionally, an in-plane electric load with the same frequency ω may be applied.

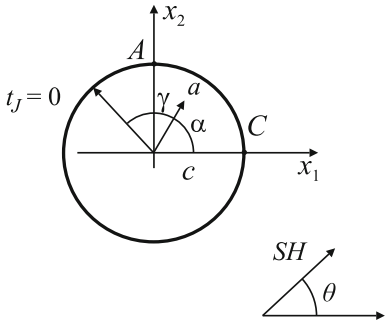

Fig. 14.1 A hole with radius c in a piezoelectric plane with direction of material inhomogeneity α subjected to incident plane SH-wave with incident angle θ. The location of the observation point is defined by angle γ

The only non-vanishing displacements are the anti-plane mechanical displacement $u_3(x, t)$ and the in-plane electrical displacements $D_j(x, t)$, $j = 1, 2$, $x = (x_1, x_2)$. In this case the field equations in absence of body forces consist of the following constitutive equations, see Sect. 2.5.2

$$\begin{aligned} \sigma_{i3} &= c_{44} s_{i3} - e_{15} E_i, \\ D_i &= e_{15} s_{i3} + \varepsilon_{11} E_i, \end{aligned} \tag{14.1}$$

$i = 1, 2$, the strain-displacement and electric field-potential relations

$$s_{i3} = u_{3,i}, \quad E_i = -\Phi_{,i}, \tag{14.2}$$

and the balance equations

$$\sigma_{i3,i} = \rho u_{3,tt}, \quad D_{i,i} = 0. \tag{14.3}$$

Here σ_{i3}, s_{i3}, E_i, ϕ are the stress tensor, strain tensor, electric field vector and electric potential, respectively, where $i = 1, 2$. Subscript commas denote partial differentiation and the summation convention over repeated indices is invoked. Since we assume that the mass density ρ, the shear stiffness c_{44}, the piezoelectric e_{15} and the dielectric permittivity ε_{11} vary in arbitrary direction α in the plane $x_3 = 0$, the field equations must be regarded as a system with non-constant coefficients.

By introducing the notation of the generalized displacement $u_J = (u_3, \Phi)$, $J = 3, 4$, the field equations may be written in the compact form

$$\sigma_{iJ,i} = \rho_{JK} u_{K,tt}, \quad J, K = 3, 4, \tag{14.4}$$

where

$$\rho_{JK} = \begin{cases} \rho, & J = K = 3, \\ 0, & J = 4 \text{ or } K = 4, \end{cases} \quad \sigma_{iJ} = \begin{cases} \sigma_{ij}, & J = 3, \\ D_i, & J = 4, \end{cases} \quad \sigma_{iJ} = C_{iJKl} u_{K,l},$$

$$C_{i33l} = \begin{cases} c_{44}, & i = l, \\ 0, & i \neq l, \end{cases} \quad C_{i34l} = \begin{cases} e_{15}, & i = l, \\ 0, & i \neq l, \end{cases} \quad C_{i44l} = \begin{cases} -\varepsilon_{11}, & i = l, \\ 0, & i \neq l. \end{cases} \tag{14.5}$$

The interaction of an incident wave with the hole induces scattered waves. The total wave field at a given field point can be written as the sum of the incident and the scattered wave field which both must fulfill the wave Eq. (14.4): $u_J = u_J^{in} + u_J^{sc}$, $\sigma_{iJ} = \sigma_{iJ}^{in} + \sigma_{iJ}^{sc}$. The boundary condition along the boundary S of the hole reads

$$t_J|_S = 0 \tag{14.6}$$

where the total generalized traction is expressed by $t_J = \sigma_{iJ} n_i$, with $n = (n_1, n_2)$ being the outward normal to S. The condition (14.6) implies that the boundary of the hole is free of mechanical traction as well as of surface charges, i.e. the hole is electrically impermeable. In the case of a circular hole in a piezoelectric material this assumption is reasonable, see Pak [18].

14.3 Exponential Material Inhomogeneity

In the following we assume that the mass density ρ and material parameters C_{iJKl} vary in the same manner exponentially with vector position x. Thus, introducing the function $h(x) = e^{2\langle a,x\rangle}$, where $\langle a, x\rangle = (a_1 x_1 + a_2 x_2)$, the parameters can be written as

$$c_{44}(x) = c_{44}^0 h(x), \quad e_{15}(x) = e_{15}^0 h(x), \quad \varepsilon_{11}(x) = \varepsilon_{11}^0 h(x), \quad \rho(x) = \rho^0 h(x), \tag{14.7}$$

and correspondingly $C_{iJKl}(x) = C_{iJKl}^0 h(x)$. Here the material constants c_{44}^0, e_{15}^0, ε_{11}^0 and ρ^0 are the reference constants, i.e. the material characteristics in the homogeneous case. The inhomogeneity parameter, the vector a, can be written in polar coordinates as $a = r(\cos\alpha, \sin\alpha)$, where α and $r = \sqrt{a_1^2 + a_2^2}$ are the direction and the magnitude of the inhomogeneity gradient. Note that for $a = 0$, i.e. $h = 1$, the material is homogeneous.

We will study the time-harmonic solutions $u_J(x, \omega)$ of the BVP (14.4), (14.6). Therefore, suppressing in the following the common multiplier $e^{i\omega t}$, Eq. (14.4) takes the form

$$\sigma_{iJ,i} + \rho_{JK}\, \omega^2 u_K = 0, \quad J, K = 3, 4. \tag{14.8}$$

This equation constitutes a system of partial differential equations with variable coefficients that govern the wave propagation in a smoothly inhomogeneous piezoelectric plane. Let us introduce the smooth change of functions

$$u_J(x,\omega) = e^{-\langle a,x\rangle} U_J(x,\omega). \tag{14.9}$$

and suppose that $U_J(x,\omega)$ satisfies the Sommerfeld-type condition at infinity, i.e., more specifically

$$U_3 = o(|x|^{-1}), \quad U_4 = o(e^{-|a||x|}) \quad \text{for} \quad |x| \to \infty. \tag{14.10}$$

Condition (14.10) ensures uniqueness of the scattering field u_J^{sc} for a given incident field u_J^{in}. Following Akamatsu and Nakamura [1] it can be proved that the boundary value problem (14.4), (14.6) admits continuous differentiable solutions.

Following the approach developed in Dineva and Rangelov [5], Manolis [16] and Chap. 11 for the solution of mechanical problems of functionally graded materials and applying the smooth transform (14.9) to Eq. (14.8), we obtain the following system with constant coefficients for $U_J(x,\omega)$:

$$C^0_{iJKl} U_{K,il} + (\rho^0_{JK}\omega^2 - C^0_{iJKi}|a|^2) U_K = 0. \tag{14.11}$$

Eliminating U_4 by inserting the second equation of (14.11) into the first one, the reduced wave equation

$$\Delta U_3 + k^2 U_3 = 0 \tag{14.12}$$

for U_3 is obtained, where $k^2 = \omega^2\rho^0/a_0 - |a|^2$, $a_0 = c^0_{44} + (e^0_{15})^2/\varepsilon^0_{11}$. Introducing a critical frequency by $\omega_0^2 = |a|^2 a_0/\rho^0$, the following three cases with respect to the frequency ω of the applied load must be distinguished, see Chap. 11:

1. $\omega > \omega_0$, in this case $k^2 > 0$,
2. $\omega = \omega_0$, in this case $k^2 = 0$,
3. $\omega < \omega_0$, in this case $k^2 < 0$.

From the mechanical point of view the 3rd case characterizes a simple vibration, while in case 2 the system behaves statically, i.e. stationary wave propagation does not occur in these cases. Only case 1 characterizes wave propagation phenomena, see Daros [3]. Thus, the type of the dynamic behavior of exponentially inhomogeneous materials is governed by the frequency of the applied dynamic load and the inertial and electro-elastic properties of the piezoelectric material. The present study focuses on case 1 and in what follows, for fixed inhomogeneity magnitude $r = |a|$, the frequency ω of the applied load is assumed to be greater than the critical frequency ω_0.

14.3.1 Electro-Mechanical Load

As already mentioned, the mechanical load is given by time harmonic SH-wave propagating in the plane $x_3 = 0$ under incident angle θ with respect to the x_1 axis. The generalized displacement field u_J^m due to this load satisfies the wave Eq. (14.8).

Denoting $\eta = (\eta_1, \eta_2)$ with $\eta_1 = \cos\theta, \eta_2 = \sin\theta$, applying the smooth transformation to the displacement vector and using the solution of Eq. (14.11), the following expressions for the incident wave are obtained

$$u_3^m = e^{-\langle x, a+ik\eta\rangle}, \qquad u_4^m = \frac{e_{15}^0}{\varepsilon_{11}^0} e^{-\langle x, a+ik\eta\rangle}. \tag{14.13}$$

Here the superscript m indicates the mechanical load. The induced traction t_J^m along the boundary S of the hole is

$$t_3^m = -a_0\langle a + ik\eta, n\rangle e^{\langle x, a-ik\eta\rangle}, \qquad t_4^m = 0. \tag{14.14}$$

Additionally an incident time-harmonic pure electric in-plane load along S is applied which is described by

$$u_3^e = 0, \qquad \phi = -E_0\langle x, \eta\rangle. \tag{14.15}$$

The corresponding traction t_J^e along the boundary S of the hole is

$$t_3^e = -e_{15}^0 E_0\langle n, \eta\rangle, \qquad t_4^e = \varepsilon_{11}^0 E_0\langle n, \eta\rangle. \tag{14.16}$$

In the case of a homogeneous solid, i.e. $|a| = 0$ and a wave with an incidence angle $\theta = 0$, formulae (14.13)–(14.16) are the same as in Shindo et al. [22]. It also should be mentioned that although the wave propagation direction η and the inhomogeneity direction α in our case are two independent parameters, only the relative direction $\eta - \alpha$ is finally of importance. This is due to the specific type of wave loading (plane SH-wave) and anisotropy (transversely isotropic). Thus, without loss of generality, the inhomogeneity direction has been chosen as fixed in an arbitrary direction, e.g. $\alpha = 0$, leaving η as the only free parameter. This has not been done in this investigation in view of generalizations of the method for any loading cases and types of anisotropy.

The total incident generalized displacement and traction fields along S are

$$u_J^{in} = u_J^m + u_J^e, \qquad t_J^{in} = t_J^m + t_J^e. \tag{14.17}$$

We will solve numerically the BVP (14.6), (14.8) by transforming it into the equivalent integro-differential equation along the boundary of the hole S. This will be done by the use of the fundamental solution of the wave Eq. (14.8) within the framework of the non-hypersingular traction BIEM.

14.3.2 BIEM Formulation

As can be seen from the governing Eq. (14.8), the solution of wave motion problems in inhomogeneous media involves the solution of partial differential equations with variable coefficients. The key role played by the fundamental solution in a BIEM

is to reduce a given BVP into a system of BIE through the usage of reciprocal theorem or conservation integrals of linear dynamic piezoelectricity as it is done for the homogeneous case in Chap. 4. The BVP formulated in Sect. 14.2 is described by a system of non-hypersingular traction based BIEs on the boundary S of the hole. This formulation was proposed for the first time by Zhang and Gross [29] for cracked homogeneous isotropic, purely elastic infinite anti-plane solids. In Part II this method was developed further and applied for the solution of dynamic in-plane and anti-plane crack problems for homogeneous piezoelectric infinite and finite solids. The same approach was used successfully to study plane fracture problems of inhomogeneous piezoelectric solids, see Chaps. 10–12.

For u_J, u^*_{JK}, where u^*_{JK} is the fundamental solution of Eq. (14.4), we apply the Green's formula in the domain $\Omega_R \setminus \Omega_\varepsilon$, where Ω_R is a circular domain with large radius R and Ω_ε is a small neighborhood of the hole. Applying the representation formulae for the generalized displacement gradient $u_{K,l}$, see Wang and Zhang [27] as in Chap. 4, an integro-differential equation on $\partial\Omega_R \cup \partial\Omega_\varepsilon$ is obtained. Using the condition (14.10), integrals over $\partial\Omega_R$ tend to 0 for $R \to \infty$. Taking the limit $\varepsilon \to 0$, i.e. $x \to S$ and using the boundary condition (14.6), i.e. $t^{sc}_J = -t^{in}_J$ on S, the following system of non-hypersingular traction BIE describes the posed problem:

$$\begin{aligned} -\tfrac{1}{2}t^{in}_J(x) = \; & C_{iJKl}(x)n_i(x)\int_S [(\sigma^*_{\eta PK}(x,\xi)u_{P,\eta}(\xi) \\ & -\rho_{QP}\omega^2 u^*_{QK}(x,\xi)u_P(\xi))\delta_{\lambda l} - \sigma^*_{\lambda PK}(x,\xi)u_{P,l}(\xi)]n_\lambda(\xi)dS \\ & -C_{iJKl}(x)n_i(x)\int_S u^*_{PK,l}(x,\xi)t^{in}_P(\xi)dS, \quad x \in S. \end{aligned} \tag{14.18}$$

Here, u^*_{QK} is the fundamental solution of (14.8) and $\sigma^*_{iJQ} = C_{iJKl}u^*_{KQ,l}$ is the corresponding stress, see Sect. 11.3. Furthermore, x and ξ denote the position vector of the observation point and source point, respectively. Equation (14.18) constitutes a system of integro-differential equations for the unknown generalized displacements u_J on the boundary S of the hole. From this solution, the generalized displacement u_J and traction t_J of the scattered wave field at each point in the inhomogeneous piezoelectric domain $R^2 \setminus H$ can be determined by using the corresponding representation formulae, see Chap. 4.

To make the BIEM analysis tractable, the focus is limited on a special class of smoothly inhomogeneous materials in which material properties vary in the same proportion. This idealization results in ratios (such as wave speeds) that are macroscopically constant. The mechanical, the electrical and piezoelectric properties of the electromechanical continuum are considered for a class of functional forms for which the fundamental solution of the considered wave equation can be derived in an efficient analytical form. In our opinion it is worth to use such an idealization because the obtained solutions reveal some new effects of the material inhomogeneity and its influence on the stress and electric field concentration. Additionally these results are useful for benchmarks of more complex mechanical models and more effective computational tools.

14.4 Numerical Results

14.4.1 Numerical Solution Procedure

Analogous as for the case of crack problems, see Chap. 4, the numerical treatment of the boundary-value problem consists of the following steps:

(a) Evaluation of the singular behavior of the fundamental solutions, their derivatives and their near and far-field asymptotics;
(b) Preparation of the discretization mesh: the displacement and traction are approximated by parabolic shape functions;
(c) Evaluation of the singularities of the kernels of the integrals obtained after discretization: they are at least Cauchy principal value integrals;
(d) Solution of all obtained regular and singular integrals and their validation: the regular integrals are computed employing the Gaussian quadrature scheme for one-dimensional integrals and Monte Carlo integration scheme for two-dimensional integrals, where integration is done over the boundary element and over the unit circumference, which is involved in the 2D fundamental solution, see Gross et al. [10] and Chap. 6. All singular integrals and integrals with logarithmic singularity are solved analytically for a small neighborhood of the source point, using the approximation of the fundamental solution for a small argument, and numerically for the remaining part of the boundary element;
(e) Assembly of the system of equations and formation of the matrix of the complex algebraic system;
(f) Solution of the algebraic system of equations;
(g) Post processing, i.e. back substitution of the boundary solutions in order to obtain additional results: the displacement and traction of the scattered wave field, and by this the total field, can be determined in the whole domain by the corresponding representation formula.

Knowing the total stress field, the generalized SCF is computed. As a result of the physical phenomena like wave diffraction and scattering, the stresses near the hole are different, i.e., in some regions essentially higher than the stresses at the same point produced by undisturbed waves. This phenomenon is known as dynamic stress concentration. Following Pao and Mow [20] for the pure elastic case and Fang [7], and Shindo [22] for the piezoelectric case, the dynamic SCF and electric field concentration factor along the perimeter of a circular hole is defined as the ratio of the stress and electric field amplitude along the circumference to the maximum amplitude of the incident stress at the same point in the homogeneous material without any defects.

The normalized dynamic SCF $|\sigma_{\gamma\theta}/\tau_0|$ and the normalized dynamic EFCF $|e_{15}E_{\gamma\theta}/\tau_0|$ are calculated by using the following formulae:

$$\begin{aligned}
\sigma_{\theta\gamma} &= -\sigma_1 \sin(\theta-\gamma) + \sigma_2 \cos(\theta-\gamma), \quad \sigma_i = \sigma_{i3} + \sigma_{i3}^{in}, \\
E_{\theta\gamma} &= -E_1 \sin(\theta-\gamma) + E_2 \cos(\theta-\gamma), \\
E_i &= \frac{e_{15}^0}{e_{15}^{02} + c_{44}^0 \varepsilon_{11}^0}(-e_{15}^0 \sigma_i + c_{44}^0 D_i), \quad D_i = \sigma_{i4} + \sigma_{i4}^{in}.
\end{aligned} \tag{14.19}$$

Here τ_0 is the amplitude of the maximal shear stress of the incident plane SH-wave, i.e. $\tau_0 = i\omega\sqrt{a_0\rho^0}$ and a_0 is defined in Sect. 14.3, see also Fig. 14.1, γ is the angle of the observation point and θ is the angle of the incident wave.

For the calculations, presented in the following, meshes of 10 quadratic boundary elements have been used. In general, BIEM mesh discretization issues such as mesh density and the element size are controlled by the well-known accuracy condition $\lambda/l \geq 10$, where l is the length of a boundary element and λ is the shear wavelength.

14.4.2 Validation Study

The present non-hypersingular, traction BIEM and its numerical realization are validated by comparison with results from the literature for homogeneous materials. This easily can be done by setting the inhomogeneity function h in the developed program code to $h(x) = 1$. Two examples from the literature are chosen, which have been solved by using the analytical wave function expansion method. The first refers to a circular hole embedded in a homogeneous piezoelectric plane, which is loaded by a mechanical SH-wave, propagating in positive Ox_1 direction in conjunction with a time-harmonic electrical in-plane load $E_1 = E_0 e^{-i\omega t}$ and $E_2 = 0$, see Shindo et al. [22]. The respective reference material data of PZT-4 piezoceramic are given in Table 4.1. A dimensionless frequency is introduced, defined as $\Omega = c\sqrt{\frac{\rho^0}{c_{44}^0}}\omega$. Furthermore, a parameter $E^* = E_0 \frac{e_{15}^0}{\tau_0}$ is used, where E_0 is the amplitude of the applied electrical load, to normalize appropriately the amplitude of the applied electrical field by the amplitude of the maximal shear stress of the incident SH-wave. The value of E^* is chosen to be 0.0, ± 0.5 and 1.0. Figures 14.2 and 14.3 show a comparison of the results for the normalized generalized concentration field—SCF and EFCF versus normalized frequency Ω at the observation point $A(0, c)$ for all four values of E^*. As can be seen, the BIEM results agree very well with those of Shindo et al. [22]. The difference of both results is below 7 %, indicating a high accuracy of the obtained solution.

As second test example serves the solution for a circular hole in a homogeneous isotropic purely elastic plane, loaded by an incident SH-wave, propagating in Ox_1 direction, see Pao and Mow [20]. The results in Fig. 14.4a are obtained by using the same numerical scheme and the same program code. They show the SCF at point $A(0, c)$ on account of an incident plane SH-wave with incident angle $\theta = 0^0$. It can

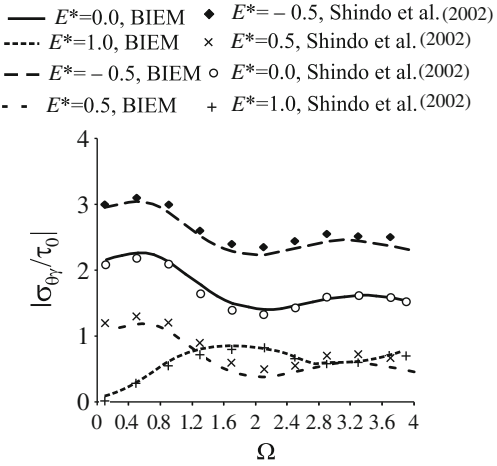

Fig. 14.2 Dynamic SCF at observer point $A(0, c)$ versus normalized frequency Ω of the incident plane SH-wave with incident angle $\theta = 0$ for different electromechanical loads E^*

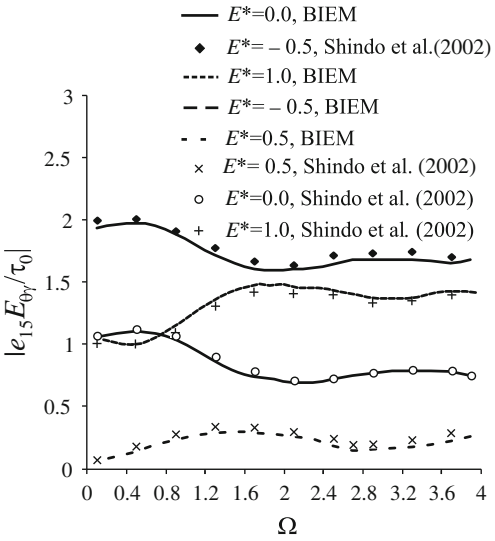

Fig. 14.3 Dynamic EFCF at observer point $A(0, c)$ versus normalized frequency Ω of the incident plane SH-wave with incident angle $\theta = 0$ for different electromechanical loads E^*

be seen that the BIEM solutions are very close to those obtained by Pao and Mow [20]. The same results are shown in Fig. 14.4b, where the angular distribution of the SCF along the hole is drawn for three fixed normalized frequencies $\Omega = 0.1$, $\Omega = 1.0$ and $\Omega = 2.0$.

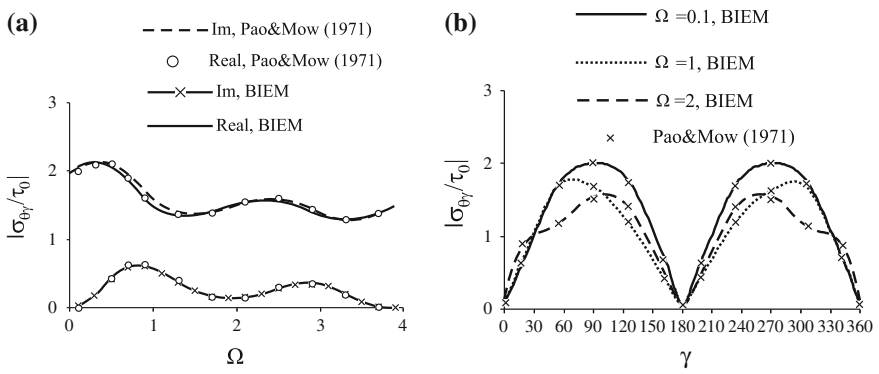

Fig. 14.4 Dynamic SCF in the case of incident plane SH-wave with incident angle $\theta = 0$: **a** at observer point $\gamma = \pi/2$, i.e. $A(0, c)$ versus normalized frequency Ω; **b** for angular distribution γ at fixed frequencies Ω

14.4.3 Simulation Results

The aim of the parametric study conducted here is to show how the stress and electrical field concentration factors are influenced by some key parameters discussed below.

Note that in all figures the condition $\Omega > \Omega_0$ is satisfied where $\Omega_0 = rc$ is the critical dimensionless frequency, see Sect. 14.3.

The FGPM under consideration is the piezoceramic PZT-4 with the reference material properties given in Table 4.1. For chosen inhomogeneity directions $\alpha = \pi/2$ or $\alpha = 3\pi/2$ and a hole radius $c = 5\,\text{mm}$, the variation of the material properties along the vertical x_2 axis is shown in Fig. 14.5 for the dimensionless inhomogeneity parameters $rc = 0.2$ and $rc = 0.3$. We consider the following specific cases: material stiffening along the Ox_1-axis when $\alpha = 0$, i.e. $a_1 > 0, a_2 = 0$, material softening along the Ox_1-axis in the case of $\alpha = \pi$, i.e. $a_1 < 0, a_2 = 0$; material stiffening along the Ox_2-axis when $\alpha = \pi/2$, i.e. $a_1 = 0, a_2 > 0$ and material softens along the Ox_2-axis when $\alpha = 3\pi/2$, i.e. $a_1 = 0, a_2 < 0$.

Figure 14.6a, b present SCF and EFCF at observer points $A(0, c)$ and $C(c, 0)$ versus normalized frequency of the incident wave with incidence angle $\theta = 0$, inhomogeneity direction $\alpha = \pi/2$ or $\alpha = 3\pi/2$ (i.e. along the Ox_2-axis) and inhomogeneity parameter $rc = 0.0, 0.1$ and 0.2. This is the case of pure mechanical load, i.e. $E^* = 0$. The stiffening and softening models are considered. It is first observed that the basic shape of SCF and EFCF curve in homogeneous case is preserved in the presence of inhomogeneity. Next, we see that the exponentially softening and stiffening inhomogeneous models yield different numerical values for dynamic stress and electric field concentrations. There is a shift of the maximum to higher frequencies with increasing value rc. The SCFs and the EFCFs at observation point $A(0, c)$ are much greater than at $C(c, 0)$. The electro-mechanical coupling and dynamic overshooting phenomena are visible from these figures.

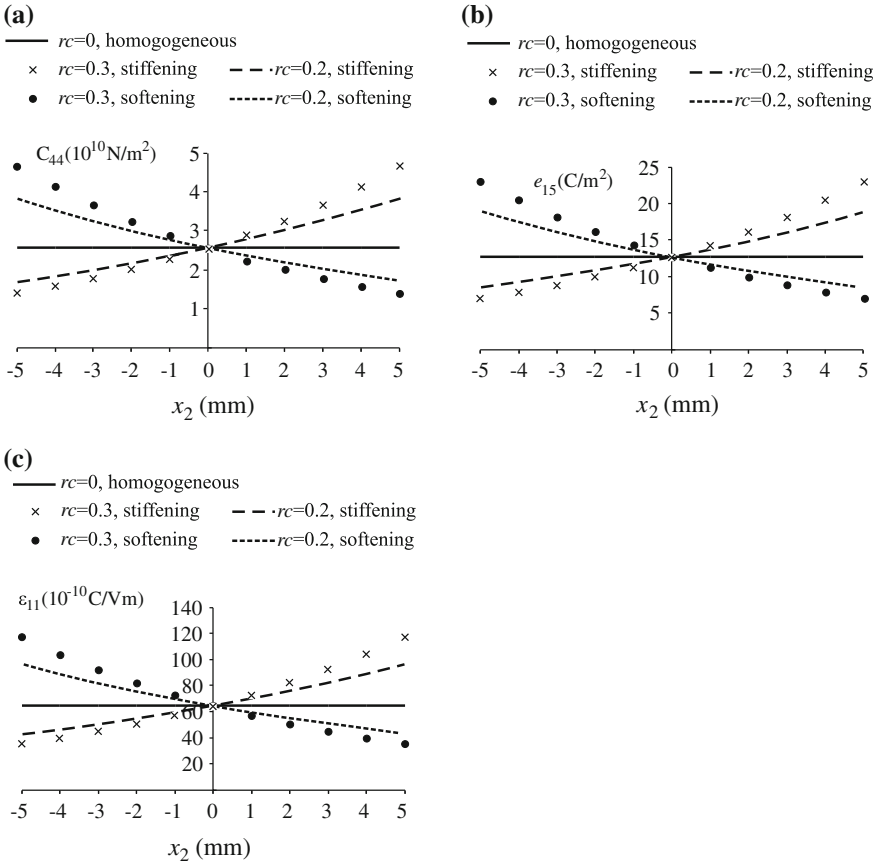

Fig. 14.5 Material properties variation along vertical direction in the case of inhomogeneity magnitude $rc = 0.2; 0.3$ and inhomogeneity direction $\alpha = \pi/2$ (stiffening model) or $\alpha = 3\pi/2$ (softening model): **a** elastic; **b** piezoelectric; **c** dielectric

Figure 14.7a, b describes analogous scenarios like those in Fig. 14.6a, b but with the inhomogeneity direction $\alpha = 0$ or $\alpha = \pi$, i.e. along the Ox_1-axis. A comparison between results in Figs. 14.6 and 14.7 show that the inhomogeneity effect is stronger, when the inhomogeneity is along the Ox_2 axis, although even in the Fig. 14.7a, b the sensitivity of the stress and electric field concentrations to different stiffening and softening models can be seen. At $\Omega = 0.53$ the maximum of the curves show the dynamic overshoot. This frequency is not shifted, when the material inhomogeneity is involved, in contrast to the case when inhomogeneity direction is along Ox_2-axis, see Fig. 14.6a, b.

As far as the proposed methodology can take into consideration the lateral inhomogeneity, the sensitivity of the stress and electric field concentrations to the inhomogeneity direction can be seen in Fig. 14.8a, b. Here the wave with a fixed fre-

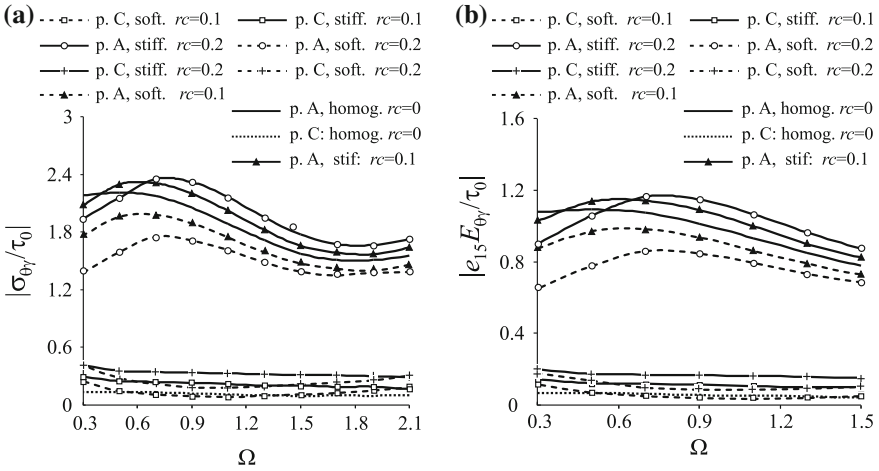

Fig. 14.6 Dynamic GCF at observer points $A(0, c)$ and $C(c, 0)$ versus normalized frequency Ω of the incident SH-wave with incident angle $\theta = 0$ at different inhomogeneity parameters rc and $\alpha = \pi/2, 3\pi/2$ for $E^* = 0$, i.e. pure mechanical load: **a** SCF; **b** EFCF

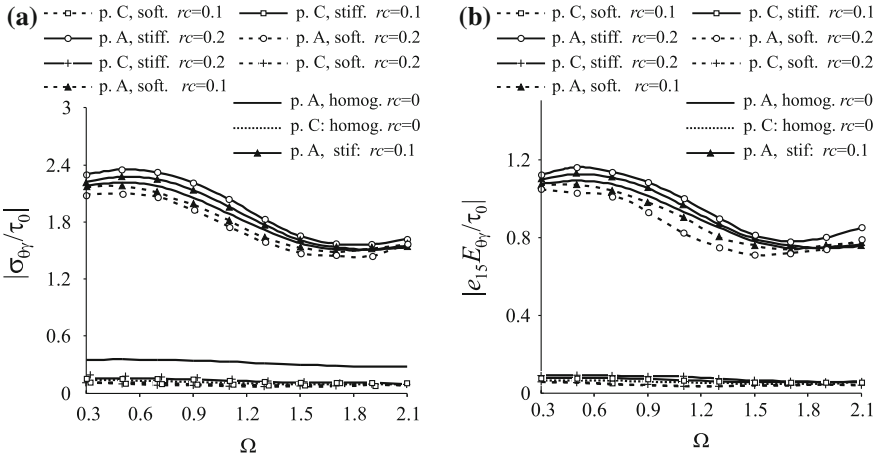

Fig. 14.7 Dynamic GCF at observer points $A(0, c)$ and $C(c, 0)$ versus normalized frequency Ω of the incident plane SH-wave with incident angle $\theta = 0$ for different inhomogeneity parameters rc and $\alpha = 0, \pi$ at $E^* = 0$, i.e. pure mechanical load: **a** SCF; **b** EFCF

quency $\Omega = 1.1$ propagates along the Ox_1-axis and the inhomogeneity parameter is $rc = 0.1, 0.2$ and 0.3. Figure 14.9a, b is analogous but for the propagating wave along the Ox_2-axis. A comparison of the results in Figs. 14.8 and 14.9 reveals that more sensitive to the direction of the material inhomogeneity are the cases, when the wave propagates along the vertical axis and when the inhomogeneous parameter rc is higher. Also, SCFs and EFCFs at point $A(0, c)$ are much bigger than those at point

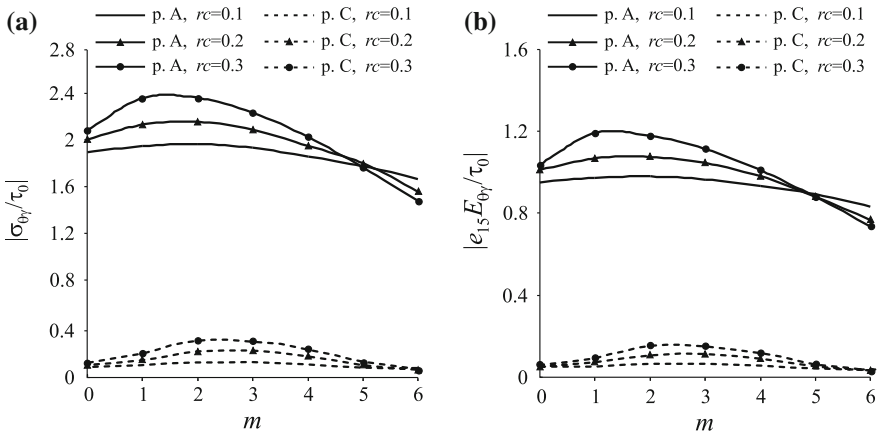

Fig. 14.8 Dynamic GCF at observer points $A(0, c)$ and $C(c, 0)$ versus inhomogeneity direction $\alpha = m\frac{\pi}{6}$ in the case of incident SH-wave with incident angle $\theta = 0$ for different inhomogeneity parameters rc, at for the normalized frequency $\Omega = 1.1$ and at $E^* = 0$, i.e. pure mechanical load: **a** SCF; **b** EFCF

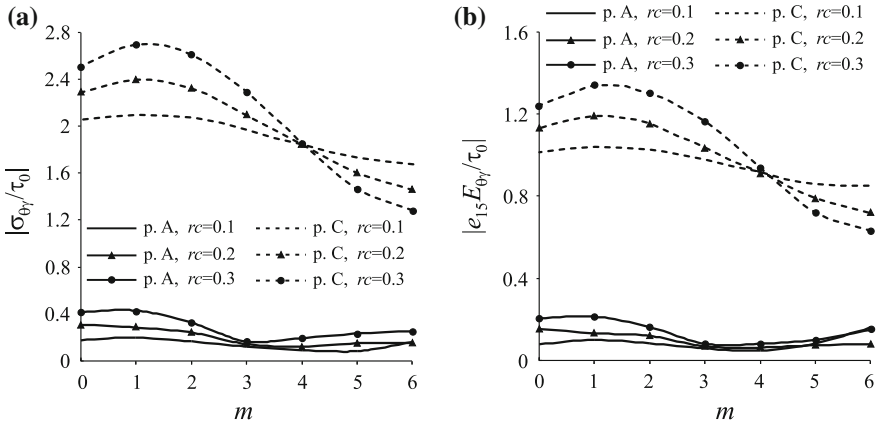

Fig. 14.9 Dynamic GCF at observer points $A(0, c)$ and $C(c, 0)$ versus inhomogeneity direction $\alpha = m\frac{\pi}{6}$ in the case of incident plane SH-wave with incident angle $\theta = \pi/2$ for different inhomogeneity parameters rc, at normalized frequency Ω and at $E^* = 0$, i.e. pure mechanical load: **a** SCF; **b** EFCF

$C(c, 0)$ in Fig. 14.8a, b. Conversely, the stress concentration is stronger at $C(c, 0)$ than in $A(0, c)$ in Fig. 14.9a, b. The maximal values of SCFs and EFCFs are obtained for inhomogeneity direction in the interval $\alpha \in [\pi/3, 2\pi/3]$.

In order to evaluate the influence of the electric load on the generalized field of stress concentration near the hole, the results obtained for $E^* = 0.5$ are shown in Figs. 14.10 and 14.11 at different values of the inhomogeneity parameter $rc = 0.05, 0.1$ and 0.2. In Figs. 14.10 and 14.11 the wave propagation direction

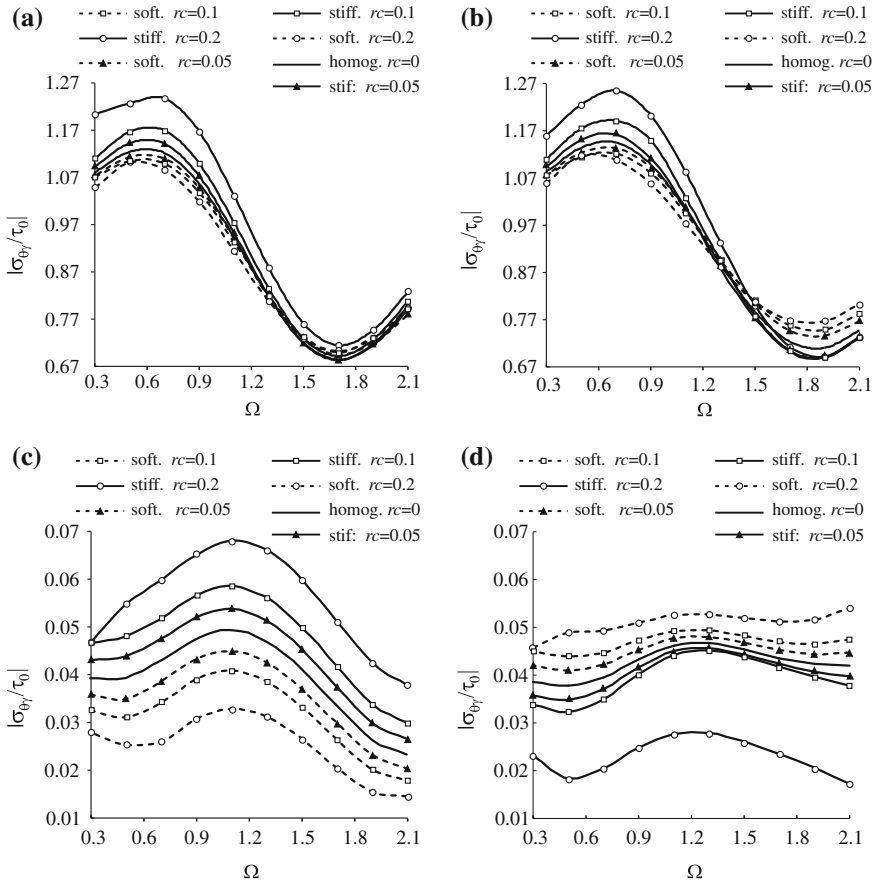

Fig. 14.10 Dynamic SCF versus normalized frequency Ω of incident plane SH-wave with incident angle $\theta = 0$ for inhomogeneity direction $\alpha = 0$ (stiffening model) or $\alpha = \pi$ (softening model) at $E^* = 0.5$ and at observer points: **a** $A(0, c)$; **b** $B(0, -c)$; **c** $C(c, 0)$; **d** $D(-c, 0)$

and inhomogeneity direction are along Ox_1 axis. Figures. 14.10 and 14.11 demonstrate convincingly that the dynamic stress and electric field concentrations can be considered as a complex result of different physical phenomena and their mutual internal interaction. These physical phenomena are: (a) wave-hole interaction; (b) wave-material interaction taking into consideration its anisotropy, inhomogeneity and electro-mechanical coupling that leads to the appearance and shifting of the resonance frequencies; (c) type and characteristics of the applied electromechanical load (pure mechanical, pure electrical and hybrid electro-mechanical); (d) coupled essence of the electro-mechanical nature of the piezoceramics. Due to the complex wave field around the hole, the place of the observer, where we determine the stress and electric field concentration is very important, see comparison between Fig. 14.10a-d and between Fig. 14.11a-d. It can be seen that the material inhomo-

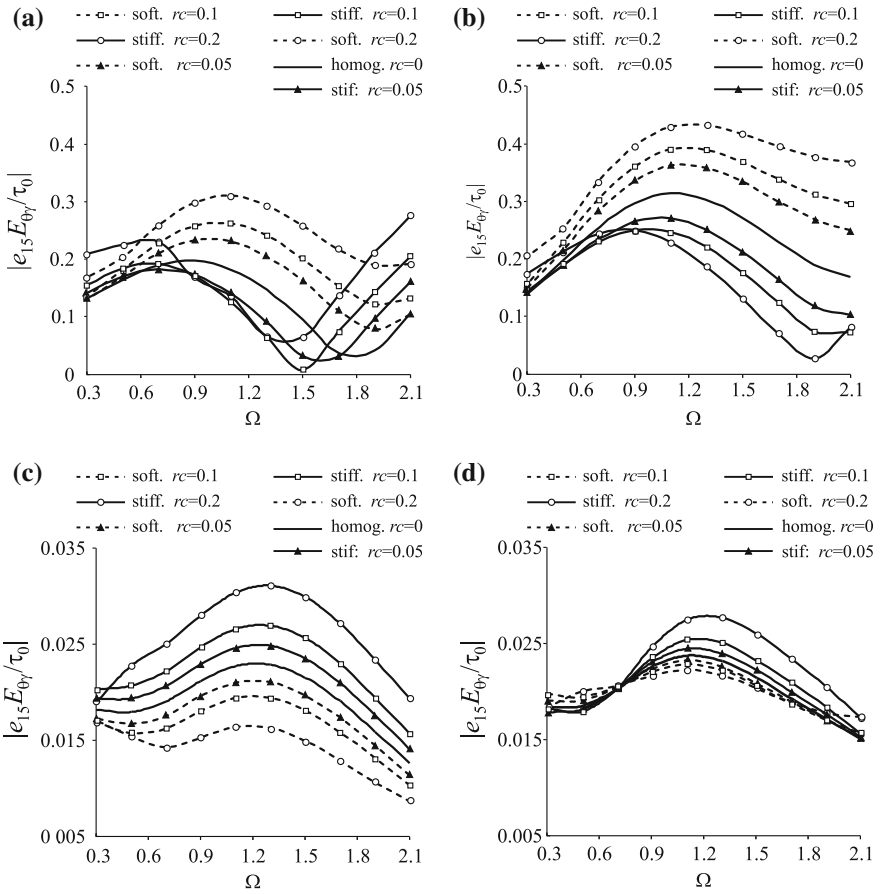

Fig. 14.11 Dynamic EFCF versus normalized frequency Ω of incident plane SH-wave with incident angle $\theta = 0$ for inhomogeneity direction $\alpha = 0$ (stiffening model) or $\alpha = \pi$ (softening model) at $E^* = 0.5$ and at observer points: **a** $A(0, c)$; **b** $B(0, -c)$; **c** $C(c, 0)$; **d** $D(-c, 0)$

geneity effect change the character of the SCF and EFCF curves for the cases of softening and stiffening material, see Fig. 14.10c and 14.11d. Note that this observer points are on the Ox_1-axis that in this case coincides with the material inhomogeneity direction.

It can be seen that the peak values of the dynamic stress and electric field concentration factor for functionally graded materials are different from that for the homogeneous material. Thus, the conclusion is that the defect driving force can be reduced by using the concept for the FGM and the idea to replace the homogeneous materials by a smoothly inhomogeneous one in the new smart structure technologies.

The simulation results show conclusively that stress and electric field concentration near the hole in a functionally graded piezoelectric material is a complex result of the interplay of many key factors as:

- the type of the material inhomogeneity and its magnitude and direction;
- the type and properties of the electromechanical load;
- the coupled nature of the electro-mechanical continuum;
- the mutual disposition of the axis of material symmetry, the axis of material inhomogeneity, the poling axis, the wave polarization axis and the direction of the wave propagation;
- the location of the observer where the stress concentration factor is evaluated;
- the relation between the inhomogeneity magnitude and the size of the hole.

14.5 Conclusion

Two-dimensional dynamic anti-plane problem of a piezoelectric plane weakened by a circular hole is described by a system of non-hypersingular traction BIEM. The material properties vary exponentially with two spatial variables. The validated numerical scheme and the implemented software provides the electro-mechanical displacements along the hole boundary, the stress concentration factors near the hole and the scattered generalized displacement and traction in any point of the inhomogeneous piezoelectric plane.

The proposed methodology can easily be extended to the problem of inclusions in a piezoelectric matrix with direct application to mechanics of composite materials and estimation of effective electromechanical properties in the case of randomly distributed inclusions.

References

1. Akamatsu M, Nakamura G (2002) Well-posedness of initial-boundary value problems for piezoelectric equations. Appl Anal 81:129–141
2. Chung MY, Ting TCT (1996) Bleustein–Gulyaev waves in some functionally graded materials. Int J Solids Struct 33:3343–3361
3. Daros CH (2010) On modelling SH-waves in a class of inhomogeneous anisotropic media via the boundary element method. ZAMM-Z Angew Math Mech 90:113–121
4. Deeg W F (1980) The analysis of dislocation, cracks and inclusion problems in piezoelectric solids. Ph.D. thesis, Stanford University, Stanford, California
5. Dineva P, Rangelov T (2009) Time-harmonic behavior of a cracked inhomogeneous piezoelectric solid by BIEM. J Theor Appl Mech 39(4):93–100
6. Dineva P, Gross D, Müller R, Rangelov T (2011) Dynamic stress and electric field concentration in a functionally graded piezoelectric solid with a hole. ZAMM-Z Angew Math Mech 91(2):110–124
7. Fang XQ (2008) Multiple scattering of electro-elastic waves from a buried cavity in a functionally graded piezoelectric material layer. Int J Solids Struct 45:5716–5729

8. Fang XQ, Hu C, Du SY (2006) Strain energy density of a circular cavity buried in a semi-infinite functionally graded materials subjected to shear waves. Theor Appl Fract Mech 46:166–174
9. Fang XQ, Hu C, Huang WH (2007) Dynamic stress of a circular cavity buried in a semi-infinite functionally graded piezoelectric material subjected to shear waves. Eur J Mech A Solids 26:1016–1028
10. Gross D, Rangelov T, Dineva P (2005) 2D Wave scattering by a crack in a piezoelectric plane using traction BIEM. Struct Integr Dur 1(1):35–47
11. Hwu C, Liao CY (1994) Special boundary element for the problems of multi-holes, cracks and inclusions. Comput Struct 51(1):23–31
12. Jiang CP, Tong ZH, Cheung YK (2001) A generalized self-consistent method for piezoelectric fiber reinforced composites under antiplane shear. Mech Mater 33:295–308
13. Lee JS (1995) Boundary element method for electroelastic interaction in piezoceramics. Eng Anal Bound Elem 15:321–328
14. Liu Y, Fan H (2001) On the conventional boundary integral formulation for piezoelectric solidwith defects or thin shapes. Eng Anal Bound Elem 25:77–91
15. Lu JF, Hanyga A (2004) Dynamic interaction between multiple cracks and a circular hole swept by SH waves. Int J Solids Struct 41:6725–6744
16. Manolis G (2003) Elastic wave scattering around cavities in inhomogeneous continua by the BEM. J Sound Vibr 226(2):281–305
17. Meguid SA, Zhong Z (1998) On the elliptical inhomogeneity problem in piezoelectric materials under antiplane sjear and inplane electric field. Int J Eng Sci 36(3):329–344
18. Pak YE (1992a) Circular inclusion problem in antiplane piezoelectricity. Int J Solids Struct 29:2403–2419
19. Pak YE (2010) Elliptical inclusion problem in antiplane piezoelectricity: implications for fracture mechanics. Int J Eng Sci 48:209–222
20. Pao YH, Mow CC (1971) Diffraction of elastic waves and dynamic stress concentration. Crane Russak, New York
21. Perez-Aparicio JL, Sosa H, Palma R (2007) Numerical investigations of field-defect interactions in piezoelectric ceramics. Int J Solids Struct 44:4892–4908
22. Shindo Y, Moribayashi H, Narita F (2002) Scattering of antiplane shear waves by a circular piezoelectric inclusion embedded in a piezoelectric medium subjected to a steady-state electrical load. ZAMM-Z Angew Math Mech 82:43–49
23. Song T, Li H, Dong J (2006) Dynamic anti-plane behaviour of the interaction between a crack and a circular cavity in a piezoelectric medium. Key Eng Mater 324(325):29–32
24. Sosa H (1991) Plane problems in piezoelectric media with defects. Int J Solids Strut 28:491–505
25. Sosa H, Khutoryansky N (1996) New developments concerning piezoelectric materials with defects. Int J Solids Struct 33:3399–3414
26. Wang BL (1992) Three-dimensional analysis on an ellipsoidal inclusion in a piezoelectric material. Int J Solids Struct 29:293–308
27. Wang CY, Zhang Ch (2005) 2D and 3D dynamic Green's functions and time-domain BIE formulations for piezoelectric solids. Eng Anal Bound Elem 29:454–465
28. Xu LY, Rajapakse RKND (1998) Boundary element analysis of piezoelectric solids with defects. Eng Fract Mech 29B:655–669
29. Zhang C, Gross D (1998) On wave propagation in elastic solids with cracks. Computational Mechanics Publications, Southampton

Chapter 15
Anti-plane Dynamic Crack–Hole Interaction in a Functionally Graded Piezoelectric Medium

Abstract The anti-plane dynamic problem of a functionally graded piezoelectric plane containing a hole–crack system is treated. The material parameters vary exponentially in the same manner in an arbitrary direction. The system is loaded by an incident SH-type wave and impermeable boundary conditions are assumed. The numerical solution yields the dynamic SIFs and SCFs. A parametric study reveals their dependence on the hole–crack scenario and its geometry, characteristics of the dynamic load and magnitude and direction of the material gradient.

15.1 Introduction

The stress and electric field analysis of piezoelectric solids, weakened by different type of defects such as inclusions, holes, cracks, voids or second phase particles, is of fundamental importance for their structural integrity and reliable service performance. Piezoelectric materials are brittle, posses low fracture resistance and both the mechanical and electric loads are responsible for eventual catastrophic failure. Physically, the stress concentration around a hole boundary may generate cracks and the interaction between holes and cracks may produce dielectric breakdown, damage and fracture. Accurate prediction of the fracture response requires an accurate assessment of the interaction between the defects during service and manufacture. As a result, the interaction between holes and cracks has been a very popular topic in the field of fracture mechanics.

One of the first solutions considering the static interaction of two circular electrically permeable holes in a piezoelectric homogeneous plane under the assumption of plane strain was presented by BIEM in [15]. The accuracy of the BIEM code was verified by comparison with analytical solutions for a single circular hole in a piezoelectric plane by Sosa [12] and with the solution of [5] for the pure elastic anisotropic case. A BIEM analysis of the crack–hole in-plane static problem in a piezoelectric plate under external heat-flux disturbance was presented in [9]. The solution was

P. Dineva et al., *Dynamic Fracture of Piezoelectric Materials*,
Solid Mechanics and Its Applications 212, DOI: 10.1007/978-3-319-03961-9_15,

based on the termoelectroelastic Green's function for a piezoelectric solid with a hole. The same methodology was applied for inclusion–crack interaction problems of plane thermopiezoelectric solids by Qin and Lu [8]. In [16] the Green's function for a piezoelectric plane with an elliptic hole was derived and further the hole–crack static interaction was studied by the method of singular integral equations. Numerical results showed that the distribution of stress and the electric field concentration near the elliptic hole depends on the location and orientation of the crack. The dynamic interaction between a crack and a circular hole in a piezoelectric plane was investigated in [11] by the method of complex variables and the Green's function for an infinite piezoelectric plane with a single hole subjected to a time-harmonic anti-plane line force.

Most of the available results are for static problems and for isotropic homogeneous pure elastic solids. In Chap. 12 a dynamic anti-plane crack problem for a functionally graded material is solved, while in Chap. 14 similar problem was solved for a single hole. The present chapter is based on the results obtained in Chaps. 12 and 14 and investigates the dynamic interaction between a hole and a crack following [6]. The main objective is to evaluate the stresses and electric field distribution of a hole–crack system in an inhomogeneous piezoelectric plane with exponentially varying properties in an arbitrary direction.

15.2 Problem Statement

In a Cartesian coordinate system $Ox_1x_2x_3$ consider an infinite, transversely isotropic functionally graded piezoelectric medium with the axis of symmetry and the poling axis along Ox_3. The anti-plane deformation state is considered in the plane perpendicular to the poling axis. The plane $x_3 = 0$ contains a crack S_{cr} with a half length c and a circular hole H of radius R, center C and boundary $S_h = \partial H$, such that $S_{cr} \cap S_h = \emptyset$, see Fig. 15.1. The direction of the incident time-harmonic shear wave with a circular frequency ω is given by the angle θ with respect to the x_1 axis. Because of the time-harmonic behavior of all field quantities, the common multiplier $e^{i\omega t}$ is suppressed here and in the following. The only non-vanishing displacements are the anti-plane mechanical displacement $u_3(x, \omega)$ and the in-plane electrical displacements $D_i(x, \omega)$, while the non-vanishing stress components are $\sigma_{i3}(x, \omega)$, $i = 1, 2$, $x = (x_1, x_2)$. The incident wave interacts with the crack–hole system and produces a scattered wave, so that the total wave field is a superposition of the incident and scattered waves. The decomposition $u_3(x, \omega) = u_3^{in}(x, \omega) + u_3^{sc}(x, \omega)$ for the displacement holds analogously for all field quantities. The boundary-value problem for the scattered wave field is formulated as follows:

The strain–displacement and electric field–potential relations are

$$s_{i3} = u_{3,i}, \quad E_i = -\phi_{,i} \tag{15.1}$$

and the constitutive equations read, see Sect. 2.5.2

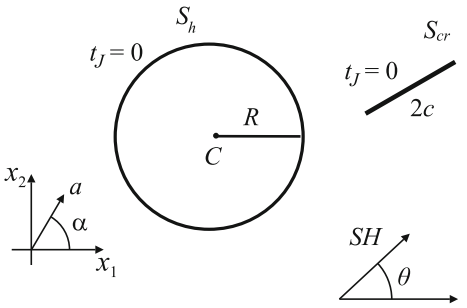

Fig. 15.1 A hole–crack system in a functionally graded piezoelectric plane under SH-type wave

$$\begin{aligned} \sigma_{i3} &= c_{44} s_{i3} - e_{15} E_i, \\ D_i &= e_{15} s_{i3} + \varepsilon_{11} E_i, \end{aligned} \tag{15.2}$$

Here s_{i3}, E_i, ϕ are the strain tensor, the electric field vector and the electric potential, respectively, $i = 1, 2$.

We assume that all material parameters, i.e. the mass density ρ, the shear stiffness c_{44}, the piezoelectric e_{15} and the dielectric permittivity ε_{11}, vary in the same manner exponentially with x:

$$c_{44} = c_{44}^0 e^{2\langle a,x\rangle}, \quad e_{15} = e_{15}^0 e^{2\langle a,x\rangle}, \quad \varepsilon_{44} = \varepsilon_{44}^0 e^{2\langle a,x\rangle}, \quad \rho = \rho^0 e^{2\langle a,x\rangle}. \tag{15.3}$$

Here, c_{44}^0, e_{15}^0, ε_{11}^0, ρ^0 are reference material constants, e.g. the material characteristics in the homogeneous case.

We use the notation of [3] where $u_J = (u_3, \phi)$, $J = 3, 4$; $s_{iJ} = \begin{cases} s_{i3}, J = 3 \\ E_i, J = 4 \end{cases}$, $\sigma_{iJ} = \begin{cases} \sigma_{i3}, J = 3 \\ D_i, J = 4 \end{cases}$ are the generalized displacement, strain and stress respectively. In absence of volume forces and electric charges the balance equations are given by

$$\sigma_{iJ,i} + \rho_{JK} \omega^2 u_K = 0, \quad J, K = 3, 4. \tag{15.4}$$

where $\rho_{JK} = \begin{cases} \rho, J = K = 3, \\ 0, J = 4 \text{ or } K = 4. \end{cases}$ Using the generalized stiffness tensor

$$C_{i33l}^0 = \begin{cases} c_{44}^0, i = l \\ 0, \quad i \neq l \end{cases}, C_{i43l}^0 = C_{i34l}^0 = \begin{cases} e_{15}^0, i = l \\ 0, \quad i \neq l \end{cases}, C_{i44l}^0 = \begin{cases} -\varepsilon_{11}^0, i = l \\ 0, \quad i \neq l \end{cases}$$

the generalized stress is $\sigma_{iJ} = C_{iJKl} u_{K,l}$, where $C_{iJKl} = C_{iJKl}^0 e^{2\langle a,x\rangle}$.

The crack's line S_{cr} and the hole's boundary S_h are assumed to be free of both mechanical traction and surface charges, i.e. an impermeable crack and hole are considered. Thus the boundary condition for the total traction on the crack or on the boundary of the hole are

$$t_J(x,\omega) = 0 \quad \text{on } S = S_{cr} \cup S_h. \tag{15.5}$$

where $t_J = \sigma_{iJ} n_i$ is the generalized traction, n_i are the components of the outward normal vector in every point of S.

The wave scattering by the hole–crack system in a functionally graded piezoelectric plane is governed by partial differential Eq. (15.4) with variable coefficients. Following the approach proposed in Chap. 14, see also Sect. 11.3 the smooth transform is applied to the displacement vector $u_J(x,\omega)$

$$u_J(x,\omega) = e^{-\langle a,x\rangle} U_J(x,\omega). \tag{15.6}$$

By this, the following system of partial differential equations with constant coefficients for the displacement vector $U_J(x,\omega)$ is obtained

$$C^0_{iJKl} U_{K,il} + (\rho^0_{JK}\omega^2 - C^0_{iJKi}|a|^2) U_K = 0. \tag{15.7}$$

Replacing the displacement component U_4 by introdusing the second equation of the system of Eq. (15.7) into the first one, the following equation for the mechanical displacement U_3 is obtained

$$U_{3,ii} + k^2 U_3 = 0. \tag{15.8}$$

where $k^2 = \dfrac{\rho^0}{a_0}\omega^2 - |a|^2$, $a_0 = c^0_{44} + \dfrac{e^{02}_{15}}{\varepsilon^0_{11}}$. Denote by $\omega_0 = \sqrt{\dfrac{a_0}{\rho^0}}|a|$ and consider the following cases with respect to the frequency ω, see Chap. 14:

(a) the case $\omega > \omega_0$, where we have $k^2 > 0$, which corresponds to the case of a wave propagation process;

(b) the case that $\omega = \omega_0$, where we have $k^2 = 0$ and no wave propagation occurs; the behavior of the solution is as in the static case;

(c) the case $\omega < \omega_0$, where we have $k^2 < 0$, which is the case of simple vibration.

The type of the dynamic behavior of the crack–hole system is governed by the frequency of the incident wave and the material properties of the inhomogeneous piezoelectric material. In this chapter we assume that the frequency of the incident wave fulfills the case (a).

Furthermore, suppose that $U_J(x,\omega)$ in Eq. (15.6) satisfies Sommerfeld-type condition at infinity, more specifically

$$U_3 = o(|x|^{-1}), \quad U_4 = o(e^{-|a||x|}) \quad \text{for} \quad |x| \to \infty. \tag{15.9}$$

Condition (15.9) ensures uniqueness of the scattering wave field u^{sc}_J for a given incident wave u^{in}_J. Following [1] it can be proved that the boundary value problem given by Eqs. (15.4), (15.5) in conjunction with condition (15.9) admits a continuous differentiable solution.

The displacement and the traction field of the incident SH-wave is a solution of Eq. (15.4). This solution is obtained by the use of the smooth functional transform

(15.6) and solution of Eq. (15.7) obtained by plane wave decomposition technique. For a plane SH-wave with an incident direction $\xi = (\xi_1, \xi_2)$, the displacement field at a given frequency and at an observer point x is as follows:

$$u_3^{in}(x,\omega) = e^{-\langle x, a+ik\xi\rangle}, \quad u_4^{in}(x,\omega) = \frac{e_{15}^0}{\varepsilon_{11}^0} u_3(x,\omega). \tag{15.10}$$

The corresponding traction field on S is

$$\begin{aligned} t_3^{in}(x,\omega) &= -a_0\langle n, a+ik\xi\rangle e^{<x,a-ik\xi>} \\ t_4^{in} &= 0. \end{aligned} \tag{15.11}$$

15.3 BIEM Formulation

The boundary value problem posed in Sect. 15.2 and consisting of Eqs. (15.4), (15.5) and (15.9) can be formulated by a system of traction boundary integral equations on S. For the considered problem it is a combination of the BIEM given in Chaps. 12 and 14:

$$\begin{aligned} & c_J(x) t_J^{in}(x) = C_{iJKl}(x) n_i(x) \int_{S_h} [(\sigma^*_{\eta PK}(x,y,\omega) u_{P,\eta}(y,\omega) \\ & - \rho_{QP}\omega^2 u^*_{QK}(x,y,\omega) u_P(y,\omega))\delta_{\lambda l} - \sigma^*_{\lambda PK}(x,y,\omega) u_{P,l}(y,\omega)] n_\lambda(y) dS_h \\ & - C_{iJKl}(x) n_i(x) \int_{S_h} u^*_{PK,l}(x,y,\omega) t_P^{in}(y,\omega) dS_h \\ & + C_{iJKl}(x) n_i(x) \int_{S_{cr}} [(\sigma^*_{\eta PK}(x,y,\omega) \Delta u_{P,\eta}(y,\omega) - \rho_{QP}\omega^2 u^*_{QK}(x,y,\omega) u_P(y,\omega))\delta_{\lambda l} \\ & - \sigma^*_{\lambda PK}(x,y,\omega) \Delta u_{P,l}(y,\omega)] n_\lambda(y) dS_{cr}, \quad x \in S. \end{aligned} \tag{15.12}$$

where $c_J(x) = \begin{cases} -\frac{1}{2}, & x \in S_h \\ -1, & x \in S_{cr} \end{cases}$, u^*_{QK} is the fundamental solution of (15.4), $\sigma^*_{iJQ} = C_{iJKl} u^*_{KQ,l}$ is the corresponding stress and $\Delta u_J = u_J|_{S_{cr}^+} - u_J|_{S_{cr}^-}$ is the generalized crack opening displacement of the crack S_{cr}. Furthermore, x and y denote the position vectors of the field and source point, respectively.

Recall that for u_J, u^*_{JK}, we apply Green's formula in the domain $\Omega_R \setminus (\Omega_\varepsilon^{cr} \cup \Omega_\varepsilon^h)$, where Ω_R is a circular domain with large radius R, Ω_ε^{cr} is a small neighborhood of the crack and Ω_ε^h is a small neighborhood of the hole. Applying the representation formulae for the generalized displacement gradient $u_{K,l}$, see [13], an integro-differential equation on $\partial\Omega_R \cup \partial\Omega_\varepsilon^{cr} \cup \partial\Omega_\varepsilon^h$ is obtained. Using the condition (15.9), the integrals over $\partial\Omega_R$ go to 0 for $R \to \infty$. Taking the limit $\varepsilon \to 0$, i.e. $x \to S$ and using the boundary condition (15.4), i.e. $t_J^{sc} = -t_J^{in}$ on S, the system of non-hypersingular traction BIE (15.12) is obtained and it is equivalent to the BVP defined by the Eqs. (15.4) and (15.5).

Equation (15.12) forms a system of integro-differential equations with respect to the unknown displacement u_J along the boundary S_h of the hole and to the crack opening displacement Δu_J along the crack line S_{cr}. The generalized displacement and traction of the scattered wave field at any point in the smoothly inhomogeneous piezoelectric plane can be determined by using the corresponding representation formulae, see Chaps. 4, 14, and the solutions of Eq. (15.12).

In order to solve Eq. (15.12) it is necessary to know the fundamental solutions for displacement and traction and their derivatives. The fundamental solution of (15.4) is defined as solution of the equation

$$\sigma^*_{iJM,i} + \rho_{JK}\omega^2 u^*_{KM} = -\delta_{JM}\delta(x,\xi), \tag{15.13}$$

where $x = (x_1, x_2)$ and $\xi = (\xi_1, \xi_2)$. The derivation of the fundamental solution was presented and discussed in Sect. 11.3.

15.4 Numerical Procedure

The numerical procedure for the solution of the posed BVP follows the numerical algorithm developed and validated in Chaps. 11 and 14. The hole boundary S_h and the crack line S_{cr} are discretized by quadratic boundary elements away from the crack-tips and special crack-tip quarter-point BE near the crack-tips to model the asymptotic behavior of the displacement and traction.

After the discretization procedure of the BIE, the solution of all types of integrals (see Chap. 4) and satisfying the boundary conditions, an algebraic system of equations for the crack opening displacement Δu_J along the crack S_{cr} and displacement u_J along the hole boundary S_h is obtained and solved. The displacement and traction wave field can subsequently be calculated in any point of the plane using the corresponding representation formulae, see Chap. 11. Following this procedure, a program code based on Mathematica and FORTRAN has been created.

The most essential quantities that characterize the mechanical and electric field concentrations are SIFs and SCFs. Following [7] for the pure elastic case, and [4, 10] for the piezoelectric case, the dynamic SCF and electric field concentration factor along the perimeter of a circular hole is defined as the ratio of the stress and electric field along the circumference to the maximum amplitude of the incident stress at the same point in the material without any defects, see Chap. 14. The normalized dynamic SCF $|\sigma_{\gamma\theta}/\tau_0|$ and the normalized dynamic EFCF $|e_{15}E_{\gamma\theta}/\tau_0|$ are calculated by using the formulae (14.19)

$$K_{III} = \lim_{x_1 \to \pm c} t_3\sqrt{2\pi(x_1 \mp c)}, \quad K_D = \lim_{x_1 \to \pm c} t_4\sqrt{2\pi(x_1 \mp c)}, \tag{15.14}$$

where t_J is the generalized traction at the point $(x_1, 0)$ close to the crack-tip.

The dynamic mechanical SIF K_{III} and the electrical displacement intensity factor K_D are obtained directly from the nodal traction values ahead of the crack-tip, see Chap. 2, Eq. (2.41). In case of a straight crack along the interval $(-c, c)$ on the Ox_1 axis, they are defined by formulae (12.14).

15.5 Numerical Results

In all examples the crack length is $2c = 5\,\text{mm}$ and the crack is discretisized by 7 BE. The first and the last BE are quarter point BE, while the remaining elements are ordinary quadratic BEs. Their lengths l_j are chosen as follows: $l_1 = l_7 = 0.375\,\text{mm}$, $l_2 = l_6 = 0.5\,\text{mm}$, $l_3 = l_5 = 1.0\,\text{mm}$, $l_4 = 1.25\,\text{mm}$. The hole has the radius $R = 5\,\text{mm}$ and its boundary is discretisized by 14 ordinary quadratic BEs.

There are in general two cases for mutual dispositions of the circular hole and finite straight line crack system in the homogeneous domain: (a) The crack ligament intersects the hole; (b) The crack line doesn't intersect the hole. For the simulation studies we will use, just for simplicity, the particular cases shortly quoted as: hole-horizontal crack configuration, i.e. the hole–crack system as shown in Fig. 15.2a and the ligament of the crack pass through the center C of the hole; hole-vertical crack configuration, i.e. the hole–crack system as shown in Fig. 15.2b and the line through the center of the hole and the center of the crack is perpendicular to the crack.

The inhomogeneity parameter $a = (a_1, a_2)$ in the inhomogeneity function $e^{2\langle a,x\rangle}$ is written in polar coordinates as $a = r(\cos\alpha, \sin\alpha)$ where α and r are the direction and the magnitude of the material gradient. Since there are no SIF and SCF results available for a hole–crack system in a piezoelectric plane with exponentially varying material properties subjected to time-harmonic SH-type wave, the validation of the numerical scheme is possible only by comparing the BIEM results with results of other authors for the homogeneous case. For this purpose the magnitude of the inhomogeneity gradient r in the developed program code is simply set to 0.

15.5.1 Validation Study

The proposed numerical procedure is validated by solution of two benchmark problems. The first test example considers an infinite homogeneous plane containing a circular hole with radius R and center $C(-e - R, 0)$ and a crack along the segment $(e, e+2c)$ on the Ox_1 axis subjected to SH-wave directed at an incident angle θ with respect to Ox_1 axis, see Fig. 15.2a. Results for this problem are published in [11], where the solution is obtained by the complex variable method based on Green's function for a single hole in a piezoelectric plane. The second benchmark example considers the first one but in the case the distance $d = 2e$ between the hole and the crack is 10 times the half-length of the crack c. In this case the computed SIFs coincide with the results obtained by: (a) Wang and Meguid [14] who studied a homogeneous

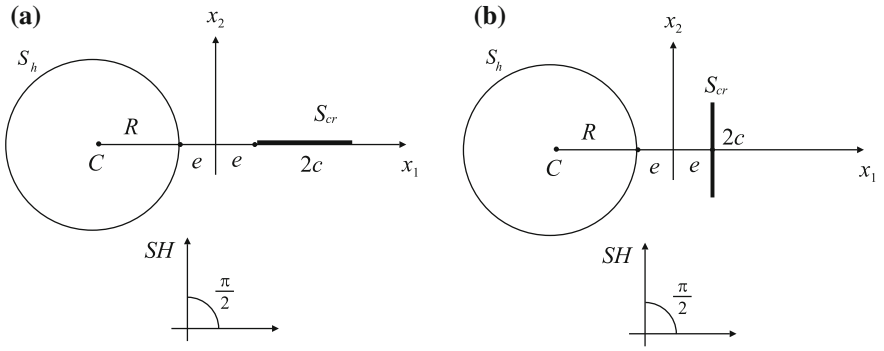

Fig. 15.2 The configurations of the hole–crack systems in numerical examples

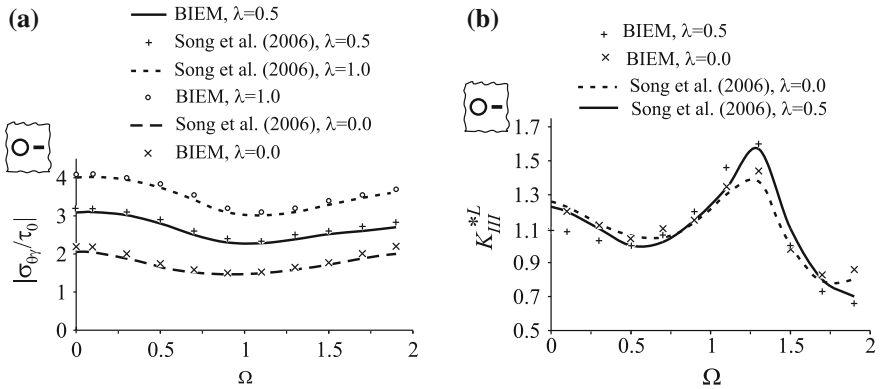

Fig. 15.3 SCF and SIF for a hole-horizontal crack system versus normalized frequency Ω of normal incident SH-wave propagating in a homogeneous piezoelectric plane: **a** SCF at observation point $\gamma = 0$; **b** K^{*L}_{III}

piezoelectric plane with a single crack; (b) Daros [2] who used a non-hypersingular traction BIEM to solve the same problem in the case of exponential inhomogeneous anisotropic plane. In the second test example the SCFs along the boundary of the hole coincide with the results obtained by Shindo et al. [10] for a single circular hole in a homogeneous piezoelectric plane under an incident SH-wave.

Figure 15.3a shows a comparison of the results for the SCF versus the normalized frequency $\Omega = c\sqrt{\rho^0/c^0_{44}}\omega$ at the observation point $A(-e, 0)$, i.e. $\gamma = 0$, obtained by the proposed method and by the complex variable method proposed in [11]. For this case the following data are used: $R = c = e$, $C = (-2e, 0)$, and $d = 2e$. Piezoelectric materials with different values of the coefficient $\lambda = \dfrac{e^{02}_{15}}{c^0_{44}\varepsilon^0_{11}}$ are considered: $\lambda = 0.5$, $\lambda = 1.0$ and $\lambda = 0$ for the case of isotropic material. The reference constants c^0_{44}, ε^0_{11} are given in Table 4.1 and the prescribed values of λ are

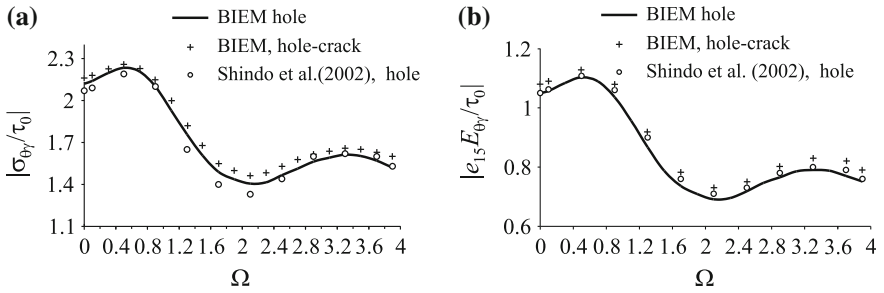

Fig. 15.4 SCF at observation point $\gamma = 0$ versus normalized frequency Ω of normal incident SH-wave propagating in a homogeneous piezoelectric plane: **a** Hole; **b** Hole-horizontal crack system at distance $d = 10c$

obtained by variation of e_{15}^0. The incident wave angle is $\theta = \pi/2$. Figure 15.3b shows the normalized dynamic SIF $K_{III}^* = K_{III}/\tau^0\sqrt{\pi c}$ at the left crack-tip for $\lambda = 0.5$, $\lambda = 0.0$. As can be seen, the BIEM results agree very well with those in [11].

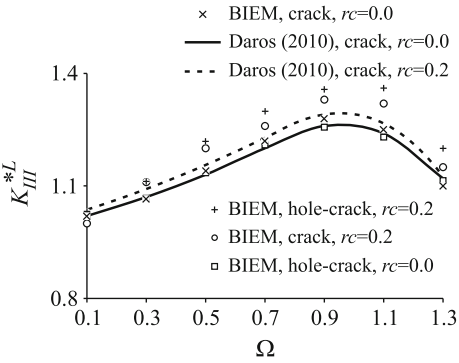

Fig. 15.5 K_{III}^{*L} for a system hole-horizontal crack at $d = 10c$ versus normalized frequency of normal incident SH-type wave propagating in an exponentially inhomogeneous piezoelectric plane

Figure 15.4 presents results for mechanical SCF and electrical field concentration factor EFCF versus normalized frequency Ω for the same hole-crack scenario as those in Fig. 15.2a but for the case that the distance between the hole and the crack is $d = 10c$. At this distance the hole–crack interaction is very weak and the solution for the hole–crack system recovers the solutions for the single hole and the single crack. In Fig. 15.4a, b the solutions are compared to the ones obtained by the proposed method for two different boundary-value problems in a piezoelectric PZT-4 homogeneous plane subjected to normal SH-wave: (a) a single anti-plane crack and (b) a system of hole–crack. Both solutions are almost identical. An additional comparison is done with solution obtained by Shindo et al. [10] for a single circular hole. The difference between three results is very small, namely less than 8 %. This indicates a high accuracy and convergence of the proposed numerical scheme in the considered frequency interval. Figure 15.5 shows SIF K_{III}^* at the left crack-tip of a crack from a

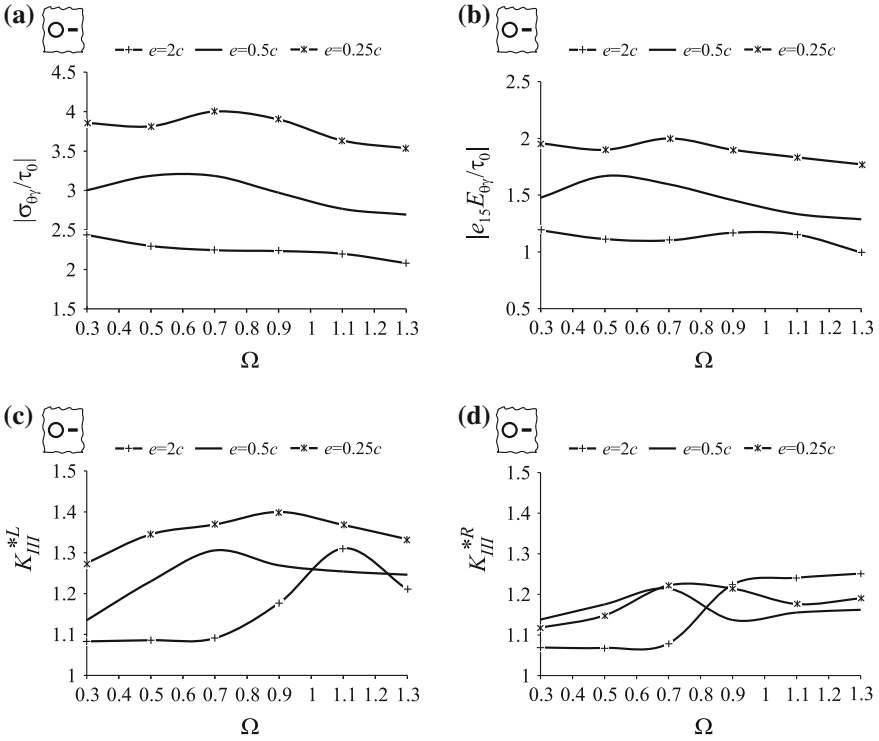

Fig. 15.6 Dynamic SCF and dynamic SIF versus normalized frequency Ω of normal incident plane SH-wave propagating in homogeneous piezoelectric plane with a hole-horizontal crack system as in Fig. 15.2a for different half-distances between hole and crack: **a** and **b** mechanical and electric field SCF at observer point $\gamma = 0$; **c** K_{III}^{*L}; **d** K_{III}^{*R}

hole–crack configuration given in Fig. 15.2a. The distance between the hole and the crack is $d = 10c$. The BIEM solutions for both: a single anti-plane crack and a hole–crack system in a homogeneous piezoelectric plane are very close. This is true also for inhomogeneous piezoelectric plane with normalized magnitude $r = 0.2/c$ and inhomogeneity direction $\alpha = 0$ where the results obtained by the non-hypersingular traction BIEM are very close to the solution obtained by Daros [2]. For the homogeneous case all three solutions are very close. For the inhomogeneous case the BIEM results are slightly higher by 7–9 % than the solutions in [2].

15.5.2 Simulation Results

The aim of the simulation study is to provide some insight in the effect of various system parameters on the stress and electric field concentrations. These parameters are: (a) the frequency and incident angle of the applied load, (b) the direction α and magnitude r of the material inhomogeneity, (c) the electro-mechanical coupling, (d)

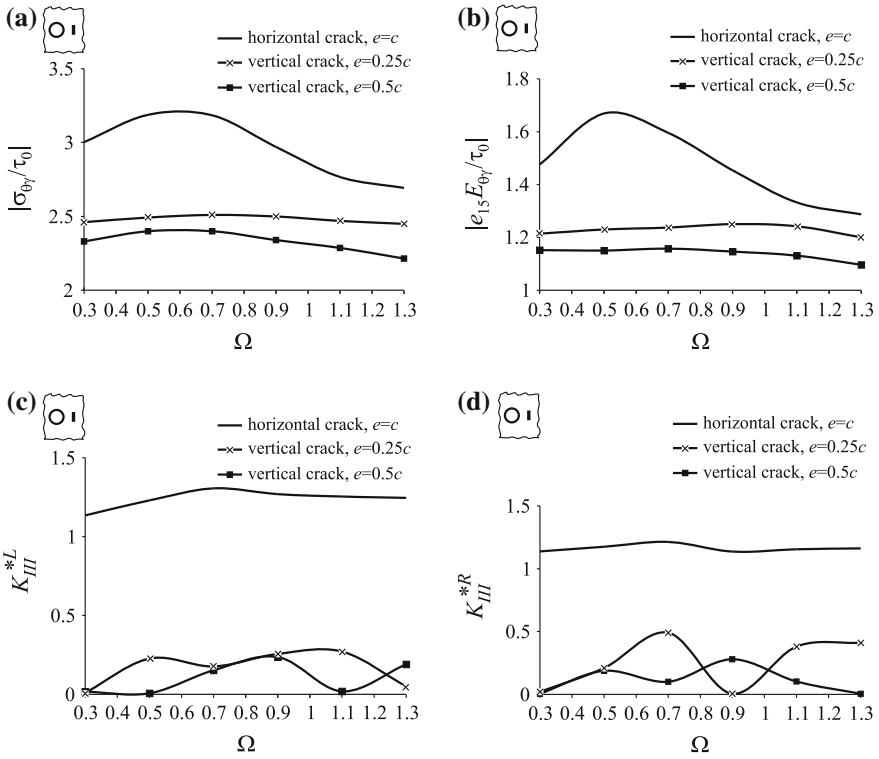

Fig. 15.7 Dynamic SCF and SIF versus normalized frequency Ω of normal incident plane SH-wave propagating in homogeneous piezoelectric plane with a hole–vertical crack system for different half-distances between hole and crack: **a** and **b** mechanical and electric field SCF at observer point $\gamma = 0$; **c** K_{III}^{*L}; **d** K_{III}^{*R}

the wave–hole–crack and wave–material interaction and (e) the geometry and type of the hole–crack scenario.

Figure 15.6 shows dynamic stress concentration fields in a system hole-horizontal crack subjected to normal incident SH-wave propagating in a homogeneous piezoelectric plane with normalized frequency Ω in the interval [0.3, 1.3]. In the hole-horizontal crack configuration (see Fig. 15.2a), the following cases for the half-distance between the hole and the crack are considered: $e = 2c$, $e = 0.5c$, and $e = 0.25c$. Figure 15.6a, b for the mechanical stress and electric field concentration factors at observer point $A(-e, 0)$, i.e. $\gamma = 0$, clearly demonstrates that the stress concentration field along the hole boundary is higher when the crack is closer. As an illustration, for example at the normalized frequency $\Omega = 0.9$, the difference between mechanical and electrical stress concentration factors at hole-horizontal crack configuration with $e = 2c$ and $e = 0.25c$ is 74.8 and 62.6 %, correspondingly. Figure 15.6c, d reveal the effect of the hole–crack geometry on the stress intensity factors K_{III}^{*L} at the left crack-tip and K_{III}^{*R} at the right crack-tip. This effect is stronger

for the left crack-tip which is closer to the hole, while at the right crack-tip the effect of hole–crack interaction is weaker.

The numerical results in Fig. 15.7 concern the hole–vertical crack configuration (see Fig. 15.2b) for two values of the half-distance between the hole and the crack: $e = 0.5c$ and $e = 0.25c$. The incident angle of the SH-wave is $\theta = \pi/2$ and the piezoelectric plane is homogeneous. The results for the hole–vertical crack configuration are compared with results for the hole–horizontal crack configuration. The following conclusions can be made: (a) The dynamic stress concentration field near the defects expressed by the stress concentration factors along the hole's boundary and stress intensity factors at the crack–tips are reduced significantly when the crack is vertical. As an illustration, for example at the normalized frequency $\Omega = 0.7$ the SCF is decreased by 32.6 and 26.8 % in the case of vertical crack with half-distance between hole and crack of $e = 0.5c$ and $e = 0.25c$, respectively. Figure 15.7c, d show that SIFs are reduced strongly in the case of vertical crack. The configuration hole–vertical crack leads to a reduced stress concentration field in comparison with the case of a horizontal crack. (b) The sensitivity of the stress field to the half-distance e is greater in the case of horizontal crack, see Fig. 15.7a, b.

The key parameters responsible for the integrity and durability of the engineering structures made by graded PEM are the factors considered here, such as characteristics of the applied dynamic load, elastic, electric and piezoelectric properties of the material, the anisotropy and the nature of material inhomogeneity, existence of defects of different type, geometry of the defect and their mutual position and interaction.

15.6 Conclusion

A two-dimensional, dynamic time–harmonic anti-plane analysis of functionally graded piezoelectric plane with an exponential spatial variation of its material properties and weakened by a system of a crack and a hole is presented. The analysis is carried out using a non-hypersingular, traction BIEM that numerically is treated by discretizing the crack and the hole boundary with quadratic boundary elements and using standard collocation schemes. The basic problem comprising of a hole–crack system in an infinite sheet of FGPM is solved for the case of propagating SH waves. The results of these numerical simulations show that the stress concentration field at the crack tips and near the hole are strongly influenced by the presence of material inhomogeneity. The simulations clearly show that the dynamic stress and electric field concentrations are sensitive to different key parameters like geometry of the defects, type and characteristics of the loading, electromechanical coupling, anisotropy, material gradient and its direction, the relation between the inhomogeneity magnitude and the defect size, the mutual hole–crack configuration, the wave-defect and wave-material interactions, etc.

References

1. Akamatsu M, Nakamura G (2002) Well-posedness of initial-boundary value problems for piezoelectric equations. Appl Anal 81:129–141
2. Daros CH (2010) On modelling SH-waves in a class of inhomogeneous anisotropic media via the boundary element method. Z Angew Math Mech (ZAMM) 90:113–121
3. Davi G, Milazzo A (2001) Multidomain boundary integral formulation for piezoelectric materials fracture mechanics. Int J Solids Struct 38:7065–7078
4. Fang XQ (2008) Multiple scattering of electro-elastic waves from a buried cavity in a functionally graded piezoelectric material layer. Int J Solids Struct 45:5716–5729
5. Lekhnitski SG (1968) Anisotropic plates. Gordon and Breach, New York
6. Müller R, Dineva P, Rangelov T, Gross D (2012) Anti-plane dynamic hole–crack interaction in a functionally gradede piezoelectric media. Arch Appl Mech 82:97–110
7. Pao YH, Mow CC (1971) Diffraction of elastic waves and dynamic stress concentration. Crane Russak, New York
8. Qin Q, Lu M (2000) BEM for crack-inclusion problems of palne thermopiezoelectric solids. Int J Numer Meth Eng 40:1071–1088
9. Qin Q, Mai W (2002) BEM for crack–hole problems in thermopiezoelectric materials. Eng Fract Mech 69:577–588
10. Shindo Y, Moribayashi H, Narita F (2002) Scattering of antiplane shear waves by a circular piezoelectric inclusion embedded in a piezoelectric medium subjected to a steady-state electrical load. Z Angew Math Mech (ZAMM) 82:43–49
11. Song T, Li H, Dong J (2006) Dynamic anti-plane behaviour of the interaction between a crack and a circular cavity in a piezoelectric medium. Key Eng Mater 324(325):29–32
12. Sosa H (1991) Plane problems in piezoelectric media with defects. Int J Solids Struct 28:491–505
13. Wang CY, Zhang Ch (2005) 2 D and 3 D dynamic Green's functions and time-domain BIE formulations for piezoelectric solids. Eng Anal Boundary Elem 29:454–465
14. Wang XD, Meguid SA (2000b) Modelling and analysis of the dynamic behaviour of piezoelectric materials containing interfacing cracks. Mech Mater 32:723–737
15. Xu LY, Rajapakse RKND (1998) Boundary element analysis of piezoelectric solids with defects. Eng Fract Mech 29B:655–669
16. Zhou ZD, Zhao SX, Kuang ZB (2005) Stress and electric displacement analysis in piezoelectric media with an elliptic hole and a small crack. Int J Solids Struct 42:2803–2822

Index

P. Dineva et al., *Dynamic Fracture of Piezoelectric Materials*,
Solid Mechanics and Its Applications 212, DOI: 10.1007/978-3-319-03961-9,